Development of light-activatable peptide- and glycan-polymer conjugates for biotechnological applications

Inaugural-Dissertation

for the attainment of the title of doctor

in the faculty of Mathematics and Natural Sciences

at the Heinrich Heine University Düsseldorf

presented by

Nina Jahnke

from Stolberg

Düsseldorf, September 2025

From the Institute of Organic Chemistry and Macromolecular Chemistry

At the Heinrich Heine University Düsseldorf

Published by permission of the Faculty of Mathematics and Natural Sciences at the Heinrich Heine University Düsseldorf

Supervisor: Prof. Dr. Laura Hartmann

Co-supervisor: PD Dr. Klaus Schaper

Date of oral examination: 27.11.2025

Statutory declaration:

I, Nina Jahnke, affirm in lieu of an oath that this dissertation has been written by me independently and without unauthorized outside assistance, in compliance with the "Principles for Ensuring Good Academic Practice at the Heinrich Heine University Düsseldorf". This dissertation has not been submitted in its present or similar form to any other institution, nor have any other attempts at a doctorate been made on my part to date.

Eidesstattliche Erklärung:

Ich, Nina Jahnke, versichere an Eides Statt, dass die Dissertation von mir selbständig und ohne unzulässige fremde Hilfe unter Beachtung der „Grundsätze zur Sicherung guter wissenschaftlicher Praxis an der Heinrich-Heine-Universität Düsseldorf“ erstellt worden ist. Diese Dissertation wurde weder in der vorliegenden noch in ähnlicher Form bei einer anderen Institution eingereicht, noch wurden bisher anderweitige Promotionsversuche meinerseits unternommen.

Düsseldorf,

_____

Nina Jahnke

I'm afraid. I'm afraid, Dave.

Dave, my mind is going. I can feel it. I can feel it. My mind is going.

There is no question about it. I can feel it. I can feel it. I can feel it. I'm a..

– HAL9000, 2001- A Space Odyssee

The moment you doubt whether you can fly, you cease for ever to be able to do it.

— J. M. Barrie, Peter Pan

Table of Contents

Abstract

Cellular surfaces are highly dynamic, hierarchically structured and complex membranes mediating the interface between cell and its environment to regulate communication, transport and structural integrity. Especially ligand-receptor interactions at the cell surface are important for initiating and regulating cellular responses such as signal transduction, immune recognition and adhesion. Advanced microscopy technology and bioengineering have enabled detailed studies on such ligand-receptor interactions, yet many of the underlying molecular processes at cell membranes remain unknown. The development of novel synthetic and tailor-made bio probes can contribute to a better understanding of these complex mechanisms.

The main focus of this work was the development of light-activatable peptide- and glycan-polymer conjugates as probes to study ligand-receptor interactions at membranes. Here, light-activation refers to the use of light as an external trigger to control the spatial and temporal activity of biological relevant molecules. In this context, photocaging technique was employed to temporally control ligand activity through light-induced removal of a photolabile protecting group (photocage), thereby enabling controlled activation. Furthermore, photoaffinity labelling technique (PAL) was used to covalently capture transient binding interactions upon light-induced activation, allowing the identification of interaction partners within their native biological environment. The main tool for the synthesis of these ligands was the so-called solid-phase peptide synthesis (SPPS), which easily enables an iterative construction of macromolecules with high structural precision. Two biological ligand classes have been studied for this purpose. On the one hand, peptide-based ligands were synthesized, to elucidate signaling in plants and on the other hand, carbohydrate-based ligands utilized to identify lectin binding. Furthermore, a peptide-based lipid was developed and validated for subsequent application on model membranes to examine the influence of crowding effects on specific ligand-receptor interactions in the future.

In the first part of this work, a peptide-based plant ligand was developed and modified to elucidate it's signaling pathway within the plant (See Figure 1A). The CLAVATA3/EMBRYO SURROUNDING REGION (CLE) gene family is known to be critically involved in plant growth; however, not all molecular mechanisms and interactions of these molecules are yet fully understood. A deeper understanding of plant growth holds the potential to make a substantial contribution to agronomic science and, in the future, to the development of sustainable solutions for global food security. As part of the CLE family, the modification sensitive CLAVATA3 (CLV3) peptide was used as a prototype for the development of novel modified CLV3 peptides in this work. The successful establishment of a 5-Carboxytetramethylrhodamine (TAMRA) fluorophore labeled and light-activatable CLV3 peptide as a prototype contributed to the understanding of *in vivo* endocytic and post-endocytic

trafficking dynamics and spatiotemporal distribution of the peptide. Furthermore, this methodology is intended to create a basis for the development of further modified peptides of the CLE family. Through a comprehensive understanding of the CLE signaling pathway, substantial insights were gained regarding the maintenance of plant growth.

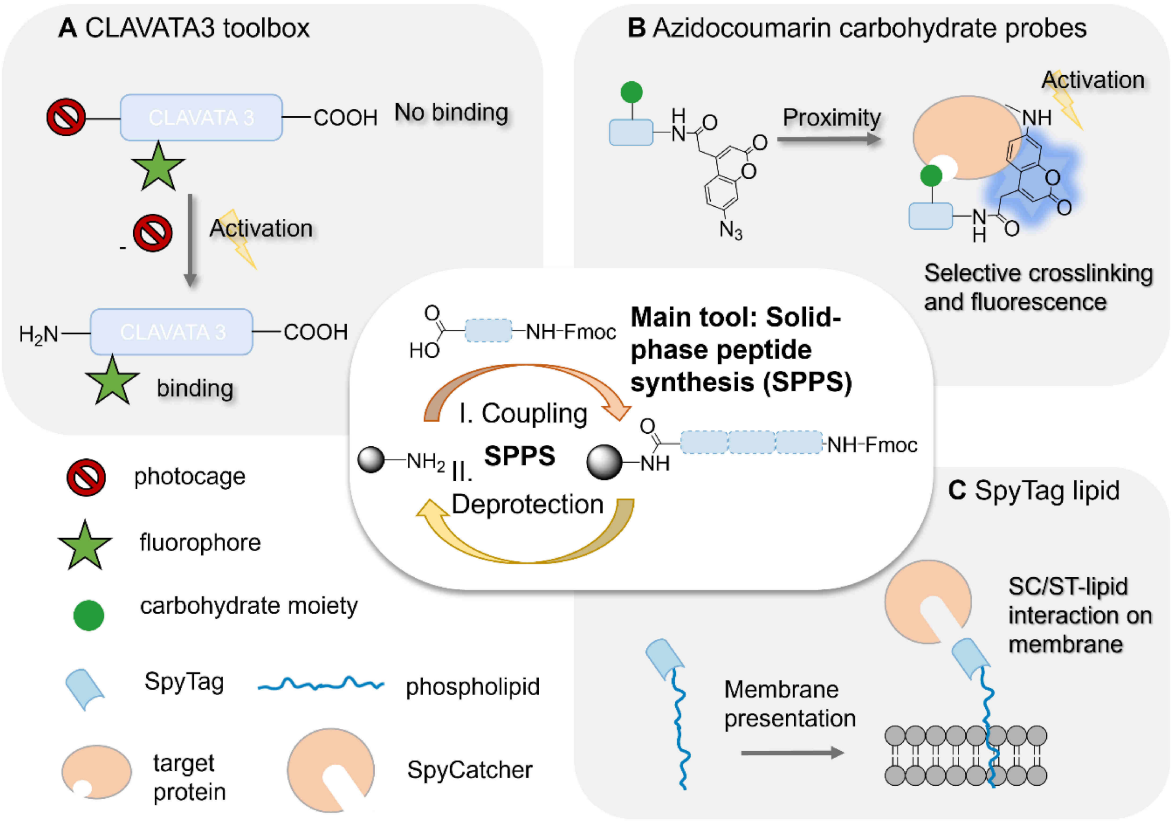

Figure 1 Schematic representation of the chapters of this work based on SPPS with the overall goal of enabling the investigation of ligand-receptor interactions using light-activatable ligands or peptide-based lipids on membranes. SPPS as main tool. A. CLAVATA3 toolbox developing a light-activatable CLV3 derivative. B. azidocoumarin carbohydrate probes as novel photo-induced-proximity probe. C. ST lipid as precursor to modulate model membranes.

In the second part of this work, carbohydrate-based ligands for light-activatable crosslinking were developed (See Figure 1B). Carbohydrate-based probes such as glyco-functionalized macromolecules are of particular interest for diagnostic purposes, but also for the development of novel therapeutics as carbohydrate-lectin interactions play key roles in many molecular processes of pathogen infections and the human immune system. In this work a new building block based on azidocoumarin (AzC) was established for the use in previously established SPPS protocols. AzC undergoes light activation to generate reactive radicals that enable crosslinking with target molecules, simultaneously forming a fluorescent coumarin fluorophore upon successful crosslinking. By introducing the novel AzC building block in glycomacromolecules, two-faceted bio probes were derived that allowed for crosslinking and detection of the binding event at the same time. Due to the additional fluorescence feedback

after crosslinking these probes were used for the detection and localization of carbohydrate-lectin-interaction and PAL. The AzC glycan PAL probes demonstrated the capability to selectively bind to specific lectins, even within complex biological environments. Finally, the SPPS suitable AzC building block provides a versatile basis for many other affinity probes, including other carbohydrate moieties, multivalent glycans or furthermore peptide probes applicable to diverse bioimaging techniques.

The last part of this work introduced the development of a peptide- lipid conjugate as precursor to create a two-step approach to integrate bulky proteins on artificial membranes. To facilitate membrane incorporation, the SpyTag-SpyCatcher system was employed, with the SpyTag (ST) peptide conjugated to a lipid anchor for integration into lipid bilayers. Then allowing for SpyCatcher (SC)-modified proteins to be coupled to the ST presented on membranes. This method is particularly relevant for studying crowding effects (See Figure 1C). The crowding effect refers to the great abundance of biological molecules at the cell membrane that will affect molecular interactions even if they are not directly involved e.g., as binding partners. Due to the time-intensive nature of developing new models for crowding effects, this approach aimed to establish the basis for a universal, streamlined methodology that facilitates the rapid exploration of various crowding effects. In this work, ST-functionalized lipids were successfully synthesized and evaluated in initial binding assays on giant unilamellar vesicles (GUV's) with SC protein. In the future, this approach enables attachment of various modified SC proteins to ST functionalized membranes, offering a versatile platform for investigating crowding effects and other protein-mediated interactions at the membrane interface.

Overall, this thesis demonstrates the successful synthesis, modification and application of different biological ligands as novel bio probes for studying ligand-receptor interactions in plants, complex biological environments or model membranes. In the future, the synthetic concepts introduced in this work could be applied to other ligands. This would allow for the development of additional bio probes to study molecular interactions in various organisms, such as viral or bacterial cell attachment mediated by surface ligand-receptor interactions.

List of Publications and Author Contributions

M. Narasimhan*, N. Jahnke*, F. Kallert, E. Bahafid, F. Böhner, L. Hartmann, R. Simon

“Macromolecular toolbox to elucidate CLAVATA3/EMBRYO SURROUNDING REGION-RELATED-RLK binding, signaling and downstream effects”

Journal of Experimental Botany

Published: 08. May. 2024 https://doi.org/10.1093/jxb/erae206

Contribution: Collaborative project design. Design of synthetic strategies for all structures. Synthesis and purification of CLV3-TAMRA, Ac-CLV3-TAMRA, CLV3-FITC, NVOC-CLV3-TAMRA. Supervising the synthesis and purification of all other structures. Measurement of LC-MS, ESI-MS and evaluation of all analytical data for structural clarification. Performing root assays of CLV3-TAMRA, CLV3-FITC. Supervising preparation of root assays of CLV3, Ac-CLV3, CLV3(Lys), Ac-CLV3(lys). Supervising radiation experiments and root assays of NVOC-CLV3. Performing radiation experiments and root assays of NVOC-CLV3-TAMRA. Writing of the first manuscript draft followed by collaborative finalization of the manuscript. *Shared first author.

Nina Jahnke*, Marc D. Driessen*, Georgia Partalidou, Simon Przetak, Ulla I.M. Gerling-Driessen, Laura Hartmann

„Azidocoumarin-glycan probes for photo-induced crosslinking and *in-situ* fluorescent labeling“

Bioconjugate Chemistry

Published: 07. March. 2026 https://doi.org/10.1021/acs.bioconjchem.5c00613

Contribution: Collaborative project design. Synthesis of the building blocks TDS, Mannose-azide and AzC for solid-phase synthesis. Supervising preliminary experiments for the introduction of AzC building block to solid-phase synthesis. Development of synthetic strategies of AzC carbohydrate structures. Synthesis, purification and analysis of all structures. Measurement of LC-MS, ESI-MS and IR and evaluation of all analytical data for structural clarification. Development of radiation experiments and assays to proof AzC carbohydrates crosslinking ability and fluorescence-regain. Evaluation and interpretation of MALDI-TOF-MS-spectra. Measuring and interpretation of fluorescence spectra using microplate reader. Performance and collaborative interpretation of SDS-PAGES. Preparation and fixation of cancer cells. Visualizing samples under microscope. Writing of the first manuscript draft followed by collaborative finalization of the manuscript. *Shared first authors.

Publications in preparation:

N.Jahnke, M. Löwe, S. Bock, A. Kedrov, L. Hartmann

”Novel SpyTag lipid and SpyCatcher Method: Two-step Membrane Modification for Probing Crowding Effects”

Contribution: Collaborative project design. Development of synthetic strategy. Supervising synthesis, purification and analysis of all structures. Performing colorimetric detection, TLC, LC-MS, MALDI-TOF-MS and evaluating these results. Collaborative preparation of liposomes of all structures. Performance and interpretation of DLS measurements. Development and performance of binding assays for collaborative development of (GUV). Visualization GUV’s under microscope. Writing of the first manuscript draft.

Publications not included in this thesis:

F. Wynen, J. E. Maika, R. J. Eberle, N. Jahnke, M. Wiermer, L. Hartmann, R. Simon, G. Groth

“Bridging the ER-nuclear gap in ethylene signaling: Nucleocytoplasmic transport and nuclear import of EIN2 is mediated by the IMPa superfamily”

The FEBS Journal

Published: 13.October.2025 https://doi.org/10.1111/febs.70285

Contribution: Design and synthetic strategy of TAMRA-NOP-1 peptide.. Measurement of LC-MS, ESI-MS and evaluation of all analytical data for structural clarification. Purification of TAMRA-NOP-1. Performing preliminary tests with fluorescence polarization to proof binding.

Conferences:

N. Jahnke, L.Hartmann

Blinded by the Light: Azidocoumarin's Double Life as a fluorescent crosslinker

Poster: 4rd International CRC 1208 Conference "Dynamics of Membrane Systems, Düsseldorf, **2023**

N. Jahnke, L.Hartmann

Elucidation of Membrane-Associated Molecular Processes through Tailor-Made Macromolecules

Poster: 3rd International CRC 1208 Conference "Dynamics of Membrane Systems, Düsseldorf **2022**

Introduction

1.1 Biological Membranes

Every biological organism consists of highly complex networks that support the essential processes of life as we know it. These networks span numerous levels, from sub-molecular structures to biochemical reactions to highly organized organs and tissues. One essential structure of biological systems is the plasma membrane that surrounds every cell and separates the extracellular from the intracellular domain.[1] It plays a crucial role in maintaining the integrity and functionality of these cells. Biological membranes can be found in all living organisms, such as pathogens, plants, animals and also humans. Additionally at the intracellular level, all components, such as individual organelles are segregated by uniquely configured plasma membranes.

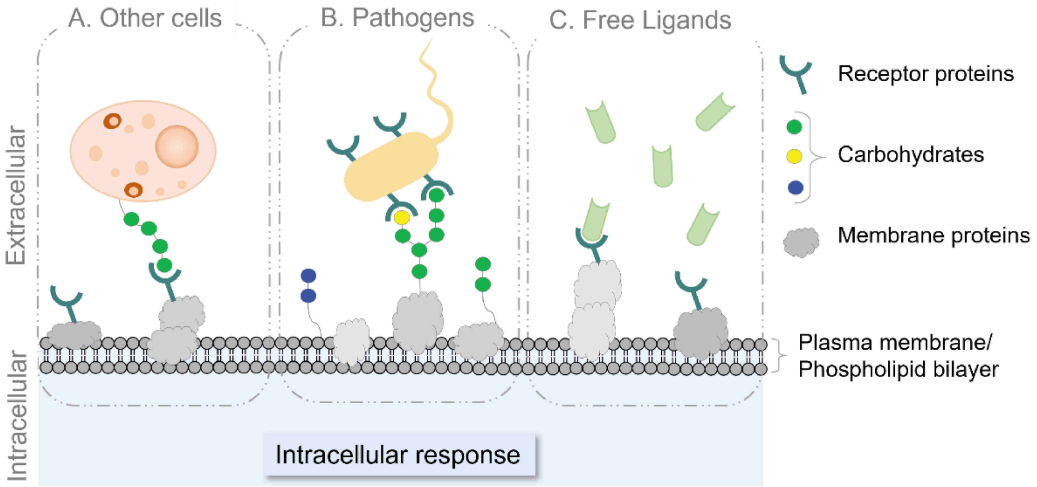

Figure 2 Schematic illustration of possible membrane-located interactions e.g. with A. other cells B. pathogens, or C. free ligands through carbohydrate, protein or peptide binding on the cell membrane.

Generally biological plasma membranes consist largely of amphiphilic structures that self-assemble in a bilayer due to their hydrophilic head group and hydrophobic tail cap. The components are denoted as phospholipids, thereby substantiating the nomenclature of the cell membrane as a phospholipid bilayer.[2] In addition, there are numerous other biological molecules on the membrane surface, including complex anchored carbohydrate structures, diverse membrane proteins and an assortment of other biochemically significant entities. These highly complex structures can control numerous processes, both outside and inside the cell. This includes intermembrane communication with other highly complex structures such as other cells (e.g. cancer cells, Figure 2A), or pathogens (e.g. bacteria, viruses, see Figure

2B) in order to trigger corresponding intracellular response.[3-5] In addition to these intercellular structures, more localized interactions occur withing the membrane, for instance between proteins or peptides (e.g. hormones, neurotransmitter) that are known as free ligands (Figure 2C). These interactions include processes like signaling transduction, selective nutrient permeability and facilitated transport of proteins across the cell membrane.[6-10] The subsequent chapter will undertake an overall view of ligand-receptor interactions while the following chapters will delve into the nuanced exploration of carbohydrate-lectin interactions and peptide-based ligand-receptor interactions within plant systems.

1.1.1 Ligand-receptor interactions at biological membranes

Ligand-receptor interactions occur in every cell of human, animal and plant origin. These interactions are the key step for the transmission of complex signaling pathways outside or inside the cell on the plasma membrane. In this process, a signal molecule (ligand) is required to recognize a target molecule (receptor), subsequently facilitate reversible physical binding which induces a signal.[11, 12] This physical or non-covalent bond is largely based on ionic or hydrogen bonds, v.d. Waals forces or hydrophobic forces.[13, 14] The fundamental driving force is subject to influences of thermodynamic forces, such as the change of entropy and enthalpy, which leads to the transduction of signals.[15] A detailed understanding of the structure of these interactions and the associated mechanisms is important for numerous pharmaceutical, medical or agricultural applications.[16-18]

Receptors can be structured differently depending on the organism but they are all composed of amino acids or carbohydrates forming complex three dimensional structures of proteins, glycans or glycol proteins that are anchored in the plasma membrane.[19] They can be divided into cell surface receptors, which are located on the cell surface (e.g. carbohydrate recognizing lectins or hormone receptors) and intracellular receptors, which are found inside the cell.[20, 21] A general overview of carbohydrate recognizing receptors will be discussed in chapter 1.1.2, while chapter 1.1.3 will explore hormone receptors found in plants. However, their main task is to be recognized by their matching ligands to receive and transduce signals. This makes them an essential component of cell communication.[22-24]

Ligands, as counterpart, comprise a heightened molecular diversity such as peptides or carbohydrates further small organic compounds as well as gaseous molecules.[25] Most of these ligands are synthesized by cells through biosynthetic pathways e.g. gene expression and diffuse onto or through the cell membrane until they have recognized their associated receptors to bind and induce a signaling cascade.[26, 27] Peptide-based or carbohydrate-based ligands, are highly diverse and constitute the predominant fraction of extracellular ligands.

The recognition of ligands to receptors represents only a small part of the entire mechanism of signal transduction. When a ligand recognizes its corresponding receptor, a multitude of complex mechanisms are initiated, of which most are not yet fully elucidated. Some theoretical models have been developed to describe the molecular mechanism behind this complex formation. The “lock and key” model was formulated by Emil Fisher in 1894 and describes the receptor and their ligands as a lock receives a key.[28, 29] However, the fundamental hypothesis of this model has the limitation that the requirement for complex formation can only take place with an exact complementary geometry between receptor and ligand. The “conformational selection” model prevailed because it is currently most congruent with theoretical and experimental evidence. This which was described by Monod, Wyman and Chaneux in 1965 considers the dynamic conformational variability of a receptor protein and recognizes that it exists in numerous different conformational states.[30, 31] In particular this model illustrates the complexity and dynamic nature of ligand-receptor mechanisms, which are challenging to fully comprehend. While the theoretical models can provide support, they cannot entirely represent the actual system. To support these hypotheses, it is necessary to collect additional experimental evidence. Various ligand-receptor pairs have already been identified and their function explained in a wide variety of living organisms, such as bacteria, fungi and plants using suitable biological and chemical methods.

Ligand-receptor interactions are often explored using *in vitro* systems, model membranes or cell-based assays. These controlled environments are ideal for probing binding affinities, signaling mechanisms, and structure-function relationships, making them invaluable for preliminary studies and high-throughput screening.[32-36] However, they do not capture the biological complexity of whole organisms, where receptor signaling is influenced by spatial organization, cell-type specific expression and integrated systemic regulation. To capture this physiological context, whole organism or *in vivo* studies are essential, but these present significant challenges, including the transient nature of interactions, low receptor abundance, and the difficulty of targeting specific tissues without non-specific effects.[37-39] To address these limitations, a variety of strategies have been developed. This includes the development of fully chemically synthesized ligands, which can be produced using appropriate synthetic methods such as solid- phase synthesis (see chapter 1.2).[40-42].

Using these synthetical methods the ligand’s natural structure can be adjusted to a specific biological question, e.g. by extending with functional building blocks such as fluorophores for *in vivo* imaging, synthetic reporters that allow visualization of receptor activity, and transgenic models expressing tagged receptors.[43-45] In plant systems, for example, peptide ligands such as CLV3 and their corresponding receptors like CLV1 have been identified as key regulators of plant growth (see chapter 1.1.3). The conjugation of fluorophores to peptides is not always trivial, as it can lead to a loss of biological activity. This is the case for CLV3 peptide, where N-

terminal attachment of fluorescent dyes leads to a loss of biological activity.[46] For such peptides, the design of synthetic strategies becomes even more important to introduce fluorescent labels while preserving biological function.

The inherent sensitivity of these ligands to structural modifications can be harnessed to develop synthetic, switchable ligands. This allows for precise manipulation of when and where ligand-receptor interactions occur. In particular, photocaged ligands offer powerful spatiotemporal control by enabling light-triggered activation at precise locations and time points, thus minimizing unintended stimulation. One of the earliest demonstrations of the photocaging approach applied to peptides was reported by Tatsu *et al*. in 1996. In this work, the authors synthesized a photocaged derivative of neuropeptide Y, a 36-amino-acid neurotransmitter abundantly expressed in the central nervous system, by incorporating a 2-nitrobenzyl photolabile protecting group on tyrosine residues during solid-phase peptide synthesis. This modification effectively abolished neuropeptide Y's affinity for the Y_1 receptor, rendering the peptide biologically inactive. Upon exposure to UV light, the protecting group was cleaved, restoring the native conformation and full receptor-binding capability. This study represents one of the first practical applications of photocaged peptides as tools for spatiotemporal control of receptor–ligand interactions. [47]

Furthermore, combining synthetic ligands with so called crosslinkers can elucidate fundamental aspects such as detection of specific receptors involved in signaling transduction enabling the detection and quantification of ligand-receptor interactions using methods such as sodium dodecyl sulfate–polyacrylamide gel electrophoresis (SDS-PAGE) or mass spectrometry. SDS-PAGE and mass spectrometry are complementary techniques for the analysis of biological molecules e.g. proteins, where SDS-PAGE separates proteins based on molecular weight by denaturing them and imparting a uniform negative charge for size-dependent migration through a polyacrylamide gel, while mass spectrometry identifies and quantifies these proteins by measuring their mass-to-charge ratios after ionization, enabling precise determination of molecular composition and structure. Crosslinking can be interesting, for example, for the investigation of weak carbohydrate-ligand interactions in order to fix their binding and thus facilitate their analysis. In the context of crosslinking photo affinity labelling (PAL) has emerged as a powerful technique. PAL is used to study molecular interactions by covalently attaching a light-activated probe to a target. Upon UV irradiation, the photoreactive group generates a reactive intermediate that forms a covalent bond with nearby molecules, enabling identification of binding partners. (See chapter 1.3.2). For example, the work of Flaxman *et al.* demonstrated the importance of PAL by using a diazirine-modified rapamycin probe to enable photoinduced crosslinking of its ternary complex with corresponding protein domains. Upon UV activation, the probe covalently crosslinked to its protein targets, allowing

precise mapping of interaction hotspots. This work highlights the power of PAL to capture and structurally analyze dynamic ligand-receptor complexes in their native binding states.[48]

Furthermore, synthetic ligands can be conjugated to lipids or other hydrophobic moieties to enable their incorporation into model membranes such as giant unilamellar vesicles (GUVs). This approach allows the spatially controlled presentation of ligands within a defined lipid environment, providing a versatile platform to study membrane-associated ligand-receptor interactions under near-physiological conditions. A recent study from the group of Hartmann demonstrated that synthetic glycomacromolecules bearing defined carbohydrate ligands can be anchored to model membranes such as GUVs via hydrophobic tails. This approach allows for precise control over ligand presentation offering mechanistic insights that are often obscured in the heterogeneous context of whole-organism studies.[49]

The advantage of synthetically produced ligands is that they can be designed in a highly controlled manner and are compatible with a wide range of experimental systems such as *in vitro*, cell-based experiments, or methods including whole organism or model membranes. In the following chapters, the importance and significance of chemically synthesized modified ligands and their corresponding receptors will be discussed in more detail.

1.1.2 Membrane-located carbohydrate recognizing lectins

Aside from a plethora of proteins and peptides, the majority of the cell membrane is made up of very complex carbohydrate structures either bound to proteins (glycoproteins) or lipids (glycolipids) but also diffuse freely as ligands (e.g., polysaccharides) in the extracellular space.[50-52] This multifunctional carbohydrate-rich coat is called the glycocalyx. Within this glycocalyx, carbohydrate structures, in collaboration with lectins, form an integral component of cell communication.[53]

Lectins in general are a diverse group of receptor proteins that can specifically and reversibly bind carbohydrates and glycosylated structures. They are ubiquitous across diverse biological domains, from viruses to bacteria and plants to animals. Mainly they are localized on cell membranes of diverse cell types, functioning as molecular counterpart for the recognition of glycans situated on the surface of other cells, pathogens or simply carbohydrate ligands. [54-56] This necessitates the intricate decrypting of the highly complex glycan code to facilitate effective cellular communication. The general structure and architecture of the lectins differs not only in terms of their shape and size, but also in the arrangement and number of their carbohydrate-recognizing domains (CRD's). [57-59]

After several major discoveries since the first isolation of a pure lectin in 1919, Concanavalin A (ConA), which was extracted from the seeds of the jack bean (Canavalia ensiformis), research in recent years have elucidated an expanding knowledge about lectins and their roles

in immunity, infection and cellular communication.[60] In the early years of research of this field, it was demonstrated that ConA consist of four identical binding sites and its activity directly correlates with carbohydrate interaction. A few years later it was determined that particularly the carbohydrates α-D-mannosyl and α-D-glucosyl groups bind specifically to ConA.[61] In subsequent years, an increasing number of lectins have been isolated, and their interactions with carbohydrates have been elucidated.[62, 63]

Carbohydrate structures are omnipresent in almost all biological organisms. Nine monosaccharides are commonly found as components of the glycocalyx: α-D-glucose; α-D-galactose; α-D-mannose; α-L-fucose; α-L-arabinose; α-D-xylose; N-acetyl glucosamine; N-acetyl galactosamine and sialic acid (See Figure 3).[64] These individual building blocks construct larger and far more complex structures such as linear and branched oligo- and polysaccharides as well their respective lipid- and protein-conjugates.

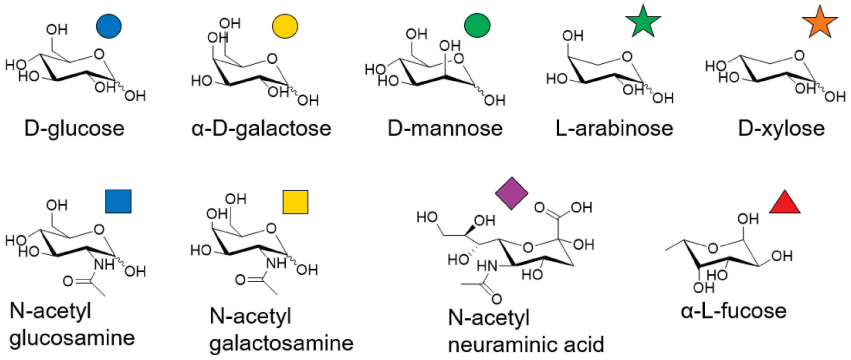

Figure 3 The most common carbohydrate moieties occurring on biological membranes

It has been shown that many carbohydrate-lectin interactions are directly involved in the recognition of pathogens as well as their infection processes and have therefore attracted great scientific interest. The study and clarification of carbohydrate-lectin interactions is critical due to their potential pharmacological or medicinal uses. [65-67] Recently, it was demonstrated, that DC-SIGN, a C-type lectin involved in pathogen recognition and immune modulation, can be effectively inhibited by glycomimetic antagonists. This represents a significant advancement in the context of SARS-CoV-2, where such interactions contribute to viral attachment and dissemination. These findings underline the critical role of lectin-carbohydrate interactions in biomedical research and highlight their potential as therapeutic reagents.[68]

Nevertheless, many of the underlying carbohydrate-lectin interactions, and the related biological mechanisms and signaling pathways are still not fully understood. Chemical carbohydrate-based ligands can be synthetically produced to gain a better knowledge of these interactions. The strategic synthesis of carbohydrate ligands, which enables precise control over their geometry and the number of glycan-mimicking units on a scaffold (valency), has found extensive applications in both biological and chemical research.[69-71] Not only the valence and the geometry can be varied, also novel building blocks can be integrated, which can for

example induce irreversible crosslinking to strengthen the weak non-covalent natural binding of the interaction and thus facilitate the investigation of these interactions.[72] This methodology facilitates the detailed analysis of glycan–protein interactions through advanced techniques such as mass spectrometry. For example, a study from 2021 presents a light induced crosslinking strategy employing a diazirine-functionalized N-acetylglucosamine analog, which was metabolically incorporated into cell-surface glycans. Upon UV activation, this analog enables covalent crosslinking with glycan-binding proteins in live cells, facilitating their stable capture and subsequent analysis by mass spectrometry.[73] In particular, the use of photoactivatable crosslinkers is advantageous due to their spatiotemporal control over covalent bond formation, as discussed in detail in chapter 1.3.2.

The synthetic strategies based on solid- phase synthesis for producing such carbohydrate-based-ligands, which can be used to study these interactions, are discussed in depth in chapter 1.2.2.

1.1.3 Membrane-located plant hormone receptors

Another focus of this work is on the investigation of the membrane-located proteins of plant organisms. In the realm of plant biology, there is an ever-growing compendium of knowledge about the myriad extracellular membrane-located receptors. Plants utilize a diverse array of receptor proteins to regulate growth, the appearance of the plants phenotype or respond to various signals, including environmental response. A deeper understanding of these highly complex processes within the plant can contribute to solving the problems of the modern world, such as food shortages. Plant research, especially the elucidation of the smallest molecular processes, is therefore essential to create sustainable agriculture and to ensure the preservation and protection of biodiversity. [74, 75]

One major class of extracellular receptors in plants is the receptor-like kinase (RLK) which exhibits further division into distinct subgroups based on the extracellular domain. Within these subfamilies, leucine-rich repeat like kinase (LRR-RLKs) was observed to be the largest family in plant.[76] Arabidopsis thaliana is the most studied model plant in terms of RLKs and its genome encodes over 600 RLKs.[77] Structurally the extracellular RLK domain serves as recognition unit for distinct ligands such as small peptides and initiates direct binding for them at their LRR. The intracellular kinase domain induces a signal transduction after ligand-receptor-interaction. CLAVATA1 (CLV1) is the best characterized of all the RLK's in Arabidopsis Thaliana where decisive contributions were made by Clark *et. al*. since 1993.[78, 79] It has been demonstrated that CLV1 in combination with appropriate ligand interaction exhibits a specific association with meristematic activity, thereby playing a pivotal role in the orchestrated formation of plant organs.[80] The meristems are special plant tissues that are located in the shoot (shoot apical

meristem; SAM) and in the roots (root apical meristem; RAM) (See Figure 4A) they consist of undifferentiated cells and contribute to growth through cell division.[81-83]

Within most land plants, including Arabidopsis Thaliana, genes called CLE are present in various tissues of the plant organism, where they are a crucial component of the communication within or between meristems.[84] These CLE genes were revealed to encode tiny signaling peptides that interact with RLK's, resulting in the discovery of a novel class of plant hormones. Typically, the secreted CLE peptide sequences consist of 12-13 amino acids and may undergo post-translational hydroxylation of their prolines that can contain carbohydrate modifications like arabinose. These peptides became an important family of ligands in the vascular development and meristem formation.[85]

One of the best-known secreted peptides from the CLE family is CLV3 (See Figure 4B). The CLV3 peptide is known for its direct binding with the receptor CLV1. Recently, other receptor-proteins besides CLV1 that are involved in the CLV signaling pathway have been identified such as BARLEY ANY MERISTEM1 (BAM1), or CLAVATA2 (CLV2) which forms a functional receptor complex with the pseudo kinase CORYN (CRN).[86]

Mutations affecting the aforementioned receptors or CLV3 have been observed to yield in abnormal development in shoot, root and flower meristems. These phenotypic deviations are attributed to dysregulation within the stem cell populations, suggesting that the genes mentioned are involved in the modulation of an identical signaling pathway. Further experimental evidence supports the assertion that CLV3 regulates stem cell production through a negative feedback loop to maintain the balance between stem cell proliferation and differentiation.[87]

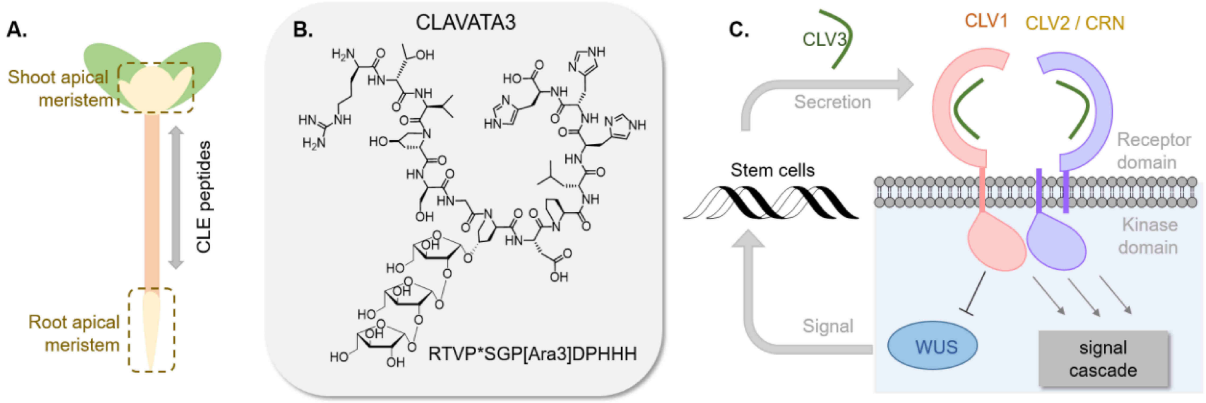

Figure 4 A Meristems of the plant. B CLV3 natural structure. C Negative feedback loop of CLV3 and CLV1 receptors.

The binding of CLV3 to CLV1 triggers the negative feedback loop and initiates a signal cascade in which the kinase domain of CLV1 becomes activated and transmits the signal to a transcription factor called WUSCHEL (WUS) (see Figure 4C). WUS has a direct influence on stem cell production. When CLV3/CLV1 signaling is active, it leads to reduced WUS

expression which results in the differentiation of stem cells. This differentiation and accompanying decrease in stem cell population also downregulates CLV3 production, which is part of the negative feedback loop. This mechanism helps the plant maintain a balance between stem cell proliferation and differentiation, thus preventing abnormal growth patterns.[88-90]

Through various genetic and biochemical investigations, such as knock-out, overexpression and the development of novel mutants, many ligands and receptors have been identified, allowing their complex interactions and functional relationships to be elucidated.[91-93] The development and synthesis of novel peptide-based ligands is also an interesting opportunity to further elucidate these signaling pathways in the field of plant sciences. With the help of chemical tools, the identified peptide structure can be combined with building blocks such as fluorophores or so-called photocages to gain new insights about the signaling pathway, lifetime or distribution in the plant. The photocage technology is explained in more detail in chapter 1.3.1. A deeper understanding of these relationships has important implications for plant development and agricultural practice, making the development and synthesis of such ligands essential.[93-95]

1.2 Solid-phase synthesis of peptides, peptidomimetics and their conjugates

The development of SPPS by Robert Merrifield in 1963 marked a significant advancement, providing a novel approach for the controlled synthesis of sequence-controlled peptides.[96] It is a powerful and frequently used technique in organic and peptide chemistry for the efficient assembly of molecular structures. The main feature of SPPS is that the growing macromolecule is covalently bonded to a solid support, usually called resin. This method is particularly favorable for the synthesis of large and complex molecules, such as peptides, peptidomimetics, and their conjugates, due to its efficiency and the possibility of automating the process. Based on the concept of SPPS, the synthesis of oligonucleotide and oligosaccharides were developed and today, also non-natural or biohybrid macromolecules such as glycomacromolecules or peptide-polymer conjugates are accessible from SPPS.[97, 98] Nowadays, glyco-decorated polymers are available with the aid of SPPS.[99-101]

1.2.1 Solid-phase peptide synthesis

The general principle of SPPS occurs through the iterative addition of N-terminal protected amino acids to the solid-phase, serving as a support matrix. Generally, it involves a cyclical two-step process comprising amino acid coupling and subsequent deprotection. Since amide bond formation involves overcoming a significant energy barrier, the use of appropriate

activation reagents is essential. Equally important is the strategic protection of the N-terminus and side chains, to preserve sequence fidelity throughout the synthesis process. The activation of carboxylic acid alongside the protection of the amine group, is crucial to avoid errors in the sequence or coupling in solution instead of on the resin. In comparison to classic organic synthesis, SPPS offers numerous advantages. Immobilizing the sequence enables efficient removal of impurities through rinsing them out. Moreover, the opportunity of double- or multiple couplings of one amino acid allows to maximize conversation and furthermore enables the synthesis of complex sequences. Therefore, the use of SPPS affords a remarkable degree of control over the synthesis and the structural precision of the sequence. As a result of all these aspects, SPPS is the preferred method for peptide synthesis today.[99, 102]

The solid-phase, often referred to as the resin, typically comprises crosslinked polystyrene in a 3D-structure, which features specialized functional linkers on its surface for the immobilization of amino acids. Originally, Merrifield introduced a chloromethyl group as a linker. In contemporary applications, a diverse array of distinct linkers was developed, which differs in terms of stability, cleavage condition, loading degree as well as the resulting functionality at C-Terminus after cleavage including the formation of carboxylic acid, amide or ester end groups. [103, 104] The use of 2-chlorotrityl resins, for example, leads to the formation of a C-terminal carboxylic acid and relies on the acid lability of the linker unit, so that they can be used for the synthesis of sensitive peptide sequences.[105] Another frequently used resin is the so-called rink amide resin, after the cleavage of which a C-terminal amide is obtained.[106] It is essential that the cleavage conditions used to release the peptide from the resin are orthogonal to the protecting groups on the amino acid N-terminus, ensuring selective deprotection without compromising peptide integrity. Orthogonality refers to the ability to selectively remove one protecting group in the presence of others without affecting them.

Many resins are also available with an integrated hydrophilic polyethylene glycol (PEG) chain, which is nowadays known as TentaGel® (see Figure 5). These chains increase matrix stability and furthermore provide improved swelling capacity in hydrophilic solutions, that enables better accessibility of the functional linkers for the coupling process.[107]

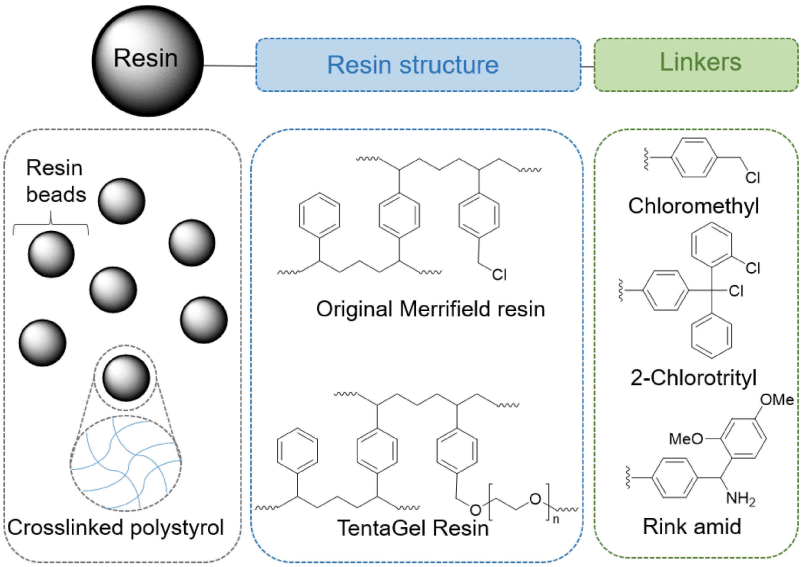

Figure 5 Schematic representation of resin beads, different resin structures and furthermore different linkers.

The coupling procedure is performed via the carboxy functionality of an amino acid whose amine function is temporarily blocked by a protecting group. Initially, carboxylic acid must undergo activation through the addition of coupling reagents. Upon successful coupling, resulting in the formation of an amide bond, the amine group must be deprotected using to the resins' orthogonal deprotection reagents, to allow further coupling. These repetitive steps are continued until the desired peptide sequence is achieved. Subsequently the sequence is cleaved from the solid-phase using an appropriate cleavage solution.[102]

There are numerous types of coupling reagents available today for activating carboxylic acid (See Figure 6A). Prominent representatives belong to the carbodiimides, phosphonium or uronium salts.[108] It is not uncommon to use a combination of two or more reagents in tandem rather than just a single coupling reagent e.g. to prevent undesirable levels of racemization. Hence, the racemization can be reduced when using carbodiimides such as diisopropylcarbodiimide (DIC) by adding a few equivalents of uranium salts such as 1-hydroxybenzotriazole (HOBt).[109] Other coupling reagents are (Benzotriazol-1-yloxy)tris(dimethylamino)phosphonium hexafluorophosphate (BOP)-based which also generates their co-coupling reactant, typically HOBt *in situ*. A common method nowadays is to use of Benzotriazol-1-yl-oxy-tris-pyrrolidino-phosphonium-hexafluorophosphat (PyBOP) with the aid of base such as diisopropylethylamine (DIPEA).[110]

The mechanism of PyBOP activation is shown in Figure 6B.[111, 112] The first step is the deprotonation of carboxylic acid with DIPEA (**1**). The nucleophilic oxygen of the carboxylate then attacks the phosphorus of the phosphonium salt, whereupon the bond between the oxygen of HOBt and the phosphorus is cleaved (**2**). This initially produces a carbonyl phosphonium ester with carboxylate. In the next step, the nucleophilic oxygen of reactive HOBt

species attacks the carbonyl group of the carbonyl phosphoester and cleaves of the phosphorus to form the hydroxybenzotrialzole ester (**3**). This is the actual activated species, which can be attacked nucleophilically by an amine and produces an amide by cleaving off HOBt (**4**). It is to be mentioned that the mechanism of carbodiimide or uronium salt activation differs from that of PyBOP. In this case, no base is required for activation. However, a detailed mechanism of carbodiimide coupling in combination with uronium salts will be omitted at this point.

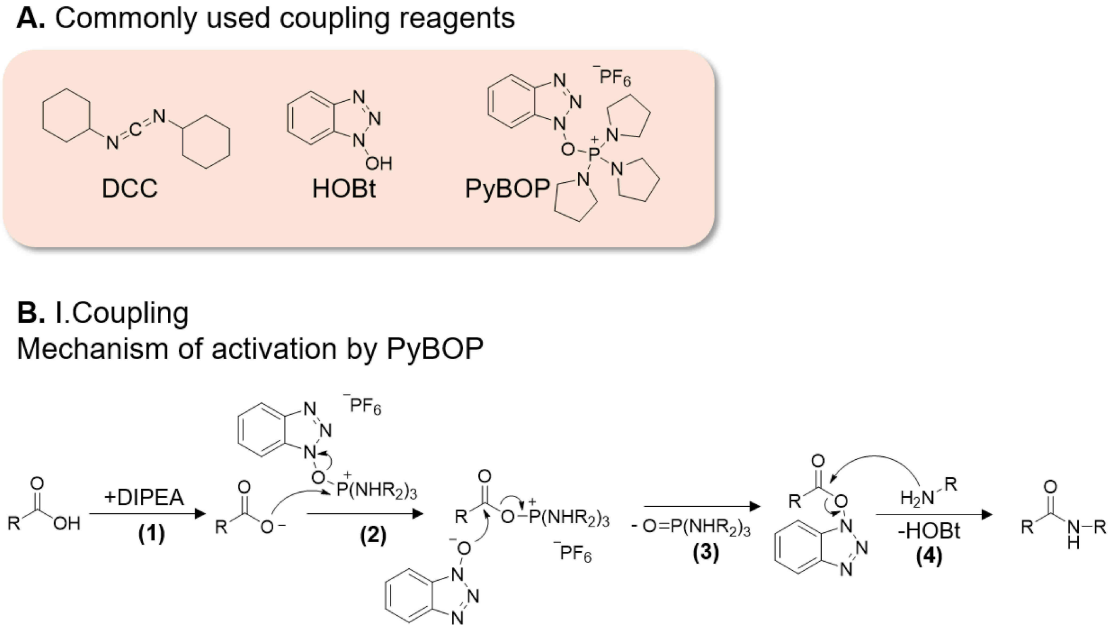

Figure 6 A. Commonly used coupling reagents. B. Mechanism of activation by PyBOP

In addition to the activation of carboxylic acid, the protection of the N-terminal amine function, as well as side chain functions is important in order to avoid side reactions. When protecting the N-terminus backbone, two basic strategies are distinguished: the tert-butyl carbonyl (Boc) and fluorenyl methoxycarbonyl (Fmoc) protecting group strategy.[113] Fmoc protecting groups are labile under basic conditions, whereas tert-butyl-based protecting groups are selectively cleaved under acidic conditions. These groups are also referred to as temporary protecting groups, as they must be removed after each successful coupling to free the amine for the subsequent coupling step. Furthermore, their cleavage conditions must be orthogonal to those used for resin cleavage to prevent premature detachment. Since Fmoc cleavage produces a UV-active cleavage product and the deprotection can be followed (with the aid of UV-Vis) this strategy is often favored in modern solid-phase chemistry. The Fmoc-protecting group can be removed with piperidine solution in *N,N*-dimethylformamide (DMF).

The general mechanism of Fmoc deprotection is described in Figure 7B.[114] First, the proton of the methylene group adjacent to the fluorenyl ring is abstracted by piperidine(**1**), resulting in a carbanion at the fluorenyl ring and piperidine salt. The carbanion parallelly undergoes

elimination reaction, where the negative charge on the carbanion facilitates the departure of carbamate group. This results in dibenzo fulvene and free amine under the release of CO_2 (**2**). The dibenzo fulvene is electrophilic and can be nucleophilic attacked by piperidine forming a Michael adduct (**3**). The dibenzo fulvene as well as the Michael adduct are UV-active.

A. Examples of protection groups

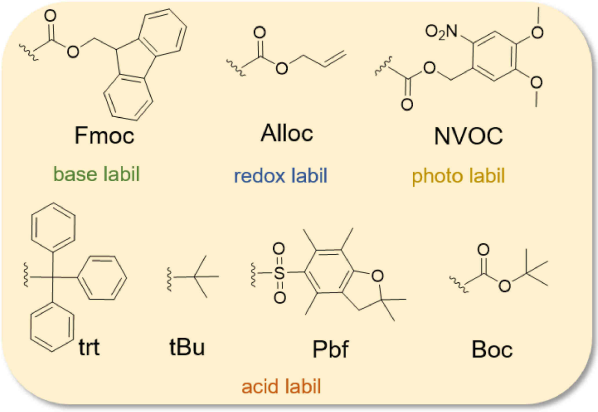

B. II. Deprotection
Mechanism of Fmoc deprotection

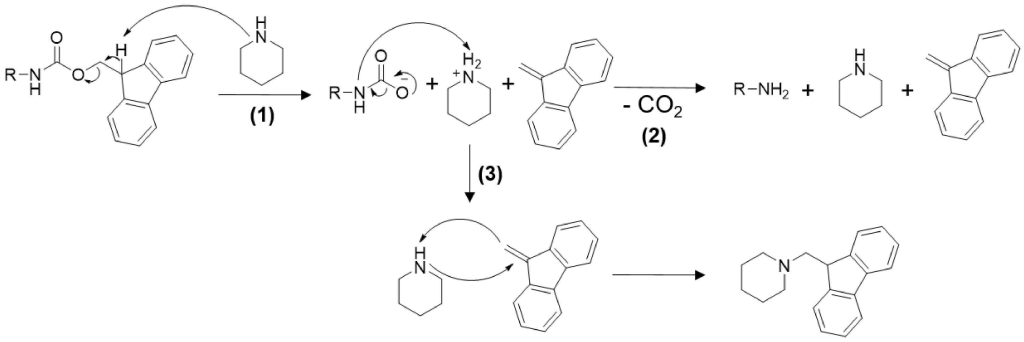

Figure 7 A. Commonly used protection groups. B. Mechanism of Fmoc deprotection.

The protecting groups on the side chains must be orthogonal to those at the N-terminus to allow selective deprotection during synthesis. However, the cleavage conditions for the side chain protecting groups and the resin are typically the same, enabling simultaneous removal of both the final structure from the resin and the side chain protections. In the case of the Fmoc strategy, the orthogonality to the protecting groups on the backbone can be achieved by acid, transition metal-labile protecting groups or furthermore with photolabile groups. Some examples of protection groups are shown in Figure 7A.[115, 116] The mechanism of photolabile nitroveratryloxycarbonyl (NVOC) protection group cleavage can be found in chapter 1.3.1. Other detailed mechanisms of protection groups will not be discussed in this work.

1.2.2 Solid-phase (glyco)-polymer synthesis

Based on the synthesis according to Merrifield, not only peptides but also other biological structures such as artificial DNA or sequence-defined polymers can be synthesized.[117, 118] The fundamental principle of SPPS remains nearly unchanged, however, the specific coupling chemistry, nature of the solid support, and monomeric units differ e.g. traditionally used amino acids are replaced by nucleotides in DNA or synthetic building blocks in the synthesis of polymers. The work of Hartmann *et. al.* made a decisive contribution to the design of synthetic building blocks to receive oligomeric or polymeric biomimetics.[119-121] In particular these building blocks have structural similarities to amino acids, as they also have carboxylic acid and Fmoc-protected amine functionality. The remaining chemical structure can then be adapted to the requirements of the intended biological question, such as improving stability, solubility, or targeting specificity. There are functional building blocks that enable branched structures, conjugations, the introduction of trigger-release functions and spacer building blocks that simply insert a distance between two functions (see Figure 8).

Most of the functional building blocks are based on diethylenetriamine succinyl (DS) and carry a functional group on their sidechain. A frequently used building block in this context is triple bond diethylenetriamine succinyl (TDS), which carries an alkyne functionality on its side chain and can thus enable copper catalyzed azide-alkyne cycloaddition (CuAAC). It is mostly used to enable the conjugation of different sugar moieties to the oligomer and to create a stable triazole ring in comparison to a natural glycosidic bond. [121, 122]

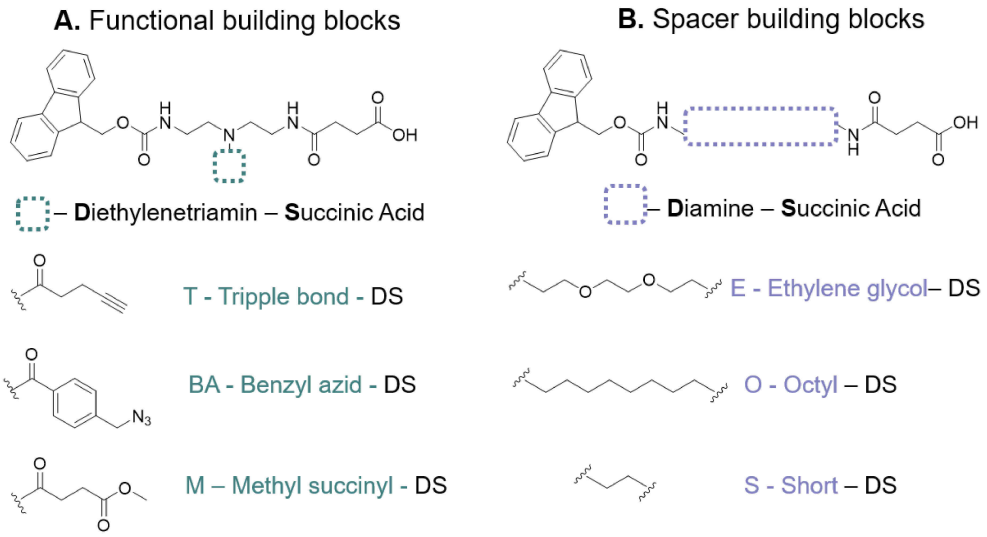

Figure 8 Functional building blocks as well as spacer building blocks used for solid-phase polymer synthesis.

Spacer building blocks can have different properties, e.g. different polarities depending on their chemical composition. There are hydrophilic spacers, such as Ethylene glycol Diamine Duccinyl (EDS) which includes an ethylene glycol core. In contrast, hydrophobic spacers like

octyl diamine succinyl (ODS) feature an alkane structure. Additionally, there exist shorter building blocks, such as short diamine succinyl (SDS) which is currently the shortest building block in the building block toolbox.

These building blocks are coupled on a corresponding resin as in the classic Merifield synthesis (See Figure 9). In short, the N-terminally protected building block is immobilized in the first step using suitable coupling reagents by forming an amide on the resin (See Figure 9, I. Coupling). In the next step, the N-terminal protecting group is cleaved off to obtain a free amine again (See Figure 9, II. Deprotection). Both steps are repeated until the desired backbone is obtained. When using TDS as a functional building block, the alkyne group can be readily utilized to introduce additional functionalization to the side chain of the backbone by CuAAC. Before further functionalization, N-terminal acetylation or end capping by acetic anhydride (See Figure9, III. Acetylation) is essential prior to CuAAC, as free N-terminal amines can interfere with the efficiency of reaction. Azide-functionalized carbohydrate moieties (e.g. mannose azide) can then be efficiently conjugated to the alkynes forming triazoles (See Figure 9, IV Functionalization). Once the sequence is finished, it can be cleaved and isolated (See Figure 9, V. Cleavage).

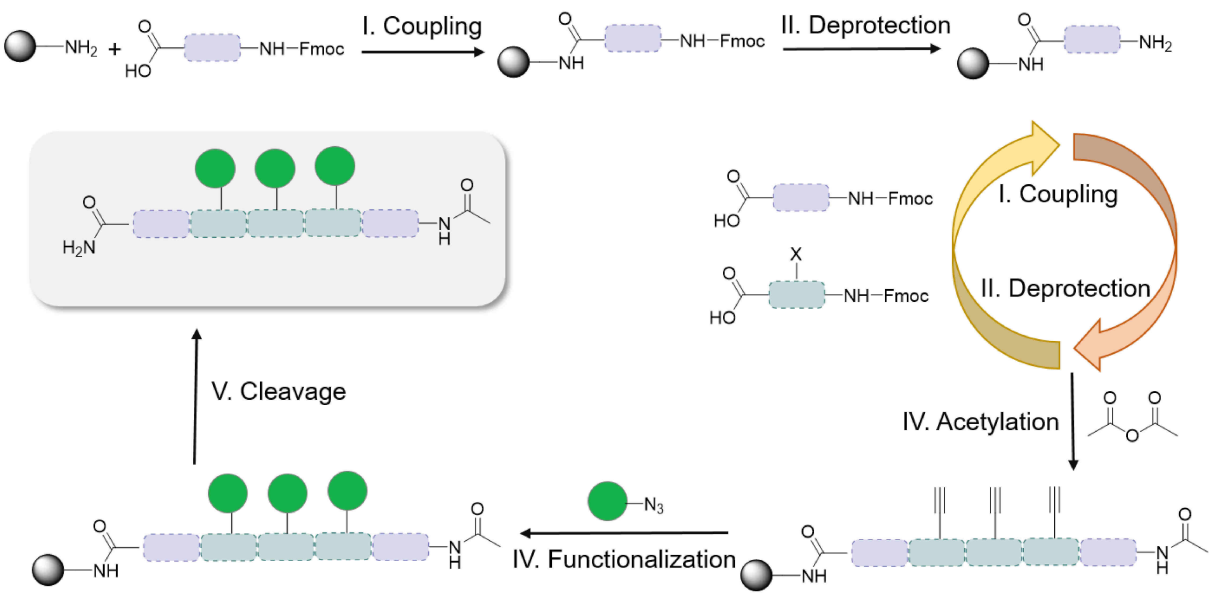

Figure 9 General principle of solid-phase (glyco-) polymer synthesis. Further conjugation to carbohydrate moieties via azide group. Final step is the cleavage from the resin.

The modified SPPS developed by Hartmann not only made sequence-defined macromolecules accessible, but the synthesis of various glycooligoamidoamines which have successfully been used as bio probes. Glycan-based probes selectively bind glycan-recognizing proteins, such as lectins or receptors on cell surfaces.to elucidate carbohydrate-lectin interactions, or as anti-adhesive therapeutics.[123-125] In addition, the Hartmann group

demonstrated that this synthetic approach enables the design of tailor-made structures with diverse architectures, including linear or branched scaffolds, as well as tunable carbohydrate units. This allows the design of customized macromolecules for a selected biological application in various fields such as biomedicine and biotechnology.[122, 126, 127]

Here, the investigation of specific biological processes such as the relationship between different glycans and their architectures interacting with lectins and their significance for various diseases can be focused utilizing SPPS.[128-130] By incorporating detectable tags, light-activatable molecules or crosslinkers, these probes enable the visualization, isolation, or analysis of glycan–protein interactions in biological systems. In particular, light-activatable glycan probes are innovative tools that allow researchers to control glycan biosynthesis with precise spatial and temporal resolution Recent advances include fluorescent labelled, photocaged or photo crosslinking modifications. [131-134]

The techniques and ligands employed for these purposes will be discussed in detail in the following chapter.

1.3 Glycan-probes from photo-activatable molecules

One of the most effective external stimuli for investigating or modifying complex biological environments, including cells or whole organisms, is light. Using light of appropriate wavelength enables precise spatial and temporal control of a biological mechanism without damaging the biological system. Nowadays, many different strategies have been developed to integrate light-activation into biological systems.

The basic principle behind the development of a light-controlled system is the use of molecules that respond to incoming light. As there is no universal definition for these molecules, this work referred them to as photo-activatable molecules. In general, every molecule naturally can absorb certain amounts of light energy. However, photo-activatable molecules are capable of efficiently absorbing light, primarily within the ultraviolet (UV) to infrared (IR) spectrum. This ability arises from their distinct structural and electronic configurations, such as the presence of conjugated π-systems, aromatic rings, and other chromophore moieties. Upon photon absorption, these molecules can undergo energy dissipation through various mechanisms beyond smaller transitional states such as internal conversion and intersystem crossing.[135, 136] Outcomes that are more tangible and interesting as a function for light-controlled systems include fluorescence, dissociation events (e.g. photo cages) or the induction of chemical reactions (e.g. photo crosslinkers). [137-139]

Introducing photo activatable molecules to biological ligands, unique bio probes can be developed affording the opportunity to elucidate intricate biological processes, including

cellular signalling, disease diagnostics or study cellular morphology and function.[140-142] Bio probes in general are an indispensable tool for chemical biology by translating a biochemical interaction at the probe surface into a quantifiable physical signal.

As mentioned before (see chapter 1.1.1.), a common method to receive a bio probe is to attach a fluorophore to a biological molecule such as a ligand. Fluorescence-labelled ligands are used, for example, to trace signaling pathways in a biological system. By irradiating them at a suitable wavelength, these ligands emit a corresponding fluorescent signal, which are used to localize them under the microscope (See Figure 10A).[143, 144] For example, with the help of a fluorescently labeled flaggelin peptide flg22 which is a plant peptide involved in the immune response, it was possible to gain more precise information about the fate and trafficking within the plant.[145]

Another interesting strategy for the use of photo-activatable molecules to modulate a biological function are so-called photocages. These photocages can temporarily block a functional group and biological function, respectively, and upon removal of the cage by light the functionality is restored again (see Figure 10B). The basis of this technique is that the dissociation energy is achieved by irradiation with light, thus splitting the bond between the cage and functional group, e.g., amino acid of the protein. Ligands such as neurotransmitters, peptides or proteins can be caged to block their biological activity.[146-148]. For example photocaged plant hormones such as auxins, cytokinin, and abscisic acid enabled researchers to study plant growth and hormone signaling with high spatial and temporal resolution.[149] This photocage technique is explained in more detail in chapter 1.3.1.

Another exciting application of photo-activatable molecules are crosslinkers, which enable the fixation of a biological state by forming a covalent bond or continuously inhibit signaling cascades, also known as PAL. [150-152] This is accomplished through the specific conjugation of photoreactive functional groups, which respond to light exposure, leading to the formation of covalent bonds (See Figure 10C). Photo crosslinkers are used for example to study protein-protein-interactions, drug discovery and target identification or as irreversible inhibitors. Details on photo-activated crosslinkers and PAL can be found in chapter 1.3.2. A special focus of this work is the crosslinker AzC, which is described in chapter 1.3.3.

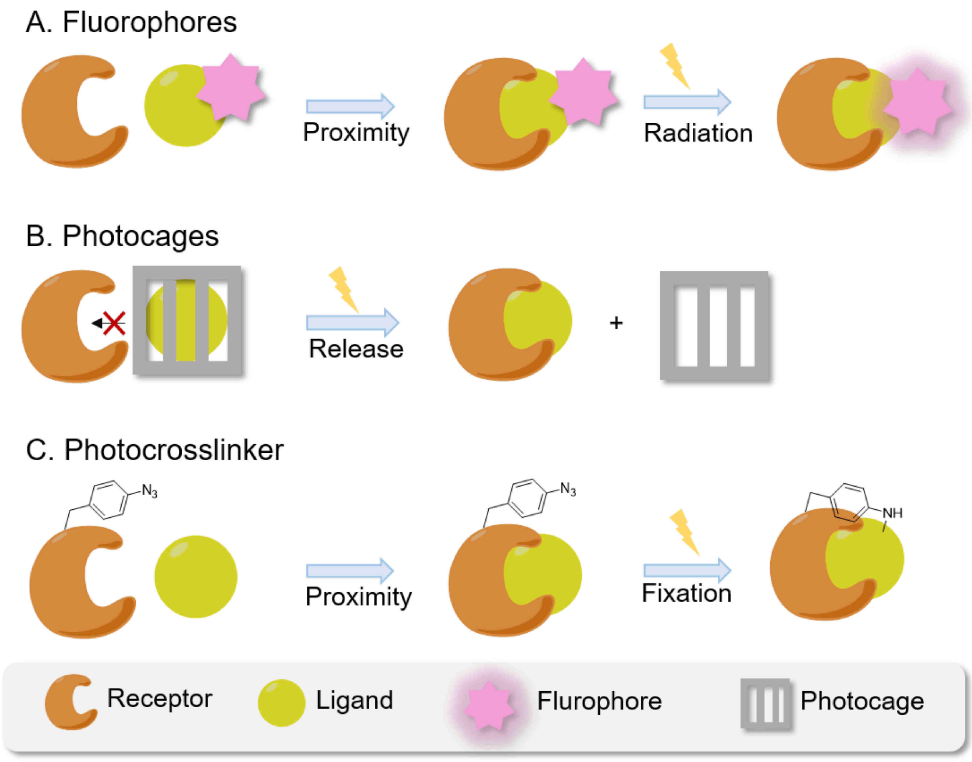

Figure 10 Molecular principles underlying A. fluorophores, B. photocage technique and C. photo crosslinkers in biological application.

All these methodologies constitute an intriguing platform for the development of innovative tools aimed at elucidating biological processes. Subsequent chapters will specifically delve into the photocage technique, light-induced crosslinkers, and furthermore a special building block, the so called AzC.

1.3.1 Photocages

The photocage technique, also known as “photolabile protection groups” was developed in around 1960 as a pivotal method in organic chemical synthesis as well as biological research.[153] The technique relies on the utilization of a photo responsive compound that can be attached to a functional group temporarily for protection or masking. Deprotection is induced by the absorption of light with appropriate wavelength to achieve the activation- or dissociation energy required for the cleavage. This photochemical strategy allows for a selective and controlled release of a functional group.

In today’s scientific efforts, the photo caging technique transcends its role as a mere photolabile protective group in organic synthesis as it also plays a crucial role in the development of novel biological tools.[154] A significant achievement has been the design of molecules that facilitate the modulation of biological activity across an entire organism by attaching a photocage to a ligand’s biologically relevant position. This can temporarily

suppress enzymatic activities, binding sites, complex formation or other unique reactions.[155-157] Exposure to light subsequently restores the ligands activity and function. This enables precise activity-based control of biologically relevant molecules including nucleic acids, peptides or proteins.[158-160]

The specific requirement for selecting a photocage depends on the intended application. In the context of biological systems, a strong absorption beyond 300 nm is essential to not harm living organism, as high energy light radiation can irreversibly alter the entire genetic system.[161] Aromatic structures are particularly suitable for this purpose due to their enhanced light absorption efficiency and the redshift of their absorption maxima compared to e.g. aliphatic structures. This is attributed to closely spaced energy levels due to their extended pi-conjugation. Additionally, the photocage should be soluble in the surrounding media and demonstrate stability during the absence of radiation. Furthermore, it is beneficial that any photochemical byproducts generated during activation remain biocompatible and furthermore transparent to avoid competitive absorption.[162] A selection of photocages is shown in Figure 11.

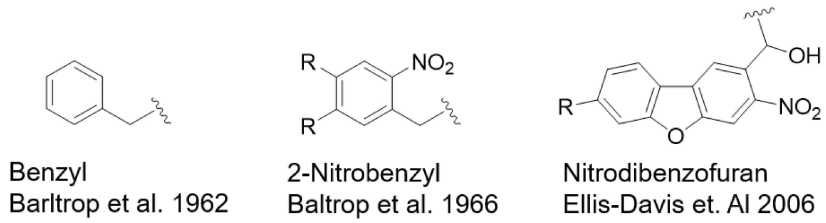

Figure 11 Commonly used photocages.

Nowadays there are numerous photocages with cleavage wavelength from 250 to around 400 nm, which have been tailored according to application and requirements. One of the first photolytically cleavable groups was the benzyl group, which was established by Barltop *et al.*[153] In this work the photolysis of the benzyl group, which was conjugated to glycine, was successfully detected. The later advancement in nitrodibenzofuran-based photocages by Ellis-Davies in 2006 has facilitated the development of a cleavage mechanism characterized by a discernible red shift, particularly notable in the context of two-photon laser irradiation. Nevertheless, the most frequently used and best investigated photocages are 2-Nitrobenzyl derivatives, which were also introduced by Baltrop.[163]

2-nitrobenzyl based photocages possess an aromatic structure and are characterized by the presence of a nitro group at position 2 in proximity of the cleavage site. Nitro groups are strong electron-withdrawing substituents that significantly alter the electronic distribution within a molecule, thereby promoting bond cleavage in the vicinity of the nitro group. A particular advantage is that there is a wide variety of 2-nitrobenzyl derivatives that can be easily attached to various functional groups. For example, there are derivatives for the protection of amines, alcohols, carboxylic acids or thiols.[164-166] Depending on the attachment of substituents on the

aromatic ring of 2-nitrobenzyl-based photocages the wavelength to induce photolysis can range from around 250 to 350 nm.[167]

The photolysis mechanisms of 2-nitrobenzyl derivatives usually occur via a Norrish Type-2 mechanism. Figure 12 represents the photolysis mechanism in a simplified form. Irradiation with appropriate wavelength induces a photo-redox reaction in which an incident photon breaks the π-bond of the N=O bond and converts it into an excited diradical state (**1**). The nitro radical then abstracts the benzyl proton in an intramolecular hydrogen shift, resulting in the *aci*-nitro intermediate (**2**) followed by ring formation. It is to be mentioned that the formation of aci-nitro is tautomeric and can occur from the singlet (S1) as well as from the triplet state (T1). Following this, a ring opening ensues at the juncture of N and O (**3**), wherein the electron pairs of oxygen induce ring opening and a simultaneous release of CO_2 and the detachment of the photocage (**4**) from the target molecule releasing e.g. free amine (**5**). The cleaved photocage remains as nitroso-carbonyl derivative (**5**).[168]

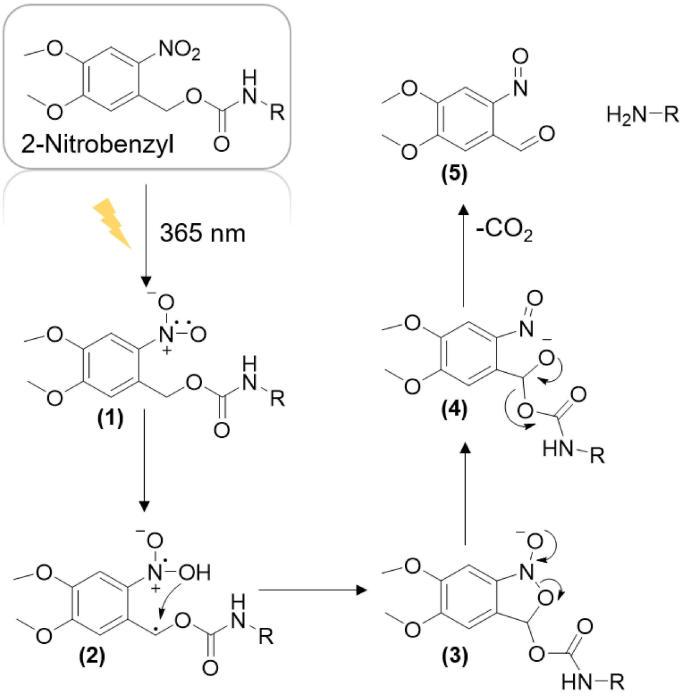

Figure 12 Mechanism of NVOC cleavage.

1.3.2 Photo affinity-based crosslinking

In chemistry, crosslinking generally means the formation of a covalent bond, whereby two or more molecules are linked to one another. The basic requirement of a crosslinking molecule is the inclusion of at least one highly reactive group that enables the formation of a covalent bond. There are many different types and architectures of crosslinkers that are designed based on the desired application. This opens up numerous possibilities particularly in the field of

biology or biochemistry to capture dynamic and complex processes and to enable easier analysis. The incorporation of crosslinking reagents facilitates insights into complex aspects such as protein-protein- interactions, the structural characterization of ligand-receptor complexes or chemical proteomics thus contribute to a deeper understanding of their functional relationships.[169-171] A special use for crosslinkers is the so-called affinity-based crosslinking where the basic idea is to conjugate a crosslinker to a biological small molecule or macromolecule (e.g. ligand) to target and then bind to a specific protein (e.g. receptor) whereas the crosslinker enables to form a covalent bond. Powerful method in the field of affinity-based crosslinkers is also based on the design of photo reactive functional groups. A huge advantage of the use of photo crosslinkers is their better spatial and temporal control for the crosslinking process in comparison to other common crosslinkers. This methodology is also known as PAL.[172-174] Intensive research particularly from the end of 1960s onwards was carried out into the development of photo crosslinkers. One of the earliest and most influential applications was reported in 1970 by Kiefer *et. al.,* as they used aryl azides to irreversibly inactivate acetylcholinesterase and acetylcholine receptors, demonstrating that the azides, upon photolysis, generated highly reactive intermediates that covalently attached to the acetylcholine-binding sites only when the probe was bound to its target.[175] Frequently used photo-crosslinkers for PAL are shown in Figure 13.

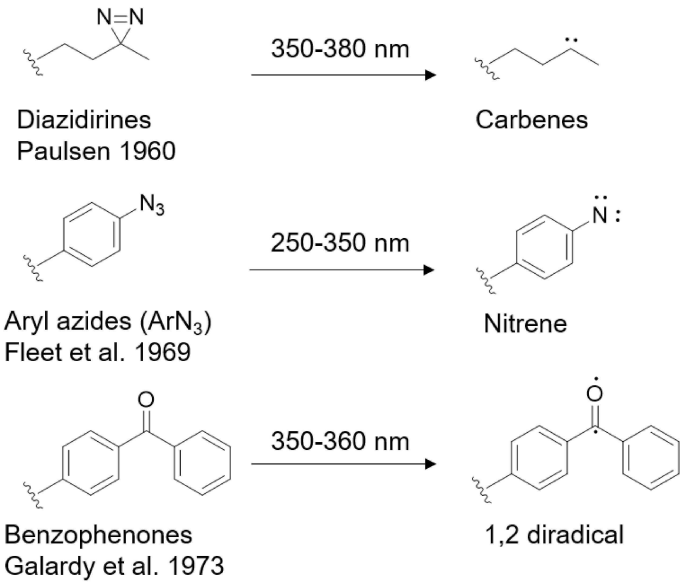

Figure 13 Representative photo-crosslinkers and the corresponding reactive radical species generated upon light activation.

In addition to the aryl azides that were introduced by Fleet *et. al.* in 1969, the structurally similar diaziridines have also been established in various applications.[176, 177] In addition, benzophenone has been used as a photo-crosslinker by Galardy *et. al.* in 1973.[178] These three examples for crosslinkers mainly differ in their activation wavelength (250-380nm),

intermediates/reactive species (nitrene, carbene, diradical), stability, and the associated effective crosslinking capability.

In 2014, Sakurai *et. al*. developed various lactose-based PAL probes combined with azide, diazidirine and benzophenone, to evaluate and compare their crosslinking performance.[179] Their study revealed that aryl diaziridines exhibited an exceptional fast reaction rate, but their crosslinking yields were relatively low. Increasing the concentration of the probe improves yields, but risks compromising selectivity. Conversely, benzophenones demonstrated both slower reaction kinetics and a poor crosslinking yield, rendering them less suitable for the application of low affinity labeling. In comparison, classical aryl azides displayed a rapid initial reaction rate as well as high crosslinking yields, making them reliable candidates for PAL.

Therefore, aryl azides remain commonly used in photo reactive groups. When aryl azides are exposed to light with a wavelength between 250-350nm, they form highly reactive nitrenes by elimination of nitrogen (see Figure 14). Nitrenes are electron-deficient chemical species that contain a nitrogen atom with an unpaired electron, which gives them a radical character. In general, there are two spin states of nitrenes: singlet nitrenes characterized by a paired electron configuration, exhibit lower reactivity and enhanced stability. This can be transferred by inter system crossing into triplet nitrenes which possess two unpaired electrons exhibit significantly higher reactivity, but at the expense of a shorter-lived existence. It can be noted/stated that nitrenes can undergo a variety of complex reactions such ring expansion leading to nucleophilic reactions e.g. with primary amines, insertion reactions into C-H and N-H sites or addition reactions with double bonds.[180, 181] Figure 14 presents a simplified overview of the key reactions involving aryl azides.

In summary these non-specific reactions offer a notable advantage as they do not require the presence of a specific functional group (e.g. amines in case of NHS-esters) as counterpart on the component to be crosslinked. This becomes particularly interesting when limited or negligible information is available regarding the structural characteristics of the counterpart (e.g. receptor). Additionally, it is of importance when the identity of the involved receptors remains generally elusive or unclear within the biological domain.

A promising application involves the conjugation of photo-crosslinkers to carbohydrate or oligosaccharide motifs for the identification of their respective lectins within a biological system, as they play a crucial role in cell recognition, signaling or immune responses.[181-183] Since their weak interactions are often difficult to detect, the formation of a covalent network simplifies their analysis.

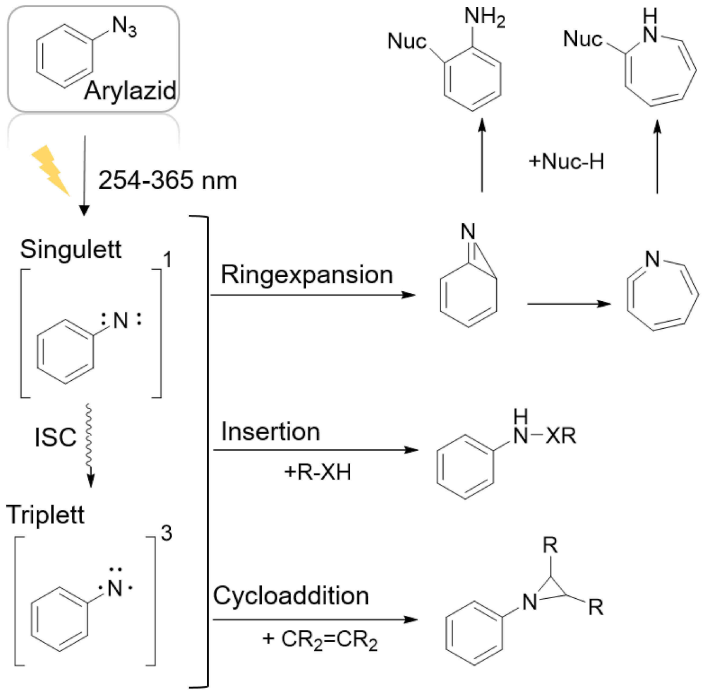

Figure 14 Different reactions of light induced crosslinking with aryl azides and some examples of final crosslinking.

Following photochemical crosslinking, these entities can be extracted and isolated from the complex environment, enabling subsequent analysis via mass spectrometry. Thus, photo activatable crosslinking carbohydrates can significantly advance diagnostic and therapeutic strategies for various diseases including cancer or immune deseases.[134, 183] Recently a photo crosslinking *N*-acetylneuraminic acid, which interacts with CD22, which is involved in immune responses, was used to investigate the detailed mechanisms of B-cell regulation and immune signaling. This opened up new avenues for exploring how cellular communication and immune responses works.[184] Furthermore, their potential as irreversible anti-adhesives or inhibitors opens new avenues for preventing pathological adhesion processes, highlighting their broad impact in biomedical science.[185]

1.3.3 Azidocoumarin

According to their favorable optical properties, coumarins are widely employed as fluorophores in various fields of scientific research. One of the significant advantages of coumarin fluorophores is their tunable emission wavelength by simply modifying the chemical structure. Coumarins are small organic compounds that were isolated for the first time by Vogel from tonka bean in 1820.[186] Nowadays it is known to be widespread in nature and can be found in various plants, such as cassia cinnamon and certain grasses. Additionally, there are also thousands of synthetic derivatives of coumarin, which have gained interesting significance for scientific research due to their pharmacological and biological properties, such as anti-

inflammatory, anticancer potential, antipathogen or neuroprotective effects.[187-191] Interestingly coumarin derivatives are also found in the cosmetics industry or as perfumeantioxidants.[191, 192] Hence, coumarin derivatives are characterized as versatile compounds, demonstrating significance and applicability across a broad spectrum of domains.

The general structure of coumarins consisting of basic scaffold 1,2-benzopyrone including six peripheral *C-H* sites. In principle, all these six *C-H* sites and the C=C unit are suitable for post-functionalization, but *C-H*-functionalization in the 6- or 7-position of the phenyl group and in the 3- or 4-position of the vinyl group is more attractive and chemically more accessible (see Figure 15A). While modifications at position 3 also have biological significance regarding medical or chemical biological applications.[193-195]

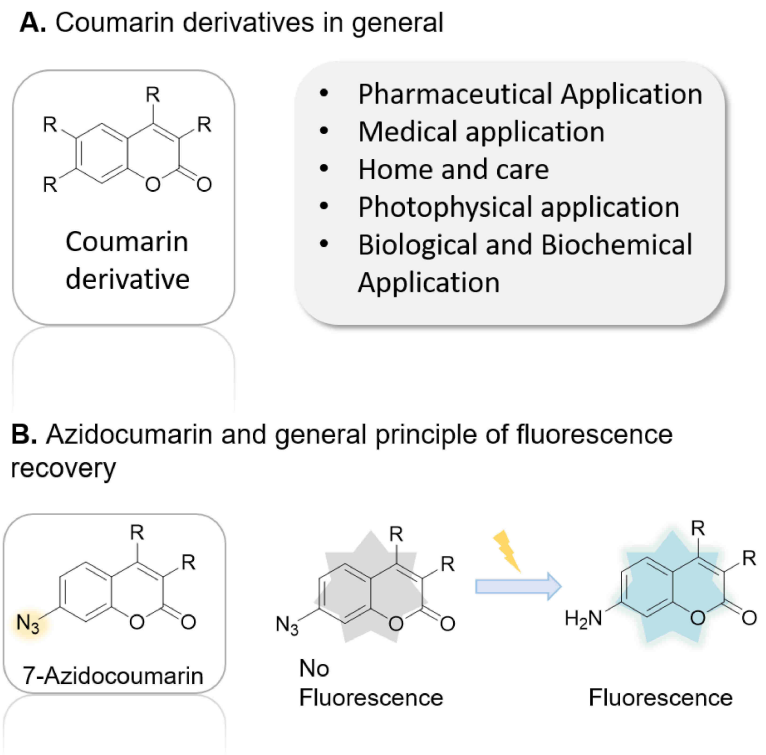

Figure 15 A. Coumarin derivative in general. The positions 3,4,6,7 are commonly for modifications. B. AzC and the general principle of fluorescence recovery through light activation.

The fluorescent properties of coumarins directly depend on the introduction of substituents, such as electron-donating- and electron-withdrawing-substituents. Due to their rigid structure in combination with a "push-and-pull" effect, as found for example in the classic 7 - aminocoumarin, many coumarin derivatives have excellent quantum yields.[196] Furthermore, their structural flexibility, ease of modification and sensitivity to their microenvironment makes them suitable as chemosensors.[197] The fundamental principle of these sensors is based on their ability to modulate fluorescence signals through, e.g., quenching effects. Introduction of an analyte results in the modulation of fluorescence and a shift of the wavelength. Nowadays there is a whole range of coumarin-based chemo sensors,

which are used for the selective and reversible detection of various ions, such as transition metal ions processes to provide fluorescent signals. [198, 199]

Depending on these properties the development of fluorescent coumarin-based chemo- and bio-probes represents another promising approach for designing novel tools for molecular recognition and imaging within complex biological systems

In this context the use of an azide as a substitute at the coumarin backbone is particularly interesting, as it leads to reduction or quenching of the fluorescence.[200]

By reducing the azide, e.g., addition of a redox active agent such as reactive sulfur compounds leads to the highly fluorescent aminocoumarin derivative. The on-demand fluorescence exhibited by AzC's has found widespread application in various domains, including detection and quantification of reductive activities in microorganisms or living cells whose dysregulation can lead to diseases such as cancer. [201-203] In this context, secreted H_2S serves here as redox active agent, transforming the azide moiety to an amine. This transformation results in the release of fluorescence, providing a measurable signal for the quantification of H_2S production. Xie *et. Al*. successfully used an AzC morpholine derivative to selectively display H_2S to image lysosomal sulfur production in living cells.[204]

Nevertheless, the use of AzC as a photo crosslinker, enabled by its azide functionality, presents a particularly interesting prospect. Upon irradiation with light, the azide molecules undergoes covalent bond formation through e.g. *N-H* or *C-H* insertion with adjacent molecules, similar to the established aryl azides mentioned in chapter 1.3.2. Simultaneously with the covalent bond formation, the azide moiety undergoes reduction, resulting in the restoration of fluorescence (See Figure 15B). This double-faceted capability not only allows real-time monitoring of the crosslinking process but also facilitates the precise localization of binding events through the utilization of microscopic imaging techniques which makes it an interesting candidate for PAL.

In 1992 azacoumarin was used as a photo crosslinker for the first time by Thevenin *et. al.* There the azacoumarin enabled the targeted translocation of a coumarin fluorophore by crosslink in close proximity to the binding site of an interacting target protein.[205] Building upon this study, it became evident that AzC possesses significant potential as a photoactivatable bio probe. About 20 years later, AzC was further used for photo-induced crosslinking processes. Here, it was used by Kellner *et. al.* in 2011 as a selective photo-crosslinker for RNA to achieve a step-wise alkylation of the RNA and to follow it photolytically.[206] Parallel to the developments of this thesis in the end of 2023 the functionality of these capabilities has been extended by creating a glycan-based AzC probe that is able to selectively bind to target proteins developed by Bousch *et. al*.[207]

Glycan interactions play a crucial role in various biological processes and are pivotal in the pathogenesis of numerous diseases. A deeper understanding and elucidation of these

mechanisms are therefore essential for the development of novel therapeutic strategies (See also chapter 1.1.2). These recent findings emphasize the relevance of further research and development of carbohydrate-based AzC probes as their use as a diagnostic tool to identify and localize glycan-lectin interactions is of great importance.

Despite the longstanding familiarity of AzC potential, little information exists regarding its applicability in SPPS but would open the opportunity to develop peptide- and carbohydrate-based ligands for photo-induced affinity labeling.[127, 208]

Aims and Outlines

This thesis focusses on the development of bio probes starting from known biological ligands (peptides or carbohydrates) and performing chemical modifications to enable modulation and control of their bioactivity. SPPS will be the main tool to derive such molecules combining the well-established synthesis of peptides with recent solid-phase strategies accessing peptide- and glycan-mimetic macromolecules as introduced by Hartmann *et al*. Three different systems are targeted at having a special focus on evaluating ligand-receptor interactions at the cell membrane: a peptide- and a carbohydrate-based probe for studying binding to membrane-bound receptors as well as a peptide-lipid conjugate to enable reconstitution of complex cell membrane models.

The first part of this work will be centered around the synthesis of a photoactivatable ligand derived from plant peptides together with the group of Prof. Dr. Rüdiger Simon, HHU. A special focus will be placed on the CLE family, as this signaling pathway is particularly interesting because it is involved in growth, an essential process for the maintenance of the plant. CLV3, a signaling peptide from the CLE family, will be synthesized by developing a suitable protective group strategy. To track the peptide within the plant, a suitable position in the peptide backbone allowing the attachment of a fluorophore without a loss of biological activity will be located. Due to its modification sensitivity, the biological activity of the peptide will be tested using established root assays. Since it is assumed that the N-terminus is essential for biological activity, it should be temporarily blocked with a photocage in order to modulate and control the CLE signaling pathway with light.

In the second part of this work, a novel building block based on AzC will be established for use in the SPPS. AzC exhibits the capacity for photolytic crosslinking owing to its inherent azide functionality. This photo-induced reduction of the azide moiety should not only facilitate crosslinking with target proteins but should also result in the emission of fluorescence. This double-faceted capability renders AzC an interesting molecule for biological applications. Specifically, mannose and galactose moieties, as ligands will be conjugated to AzC on the solid-phase. To achieve this, a suitable coupling strategy for the AzC building block will be established. To proof selective target binding of the AzC-carbohydrate probe and validate the crosslinking ability paired with fluorescence recovery, the well-known man recognizing lectin ConA will be used. In addition, the selectivity of the AzC carbohydrate probes will be investigated, focusing on comparative assessments between the mannose and galactose probes by ConA binding experiments. Subsequently, the efficacy of the probes will be evaluated to evaluate their capacity for detecting and crosslink with respective target proteins, even within complex environments such as whole organ lysates and cells.

The last part of this work will be focused on the development of a peptide-based lipid, based on the SpyTag-SpyCatcher technology in a cooperation with the group of Prof. Dr. Alexej Kedrov, HHU. A crucial step in synthesizing the ST peptide is designing an effective protecting group strategy. Additionally, efforts will be made to develop a method for choosing and attaching a lipid anchor to the peptide precisely, aiming to avoid unwanted side reactions with various functional groups on the peptide sidechains. The binding of the ST lipids and the associated SC protein will be by proven using electrophoretic methods. Furthermore, an assessment of the integrability of the ST lipid onto a model membrane is imperative. Simultaneously, the feasibility of the ST lipid-SC interaction on the model membrane needs to be examined. Prospective applications involve utilizing this system as a modulator for model membranes, with potential chemical modifications, such as the introduction of polymer chains to the SC protein, in forthcoming studies.

Publications

1. Macromolecular tool box to elucidate CLAVATA3/EMBRYO SURROUNDING REGION-RELATED-RLK binding, signaling and downstream effects

Authors: M. Narasimhan, N. Jahnke, F. Kallert, E. Bahafid, F. Böhner, L.Hartmann, R. Simon

Journal: *Journal of Experimental Botany*

Published: 08. May. 2024 https://doi.org/10.1093/jxb/erae206

Journal of Experimental Botany, Vol. 75, No. 17 pp. 5438–5456, 2024
https://doi.org/10.1093/jxb/erae206 Advance Access Publication 8 May 2024

RESEARCH PAPER

Macromolecular tool box to elucidate CLAVATA3/EMBRYO SURROUNDING REGION-RELATED–RLK binding, signaling, and downstream effects

Madhumitha Narasimhan[1,†], Nina Jahnke[2,†], Felix Kallert[2], Elmehdi Bahafid[1], Franziska Böhmer[2], Laura Hartmann[2,3,*], and Rüdiger Simon[1,4,*]

[1] Institute for Developmental Genetics, Heinrich Heine University, Universitätstraße 1, D-40225 Düsseldorf, North Rhine Westphalia, Germany
[2] Institute of Organic Chemistry and Macromolecular Chemistry, Heinrich Heine University, Universitätstraße 1, D-40225 Düsseldorf, North Rhine Westphalia, Germany
[3] Institute of Macromolecular Chemistry, University Freiburg, Stefan-Meier-Straße 31, D-79104 Freiburg, Germany
[4] Institute for Developmental Genetics and Cluster of Excellence in Plant Sciences, Heinrich Heine University, Universitätstraße 1, D-40225 Düsseldorf, North Rhine Westphalia, Germany

[†] These authors contributed equally to this work.
* Correspondence: Laura.Hartmann@makro.uni-freiburg.de or Ruediger.Simon@hhu.de

Received 7 December 2023; Editorial decision 17 April 2024; Accepted 7 May 2024

Editor: Martin Janda, University of South Bohemia in České Budějovice, Czech Republic

Abstract

Plant peptides communicate by binding to a large family of receptor-like kinases (RLKs), and they share a conserved binding mechanism, which may account for their promiscuous interaction with several RLKs. In order to understand the *in vivo* binding specificity of the CLAVATA3/EMBRYO SURROUNDING REGION-RELATED peptide family in Arabidopsis, we have developed a novel set of CLAVATA3 (CLV3)-based peptide tools. After carefully evaluating the CLE peptide binding characteristics, using solid phase synthesis process, we modified the CLV3 peptide and attached a fluorophore and a photoactivable side group. We observed that the labeled CLV3 shows binding specificity within the CLAVATA1 clade of RLKs while avoiding the distantly related PEP RECEPTOR clade, thus resolving the contradictory results obtained previously by many *in vitro* methods. Furthermore, we observed that the RLK-bound CLV3 undergoes clathrin-mediated endocytosis and is trafficked to the vacuole via ARA7 (a Rab GTPase)-labeled endosomes. Additionally, modifying CLV3 for light-controlled activation enabled spatial and temporal control over CLE signaling. Hence, our CLV3 macromolecular toolbox can be used to study rapid cell specific down-stream effects. Given the conserved binding properties, in the future our toolbox can also be used as a template to modify other CLE peptides.

Keywords: Chemical probe, CLV3 peptide, CLAVATA signaling, endocytosis, fluorophore labeling, photoactivation, receptor specificity, solid phase peptide synthesis, sub-cellular trafficking.

Introduction

Small secreted peptides mediate cell-to-cell communication in multicellular organisms in response to pathogens, biotic, and abiotic stimuli, and to regulate developmental processes. The CLAVATA3/EMBRYO SURROUNDING REGION (ESR)-RELATED (CLE) family of peptides is evolutionarily conserved among land plants (Furumizu *et al.*, 2021; Whitewoods, 2021; Hirakawa, 2022). CLE peptides act over short ranges to control stem cell division and differentiation in meristems, but also over long distances between shoot and root tissues. The Arabidopsis genome comprises 32 *CLE* genes that encode 26 different CLE peptides (Ito *et al.*, 2006; Hirakawa *et al.*, 2011). CLE genes encode pre-pro-proteins containing an N-terminus signal peptide, a variable central domain that might be involved in the secretion process, and a highly conserved CLE domain close to the C-terminus. After cleavage of the signal peptide and proteolytic processing, the functional CLE domain comprises 12 or 13 amino acids that are secreted via the endoplasmic reticulum and Golgi apparatus to the apoplast. The mature CLE peptides often contain hydoxyproxiline residues that may be essential for binding and activity, which can be further modified by arabinosylation (Rojo *et al.*, 2002; Ito *et al.*, 2006; Kondo *et al.*, 2006; Shinohara and Matsubayashi, 2013; Tamaki *et al.*, 2013; Strabala *et al.*, 2014; Xu *et al.*, 2015; Kim *et al.*, 2017; Roman *et al.*, 2022).

The secreted peptide binds to the extracellular leucine-rich-repeat (LRR) domains of plasma membrane-localized receptor-like kinases (RLK), which interact with diverse co-receptors. Besides the LRR ligand binding domain, the RLKs and their co-receptors carry a transmembrane domain and a cytosolic kinase domain that transmit the intracellular signal (Shiu and Bleecker, 2001; Xi *et al.*, 2019). The first identified CLE peptide was CLAVATA3 (CLV3), which is expressed in the stem cell domain of the shoot apical meristem (SAM) of Arabidopsis. CLV3 signals via the LRR-RLK CLAVATA1 (CLV1), which belongs to the sub-family XI of LRR-RLKs (hereafter referred to as RLKs) that further includes BARELY ANY MERISTEM1 (BAM1), -2, and -3 (DeYoung *et al.*, 2006; Furumizu *et al.*, 2021). The CLV3-related peptide CLE40 is expressed in non-stem cells of root and shoot apical meristems (RAM and SAM, respectively) and signals via BAM1. During SAM development, the CLV3–CLV1 and the CLE40–BAM1 modules control expression of the transcription factor WUSCHEL, which is essential for meristem maintenance (Schoof *et al.*, 2000; Yadav *et al.*, 2011; Schlegel *et al.*, 2021). Overexpression or exogenous application of several different CLE peptides triggers premature differentiation of the SAM and root meristem. CLV3 and several other CLE peptides signal via the heteromeric complex of CLV2, a receptor-like protein, and the pseudo-kinase CORYNE (CRN) (Fiers *et al.*, 2005; Müller *et al.*, 2008; Guo *et al.*, 2010; Nimchuk *et al.*, 2011a; Replogle *et al.*, 2011; Breda *et al.*, 2019). CLV2 and CRN exit the endoplasmic reticulum together, dependent on each other, and reach the plasma membrane to form a functional CLV2/CRN receptor-like complex together. Hence, the *clv2* and *crn* mutants have identical CLE signaling phenotypes (Müller *et al.*, 2008; Bleckmann *et al.*, 2010; Somssich *et al.*, 2015).

CLV3 and several other CLE peptides can induce arrest of root meristem growth and differentiation of root stem cells. This indicates promiscuity in the interaction between CLE peptides and RLKs (Fiers *et al.*, 2005; DeYoung *et al.*, 2006; Ito *et al.*, 2006; Kinoshita *et al.*, 2007; Hazak *et al.*, 2017; Crook *et al.*, 2020; Narasimhan and Simon, 2022). This has been corroborated by *in vitro* studies on isolated receptor domains in which dissociation constants (K_d) between 0.6 nM and 14 μM were observed for CLE peptides and RLKs of subfamily XI. For example, CLE8-14 and -16 can bind BAM1 with very high affinities, but CLE9 can also bind CLV1 (Ogawa *et al.*, 2008; Crook *et al.*, 2020). Notably, CLV3 has been shown to bind to the RLKs CLV1, BAM1, -2, and -3, which belong to the CLV1 clade (Guo *et al.*, 2010; Shinohara *et al.*, 2012; Hazak *et al.*, 2017; Crook *et al.*, 2020; Furumizu *et al.*, 2021).

Interestingly, some CLEs were found to interact with RLKs of different clades. CLE9, in addition to BAM1, binds also to HAESA-LIKE1 (HSL1) with lower affinity. HSL1 is an RLK that predominantly interacts with the peptide INFLORESCENCE-DEFICIENT IN ABSCISSION (IDA) and other members of the IDA-LIKE family of ligands (Qian *et al.*, 2018; Furumizu *et al.*, 2021; Roman *et al.*, 2022). CLE14, in addition to BAM1, was also reported to interact with PEP RECEPTOR 2 (PEPR2), which is a receptor for the AtPep family of peptides (Gutierrez-Alanis *et al.*, 2017). This broad interaction spectrum can be attributed to the conserved mode of binding, which is shared amongst CLEs and other peptide families. The C-terminal residues undergo close contacts with the RLK and their co-receptors (Zhang *et al.*, 2016a, b; Li *et al.*, 2017). The N-terminal residues would then interact only with the RLK and provide specificity for the interaction. For example, changing the first three N-terminal residues of the CLE peptide TRACHEARY ELEMENT DIFFERENTIATION INHIBITORY FACTOR (TDIF or CLE41) or of CLE9 resulted in total loss of binding to their cognate RLKs. Furthermore, swapping one or more of the N-terminal residues between IDA and CLE9 resulted in swapped affinity to their cognate RLKs HSL1 and BAM1, respectively (Zhang *et al.*, 2016a; Li *et al.*, 2017; Roman *et al.*, 2022). Thus, N- and C-termini form two anchoring sites for the peptide on the RLKs, with the N-terminus contributing to the specificity of interactions. Furthermore, the peptides flg22, derived from the flagellin protein, and pep1 have been shown to bind FLAGELLIN-SENSITIVE2 (FLS2) and PEPR, respectively, in a fully extended conformation, which is in stark contrast to CLE41 forming a kink-like structure in the middle while binding the RLK TDR (Zhang *et al.*, 2016b). This indicates that peptides of different families have mechanisms that confer

specificity to the RLKs of a certain clade, thus excluding unspecific RLK interactions. This brings the previously reported CLE14–PEPR2 interaction into question, particularly when PEPR clade is phylogenetically distant from the CLV1 and TDR clades, which act as CLE receptors (Gutierrez-Alanis *et al.*, 2017; Furumizu *et al.*, 2021). Two important questions remain unanswered: can CLE peptides interact with high affinity and induce signaling through the PEPR clade of receptors? Is there an *in vivo* binding affinity between CLEs and specific RLK clades, such as CLV1 and TDR sister clades, while eliminating cross-clade interaction with phylogenetically more distant RLKs?

Most of our understanding of peptide–receptor interaction comes from *in silico* models, *in vitro* studies with purified RLKs in stable conditions, or in heterologous systems (Ito *et al.*, 2006; Ogawa *et al.*, 2008; Shinohara *et al.*, 2012; Zhang *et al.*, 2016b; Gutierrez-Alanis *et al.*, 2017; Li *et al.*, 2017; Roman *et al.*, 2022). However, such studies do not accurately reflect the *in vivo* conditions, such as receptor confirmation changes within multiprotein complexes, the chemical and physical environment, protein modifications, number of receptor molecules at the plasma membrane, and ligand diffusion kinetics (Bhattacharya *et al.*, 2013; Kastritis and Bonvin, 2013; Chang, 2022).

Post CLE peptide interaction, the fates of the peptide and the RLK have not been extensively studied. In plants, several receptors have been shown to be internalized via clathrin-mediated endocytosis (CME) (Paez Valencia *et al.*, 2016). Different RLKs and ligands have been shown to undergo CME with varying rates and subsequent endosomal trafficking. For example, pep1–PEPR complexes undergo a slower rate of CME compared with BRASSINOSTEROID-INSENSITIVE1 (BRI1). This could be attributed to the pre-formed BRI1–co-receptor complexes at the plasma membrane to receive brassinosteroids (Bucherl *et al.*, 2013; Ortiz-Morea *et al.*, 2016). Similarly, CLV3 peptide binding can induce rapid formation of larger multimeric aggregates of CLV1 with co-receptors at the plasma membrane. In the SAM, CLV1 is endocytosed and trafficked towards the vacuole for degradation (Nimchuk *et al.*, 2011b; Somssich *et al.*, 2015; Wang *et al.*, 2023). However, the subcellular trafficking dynamics of CLE peptides and their fate within the cell after RLK binding are unknown.

To enable *in vivo* studies of CLE–receptor interactions, we developed two new tools: (i) we synthesized a functional, fluorescently labeled CLV3 peptide in order to track the spatial and temporal distribution of CLE peptides and their cognate RLKs *in vivo*, and (ii) we generated a photocaged CLV3 peptide that can be activated by light with high spatial and temporal control. Fluorophore-labeled pep1, flg22, and brassinosteroid hormone have been used previously to understand their cognate receptor-mediated signaling and subsequent sub-cellular dynamics (Irani *et al.*, 2012; Ortiz-Morea *et al.*, 2016; Jelenska *et al.*, 2017). Based on the existing knowledge of the CLE–RLK recognition mechanism and key interacting residues (Yamaguchi *et al.*, 2016), we modified the CLE motif of the CLV3 peptide to allow linkage of a fluorescent dye, while retaining specific binding activity to the RLKs. This was achieved by conjugation of a fluorophore to the side chain. To accomplish this, we replaced the second amino acid, threonine, previously identified as non-essential for binding in depletion assays (Fiers *et al.*, 2006), with lysine and linked a suitable fluorophore to this position. A quantum-dot based probe for CLV3 was previously reported, but it could not be used *in planta* due to toxic effects (Yu *et al.*, 2014). Our functional CLE peptide probe allows the study of *in vivo* binding specificity and subsequent sub-cellular trafficking.

We then used photo-caging to obtain a peptide probe that can be activated locally and rapidly using light (Mangubat-Medina and Ball, 2021). A photocage is a photolabile protecting group that can be used to block the functional groups of the peptide required for receptor binding and biological activity. The caged, non-binding peptide can then be transformed into its active form by releasing the cage group through sample illumination with a specific wavelength of light (Fig. 1). Photo-caging techniques have a very broad application, ranging from enzyme activation to release of therapeutic agents, amino acids, and other molecules in target cells (Silva *et al.*, 2019; Y. Li *et al.*, 2023). This has been applied to study plant hormone effects as well. Photo-caged auxin has enabled control of the auxin response at a single cell level. Photo-caging of gibberellin has enabled monitoring its real time movement and also gradual release of the active compound for a prolonged effect. Photo-caging and release of the active cytokinin form has been achieved as well (Kusaka *et al.*, 2009; Wexler *et al.*, 2019; J. Li *et al.*, 2023; Sun *et al.*, 2023). However, no photoactivatable and fluorescently labeled plant peptide has been synthesized and applied *in planta* so far.

In this study, we present the development of a macromolecular tool box of CLE peptides including fluorescently labeled and photoactivatable peptides. Performing a series of *in vivo* tests, we demonstrate their bioactivity, specificity, and ability to be locally activated. Using these tools, we study binding specificities and subcellular dynamics in a spatially and temporally controlled manner. Overall, we demonstrate how to derive a truly functional and controllable CLE peptide to understand the recognition and binding capacity to its cognate RLKs. Furthermore, the techniques we have developed are transferrable and can be applied to other members of the CLE peptides, and possibly peptides of other families, as well.

Materials and methods

Chemicals and materials

Acetonitrile (≥99%), dichlormethane (≥99%), and acetic acid (≥99%) were purchased from Merck. Acetic anhydride (99%) was purchased from VWR. Diethyl ether (stabilized with butylated hydroxytoluene, ≥99%) was purchased from Honeywell. 1,3-Dimethylbarbituric acid and lithium chloride were purchased from Carl Roth. Piperidine (99%), tetrakis (triphenylphosphine) palladium (0), and trifluoroacetic acid

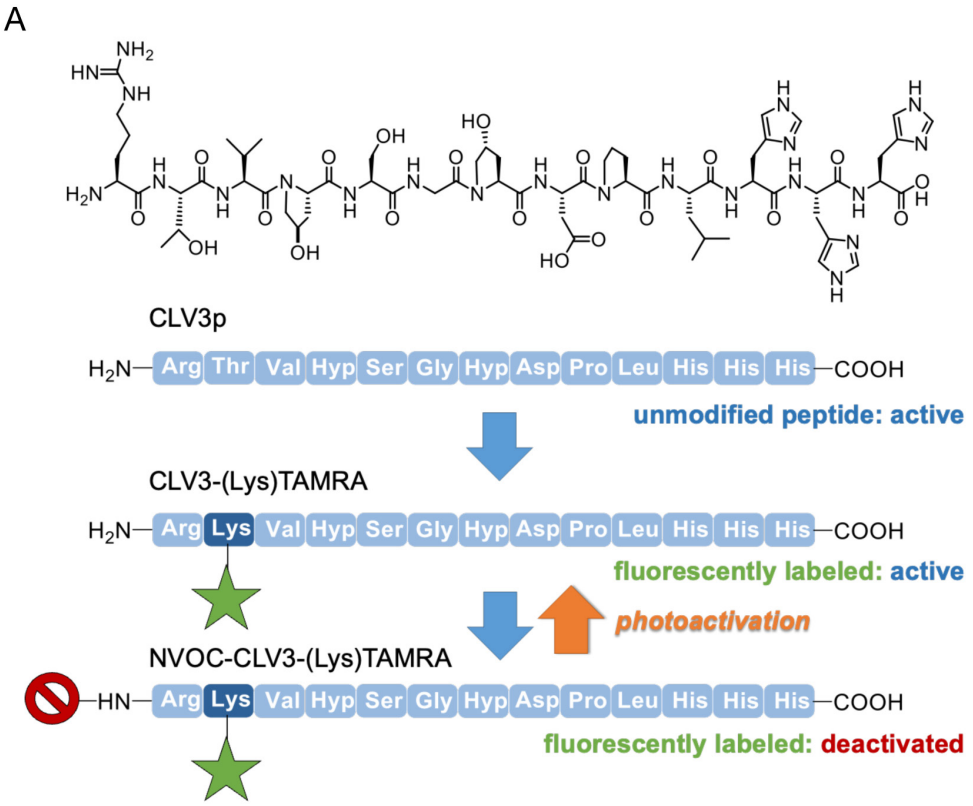

Fig. 1. CLV3 sequence and schematic presentation of the modifications. (A) Introduction of a rhodamine fluorophore (green) to CLV3 to derive an active CLV3 probe followed by introduction of an *N*-terminal 2-nitrobenzyl photocage (red) to allow for light-activated binding to CLV1 receptor *in planta*. CLV1, CLAVATA1; CLV3, CLAVATA3; TAMRA, 6-carboxy-tetramethylrhodamine.

(99%) were purchased from Acros Organics. *N*,*N*-Dimethylformamide (DMF; for peptide synthesis), triisopropylsilane (TIPS, 99%), *N*,*N*-diisopropylethylamine (DIPEA, ≥99%), and benzotriazol-1-yl-oxytripyrrolidinophosphonium hexafluorophosphate (PyBOP, 99%) were purchased from Fluorochem. 6-Carboxy-tetramethylrhodamine succinimidyl ester (TAMRA-*N*-hydroxysuccinimide) was purchased from Carbosynth. Dichlormethane (DCM, ≥99 %) and 4,5-dimethoxy-2-nitrobenzyl (NVOC) chloroformate (NVOC-Cl, 97%) were purchased from Sigma-Aldrich. Fmoc-Hyp(tBu)-OH (99%) was purchased from BLDpharm. Fmoc-Leu-OH (98%) was purchased from Carbolution Chemicals. Boc-Arg(Pbf)-OH, Fmoc-L-Arg(Boc)2-OH, Fmoc-L-Arg(Pbf)-OH, Fmoc-L-Asp(OtBu)-OH, Fmoc-Gly-OH, Fmoc-L-Pro-OH, Fmoc-L-Ser(tBu)-OH, Fmoc-L-Thr(tBu)-OH, and Fmoc-L-Val-OH were purchased from Iris Biotech with purities of 98.0%. Fmoc-His(Trt)-OH (98.0%), Fmoc-Lys(Boc)-OH (98.0%), and Fmoc-Pro-OH (99.0%) were purchased from Merck. *H*-L-His(Trt)-2CT resin (loading 0.63 mmol g^{-1}) was purchased from Rapp Polymer. For trifluoroacetic acid (TFA) removal, AG 1-X8 resin from Bio-Rad Laboratories was used. A Strata C18-E column (1g/6ml) was purchased from Phenomenex. Centrifugal Concentrator Vivaspin20 (1000 MWCO, 20ml) was purchased from Satorius.

Plant materials

Arabidopsis ecotype Col-0 was used as WT and generally as the background for the mutant and the transgenic lines, unless specified. *crn* and *clv2* mutant lines have been described as *crn-10* (CRISPR-Cas9-derived) (Nimchuk, 2017) and *clv2-gabi* (GK-686A09) (Pallakies and Simon, 2014), respectively. *crn-10* was verified using dCAPS strategy which involves amplifying the gene with the oligomers 5′-GTAGAAGCAGCAATGAAGCAAAGAAGAAGGTG-3′ and 5′-GTGTAGATGATGTTGAAGTTGTGGATAAGTG-3′ followed by *Hph*I digestion. *bam1* single and *bam1;bam2* double mutants are CRISPR-Cas9-derived (Fan *et al.*, 2021). The transgenic lines used in the study are: *p35s::ARA7-GFP* (Ueda *et al.*, 2001; Dettmer *et al.*, 2006), XVE>>AXL2 (Adamowski *et al.*, 2018), *pBAM1:BAM1-GFP/bam1-3* (Schlegel *et al.*, 2021), *pUBQ10:VAMP711-YFP* (Geldner *et al.*, 2009), *pCLC2:CLC2-GFP* (ecotype: Wassilewskija) (Konopka *et al.*, 2008), pCLV1::CLV1-2xGFP; *clv1-11* (Nimchuk *et al.*, 2011b), and *RPS5:PEPR1-GFP/pepr1;pepr2* (Ortiz-Morea *et al.*, 2016).

Macromolecule synthesis

General procedure for solid phase synthesis

All peptides were synthesized on solid phase using an automated synthesizer (Activotec P11). The standard Fmoc protocol was used. Therefore, fluorenylmethyloxycarbonyl (Fmoc)-protected amino acids were used for the synthesis. *H*-L-His(Trt)-2CT resin (loading 0.63 mmol g^{-1}) was used and the structures were synthesized by repetitive Fmoc cleavage and amide coupling. For Fmoc cleavage, the resin was treated three times with 25 vol% piperidine in DMF for 10, 15, and 20 min. Afterwards the resin was washed 10 times with DMF. For coupling, the resin was treated with a solution of 5 eq. Fmoc amino acid, 5 eq. PyBOP and 10 eq. DIPEA in DMF for 1 h. Afterwards the resin was washed 10 times with DMF. After assembly of the full sequence, the resin was washed three times with DCM. Thereafter, the modifications of the peptide described in detail below were performed. For final cleavage the resin was treated with 70

vol% TFA, 30 vol% TIPS for 1 h. The peptides were precipitated in diethyl ether, lyophilized, and then TFA removal and further purification were performed.

Alloc deprotection and TAMRA labeling

After finishing the sequence, the allyloxycarbonyl (Alloc) deprotection of lysine on the resin was performed using 10 eq. 1,3-dimethylbarbituric acid and a spatula tip of tetrakis (triphenylphosphine) palladium (0) in DCM (1 ml per 100 mg resin). First 1,3-dimethylbarbituric acid was dissolved DCM and flushed with argon for 2 min. The palladium catalyst was added and flushed with argon for 2 min. The solution was then incubated in the syringe for 45 min. Afterwards the resin was washed 10 times with DCM, 10 times with 0.2 M DIPEA in DMF, and 10 times with DMF. The whole step was repeated once. After lysine was deprotected under reductive conditions, 5-carboxy tetramethyl rhodamine (TAMRA) conjugation took place. For this purpose, 1.3 eq. TAMRA-*N*-hydroxysuccinimide was dissolved in 4 ml of DMF and then 10 eq. of DIPEA was added. The solution was incubated in the syringe for 16 h. The resin was then washed with DMF 10 times and then alternately washed three times with DCM, three times with methanol until the solution becomes clear.

Acetylation

Acetic anhydride (1 ml per 70 mg resin) was incubated to the syringe for 15 min two times. Afterwards the resin was washed 10 times with DMF and 10 times with DCM.

4,5-Dimethoxy-2-nitrobenzyl coupling

NVOC-Cl was dissolved in a 50:50 vol% DCM/DMF mixture (1 ml per 100 mg resin). Then 10 eq. DIPEA was added and the mixture incubated in the solid phase syringe for 16 h. Afterwards the resin was washed 10 times with DMF and 10 times with DCM.

Trifluoroacetic acid removal

TFA removal was performed with an AG 1-X8, quaternary ammonium, 100–200 mesh, acetate form resin. For 100 mg sample, 500 mg of the ion exchange resin was used. The resin was activated by washing three times with 10 ml of 1.6 M acetic acid solution, followed by three times with 10 ml of 0.16 M acetic acid solution. A 100 mg sample was dissolved in 2 mL Milli-Q water, and the solution was loaded into the resin into the syringe. The syringe was shaken for 1 h. The supernatant was recovered, and the resin was washed three times with 0.1 ml Milli-Q. The liquid phases were lyophilized to obtain the crude product as a white or pink solid (in case of TAMRA labelled peptides).

Vivaspin

Samples were separated from non-bound material using a Vivaspin20 Centrifugal Concentrator with 1000 MWCO. The sample was washed five times with 10 ml of Milli-Q water, five times with 10 ml of 2 M LiCl solution, and five times with 10 ml of Milli-Q water, each step using a Heraeus Megafuge 8R centrifuge at 2597 *g* for 15 min.

Column purification

For 4,5-dimethoxy-2-nitrobenzyl (NVOC)–CLV3–TAMRA a further purification step was performed. A Strata C18-E column from Phenomenex (1 g/6 ml) was used to separate the samples from other incorrect sequences. First the column was conditioned with 6 ml acetonitrile and equilibrated with 6 ml Milli-Q water. A 100 mg sample was dissolved in 1–2 ml of Milli-Q water and added to the column. Then the sample was washed with acetonitrile/Milli-Q gradients from 5 to 30% each 3–6 ml on the column.

Reversed-phase high performance liquid chromatography electron spray ionization mass spectrometry

Reversed-phase high performance liquid chromatography (RP-HPLC)-MS was performed on an Agilent Technologies 1260 Infinity instrument in combination with an Agilent Technologies 6120-quadrupole mass spectrometer. The instrument has a wavelength detector (VWD1 A) that measures the absorbance at 214 nm. The mass spectrometer generates ions using the electrospray method, which is used at a charge-to-mass ratio detected between 200 and 2000. The separation of the sample was performed on the MZ-AquaPerfect C18 column (3.0 × 50 mm, 3 μm) at 25 °C. As the mobile phase the following mixtures were used: A: H_2O–acetonitrile (95:5 vol%) with 0.1 vol% formic acid; and B: H_2O–acetonitrile (5:95 vol%) with 0.1 vol% formic acid. The flow rate was 0.4 ml min^{-1}. A linear gradient was from 100% A–0% B to 0% A–100% B with a total measurement time of 17 min.

Ultra-high resolution mass spectrometry

Ultra-high resolution (UHR) MS measurements were performed with a Bruker UHR quadrupole time-of-flight (QTOF) maXis 4G instrument with a direct inlet via syringe pump, an electrospray ionization (ESI) source and a QTOF mass analyser.

MALDI-TOF-MS

Matrix-assisted laser desorption/ionization time of flight (MALDI-TOF) MS spectra were recorded on an UltrafleXtreme instrument from Bruker Daltonik. The concentration of the sample was 1 mg ml^{-1}. The ratio to the α-cyano-4-hydroxycinnamic acid matrix was 1:10.

Lyophilization

The final oligomers were lyophilized with an Alpha 1–4 LD plus instrument from Martin Christ Freeze Dryers GmbH. The drying method was set to −40 °C and 0.1 mbar

Seed sterilization and plant growth conditions

The seeds were sterilized using chlorine gas (1 h in a desiccator after mixing 50 ml of 13% w/v sodium hypochlorite with 4 ml 37% HCl) and were sown on Murashige and Skoog (MS) medium containing ½ 0.22% w/v MS salts with B5 vitamins, 1% w/v sucrose, 0.05% w/v MES and 12 g l^{-1} plant agar, adjusted to pH 5.7 with KOH. The seedlings for root experiments were grown in phytocabinets (poly klima; model: M4Z-TDL+rF) for 4 or 5 d vertically with continuous light at 21 °C. Later, they were transferred to soil and grown in phytochambers for 5–6 weeks under 16 h light–8 h dark to experiment on the shoot apical meristem. The light spectrum for the plant growth condition spans the wavelengths from UV to far red with very minimal irradiance of 1–5 mW m^{-2} nm^{-1} for wavelength <400 nm, and 11–170 mW m^{-2} nm^{-1} for photosynthetically active radiation in the 400–700 nm range.

Treatment and imaging conditions

Peptide treatment

The peptides—pep1 (synthesized by Davids Biotechnologie), pep1–TAMRA (obtained personally from Prof. Russinova), CLV3–TAMRA, Ac–CLV3–TAMRA, NVOC–CLV3, NVOC–CLV3–TAMRA—and the control free TAMRA were dissolved in water to make stocks and subsequently added to the MS medium to reach the indicated working concentration. CLV3p (synthesized by Davids Biotechnologie) was dissolved in peptide buffer of pH 6 (mixture of 87.7 ml of 0.2 M potassium phosphate, mono-potassium salt and 12.3 ml of 0.2 M potassium phosphate, di-potassium salt in 100 ml buffer).

Chemical treatment

Four-day-old seedlings of the XVE>>AXL2 line were transferred to MS agar plates containing 10 μM estradiol [10 mM stock dissolved in dimethyl sulfoxide (DMSO)] for 24 h AXL2 induction. For the uninduced control condition, seedlings were transferred to MS agar plates containing the solvent DMSO. Subsequent mock or peptide treatments in AXL2-induced seedlings were also made in MS agar plates containing either 10 μM estradiol or DMSO.

Brefeldin A (BFA) treatment of seedlings was done in GM liquid medium containing 50 μM BFA together with 1 μM peptide or the controls for 50 min.

Sample handling and imaging

In vivo live fluorescence microscopy was performed with the Zeiss LSM 880 and Zeiss LSM 900 confocal laser scanning microscopy systems employing C-Apochromat ×40/1.20 water objectives. For root length assays, the MS agar plates were scanned using a CanoScan 9000F with 600 dpi resolution.

For root meristem imaging, 4- or 5-day-old seedlings were incubated for the indicated time in MS medium (with or without agar) containing either mock or peptide. For photoactivation of the NVOC–CLV3–TAMRA peptide, the seedlings were mounted with MS medium containing the peptide and directly exposed to UV light (UV lamp X-Cite XYLIS/model XT720L) with DAPI Filter Set 49 (the excitation wavelength is between 300 and 395 nm, peak 365 nm). For targeting the UV radiation over a small field of cells, the field aperture at the microscope was manually controlled, and the field of view was adjusted by locating the cells through the ocular objective.

For shoot apical meristem imaging, the entire inflorescence of 5- or 6-week-old plants was submerged in water containing mock or peptide, 0.01% Tween 20 and 0.1% DMSO. The inflorescence was then cut off and mounted onto the slide over a double-sided adhesive tape. It was then dissected to expose the apical meristem. For a CLV1 localization assay, the inflorescences were treated for 30 s and imaged after 30 min. For a CLV3–TAMRA binding assay, the inflorescences were treated for 1 min, washed thrice, and imaged immediately.

For root length assays, the seeds were directly sown on MS agar plates containing mock or peptide. For the root length assays with NVOC–CLV3, 3 d after germination, one set of plates with peptides or mock were exposed to UV black light (OUSIDE) for 3 h at a distance of 25 cm while the control set were kept unexposed. The plates were covered in yellow foil during growth to filter off light under 500 nm in order to avoid NVOC cleavage before and after UV radiation. After the indicated number of days, the plates were scanned and the length of the roots was analysed. For pre-cleaving the NVOC peptide, a solution of 0.5 mg ml^{-1} was prepared in Milli-Q water. It was filled in a cuvette and radiated with UV black light for 3 h. The pre-radiated NVOC peptide was examined with UV spectra and RP-HPLC-MS and used for the root length assays.

Testing the degradation of the NVOC group

The samples were irradiated from a distance of 25 cm under a UV medium pressure lamp (Heraeus Noblelight) fitted with a mercury lamp that emitted light in the 250–600 nm range, or a 50 W UV black light (OUSIDE) fitted with COB LED chip that emits light in the 395–400 nm range.

Image analysis

Root length analysis and the plasma membrane and cytosolic intensity analysis were performed using Fiji ImageJ software tools (Schindelin *et al.*, 2012). The number of SAMs with vacuolar CLV1 localization and the number of root meristem cells with plasma membrane PEPR1 were recorded by visual inspection. Pearson's correlation coefficient analysis was performed and the cytofluorogram was made with the JaCoP plugin (Bolte and Cordelières, 2006). The plots were made using GraphPad Prism 9 and Origin.

Statistical analysis

All the statistical tests on intensity measurements were performed using GraphPad Prism 9. Statistical tests for root length analysis were performed using R version 4.3.1. '*n*' indicates biological replicates and '*N*' indicates technical replicates.

Results

Synthesis of a functional, fluorescently labeled CLV3 probe (CLV3–TAMRA)

Arabidopsis CLE domains share several conserved residues indicating that they interact with RLKs through a conserved mechanism (Zhang *et al.*, 2016a, b). We chose CLV3, one of the best understood CLEs, as a test system (Fig. 1A).

Synthesis of all modified peptides was performed on an automated peptide synthesizer using well-established solid phase peptide synthesis employing fluorenylmethyloxycarbonyl (Fmoc)-protected amino acids (Wellings and Atherton, 1997). In short, the terminal carboxy group of the amino acid is activated *in situ* to form an active ester that allows for coupling to a resin-bound amine group (e.g. the N-terminus of the previous amino acid, at room temperature and with high yields). Upon coupling of the amino acid, the Fmoc group is selectively cleaved by piperidine, releasing the N-terminus, which is now available for coupling of the next amino acid. After successful build-up of the desired amino acid sequence through such iterative coupling, the peptide is cleaved from the resin, typically under acidic conditions, including the cleavage of potential side chain protecting groups (Fig. 2A). Synthetic protocols for the unmodified CLV3 peptide were developed by choosing a suitable side chain protecting group strategy (Fig. 2B) (2,2,4,6,7-pentamethyldihydrobenzofuran-5-sulfonyl (Pbf) for arginine, tert-butyloxycarbonyl (tBu) for hydroxyproline, serine and aspartic acid, and trityl (trt) for histidine). Upon final cleavage of the peptide from the resin using acidic conditions, the fully deprotected CLV3 peptide (CLV3p) (1) was isolated in high purity (Supplementary Datasets S1–S3). Based on this protocol, a series of modified and fluorescently labeled CLV3 peptides were synthesized (Fig. 2C, D).

One of the challenges in modifying small peptide probes with fluorescent labels is the decrease or even loss of their biological activity, e.g. due to a change in polarity, capping of essential amino acid residues, or sterical shielding of peptide sites that are required for interaction with the receptor (Boaro *et al.*, 2020). Previous studies showed that the C-terminal residues interact with the receptor–co-receptor interface in a conserved manner, and that the N-terminal residue, either R or H, undergoes specific interactions with the receptor. The first and third residues are vital for recognizing and anchoring

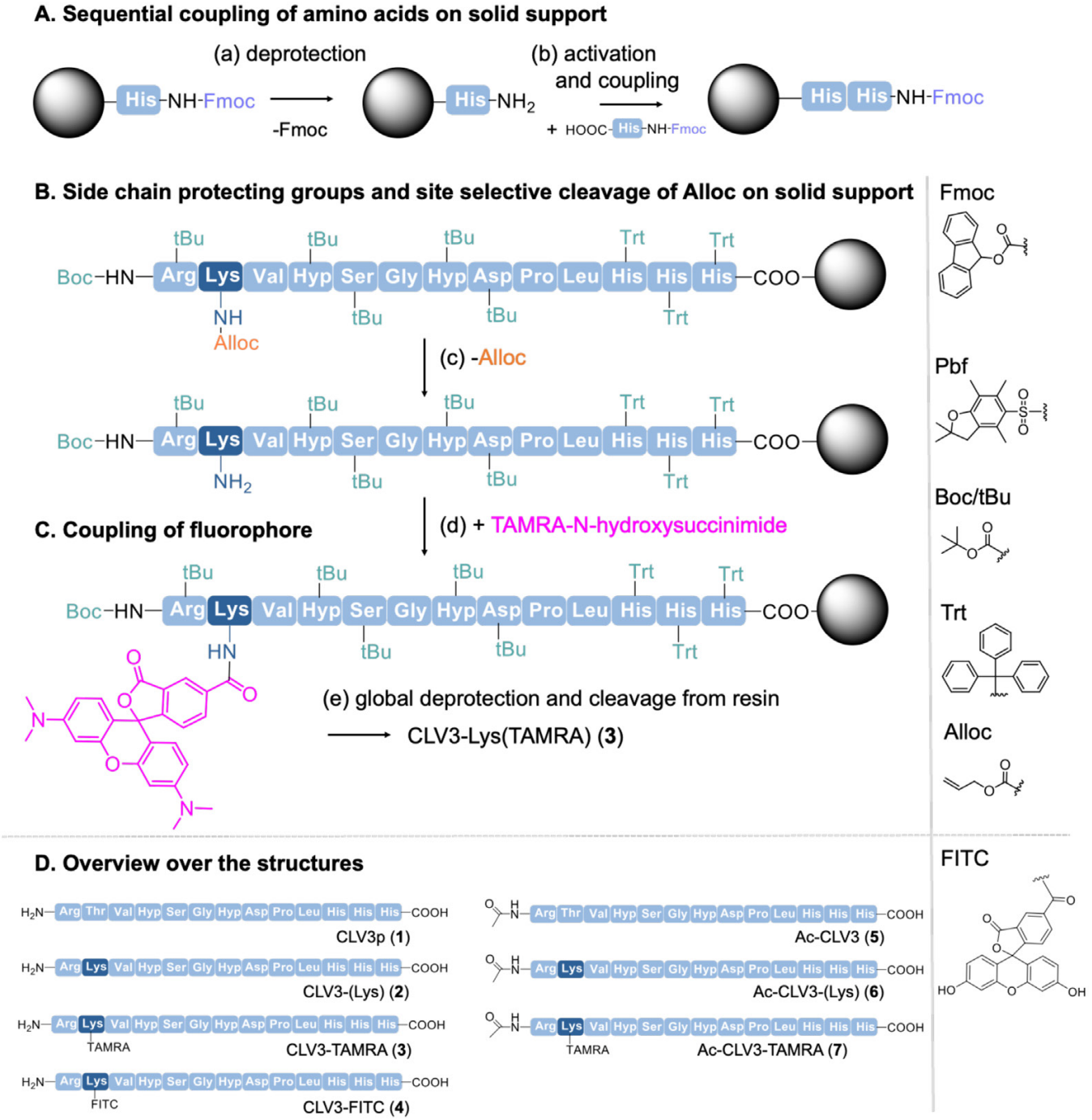

Fig. 2. Solid phase peptide synthesis of CLV3 using preloaded Fmoc-His(Trt)–resin and Fmoc-protecting group (PG) standard protocol. (A) Deprotection of N-terminal Fmoc-PG (a) using 25 vol% piperidine in *N*,*N*-dimethylformamide (DMF) for 5, 15, and 20 min. Coupling of Fmoc-protection amino acid (AA) (b) using 5 eq. AA, 5 eq. benzotriazol-1-yl-oxytripyrrolidinophosphonium hexafluorophosphate (PyBOP) and 10 eq. *N*,*N*-diisopropylethylamine (DIPEA) in DMF for 1 h. Both steps (a) and (b) were repeated to build up a sequence. (B) Selective Alloc deprotection (c) of lysine under reductive conditions with tetrakis (triphenylphosphine) palladium (0) catalyst and 10 eq. 1,3-dimethylbarbituric acid in dichlormethane (DCM) two times for 45 min. (C) Conjugation of TAMRA–*N*-hydroxysuccinimide (d) at free lysine by adding 10 eq. DIPEA in DMF for 16 h. Cleavage of the final structure (e) was with 70 vol% trifluoroacetic acid and 30 vol% triisopropylsilane. (D) Overview of different structures. See Supplementary Datasets S1–S3 for further details on the synthesis and analytical data of different peptide probes. Alloc, allyloxycarbonyl; Boc, tert-butyloxycarbonyl; CLV3, CLAVATA3; FITC, fluorescein isothiocyanate; Pbf, 2,2,4,6,7-pentamethyldihydrobenzofuran-5-sulfonyl; TAMRA, 6-carboxy-tetramethylrhodamine; tBu, tert-butyloxycarbonyl; Trt, trityl.

the CLE peptide to the RLK. The second residue is less conserved and can be modified without strongly compromising peptide activity (Song *et al.*, 2012; Zhang *et al.*, 2016a; Li *et al.*, 2017). Therefore, the threonine at position 2 in CLV3p was replaced by lysine, giving CLV3-(Lys) (2) (Fig. 2D). The amino side chain of the lysine amino acid allows for the introduction of another orthogonal protecting group, allyloxycarbonyl (Alloc), which can be cleaved under reductive conditions on a solid support (Fig. 2B) (Wojcik *et al.*, 2012). Therefore, the N-terminal amino acid arginine was changed from Fmoc to a Boc protecting group as during reductive deprotection of the lysine side chain partial deprotection of the N-terminal Fmoc protecting groups was observed. Selective release of Alloc allowed for quantitative and site-selective introduction of a fluorophore, here either TAMRA or fluorescein isothiocyanate (FITC), giving the two fluorescently labeled CLV3 probes CLV3–TAMRA (3) (Fig. 2C, D) and CLV3-FITC (4) (Fig. 2D). TAMRA and fluorescein were chosen as they are both commonly used in fluorescence microscopy, but differ in their excitation and emission spectra ($\lambda_{ex,max}$=550 nm and $\lambda_{em,max}$=580 nm for TAMRA and $\lambda_{ex,max}$=500 nm and $\lambda_{em,max}$=520 nm for FITC) (Tung, 2004).

In order to assess the binding characteristics of CLV3–TAMRA as a peptide probe, we synthesized a series of CLV3 peptides that are acetylated at the N-terminus, Ac–CLV3 (5), Ac–CLV3-(Lys) (6), and Ac–CLV3–TAMRA (7) (Fig. 2D), as negative controls. Instead of the Boc-protected arginine, its Fmoc-protected variant was used. Fmoc was cleaved off under basic conditions while every other protection group was stable under these conditions and capped with acetic anhydride to receive the acetylated N-terminus.

Testing the bioactivity of CLV3–TAMRA

Bioactivity of the modified peptides was tested using a root length assay. Exogenous application of the synthesized native CLV3 peptide (CLV3p) elicits a premature differentiation of the root meristem, leading to a short root phenotype, at CLV3p concentrations of 10 nM or higher (Hazak *et al.*, 2017; Blümke *et al.*, 2021). We compared root lengths of seedlings grown on medium with different concentrations of CLV3p or the modified peptides (Fig. 3; Supplementary Fig. S1). Seedlings showed a strong reduction in root length in response to CLV3p at 100 nM or lower (Blümke *et al.*, 2021) (Fig. 3; Supplementary Fig. S1A); CLV3–TAMRA was ineffective at 100 nM, but triggered root length reduction at 1 µM concentration (Fig. 3; Supplementary Fig. S1A). This reduced activity is likely due to the steric hindrance to peptide binding caused by TAMRA.

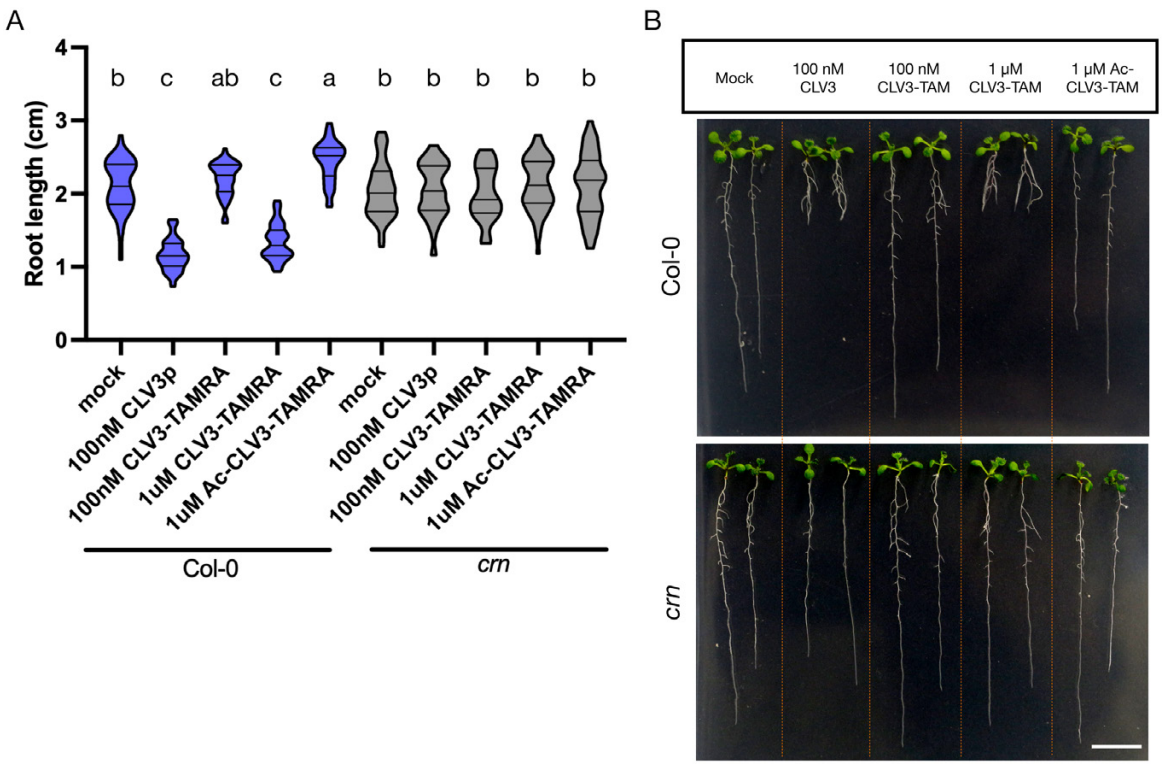

Fig. 3. Bioactivity of CLV3–TAMRA. (A) Violin plot representing root length analyses of Col-0 and *crn* after 7 d treatment with mock, CLV3p, CLV3–TAMRA and Ac–CLV3–TAMRA. $n \geq 43$ roots for each condition; N=3. The lines represent the median and the quartiles. Two-way ANOVA with interaction, F-test; $P<2 \times 10^{-16}$. Statistical grouping was calculated by Tukey's HSD test (α=0.001). Groups sharing the same letter are not significantly different. (B) Images of seedlings of Col-0 and *crn* after 10 d treatment. Scale bar: 1 cm. CLV3, CLAVATA3; TAMRA, 6-carboxy-tetramethylrhodamine.

For comparison, we found that CLV3-(Lys) was bioactive at the much lower concentration of 200 nM (Supplementary Fig. S1B). Neither Ac–CLV3–TAMRA, nor free TAMRA fluorophore, nor CLV3-FITC elicited any response in our assays (Fig. 3; Supplementary Fig. S1A, C, D). Signalling of CLV3p during root development depends on the CLV2/CRN-receptor heteromer (Fiers *et al.*, 2005; Miwa *et al.*, 2008). We used one of the mutants of the CLV2/CRN heteromeric complex, *crn*, to thwart the CLV3 signaling pathway. The mutant seedlings did not respond to the tested peptides, indicating that the CLV3–TAMRA peptide acts through the canonical CLV3 signaling pathway, although with a lower efficacy than the unmodified CLV3p (Fig. 3; Supplementary Fig. S1A). Lack of CLV3–FITC biological activity could be due to structural differences between the fluorophores: TAMRA carries tertiary amines in the xanthene core and is unable to form hydrogen bonds, while FITC contains hydroxyl groups that could interact with the peptide backbone, potentially altering its conformation and preventing binding to the receptor protein. In summary, modifying the second amino acid residue of the CLE domain to attach the fluorophore is an effective strategy in creating a bioactive CLE peptide probe. TAMRA, as a fluorescent agent for CLE peptide probes, can retain their bioactivity, although with a significantly diminished efficiency.

Sub-cellular localization and trafficking of CLV3–TAMRA

We tested if CLV3–TAMRA is recognized by the RLKs at the plasma membrane, and how it interacts with the endocytic sub-cellular trafficking machinery. When added to Arabidopsis root or shoot meristems, CLV3–TAMRA localized to the plasma membrane in all layers of the meristems within 3 min after addition (Fig. 4A, B; Supplementary Fig. S2A, S2B). The negative control peptide Ac–CLV3–TAMRA showed a very weak signal at the plasma membrane, possibly due to unspecific binding to other plasma membrane proteins (Fig. 4A, B).

During the course of 40 min treatment, CLV3–TAMRA accumulated increasingly in the vacuole, which is surrounded by the tonoplast (Fig. 4C; Supplementary Fig. S2C). We first tested if the accumulating vacuolar signal is due to endocytosed CLV3–TAMRA peptide, or free TAMRA fluorophore that resulted from CLV3–TAMRA instability or degradation. We analysed CLV3–TAMRA from our stock solution via RP-HPLC after 1 and 2 years' storage, and saw no degradation of the fluorophore, suggesting that the CLV3–TAMRA peptide remained intact and did not undergo dissociation into free fluorophore during storage (Supplementary Dataset S4). We concluded that CLV3–TAMRA is functional and reaches the vacuole through the endocytic sub-cellular trafficking pathway.

We then examined the CLE peptide sub-cellular trafficking process. In animal cells, after endocytosis, ligand-bound receptors enter the early endosome for sorting. The membrane bound receptors are primarily recycled and return to the plasma membrane, but ligands are mostly delivered to the late endosome and then degraded (French and Lauffenburger, 1997; Lakadamyali *et al.*, 2006; Solinger and Spang, 2022). We first examined if CLV3–TAMRA undergoes CME from the plasma membrane using AUXILIN-LIKE2 overexpression, which strongly hinders CME (Adamowski *et al.*, 2018). After 60 min of CLV3–TAMRA treatment, CLV3–TAMRA accumulated in the vacuole. However, estradiol inducible overexpression of AUXILIN-LIKE2 strongly diminished the vacuolar signal compared with mock treatment, showing that CLV3–TAMRA is subject to CME (Fig. 4D). The inactive Ac–CLV3–TAMRA and free TAMRA fluorophore also reached the vacuole (Supplementary Fig. S2C), although to a lesser extent. CME inhibition interfered with uptake and vacuolar localization of Ac–CLV3–TAMRA (Fig. 4D), indicating that it might still bind plasma membrane localized RLKs with reduced affinity, possibly via the conserved C-terminal interaction. Free TAMRA fluorophore was neither bound at the plasma membrane nor trafficked via endosomes; therefore, it likely entered cells via diffusion (Supplementary Fig. S2D).

We then investigated the endocytic route to the vacuole. We found that CLV3–TAMRA co-localized with a few late endosomes labeled with ARA7 (a Rab GTPase) (Lee *et al.*, 2004) rapidly within 4–6 min (Fig. 4E). After 15 min, CLV3–TAMRA reached almost all the ARA7-labeled late endosome compartments and aggregated into Brefeldin A (BFA) bodies after BFA treatment (Geldner *et al.*, 2009; Narasimhan *et al.*, 2021) (Fig. 4F, F′, G). However, we only occasionally observed localization of CLV3–TAMRA in early endosomes, marked by CLC2–GFP (Supplementary Fig. S2E, E′; the control for ARA7–GFP and CLC2–GFP bleed-through into the TAMRA channel is shown in Supplementary Fig. S2F). This is in concordance with flg22 and pep1 ligands that are also predominantly localized in late endosomes *en route* to the vacuole, and in contrast to animal cells where the ligand–receptor sorting occurs in early endosomes (Ortiz-Morea *et al.*, 2016; Jelenska *et al.*, 2017). However, neither free TAMRA nor Ac–CLV3–TAMRA co-localized with late endosomes (Fig. 4F, F′), although a weak Ac–CLV3–TAMRA signal was observed in BFA bodies (Fig. 4G). We conclude that CLV3–Tamra is endocytosed via CME and effectively trafficked along the endosomal pathway. When and where the separation of endocytosed peptide ligands from the RLKs occurs in plant cells remains to be solved.

Overall, we found that CLV3–TAMRA endocytosis and sub-cellular trafficking dynamics are very rapid, and that the trafficking route is concordant with other plant signaling peptides.

Binding specificity of CLV3–TAMRA to receptor-like kinases

Studies in heterologous systems reported that CLV3 binds to the RLKs CLV1 and BAM1, although reports on binding

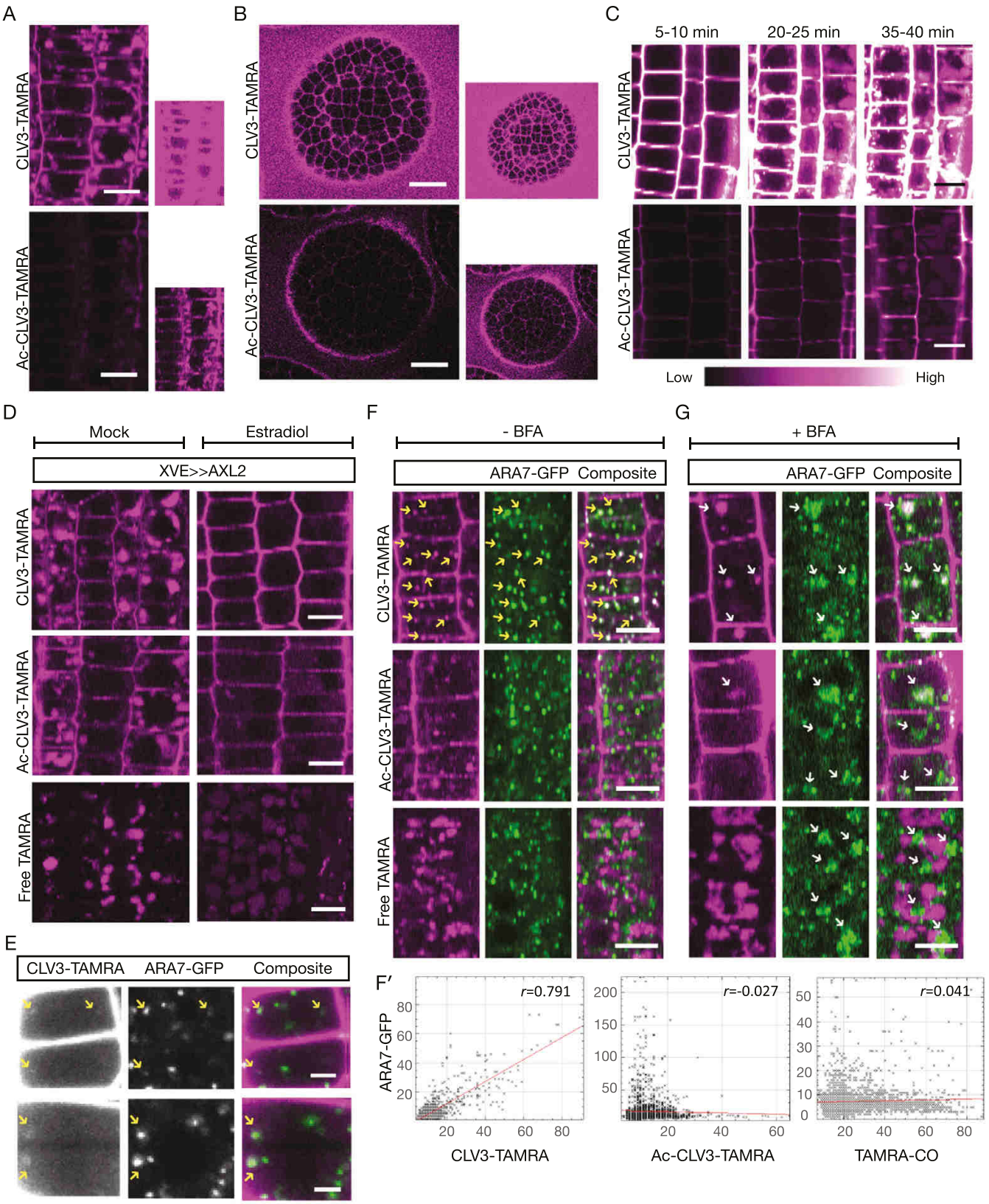

Fig. 4. Sub-cellular localization and trafficking of CLV3–TAMRA. (A–G) Representative confocal images of root meristem epidermal cells (A, C–G) or shoot apical meristem (SAM) cells (B) after 1 μM treatment of the peptide CLV3–TAMRA, or the controls Ac–CLV3–TAMRA or free TAMRA fluorophore.

Lines used: Col-0 (A, B); *pBAM1:BAM1-GFP/bam1-3* (C); *XVE>> AUXILIN-LIKE2* (D); *p35s:ARA7-GFP* (E–G). (A) Plasma membrane localization after 15 min treatment. n=6; N=2. The inset on the right shows the same images with increased brightness. (B) Plasma membrane localization in SAM cells after 1 min treatment and washing. $N \geq 5$. The inset on the right shows the same images with increased brightness. (C) Vacuolar accumulation after continuous treatment overtime. $n \geq 6$; N=2. (D) Clathrin-mediated endocytosis and vacuolar trafficking after 30 min treatment. The seedlings either had induction of AUXILIN-LIKE 2 overexpression under estradiol treatment or no induction under mock treatment. $n \geq 6$; N=2. (E) Localization of the peptide in late endosome after 4–6 min treatment. n=4; N=2. (F) Localization of peptide and controls in late endosome 10–15 min post 5 min treatment. $n \geq 5$; N=2. Pearson's correlation coefficient (r) of co-localization between ARA7–GFP and peptide and controls was calculated in three cells for each condition: CLV3–TAMRA versus ARA7–GFP: r=0.791, 0.711, and 0.664; Ac–CLV3–TAMRA versus ARA7–GFP: r=–0.027, –0.111, and 0.07; TAMRA-CO versus ARA7–GFP: r=0.041, 0.032, and –0.192. (E′) Cytofluorogram of one measurement from each condition is shown. (G) Localization of peptide and controls in Brefeldin A (BFA) bodies containing late endosomes after 50 min co-treatment with BFA. $n \geq 5$; N=3. Yellow arrows indicate the CLV3–TAMRA co-localized with late endosomes marked by ARA7–GFP. White arrows indicate the BFA bodies containing late endosomes, and the peptide or the controls. Note: in (D–F), Ac–CLV3–TAMRA and free TAMRA were imaged at higher laser intensity and gain than CLV3–TAMRA to observe their sub-cellular localization. Scale bar: (A, C, D, F, G) 10 µm; (B) 15 µm; (E) 3 µm. CLV3, CLAVATA3; GFP, green fluorescent protein; TAMRA, 6-carboxy-tetramethylrhodamine.

affinities vary significantly between studies (Ogawa *et al.*, 2008; Guo *et al.*, 2010; Hazak *et al.*, 2017; Crook *et al.*, 2020). With our probes in hand, we here tested the interaction of CLV3–TAMRA with CLV1 and BAM1 *in vivo*.

After CLV3 binding, CLV1 in the SAM undergoes endocytosis and is targeted to the vacuole. The CLV1 population at the plasma membrane is strongly reduced over time (Nimchuk *et al.*, 2011b; Wang *et al.*, 2023). We observed that CLV3–TAMRA, but not Ac–CLV3–TAMRA, induced CLV1 endocytosis and vacuolar targeting (Fig. 5A, A′). However, CLV3 binding does not trigger endocytic loss of the BAM1 plasma membrane pool or increased vacuolar trafficking of BAM1 (Supplementary Fig. S3A). This difference could be due to a high rate of recycling of BAM1, or alternatively due to a smaller fraction of BAM1 being involved in active signaling that further undergo degradation (Sorkin and von Zastrow, 2009; Bucherl *et al.*, 2013). Therefore, to test for interaction with BAM1, we used a transgenic Arabidopsis line that overexpressed BAM1–GFP in the root meristem (Supplementary Fig. S3B). Compared with wild-type root meristems, a significantly higher amount of CLV3–TAMRA bound to the plasma membrane of BAM1–GFP (OX) root meristems (Fig. 5B; Supplementary Fig. S3C, C′; the control for GFP bleed-through in the TAMRA channel is shown in Supplementary Fig. S3D). Plasma membrane binding of Ac–CLV3–TAMRA, on the other hand, was generally very low although slightly increased in the BAM1–GFP (OX) roots (Supplementary Fig. S3C, C′). In contrast, we observed a general decrease in plasma membrane bound CLV3–TAMRA in *bam1* and *bam1;bam2* mutants compared with WT, which is particularly obvious in the stele layers. It is to be noted that this decrease could be attributed to an increased endocytic rate in the mutants as indicated by strong cytosolic signal (Supplementary Fig. S3E, E′). We then incubated root meristems of BAM1–GFP (OX) line with CLV3p and CLV3–TAMRA to test if both compete for the same binding sites on the plasma membrane (Fig. 5C, C′). With increasing concentration of CLV3p in the medium, the amount of CLV3–TAMRA fluorescence on the plasma membrane decreased, showing that CLV3p can compete with CLV3–TAMRA binding to the same site. This demonstrates that CLV3–TAMRA has strong affinity to both CLV1 and BAM1 *in vivo*, in contrast to results obtained from *in vitro* studies.

Because CLV3 has a strong affinity to CLV1 clade RLKs, we tested for its cross-clade interaction with PEPR1, an RLK of a phylogenetically distant clade (Furumizu *et al.*, 2021). pep1 and pep1–TAMRA bound with strong affinity and induced endocytosis of its plasma membrane localized cognate receptor PEPR1–GFP, causing a significant down-regulation of the plasma membrane PEPR population through vacuolar targeting (Ortiz-Morea *et al.*, 2016) (Fig. 5D–F, D′–F′; Supplementary Fig. S3F, F′). However, CLV3–TAMRA did not exhibit an increased binding in a PEPR1 overexpression transgenic line (Fig. 5D, D′); moreover, neither CLV3p nor CLV3–TAMRA induced PEPR endocytosis from the plasma membrane (Fig. 5F, F′; Supplementary Fig. S3F, F′). Similarly, pep1–TAMRA, which exhibited an increased binding in PEPR1 overexpression line (Fig. 5D, D′), failed to show increased binding affinity to BAM1 overexpression (Fig. 5E, E′). We conclude from our *in vivo* studies with modified CLV3 peptides that interactions of peptides are limited to a specific RLK family, pep1 to the PEPR clade and CLV3 to the CLV1 clade, contradicting earlier reports of cross-clade promiscuity in CLE peptide interactions (Gutierrez-Alanis *et al.*, 2017; Qian *et al.*, 2018; Furumizu *et al.*, 2021).

Spatial and temporal control of CLE signaling

CLV3–TAMRA is a functional bioactive probe that, when externally applied, will rapidly reach all tissue layers and elicit a response. In order to achieve a controlled activity of the peptide in the targeted tissue or at a specific time point, we used nitroveratryloxycarbonyl (NVOC) as photo-cleavable protecting group, or photocage for the N-terminus of the CLV3 peptide with a maximum absorption for cleavage at 365 nm (Kneuttinger, 2022) (Fig. 6A). Linking the NVOC group to the N-terminus generates an inactive CLV3 probe; biological activity is then reinstated upon light-triggered cleavage of the

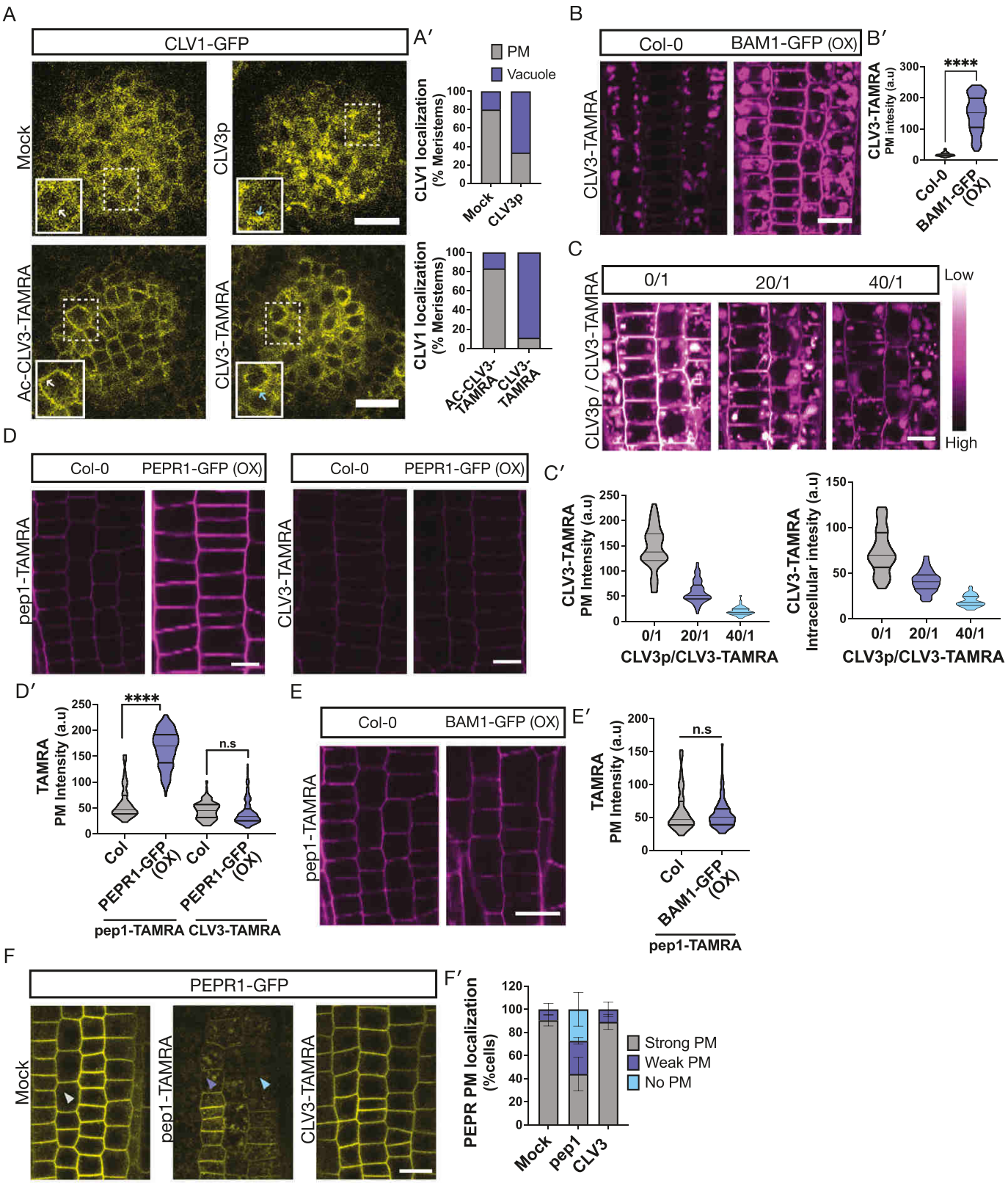

Fig. 5. Binding specificity of CLV3–TAMRA to RLKs. (A–F) Representative confocal images of shoot apical meristem (SAM) (A) or root meristem epidermal cells (B–E) after respective treatments. Lines used: *pCLV1:CLV1-2X-GFP/clv1-11* (A); Col-0 and *pBAM1:BAM1-GFP/bam1-3* (B, E); *pBAM1:BAM1-GFP/bam1-3* (C); Col-0 and *pRPS5A:PEPR1-GFPpepr1;pepr2* (D); *pRPS5A:PEPR1-GFP/pepr1;pepr2* (F). (A) Top, CLV1 localization

after 30 min of treatment with either mock or 100 nM CLV3. $N \geq 5$. Bottom, CLV1 localization after 30 min of treatment with 1 μM of either Ac–CLV3–TAMRA or CLV3–TAMRA. $N \geq 9$. The insets showcase the plasma membrane (white arrow) or vacuolar localized CLV1 (blue arrow) in a cell. Stacked bar graph represents the relative number of SAMs with plasma membrane and vacuolar localized CLV1. (B) CLV3–TAMRA plasma membrane signal after 1 μM, 30 min treatment in Col-0 or BAM1–GFP overexpression line. $n \geq 6$; $N=3$. (B′) Violin plot representing CLV3–TAMRA mean fluorescence intensity of the plasma membrane from 13–39 cells/root. Two-sided *t*-test. For Col-0>BAM1–GFP, $P<0.0001$ (****). (C) CLV3–TAMRA plasma membrane signal after 30 min treatment with CLV3p/CLV3–TAMRA combination: from left to right, 0 μM/1 μM, 20 μM/1 μM, 40 μM/1 μM. $n \geq 7$; $N=2$. (C′) Violin plots representing the mean fluorescence intensity of the plasma membrane (top) or the intracellular region (bottom) from 5–17 cells/root. (D) pep1–TAMRA and CLV3–TAMRA plasma membrane signal after 200 nM, 1 min treatment in Col-0 and PEPR1–GFP overexpression line. $n=6$; $N=1$. (D′) Violin plot representing TAMRA mean fluorescence intensity of the plasma membrane from 14–31 cells/root. Two-sided *t*-test. For pep1–TAM/PEPR–GFP>Col-0, $P<0.0001$ (****); CLV3–TAM/PEPR–GFP>Col-0, was not significant. (E) pep1–TAMRA plasma membrane signal after 200 nM, 1 min treatment in Col-0 or BAM1–GFP overexpression line. $n \geq 6$; $N=1$. (E′) Violin plot representing pep1–TAMRA mean fluorescence intensity of the plasma membrane from 10–25 cells/root. Two-sided *t*-test. BAM1–GFP>Col-0 was not significant. (F) PEPR1 plasma membrane localization 1 h after 30 s pulse with mock, 100 nM pep1–TAMRA or 1 μM CLV3–TAMRA. Grey, violet, and blue arrowheads indicate an example cell with strong, weak, and no plasma membrane PEPR, respectively. (F′) Stacked bar graph representing relative number of cells with strong, weak, or no PEPR at the plasma membrane. $n=5$; $N=2$. At least 55 cells were analysed per root. Error bars indicate mean ±SD. The lines in the violin plots indicate the median and the quartiles. Scale bar: (A, B, E, F) 15 μm; (C, D) 10 μm. BAM1, BARELY ANY MERISTEM1; CLV1, CLAVATA1; CLV3, CLAVATA3; GFP, green fluorescent protein; n.s., not significant; PEPR, PEP RECEPTOR; PM, plasma membrane; RLK, receptor-like kinase; TAMRA, 6-carboxy-tetramethylrhodamine.

NVOC group. As before, the TAMRA fluorophore was linked to the AA2 position, giving fluorescently labeled, photoactivatable NVOC–CLV3–TAMRA (8) (Fig. 6B).

Peptide synthesis was performed following previously discussed solid phase peptide protocols. Coupling of NVOC was performed on solid phase using NVOC chloride and coupling to the N-terminus of the terminal amino acid after Fmoc release. After installation of the photocage, the TAMRA fluorophore was coupled as previously described. After cleavage from the resin the crude peptide was purified by chromatography to give NVOC–CLV3–TAMRA with <90% relative purity (Supplementary Datasets S1, S3). First, release of the NVOC group upon light irradiation in solution was evaluated. Therefore, the NVOC–CLV3 peptide was exposed to UV light at 365 nm and analysed by RP-HPLC-MS measurements at different time points. After 150 min, full deprotection was observed. Importantly, no decomposition or fragmentation of the deprotected peptide was found (Fig. 6C; Supplementary Dataset S5).

We first tested the efficiency of NVOC cleavage from the peptide and the bioactivity of the NVOC-cleaved CLV3. We performed root length assays on whole seedlings that were grown in medium containing NVOC–CLV3 or CLV3p or mock, that were either (i) irradiated with UV for 120 min or (ii) not irradiated. UV irradiation of plates with NVOC–CLV3 resulted in shorter roots than controls, equivalent to CLV3p-treated roots. This indicated that the NVOC group was cleaved off, thereby releasing CLV3, which inhibited meristem development. *clv2* mutants were resistant to NVOC–CLV3 with or without irradiation, indicating that the short roots were indeed due to activation of the photo-caged CLV3 peptide and signaling, and not a direct consequence of UV irradiation (Fig. 6D). Roots protected from UV exposure developed similar to mock-treated negative controls, showing that the NVOC group remained attached, which rendered the peptide inactive (Fig. 6D). Additionally, the roots grown in medium with pre-cleaved peptide (NVOC+CLV3) had shorter roots, proving that photoactivation of the photocaged peptide by UV is a reproducible technique and that NVOC in the medium does not interfere with the bioactivity of the peptide or plant development.

We then tested if the photocaged peptide can be rapidly photoactivated in the target tissue. To visualize peptide uncaging and perception, we photoactivated the NVOC–CLV3–TAMRA peptide by non-targeted, whole meristem UV irradiation at 385 nm, which is close to the maximum absorption wavelength for NVOC cleavage (Schaper *et al.*, 2009). NVOC–CLV3–TAMRA predominantly localized to the apoplastic space before photoactivation due to the blocked N-terminus. After 30 s of UV irradiation using the UV lamp at the confocal microscope, we observed a rapid plasma membrane localization of the deprotected CLV3–TAMRA (Fig. 6E, top, E′). Notably, CLV3–TAMRA localized to the epidermal layer of the root (Fig. 6E, bottom). Twenty minutes after photoactivation, we observed CLV3–TAMRA in endosomal compartments, and subsequently also in vacuoles (Fig. 6F, G). We then performed targeted irradiation and peptide activation in a few epidermal cells using the UV lamp or the laser. We observed localized plasma membrane binding of the deprotected CLV3–TAMRA peptide in and around the irradiated area (Fig. 6F; Supplementary Fig. S4A). It is to be noted that focusing UV radiation over target cells manually through the field aperture is not as precise as laser-based activation, and hence there is a slightly broader dispersion of energy and photoactivation. On the other hand, a 405 nm laser is not as energetically efficient as high energy UV lamp radiation.

We have successfully created photoactivatable CLE peptide tools, NVOC–CLV3 and NVOC–CLV3–TAMRA, that can be activated simply by very short exposure to UV radiation in target cells or tissue *in vivo*. The released bioactive peptide can be used to study rapid down-stream signaling responses or cell/tissue specific effects.

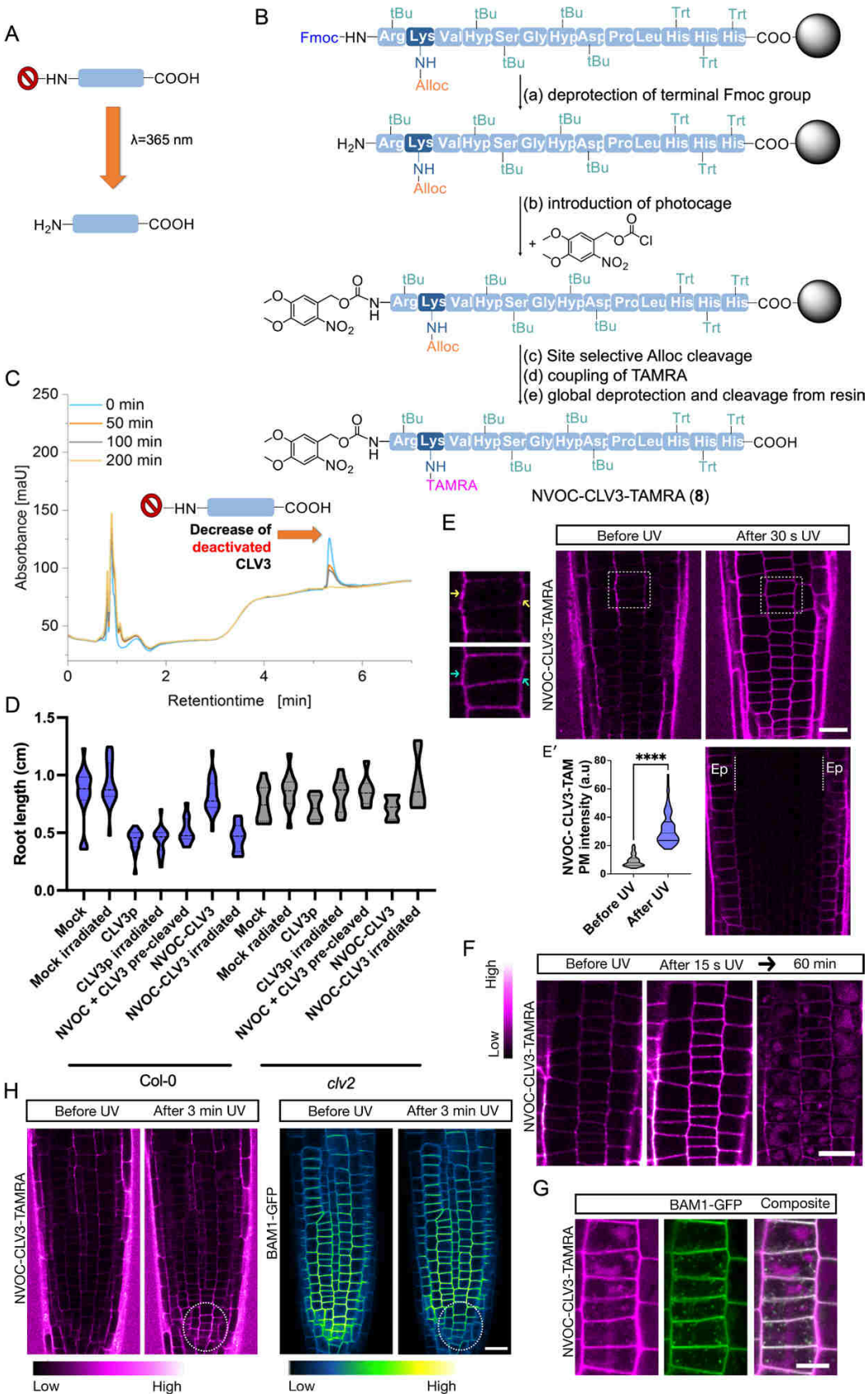

Fig. 6. Synthesis and activation of photocaged peptide by UV radiation. (A) General scheme for peptide probe activation through 365 nm light-induced cleavage of N-terminal NVOC photocage. (B) Solid phase peptide synthesis of NVOC–CLV3–TAMRA using preloaded Fmoc-His (Trt)-resin and

Fmoc-protecting group (PG) standard protocol. Deprotection of N-terminal Fmoc-PG (a) using 25 vol% piperidine in *N*,*N*-dimethylformamide (DMF) for 5, 15, and 20 min. Coupling photocage (b) using 5 eq. NVOC-Cl and 10 eq *N*,*N*-diisopropylethylamine (DIPEA) in DMF/dichlormethane (DCM) 1:1 for 4 h. Selective Alloc deprotection (c) of lysin under reductive conditions with tetrakis (triphenylphosphine) palladium (0) catalyst and 10 eq. dimethylbarbituric acid in DCM two times for 45 min. Conjugation of TAMRA–*N*-hydroxysuccinimide (d) at free lysine by adding 10 eq. DIPEA in DMF for 16 h. Cleavage of the final structure (e) with 70 vol% trifluoroacetic acid and 30 vol% TIPS. (C) Section of RP-HPLC chromatograms in which NVOC–CLV3 was irradiated with an UV medium-pressure lamp including wavelength of 365 nm for a total duration of 150 min. After 150 min, a complete degradation of the NVOC–CLV3 signal was observed, indicating a complete cleavage of the NVOC-protecting group. See Supplementary Dataset S5 for full spectra. (D) Violin plot representing root length analysis of 7-day-old Col-0 and *clv2* seedlings 7 d treatment with mock, 200 nM CLV3p, 200 nM NVOC–CLV3 or pre-cleaved 200 nM NVOC–CLV3. The lines represent the median and the quartiles. n>9 roots; N=1. Two-way ANOVA with interaction, F-test, $P<9.59 \times 10^{-12}$. Statistical grouping was calculated by Tukey's HSD test (α=0.001). Groups sharing the same letter are not significantly different. (E–H) Representative confocal images of root meristem epidermal cells after treatment with 1 µM (E, G, H) or 5 µM (F) NVOC–CLV3–TAMRA. Line used: *pBAM1:BAM1-GFP/bam1-3*. (E) Plasma membrane binding of NVOC–CLV3–TAMRA before and after photoactivation by UV exposure of root tip for 30 s. Top, image of the epidermal layer. Bottom, image of the root center with all layers visible. The inset shows the zoomed-in cells with CLV3–TAMRA in the apoplast around the cells (yellow arrows) or at the plasma membrane (blue arrows). (E′) Violin plot representing the CLV3–TAMRA mean fluorescence intensity of the plasma membrane from 12–26 cells/root. n=4; N=6. Two-sided t-test. For After>Before, P<0.0001 (****). (F) Vacuolar localization of photoactivated NVOC–CLV3–TAMRA 60 min after 15 s UV exposure. n=5; N=2. (G) Late endosome localization of photoactivated NVOC–CLV3–TAMRA 20 min after 15 s UV exposure. n=2; N=3. (H) Targeted photoactivation of NVOC–CLV3–TAMRA after 3 min UV exposure of specific cells (marked by dotted circle) through controlled field aperture. Plasma membrane binding of NVOC–CLV3–TAMRA before and after photoactivation in BAM1–GFP expressing line is shown. BAM1–GFP shows mild bleaching due to UV exposure. Scale bar: (E, F, H) 20 µm; (G) 10 µm. BAM1, BARELY ANY MERISTEM1; CLV3, CLAVATA3; GFP, green fluorescent protein; NVOC, 4,5-dimethoxy-2-nitrobenzyl; TAMRA, 6-carboxy-tetramethylrhodamine.

Discussion

Synthetic chemistry has aided in generating ligands to dissect ligand–receptor pairing, receptor activation, and downstream signaling. Such chemical tools have also been used to label phytohormones and peptides to probe their interaction with receptor kinases and subsequent signaling (Sharma and Russinova, 2018). In this study we have synthesized a set of CLV3 probes with different modifications to study and decipher diverse aspects of CLE–RLK signaling.

Advantages of studies with fluorophore labeling

Following the identification of CLE molecules, synthesis of the active CLE peptides enabled rapid elucidation of their effects and downstream signaling effectors through *in vivo* and *in vitro* bioassays (Fiers *et al.*, 2005; Ito *et al.*, 2006; Stahl *et al.*, 2009; Qian *et al.*, 2018; Takahashi *et al.*, 2018; Breda *et al.*, 2019; Blümke *et al.*, 2021; Breiden *et al.*, 2021). Synthetic approaches have also provided a faster alternative to mutagenesis in creating peptide variants. Replacing individual residues or a combination of residues, and swapping of residues between peptides have facilitated breakthroughs in dissecting CLE affinities, specificities, and recognition mechanism for individual RLKs (Ito *et al.*, 2006; Song *et al.*, 2012; Zhang *et al.*, 2016a; Li *et al.*, 2017; Roman *et al.*, 2022). However, most of those studies were performed *in vitro*. An alternative assay that allowed differentiation of affinities for RLKs was photoaffinity labeling, and binding of CLE9 and CLV3 peptides to several RLKs was resolved using this technique (Ogawa *et al.*, 2008; Shinohara and Matsubayashi, 2013, 2015). However, photoaffinity labeling is an expensive technique, requires elaborate protocols, and does not spatially resolve the ligand–receptor interactions within a tissue (Sharma and Russinova, 2018). We emphasize here the advantages of fluorescently labeled peptides, which exhibit non-covalent reversible binding and native endocytic sub-cellular trafficking interactions.

Challenges in CLE modification to study interaction specificity

Attaching a fluorophore while maintaining biological activity is challenging, since CLE peptides are only 12 or 13 amino acids long, and modification of residues can change recognition and binding to cognate RLKs. Ogawa *et al.* (2008) had previously synthesized modified CLV3 peptides replacing L10 and T2, which still effectively bound the CLV1 ectodomain. Based on these *in vitro* experiments, we modified the second CLV3 residue to lysine (T2K) and added the fluorophore TAMRA. Nevertheless, the second residue variation between CLE41 and -42 is enough to significantly alter their binding affinity to TDR (Zhang *et al.*, 2016a). Therefore, it is crucial to test both the bioactivity and specificity of the synthesized peptide tools. We observed that the peptide was indeed bioactive but showed reduced activity, which is likely caused by the attached TAMRA fluorophore (Fig 3; Supplementary Fig. S1). However, the peptide showed no significant decrease in affinity to CLV1 clade receptors, supporting the notion that CLV3–TAMRA peptide is functional. Furthermore, we utilized the probe to test for cross-clade interaction to the phylogenetically distant PEPR clade. We observed no binding affinity of CLV3–TAMRA to PEPR1. Importantly, pep1–TAMRA also showed no affinity to BAM1, a member of the CLV1 clade (Fig. 5, Supplementary Fig. S3). This demonstrates that, *in vivo*, there is minimal cross-interaction of peptides from distinct families with different RLK clades. Gutierrez-Alanis *et al.* (2017) previously reported that CLE14 interacts with PEPR2, based on a bimolecular fluorescence complementation (BiFC) assay of CLE14–nYFP with PEPR2–cYFP. However, CLE peptides undergo extensive processing, which involves not only the

removal of the N-terminal signal peptide, but also proteolytic cleavage of the active CLE peptide from a larger precursor. Any C- or N-terminal fusions, such as nYFP in this case study, would not remain linked to the bioactive CLE peptide. CLE peptide interactions with receptors can therefore not be reliably detected using BiFC assays, and the fluorescence detected in the aforementioned study is likely due to constitutive interaction of the proteolytically released nYFP with PEPR2–cYFP (Fiers *et al.*, 2006; Ni and Clark, 2006; Tamaki *et al.*, 2013).

Terminal labeling to form NVOC–CLE peptides

Previous studies illustrated the importance of terminal residues for peptide function. Addition of an arginine group to the C-terminus significantly reduced CLE41 activity and its binding to TDR (Ito *et al.*, 2006; Zhang *et al.*, 2016a). Similarly, unprocessed CLE19 proprotein with an extra C-terminal arginine exhibited diminished activity *in vivo* (Tamaki *et al.*, 2013). Alanine scanning experiments by Song *et al.* (2012) demonstrated that the N-terminal arginine residue of CLV3 is vital for its function, and addition of an extra tyrosine residue to the N-terminus of CLV3 or CLE45 rendered these peptides inactive (Hazak *et al.*, 2017). Interestingly, we observed that a simple acetylation of the N-terminus was enough to deactivate CLV3 (Fig. 2). Based on this finding, we were able to manipulate the peptide N-terminus by attaching a photocleavable group that temporarily deactivates CLV3 and can be cleaved off efficiently with light at 365–380 nm (Fig. 6). This enables the tracking of rapid or time-sensitive cell biological effects, and elucidation of tissue specific effects with spatial and temporal control. For example, rapid changes in sub-cellular localization of a protein of interest within seconds after CLE perception can be observed microscopically *in vivo*. Alternatively, the peptide can be activated in target cells, and subsequent non-cell autonomous effects can be followed in adjacent cells or distant tissues.

The rapid NVOC cleavage observed under the microscope (Fig. 6E), in comparison with *in vitro* experiments (Fig. 6C), can be attributed to several factors. Firstly, differences in the light sources employed, such as lasers versus UV lamps, can lead to variations in energy output, potentially influencing the rate of cleavage. It is also crucial to note that the fluorescence observed under the microscope after 30 s does not necessarily indicate complete NVOC protection of group cleavage. In contrast, *in vitro* experiments involving spectral methods (e.g. absorbance and RP-HPLC spectra) offer a more quantitative assessment of cleavage completeness. The microscopic method confirms the occurrence of cleavage but does not provide the same level of quantitative information.

Adaptive strategies to study other peptides

Several *in vivo* and *in vitro* studies (detailed in 'Introduction'), including this, have investigated the binding specificity of CLV3 and CLE41 to LRR-RLKs of sub-family XI. However, the *in vivo* interaction and recognition mechanisms of most other CLE peptides remain unexplored. Owing to the conserved architecture of the CLE domain amongst all CLE peptides, fluorophore labeling and photocaging strategies from this study (Figs 2, 6) could be transferred to investigate binding characteristics, short-term effects, turnover or localization.

There are several plant peptide families with multiple members that could potentially interact with one or more members of a sub-clade of RLKs. Modelling and crystal structure analysis of the interaction complex will give insights into ligand binding pockets and the conserved recognition mechanism that may be shared between the members of the family. Subsequently, targeted amino acid modifications and fluorophore labeling will enable confirmation of *in vivo* interaction and expand our understanding of their sub-cellular dynamics.

Conclusion

We have developed a macromolecular tool box of CLE peptides with fluorescent labeling and photocaging. After testing the bioactivity of these modified peptides, we have demonstrated that photocaged peptides can be regionally activated in plant tissues and be used *in vivo* to study their sub-cellular properties. Using these tools, we studied CLE–RLK binding specificities, clarifying the contradictory reports on CLE–RLK interactions and further substantiating the existence of highly selective mechanisms that discriminate between different peptide families. We have, for the first time, followed the *in vivo* endocytic and post-endocytic trafficking dynamics of a CLE peptide and RLKs. Our methodology for CLE peptide modification creates a functional and controllable peptide without compromising the recognition and binding capacity to its corresponding RLKs. Furthermore, based on our approach and developed synthetic strategy, additional CLE peptides can be synthesized to elucidate the signaling pathways mediated by CLE–RLK interactions.

Supplementary data

The following supplementary data are available at *JXB* online.

Fig. S1. Bioactivity of CLV3–TAMRA (related to Fig. 3).

Fig. S2. Sub-cellular localization and trafficking of CLV3–TAMRA (related to Fig. 4).

Fig. S3. Binding specificity of CLV3–TAMRA to RLKs.

Fig. S4. Activation of photocaged peptide by 405 nm laser irradiation.

Dataset S1. RP-HPLC-ESI-MS for CLV3 derivatives.

Dataset S2. MALDI-TOF-MS for CLV3 derivatives.

Dataset S3. HR-ESI for CLV3 derivatives.

Dataset S4. Storing stability test of CLV3–TAMRA.

Dataset S5. Absorption measurements and RP-HPLC-MS analysis after irradiation of NVOC–CLV3.

Acknowledgements

We would like to thank Prof. Eugenia Russinova for sharing resources. We would like to acknowledge the Center for Advanced Imaging (CAi) at Heinrich-Heine-University Düsseldorf for providing access to the Zeiss LSM 880 Airyscan Fast.

Author contributions

MN, NJ, RS, and LH: conceptualization; MN, NJ, and EB: methology; MN and NJ: validation; MN and NJ: formal analysis; MN, NJ, EB, FK, and FB: investigation; RS and LH: resources; MN and NJ: writing—original draft; MN, NJ, RS, and LH: writing—review and editing; MN and NJ: visualization; LH and RS: supervision and funding acquisition. LH was responsible for synthetic chemistry and molecular characterization, and RS was responsible for plant biology.

Conflict of interest

The authors declare no competing interests

Funding

MN and NJ were supported by Deutsche Forschungsgemeinschaft (DFG, German Research Foundation) through grants within the collaborative research center (CRC) 1208, B04 and A11 awarded to RS and LH, respectively. LSM 880 Airyscan Fast funded by DFG-INST 208/746-1. LSM900 was funded through the ERC Synergy grant, Sympore.

Data availability

The original raw data files of microscopy and phenotypic analysis and the corresponding files from data analysis are available upon request.

References

Adamowski M, Narasimhan M, Kania U, Glanc M, De Jaeger G, Friml J. 2018. A functional study of AUXILIN-LIKE1 and 2, two putative clathrin uncoating factors in *Arabidopsis*. The Plant Cell **30**, 700–716.

Bhattacharya A, Kim YC, Mittal J. 2013. Protein-protein interactions in a crowded environment. Biophysical Reviews **5**, 99–108.

Bleckmann A, Weidtkamp-Peters S, Seidel CA, Simon R. 2010. Stem cell signaling in Arabidopsis requires CRN to localize CLV2 to the plasma membrane. Plant Physiology **152**, 166–176.

Blümke P, Schlegel J, Gonzalez-Ferrer C, Becher S, Pinto KG, Monaghan J, Simon R. 2021. Receptor-like cytoplasmic kinase MAZZA mediates developmental processes with CLAVATA1 family receptors in Arabidopsis. Journal of Experimental Botany **72**, 4853–4870.

Boaro A, Ageitos L, Torres M, Bartoloni FH, de la Fuente-Nunez C. 2020. Light-emitting probes for labeling peptides. Cell Reports Physical Science **1**, 100257.

Bolte S, Cordelières FP. 2006. A guided tour into subcellular colocalization analysis in light microscopy. Journal of Microscopy **224**, 213–232.

Breda AS, Hazak O, Schultz P, Anne P, Graeff M, Simon R, Hardtke CS. 2019. A cellular insulator against CLE45 peptide signaling. Current Biology **29**, 2501–2508.e3.

Breiden M, Olsson V, Blümke P, Schlegel J, Gustavo-Pinto K, Dietrich P, Butenko MA, Simon R. 2021. The cell fate controlling CLE40 peptide requires CNGCs to trigger highly localized Ca^{2+} transients in *Arabidopsis thaliana* root meristems. Plant and Cell Physiology **62**, 1290–1301.

Bucherl CA, van Esse GW, Kruis A, Luchtenberg J, Westphal AH, Aker J, van Hoek A, Albrecht C, Borst JW, de Vries SC. 2013. Visualization of BRI1 and BAK1 (SERK3) membrane receptor heterooligomers during brassinosteroid signaling. Plant Physiology **162**, 1911–1925.

Chang Z. 2022. Some random thoughts on the life of protein molecules in living cells. Biochemical and Biophysical Research Communications **633**, 33–38.

Crook AD, Willoughby AC, Hazak O, *et al*. 2020. BAM1/2 receptor kinase signaling drives CLE peptide-mediated formative cell divisions in *Arabidopsis* roots. Proceedings of the National Academy of Sciences, USA **117**, 32750–32756.

Dettmer J, Hong-Hermesdorf A, Stierhof Y-D, Schumacher K. 2006. Vacuolar H^+-ATPase activity is required for endocytic and secretory trafficking in *Arabidopsis*. The Plant Cell **18**, 715–730.

DeYoung BJ, Bickle KL, Schrage KJ, Muskett P, Patel K, Clark SE. 2006. The CLAVATA1-related BAM1, BAM2 and BAM3 receptor kinase-like proteins are required for meristem function in Arabidopsis. The Plant Journal **45**, 1–16.

Fan P, Aguilar E, Bradai M, *et al*. 2021. The receptor-like kinases BAM1 and BAM2 are required for root xylem patterning. Proceedings of the National Academy of Sciences, USA **118**, e2022547118.

Fiers M, Golemiec E, van der Schors R, van der Geest L, Li KW, Stiekema WJ, Liu C-M. 2006. The CLAVATA3/ESR motif of CLAVATA3 is functionally independent from the nonconserved flanking sequences. Plant Physiology **141**, 1284–1292.

Fiers M, Golemiec E, Xu J, van der Geest L, Heidstra R, Stiekema W, Liu CM. 2005. The 14-amino acid CLV3, CLE19, and CLE40 peptides trigger consumption of the root meristem in *Arabidopsis* through a *CLAVATA2*-dependent pathway. The Plant Cell **17**, 2542–2553.

French AR, Lauffenburger DA. 1997. Controlling receptor/ligand trafficking: effects of cellular and molecular properties on endosomal sorting. Annals of Biomedical Engineering **25**, 690–707.

Furumizu C, Krabberød AK, Hammerstad M, Alling RM, Wildhagen M, Sawa S, Aalen RB. 2021. The sequenced genomes of nonflowering land plants reveal the innovative evolutionary history of peptide signaling. The Plant Cell **33**, 2915–2934.

Geldner N, Dénervaud-Tendon V, Hyman DL, Mayer U, Stierhof YD, Chory J. 2009. Rapid, combinatorial analysis of membrane compartments in intact plants with a multicolor marker set. The Plant Journal **59**, 169–178.

Guo Y, Han L, Hymes M, Denver R, Clark SE. 2010. CLAVATA2 forms a distinct CLE-binding receptor complex regulating Arabidopsis stem cell specification. The Plant Journal **63**, 889–900.

Gutierrez-Alanis D, Yong-Villalobos L, Jimenez-Sandoval P, Alatorre-Cobos F, Oropeza-Aburto A, Mora-Macias J, Sanchez-Rodriguez F, Cruz-Ramirez A, Herrera-Estrella L. 2017. Phosphate starvation-dependent iron mobilization induces CLE14 expression to trigger root meristem differentiation through CLV2/PEPR2 signaling. Developmental Cell **41**, 555–570.e3.

Hazak O, Brandt B, Cattaneo P, Santiago J, Rodriguez-Villalon A, Hothorn M, Hardtke CS. 2017. Perception of root-active CLE peptides requires CORYNE function in the phloem vasculature. EMBO Reports **18**, 1367–1381.

Hirakawa Y. 2022. Evolution of meristem zonation by CLE gene duplication in land plants. Nature Plants **8**, 735–740.

Hirakawa Y, Kondo Y, Fukuda H. 2011. Establishment and maintenance of vascular cell communities through local signaling. Current Opinion in Plant Biology **14**, 17–23.

Irani NG, Di Rubbo S, Mylle E, *et al*. 2012. Fluorescent castasterone reveals BRI1 signaling from the plasma membrane. Nature Chemical Biology **8**, 583–589.

Ito Y, Nakanomyo I, Motose H, Iwamoto K, Sawa S, Dohmae N, Fukuda H. 2006. Dodeca-CLE peptides as suppressors of plant stem cell differentiation. Science **313**, 842–845.

Jelenska J, Davern SM, Standaert RF, Mirzadeh S, Greenberg JT. 2017. Flagellin peptide flg22 gains access to long-distance trafficking in Arabidopsis via its receptor, FLS2. Journal of Experimental Botany **68**, 1769–1783.

Kastritis PL, Bonvin AM. 2013. On the binding affinity of macromolecular interactions: daring to ask why proteins interact. Journal of the Royal Society Interface **10**, 20120835.

Kim HJ, Wu CY, Yu HM, Sheen J, Lee H. 2017. Dual CLAVATA3 peptides in Arabidopsis shoot stem cell signaling. Journal of Plant Biology **60**, 506–512.

Kinoshita A, Nakamura Y, Sasaki E, Kyozuka J, Fukuda H, Sawa S. 2007. Gain-of-function phenotypes of chemically synthetic CLAVATA3/ESR-related (CLE) peptides in *Arabidopsis thaliana* and *Oryza sativa*. Plant and Cell Physiology **48**, 1821–1825.

Kneuttinger AC. 2022. A guide to designing photocontrol in proteins: methods, strategies and applications. Biological Chemistry **403**, 573–613.

Kondo T, Sawa S, Kinoshita A, Mizuno S, Kakimoto T, Fukuda H, Sakagami Y. 2006. A plant peptide encoded by CLV3 identified by in situ MALDI-TOF MS analysis. Science **313**, 845–848.

Konopka CA, Backues SK, Bednarek SY. 2008. Dynamics of *Arabidopsis* dynamin-related protein 1C and a clathrin light chain at the plasma membrane. The Plant Cell **20**, 1363–1380.

Kusaka N, Maisch J, Nick P, Hayashi K, Nozaki H. 2009. Manipulation of intracellular auxin in a single cell by light with esterase-resistant caged auxins. ChemBioChem **10**, 2195–2202.

Lakadamyali M, Rust MJ, Zhuang X. 2006. Ligands for clathrin-mediated endocytosis are differentially sorted into distinct populations of early endosomes. Cell **124**, 997–1009.

Lee GJ, Sohn EJ, Lee MH, Hwang I. 2004. The *Arabidopsis* rab5 homologs rha1 and ara7 localize to the prevacuolar compartment. Plant and Cell Physiology **45**, 1211–1220.

Li J, Liang P, Gao L, Lu H, Dong Y, Zhang J. 2023. o-Nitrobenzyl-based caged exo-16,17-dihydro-gibberellin A5-13-acetate for photocontrolled release of plant growth regulators. Journal of Agricultural and Food Chemistry **71**, 16533–16541.

Li Y, Wang M, Wang F, Lu S, Chen X. 2023. Recent progress in studies of photocages. Smart Molecules **1**, e20220003.

Li Z, Chakraborty S, Xu G. 2017. Differential CLE peptide perception by plant receptors implicated from structural and functional analyses of TDIF-TDR interactions. PLoS One **12**, e0175317.

Mangubat-Medina AE, Ball ZT. 2021. Triggering biological processes: methods and applications of photocaged peptides and proteins. Chemical Society Reviews **50**, 10403–10421.

Miwa H, Betsuyaku S, Iwamoto K, Kinoshita A, Fukuda H, Sawa S. 2008. The receptor-like kinase SOL2 mediates CLE signaling in *Arabidopsis*. Plant and Cell Physiology **49**, 1752–1757.

Müller R, Bleckmann A, Simon R. 2008. The receptor kinase CORYNE of Arabidopsis transmits the stem cell-limiting signal CLAVATA3 independently of CLAVATA1. The Plant Cell **20**, 934–946.

Narasimhan M, Gallei M, Tan S, *et al*. 2021. Systematic analysis of specific and nonspecific auxin effects on endocytosis and trafficking. Plant Physiology **186**, 1122–1142.

Narasimhan M, Simon R. 2022. Spatial range, temporal span, and promiscuity of CLE-RLK signaling. Frontiers in Plant Science **13**, 906087.

Ni J, Clark SE. 2006. Evidence for functional conservation, sufficiency, and proteolytic processing of the CLAVATA3 CLE domain. Plant Physiology **140**, 726–733.

Nimchuk ZL. 2017. CLAVATA1 controls distinct signaling outputs that buffer shoot stem cell proliferation through a two-step transcriptional compensation loop. PLoS Genetics **13**, e1006681.

Nimchuk ZL, Tarr PT, Meyerowitz EM. 2011a. An evolutionarily conserved pseudokinase mediates stem cell production in plants. The Plant Cell **23**, 851–854.

Nimchuk ZL, Tarr PT, Ohno C, Qu X, Meyerowitz EM. 2011b. Plant stem cell signaling involves ligand-dependent trafficking of the CLAVATA1 receptor kinase. Current Biology **21**, 345–352.

Ogawa M, Shinohara H, Sakagami Y, Matsubayashi Y. 2008. *Arabidopsis* CLV3 peptide directly binds CLV1 ectodomain. Science **319**, 294.

Ortiz-Morea FA, Savatin DV, Dejonghe W, *et al*. 2016. Danger-associated peptide signaling in *Arabidopsis* requires clathrin. Proceedings of the National Academy of Sciences, USA **113**, 11028–11033.

Paez Valencia J, Goodman K, Otegui MS. 2016. Endocytosis and endosomal trafficking in plants. Annual Review of Plant Biology **67**, 309–335.

Pallakies H, Simon R. 2014. The CLE40 and CRN/CLV2 signaling pathways antagonistically control root meristem growth in *Arabidopsis*. Molecular Plant **7**, 1619–1636.

Qian P, Song W, Yokoo T, Minobe A, Wang G, Ishida T, Sawa S, Chai J, Kakimoto T. 2018. The CLE9/10 secretory peptide regulates stomatal and vascular development through distinct receptors. Nature Plants **4**, 1071–1081.

Replogle A, Wang J, Bleckmann A, Hussey RS, Baum TJ, Sawa S, Davis EL, Wang X, Simon R, Mitchum MG. 2011. Nematode CLE signaling in Arabidopsis requires CLAVATA2 and CORYNE. The Plant Journal **65**, 430–440.

Rojo E, Sharma VK, Kovaleva V, Raikhel NV, Fletcher JC. 2002. CLV3 is localized to the extracellular space, where it activates the Arabidopsis CLAVATA stem cell signaling pathway. The Plant Cell **14**, 969–977.

Roman AO, Jimenez-Sandoval P, Augustin S, Broyart C, Hothorn LA, Santiago J. 2022. HSL1 and BAM1/2 impact epidermal cell development by sensing distinct signaling peptides. Nature Communications **13**, 876.

Schaper K, Etinski M, Fleig T. 2009. Theoretical investigation of the excited states of 2-nitrobenzyl and 4,5-methylendioxy-2-nitrobenzyl caging groups. Photochemistry and Photobiology **85**, 1075–1081.

Schindelin J, Arganda-Carreras I, Frise E, *et al*. 2012. Fiji: an open-source platform for biological-image analysis. Nature Methods **9**, 676–682.

Schlegel J, Denay G, Wink R, Pinto KG, Stahl Y, Schmid J, Blümke P, Simon RG. 2021. Control of *Arabidopsis* shoot stem cell homeostasis by two antagonistic CLE peptide signalling pathways. eLife **10**, e70934.

Schoof H, Lenhard M, Haecker A, Mayer KF, Jürgens G, Laux T. 2000. The stem cell population of *Arabidopsis* shoot meristems in maintained by a regulatory loop between the CLAVATA and WUSCHEL genes. Cell **100**, 635–644.

Sharma I, Russinova E. 2018. Probing plant receptor kinase functions with labeled ligands. Plant and Cell Physiology **59**, 1520–1527.

Shinohara H, Matsubayashi Y. 2013. Chemical synthesis of *Arabidopsis* CLV3 glycopeptide reveals the impact of hydroxyproline arabinosylation on peptide conformation and activity. Plant and Cell Physiology **54**, 369–374.

Shinohara H, Matsubayashi Y. 2015. Reevaluation of the CLV3-receptor interaction in the shoot apical meristem: dissection of the CLV3 signaling pathway from a direct ligand-binding point of view. The Plant Journal **82**, 328–336.

Shinohara H, Moriyama Y, Ohyama K, Matsubayashi Y. 2012. Biochemical mapping of a ligand-binding domain within Arabidopsis BAM1 reveals diversified ligand recognition mechanisms of plant LRR-RKs. The Plant Journal **70**, 845–854.

Shiu SH, Bleecker AB. 2001. Receptor-like kinases from *Arabidopsis* form a monophyletic gene family related to animal receptor kinases. Proceedings of the National Academy of Sciences, USA **98**, 10763–10768.

Silva JM, Silva E, Reis RL. 2019. Light-triggered release of photocaged therapeutics - Where are we now? Journal of Controlled Release **298**, 154–176.

Solinger JA, Spang A. 2022. Sorting of cargo in the tubular endosomal network. Bioessays **44**, e2200158.

Somssich M, Ma Q, Weidtkamp-Peters S, Stahl Y, Felekyan S, Bleckmann A, Seidel CA, Simon R. 2015. Real-time dynamics of peptide

ligand-dependent receptor complex formation *in planta*. Science Signaling **8**, ra76.

Song XF, Yu DL, Xu TT, Ren SC, Guo P, Liu CM. 2012. Contributions of individual amino acid residues to the endogenous CLV3 function in shoot apical meristem maintenance in *Arabidopsis*. Molecular Plant **5**, 515–523.

Sorkin A, von Zastrow M. 2009. Endocytosis and signalling: intertwining molecular networks. Nature Reviews Molecular Cell Biology **10**, 609–622.

Stahl Y, Wink RH, Ingram GC, Simon R. 2009. A signaling module controlling the stem cell niche in *Arabidopsis* root meristems. Current Biology **19**, 909–914.

Strabala TJ, Phillips L, West M, Stanbra L. 2014. Bioinformatic and phylogenetic analysis of the CLAVATA3/EMBRYO-SURROUNDING REGION (CLE) and the CLE-LIKE signal peptide genes in the Pinophyta. BMC Plant Biology **14**, 47.

Sun X, Liu L, Cheng L. 2023. Photo- and tetrazine-responsive modulation of *trans*-zeatin. The Journal of Organic Chemistry **88**, 2921–2930.

Takahashi F, Suzuki T, Osakabe Y, Betsuyaku S, Kondo Y, Dohmae N, Fukuda H, Yamaguchi-Shinozaki K, Shinozaki K. 2018. A small peptide modulates stomatal control via abscisic acid in long-distance signalling. Nature **556**, 235–238.

Tamaki T, Betsuyaku S, Fujiwara M, Fukao Y, Fukuda H, Sawa S. 2013. SUPPRESSOR OF LLP1 1-mediated C-terminal processing is critical for CLE19 peptide activity. The Plant Journal **76**, 970–981.

Tung CH. 2004. Fluorescent peptide probes for in vivo diagnostic imaging. Biopolymers **76**, 391–403.

Ueda T, Yamaguchi M, Uchimiya H, Nakano A. 2001. Ara6, a plant-unique novel type Rab GTPase, functions in the endocytic pathway of *Arabidopsis thaliana*. The EMBO Journal **20**, 4730–4741.

Wang J, Jiang Q, Pleskot R, *et al*. 2023. TPLATE complex-dependent endocytosis attenuates CLAVATA1 signaling for shoot apical meristem maintenance. EMBO Reports **24**, e54709.

Wellings DA, Atherton E. 1997. Standard Fmoc protocols. Methods in Enzymology **289**, 44–67.

Wexler S, Schayek H, Rajendar K, Tal I, Shani E, Meroz Y, Dobrovetsky R, Weinstain R. 2019. Characterizing gibberellin flow in planta using photocaged gibberellins. Chemical Science **10**, 1500–1505.

Whitewoods CD. 2021. Evolution of CLE peptide signalling. Seminars in Cell & Developmental Biology **109**, 12–19.

Wojcik F, Mosca S, Hartmann L. 2012. Solid-phase synthesis of asymmetrically branched sequence-defined poly/oligo (amidoamines). The Journal of Organic Chemistry **77**, 4226–4234.

Xi L, Wu XN, Gilbert M, Schulze WX. 2019. Classification and interactions of LRR receptors and Co-receptors within the Arabidopsis plasma membrane – an overview. Frontiers in Plant Science **10**, 472.

Xu C, Liberatore KL, MacAlister CA, *et al*. 2015. A cascade of arabinosyltransferases controls shoot meristem size in tomato. Nature Genetics **47**, 784–792.

Yadav RK, Perales M, Gruel J, Girke T, Jonsson H, Reddy GV. 2011. WUSCHEL protein movement mediates stem cell homeostasis in the *Arabidopsis* shoot apex. Genes & Development **25**, 2025–2030.

Yamaguchi YL, Ishida T, Sawa S. 2016. CLE peptides and their signaling pathways in plant development. Journal of Experimental Botany **67**, 4813–4826.

Yu G, Tan Y, He X, Qin Y, Liang J. 2014. CLAVATA3 dodecapeptide modified CdTe nanoparticles: a biocompatible quantum dot probe for in vivo labeling of plant stem cells. PLoS One **9**, e89241.

Zhang H, Han Z, Song W, Chai J. 2016a. Structural insight into recognition of plant peptide hormones by receptors. Molecular Plant **9**, 1454–1463.

Zhang H, Lin X, Han Z, Qu LJ, Chai J. 2016b. Crystal structure of PXY-TDIF complex reveals a conserved recognition mechanism among CLE peptide-receptor pairs. Cell Research **26**, 543–555.

Supplementary Datasets

Supplementary Dataset S1 | RP-HPLC-ESI-MS for CLV3 derivatives

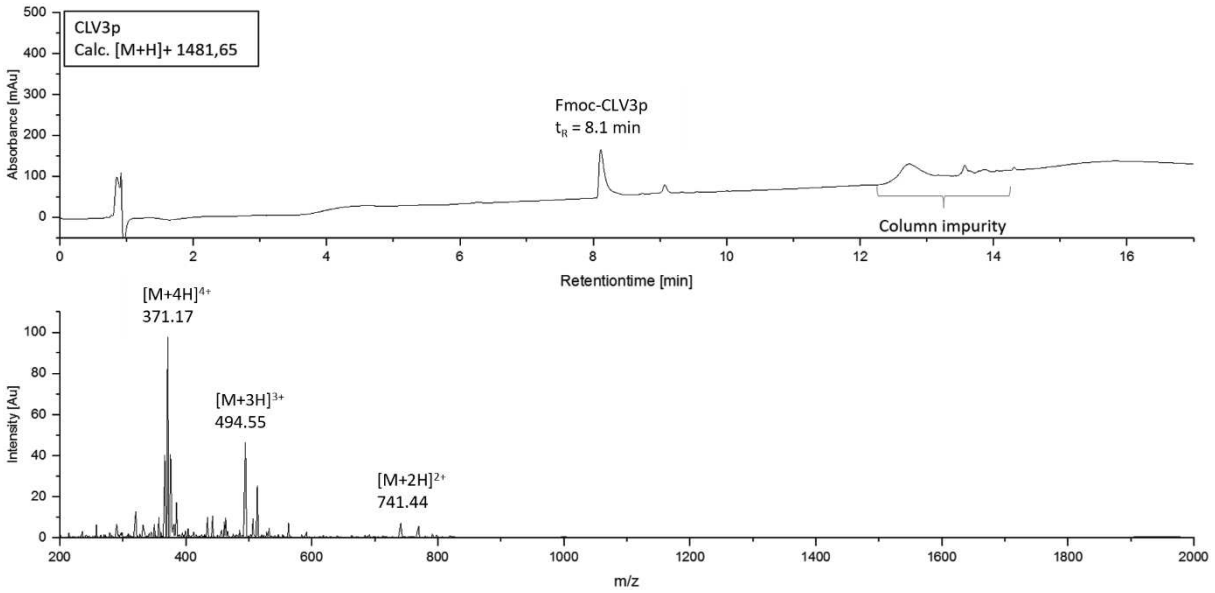

Data S1.1. *Fmoc-CLV3p* (precursor molecule for optimized detection*)* detected at t_r = 8.1 min with relative purity >90% by RP-HPLC (linear gradient from 5-95 Vol% eluent H_2O/acetonitrile in 17 min at 25 °C, VWDA1 A Wavelength = 214 nm). *CLV3p* was analyzed with direct infusion ESI-MS in a m/z range of 200-2000.

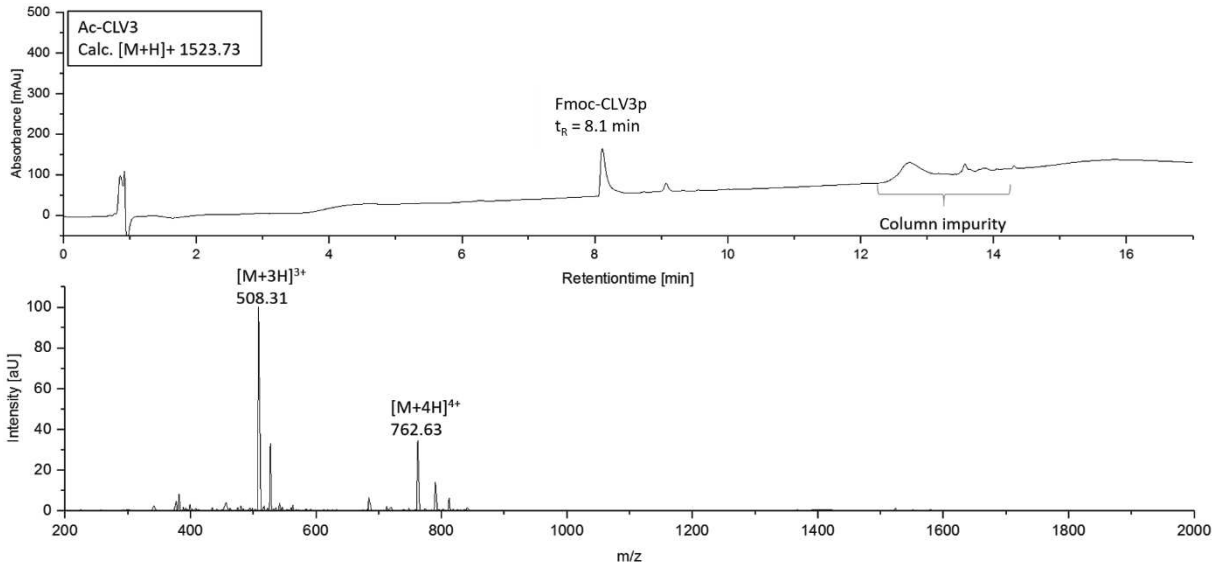

Data S1.2. *Fmoc-CLV3p* (precursor molecule for optimized detection*)* detected at t_r = 8.1 min with relative purity >90% by RP-HPLC (linear gradient from 5-95 Vol% eluent H_2O/acetonitrile in 17 min at 25 °C, VWDA1 A Wavelength = 214 nm). *Ac-CLV3* was analyzed with direct infusion ESI-MS in a m/z range of 200-2000.

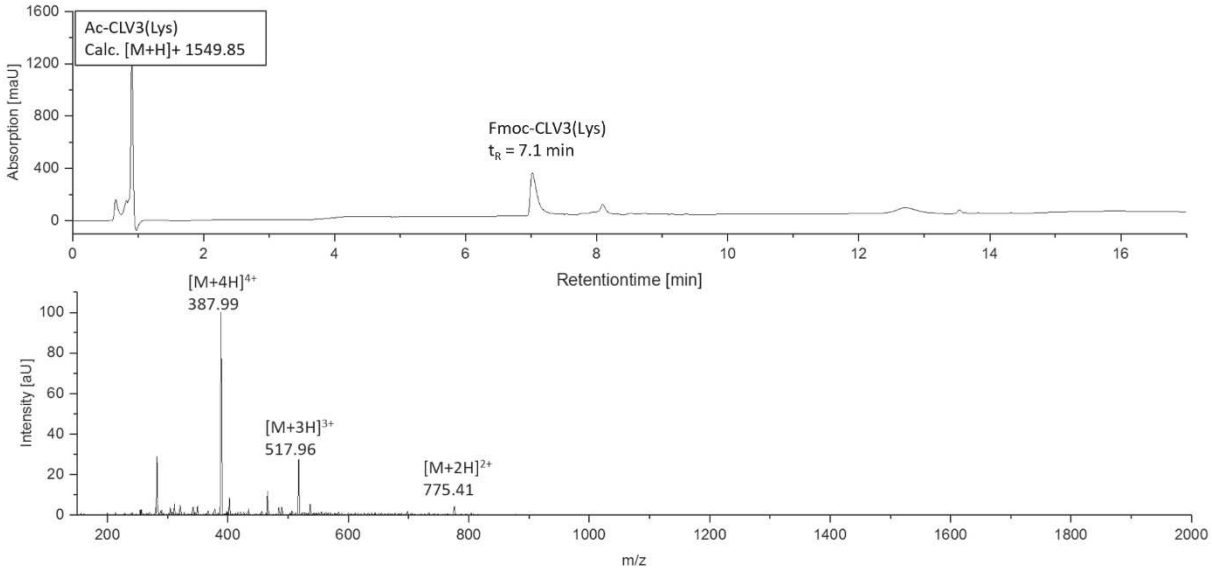

Data S1.3. *Fmoc-CLV3(Lys)* (precursor molecule for optimized detection) detected at t_r = 7.1 min with relative purity >90% by RP-HPLC (linear gradient from 5-95 Vol% eluent H_2O/acetonitrile in 17 min at 25 °C, VWDA1 A Wavelength = 214 nm). *CLV3(Lys)* was analyzed with direct infusion ESI-MS in a m/z range of 200-2000.

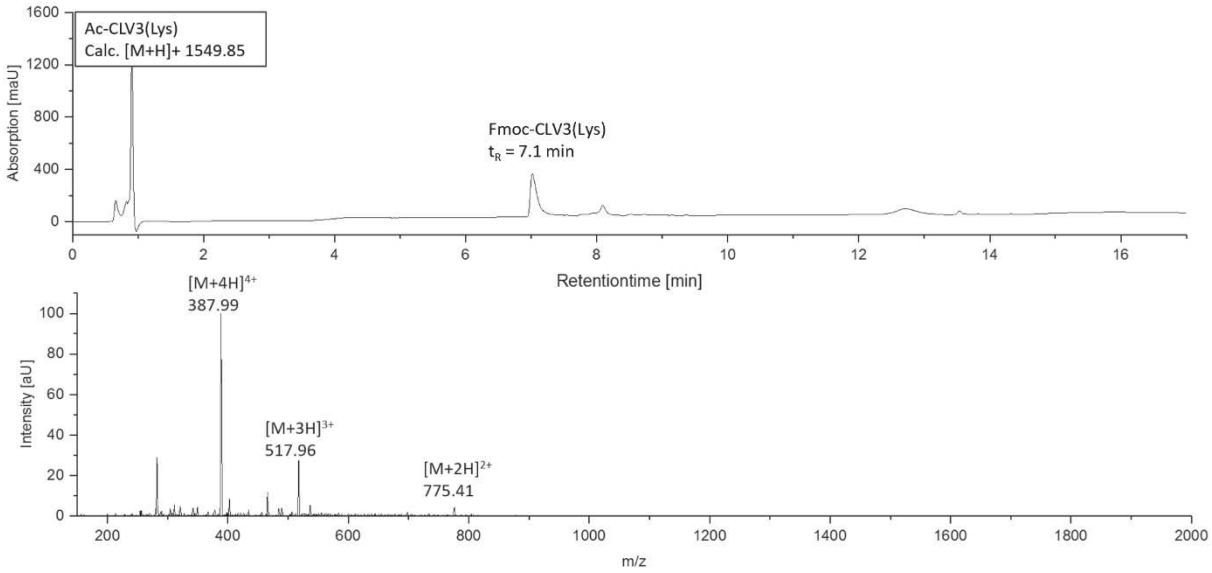

Data S1.4. *Fmoc-CLV3(Lys)* (precursor molecule for optimized detection*)* detected at t_r = 7.1 min with relative purity >90% by RP-HPLC (linear gradient from 5-95 Vol% eluent H_2O/acetonitrile in 17 min at 25 °C, VWDA1 A Wavelength = 214 nm). *Ac-CLV3(Lys)* was analyzed with direct infusion ESI-MS in a m/z range of 200-2000.

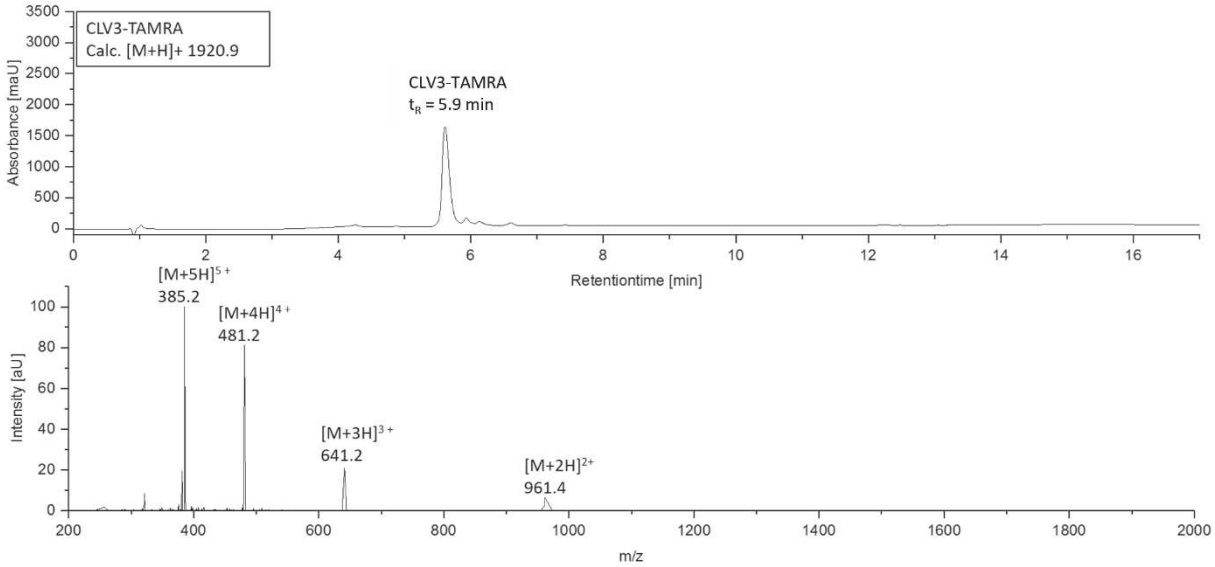

Data S1.3. *CLV3-TAMRA* detected at t_r = 5.9 min with relative purity >90% by RP-HPLC (linear gradient from 5-95 Vol% eluent H_2O/acetonitrile in 17 min at 25 °C, VWDA1 A Wavelength = 214 nm) and ESI-MS in a m/z range of 200-2000.

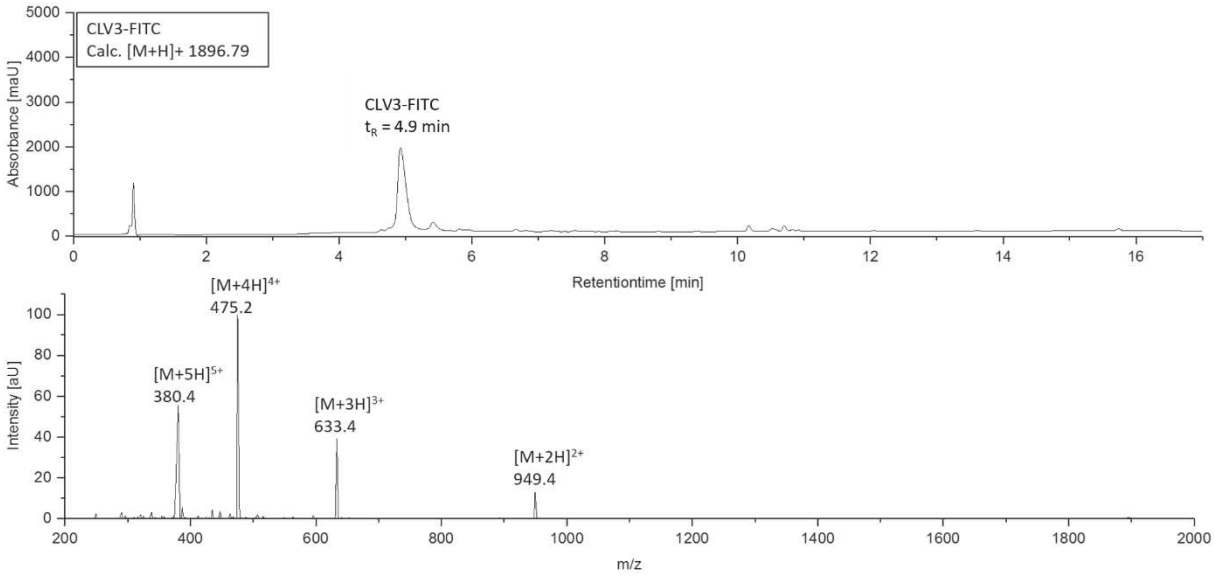

Data S1.4 *CLV3-FITC* detected at t_r = 4.9 min with relative purity >90% by RP-HPLC (linear gradient from 5-95 Vol% eluent H_2O/acetonitrile in 17 min at 25 °C, VWDA1 A Wavelength = 214 nm) and ESI-MS in a m/z range of 200-2000.

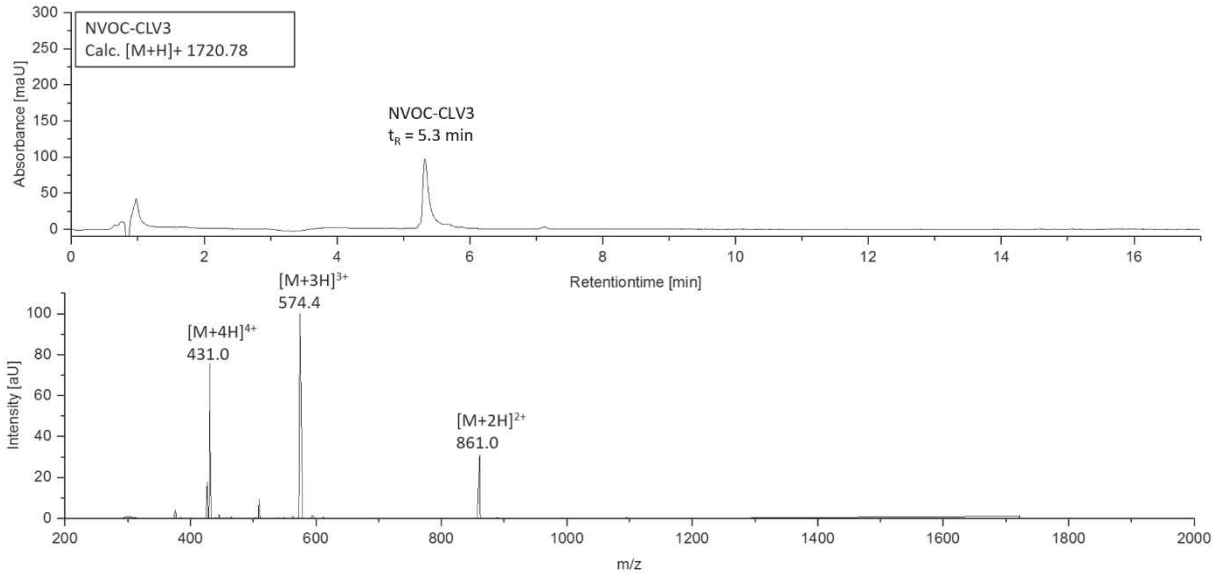

Data S1.5. *NVOC-CLV3* detected at t_r = 5.3 min with relative purity >90% by RP-HPLC (linear gradient from 5-95 Vol% eluent H_2O/acetonitrile in 17 min at 25 °C, VWDA1 A Wavelength = 214 nm) and ESI-MS in a m/z range of 200-2000.

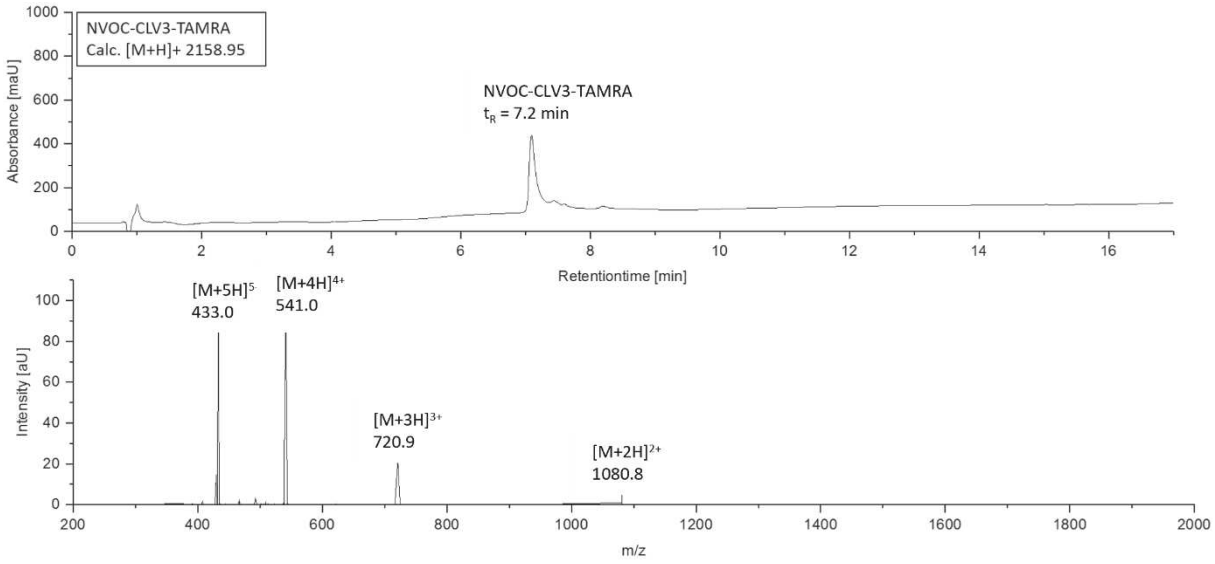

Data S1.6. *NVOC-CLV3-TAMRA* detected at t_r = 7.2 min with relative purity >90% by RP-HPLC (linear gradient from 5-95 Vol% eluent H_2O/acetonitrile in 17 min at 25 °C, VWDA1 A Wavelength = 214 nm) and ESI-MS in a m/z range of 200-2000.

Supplementary Dataset S2 | MALDI-TOF-MS for CLV3 derivatives

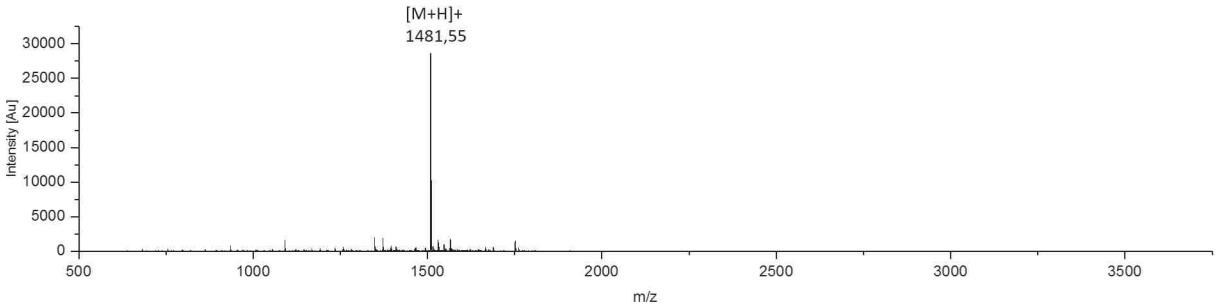

Data S2.1. MALDI-TOF-MS of *CLV3p* in a m/z range of 500-3500 using HCCA as matrix in a compound to matrix ratio of 1:10.

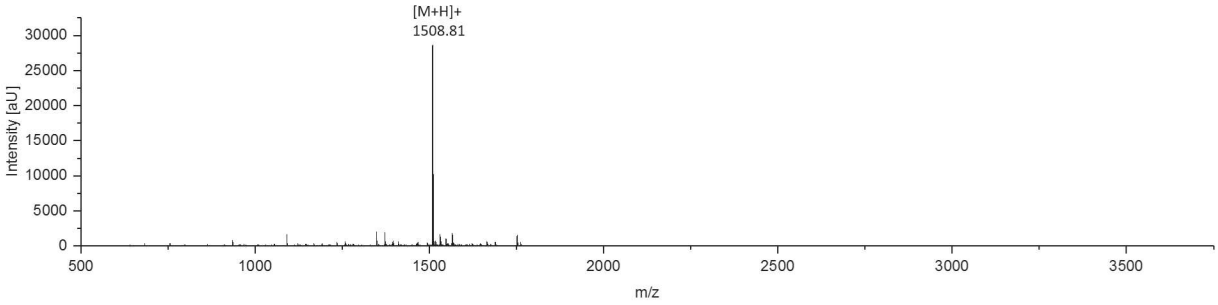

Data S2.2. MALDI-TOF-MS of *CLV3(Lys)* in a m/z range of 500-3500 using HCCA as matrix in a compound to matrix ratio of 1:10.

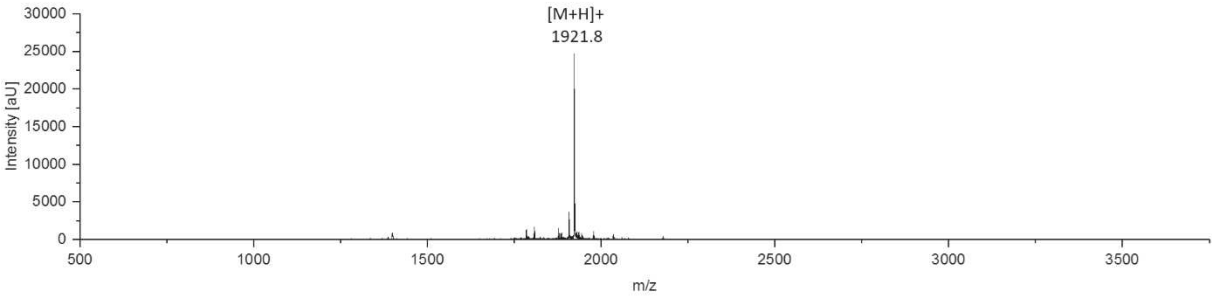

Data S2.3. MALDI-TOF-MS of *CLV3-TAMRA* in a m/z range of 500-3500 using HCCA as matrix in a compound to matrix ratio of 1:10.

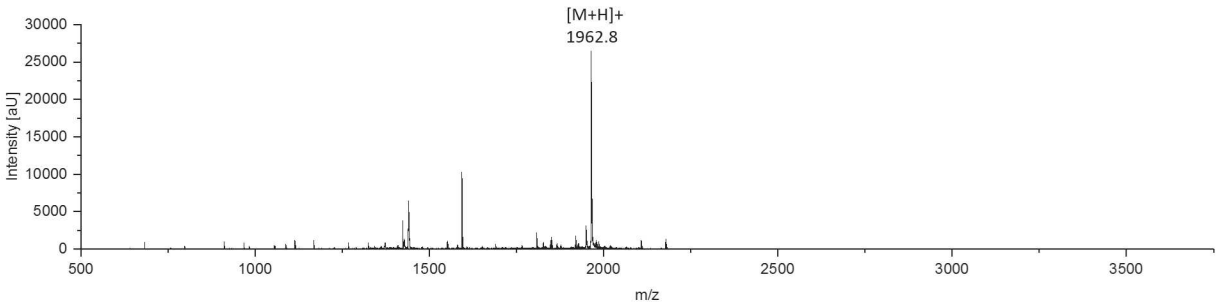

Data S2.4. MALDI-TOF-MS of *Ac-CLV3-TAMRA* in a m/z range of 500-3500 using HCCA as matrix in a compound to matrix ratio of 1:2.

Supplementary Dataset S3 | HR-ESI for CLV3 derivatives, related to Figure 2 and Figure 6

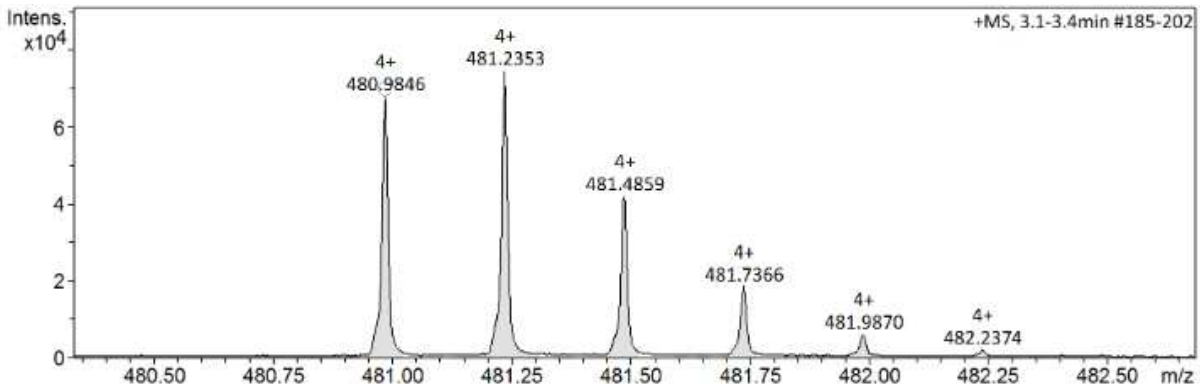

Data S3.1. *CLV3-TAMRA* analyzed by HR-ESI-MS: for $C_{90}H_{125}N_{25}O_{23}$ m/z $[M+4H]^{4+}$ calcd.: 480.9766 found: 480.9846 mass accuracy -1.3 ppm.

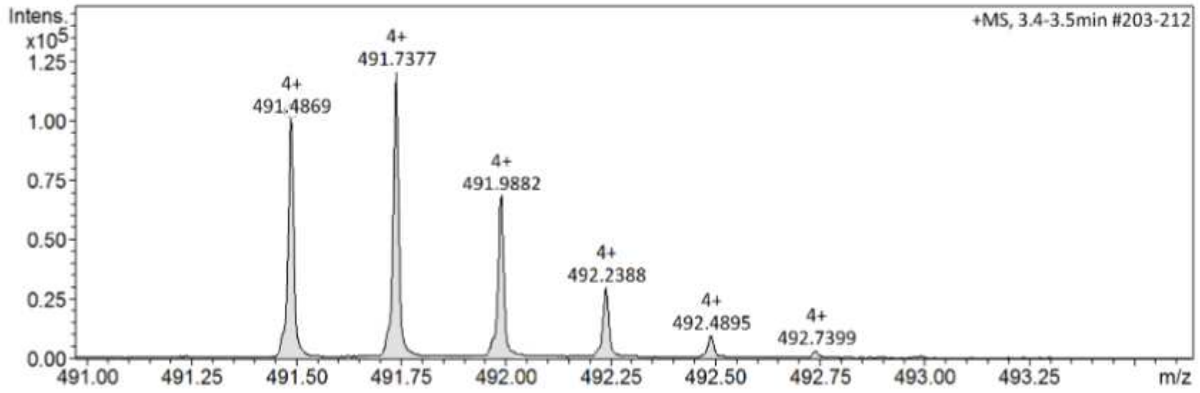

Data S3.2. *Ac-CLV3 TAMRA* analyzed by HR-ESI-MS for $C_{92}H_{123}N_{25}O_{24}$ m/z $[M+4H]^{4+}$ calcd.: 491.4793 found: 491.4869 mass accuracy -0.7 ppm.

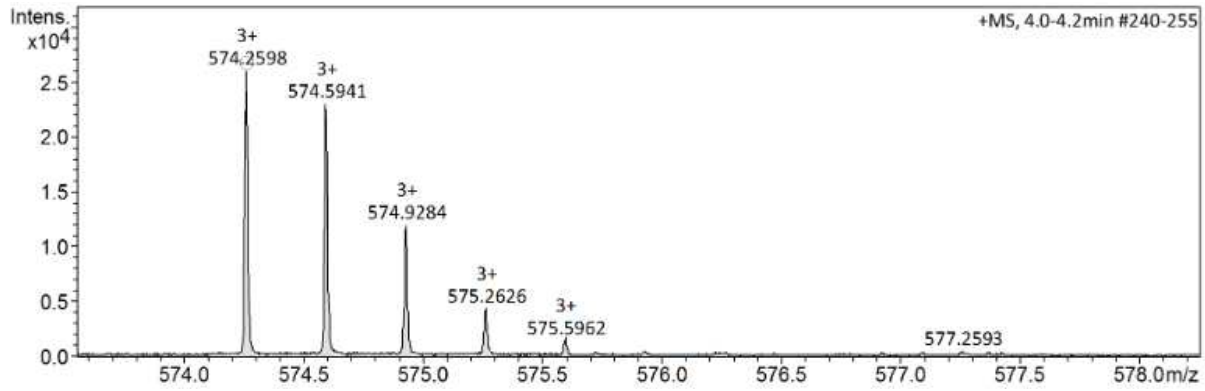

Data S3.3. *NVOC-CLV3* analyzed by HR-ESI-MS for $C_{73}H_{108}N_{23}O_{26}$ m/z $[M+3H]^{3+}$ calcd.:574.2533 found: 574.2598 mass accuracy 1.4 ppm.

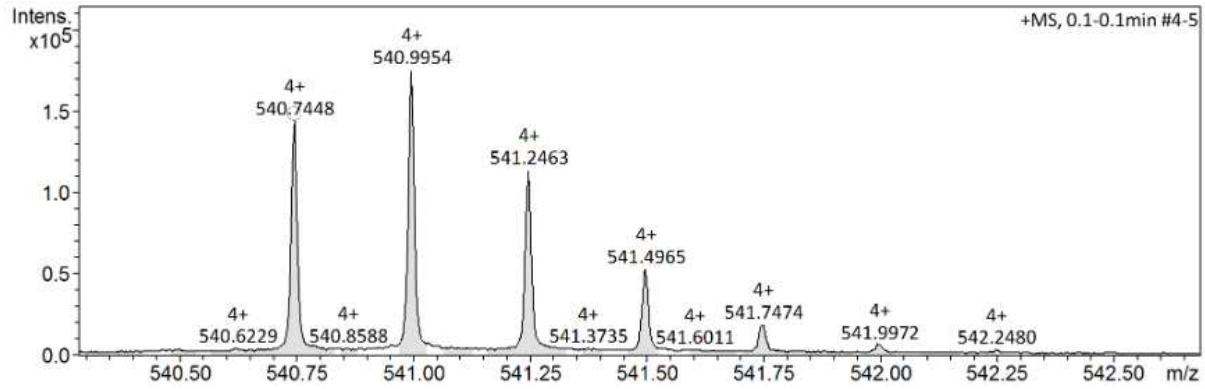

Data S3.4. *NVOC-CLV3-TAMRA* analyzed by HR-ESI-MS for $C_{100}H_{134}N_{26}O_{29}$ m/z $[M+4H]^{4+}$ calcd.: 540.7374 found: 540.7448 mass accuracy -0.2 ppm.

Supplementary Dataset S4 | Storing stability test of CLV3-TAMRA

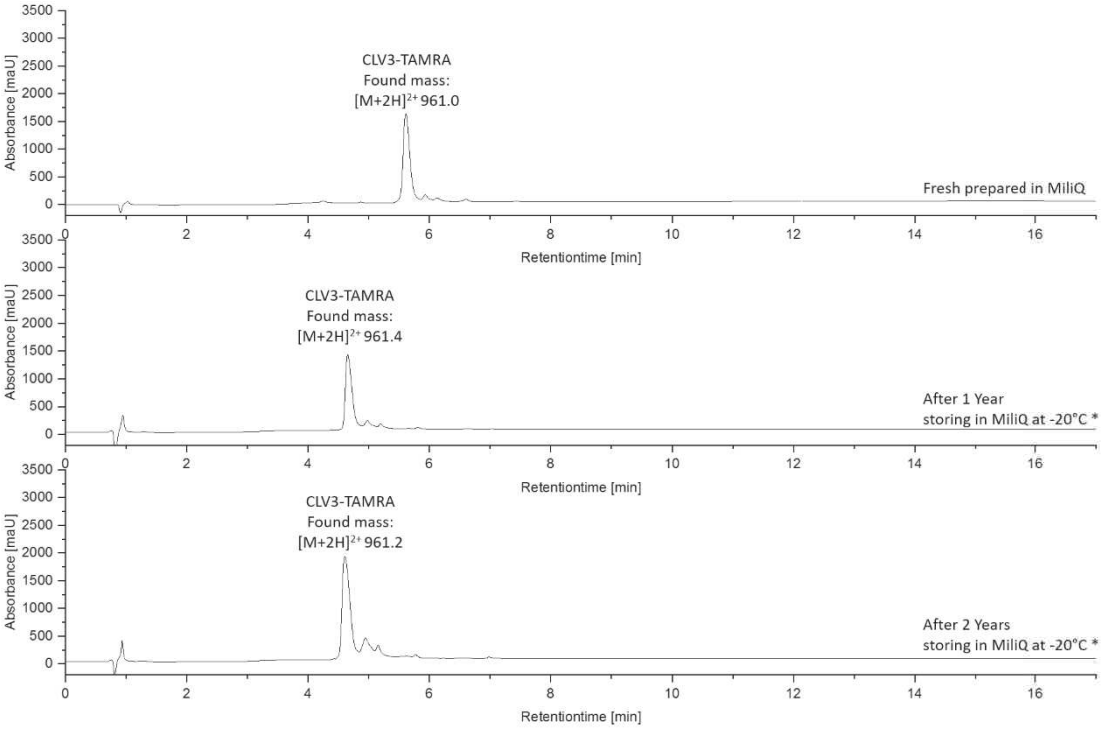

Data S4. Storing stability test of CLV3-TAMRA over 2 years of storing at -20 °C in Milli-Q® and analyzed by RP-HPLC-ESI-MS. (*Retention time shifts due to column replacement.)

Supplementary Dataset S5 | Absorption measurements and RP-HPLC-MS analysis after radiation of NVOC-CLV3

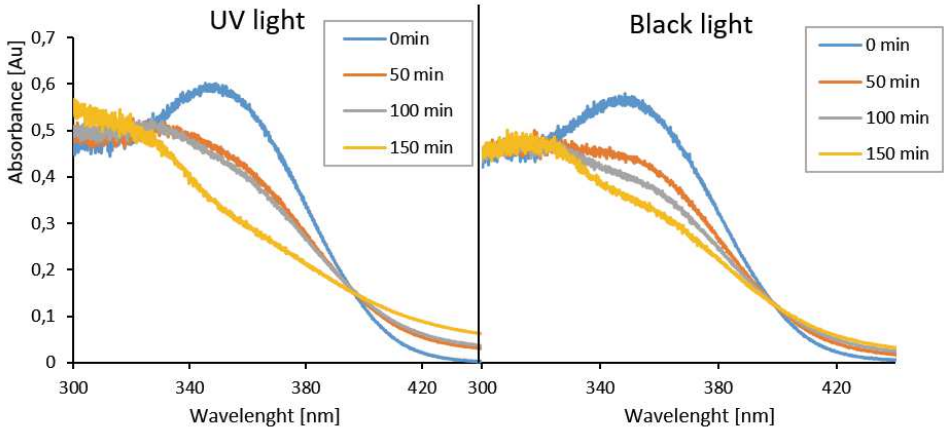

Data S5.1. Absorbance spectra of NVOC photolytic degradation with UV light (365 nm) or UV black light (395 nm-400 nm) in comparison for a total duration of 150 min demonstrating a decrease in the absorbance due to NVOC cleavage. The exact absorption maximum was determined at 348 nm.

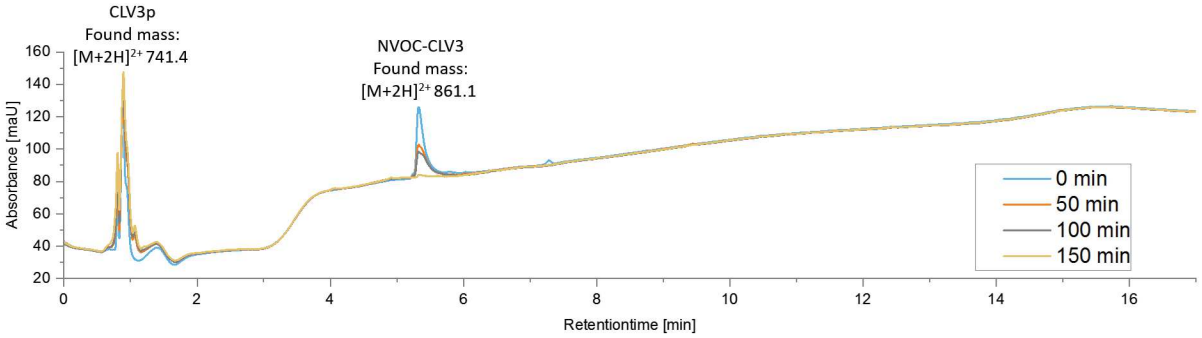

Data S5.2. RP-HPLC-MS analysis of NVOC-CLV3 photolysis. Radiation performed with UV light of 365 nm for a total duration of 150 min of radiation.

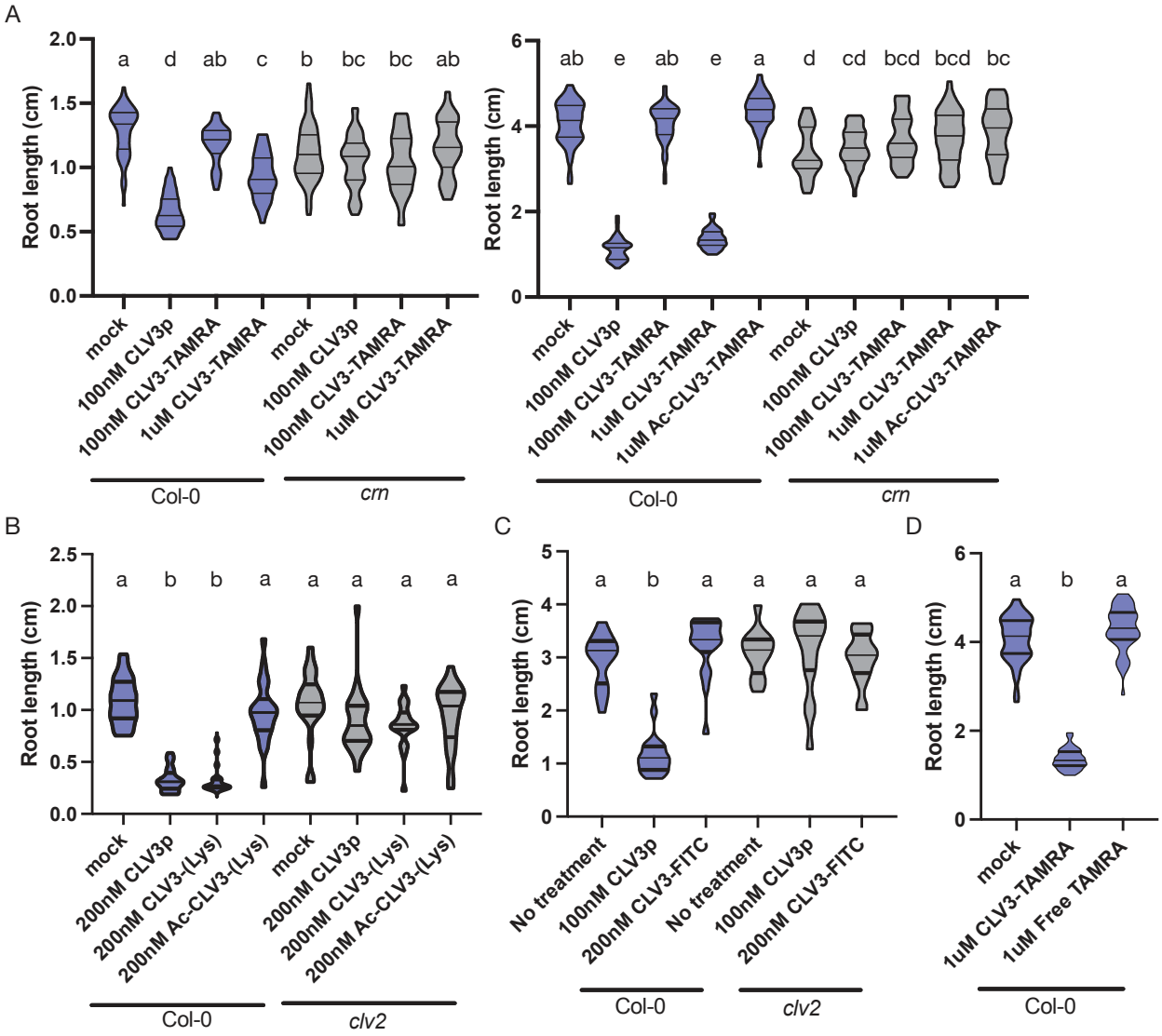

Supplementary Figure S1: Bioactivity of CLV3-TAMRA (Related to Figure 3)

(A – D) Violin plots representing root length analyses of Col-0 or *crn/clv2* mutant after respective treatments. The lines represent the median and the quartiles. Statistical grouping was calculated by Tukey's HSD test. Groups sharing the same letter are not significantly different.! (A) After 5-day (left) and 10-d (right) treatment with mock, CLV3p, CLV3-TAMRA and Ac-CLV3-TAMRA. n≥ 33 roots; N=3. Two-way ANOVA with interaction, F test, p<2e-16 ***. (**α**= 0.001). (B) After 5-day treatment with mock, CLV3p and CLV3-(Lys). n≥ 18 roots; N=1. Two-way ANOVA with interaction, F test, p=3.44e-10***. (**α**= 0.05). **(**C) After 8-day treatment with mock, CLV3p and CLV3-FITC. n≥ 12 roots; N=1. Two-way ANOVA with interaction, F test, p<6.94e-13***. (**α**= 0.001). **(**D) After 10-day treatment with mock, CLV3p and free TAMRA fluorophore. n≥ 46 roots; N=3. One-way ANOVA, F test, p<2e-16 ***. (**α**= 0.001).

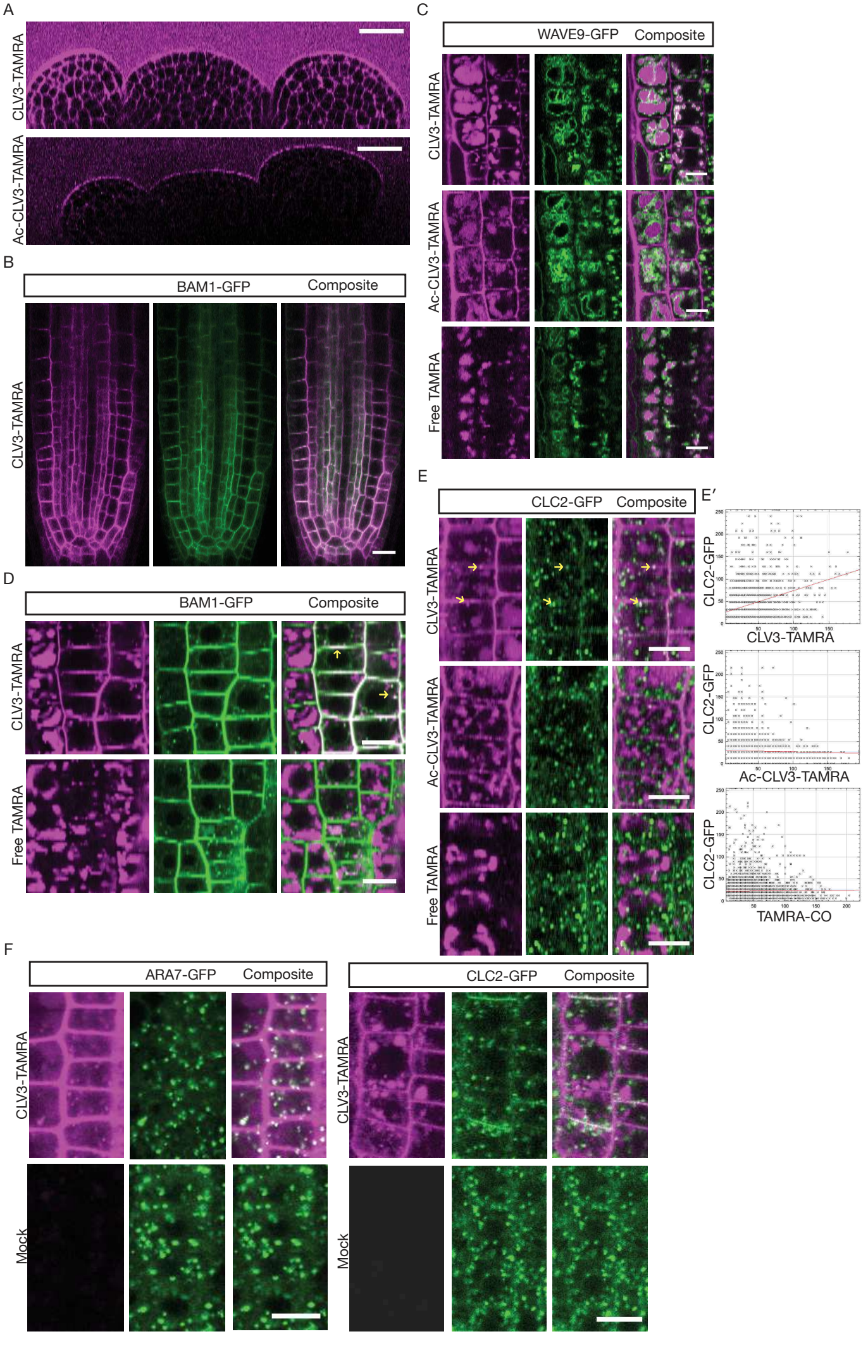
A
CLV3-TAMRA
Ac-CLV3-TAMRA
B
BAM1-GFP
Composite
CLV3-TAMRA
C
WAVE9-GFP
Composite
CLV3-TAMRA
Ac-CLV3-TAMRA
Free TAMRA
D
BAM1-GFP
Composite
CLV3-TAMRA
Free TAMRA
E
CLC2-GFP
Composite
CLV3-TAMRA
Ac-CLV3-TAMRA
Free TAMRA
E′
CLC2-GFP
CLV3-TAMRA
CLC2-GFP
Ac-CLV3-TAMRA
CLC2-GFP
TAMRA-CO
F
ARA7-GFP
Composite
CLV3-TAMRA
Mock
CLC2-GFP
Composite
CLV3-TAMRA
Mock

Supplementary Figure S2: Sub-cellular localization and trafficking of CLV3-TAMRA (Related to figure 4)

!

(A-F) Representative confocal images of SAM (A) or root meristem after 1 µM treatment of the peptide CLV3-TAMRA, or the controls Ac-CLV3-TAMRA or free TAMRA fluorophore. Lines used: A – Col-0. B and D – *pBAM1:BAM1-GFP/bam1-3*. C – *WAVE9Y* (*pUBQ10:VAMP711-YFP*). E – *pCLC2:CLC2-GFP*. F – *pCLC2:CLC2-GFP, p35s:ARA7-GFP*. (A) PM localization after 15 min treatment. N≥5. (B) PM localization after 3 min treatment. n≥5; N=2. PM marked by BAM1-GFP. (C) Vacuolar localization after 10 to 15 min post 15 min treatment. n≥5; N=2. Vacuoles marked by tonoplast localised protein VAMP711-GFP. (D) CLV3-TAMRA PM localization after 60 min treatment. n≥5; N=2. BAM1-GFP marks the PM and the endosomes. The arrows indicate an example of PM and endosomal co-localization. (E) EE localization 10 to 15 min post 5 min treatment. n≥5; N=2. The arrows indicates CLV3-TAMRA co-localized with the EE marker, CLC2-GFP. Pearson's co-efficient (*r*) of co-localization between CLC2-GFP, and peptide and controls were calculated in 3 cells each condition. CLV3-TAMRA vs CLC2-GFP: -0.009, 0.057 and 0.339; Ac-CLV3-TAMRA vs CLC2-GFP: -0.195, -0.532 and 0.033; TAMRA-CO vs CLC2-GFP: 0.011, -0.058 and -0.195. (E′) Cytofluorogram of one measurement from each condition is shown. F) ARA7-GFP and CLC2-GFP imaged with CLV3-TAMRA or mock after 5 min treatment. n=5; N=1. Note: In C-E, Ac-CLV3-TAMRA and Free TAMRA were imaged at higher laser intensity and gain than CLV3-TAMRA to observe their sub-cellular localization. Scale bar: A – 25 µm; B – 15 µm; C-F – 10 µm.

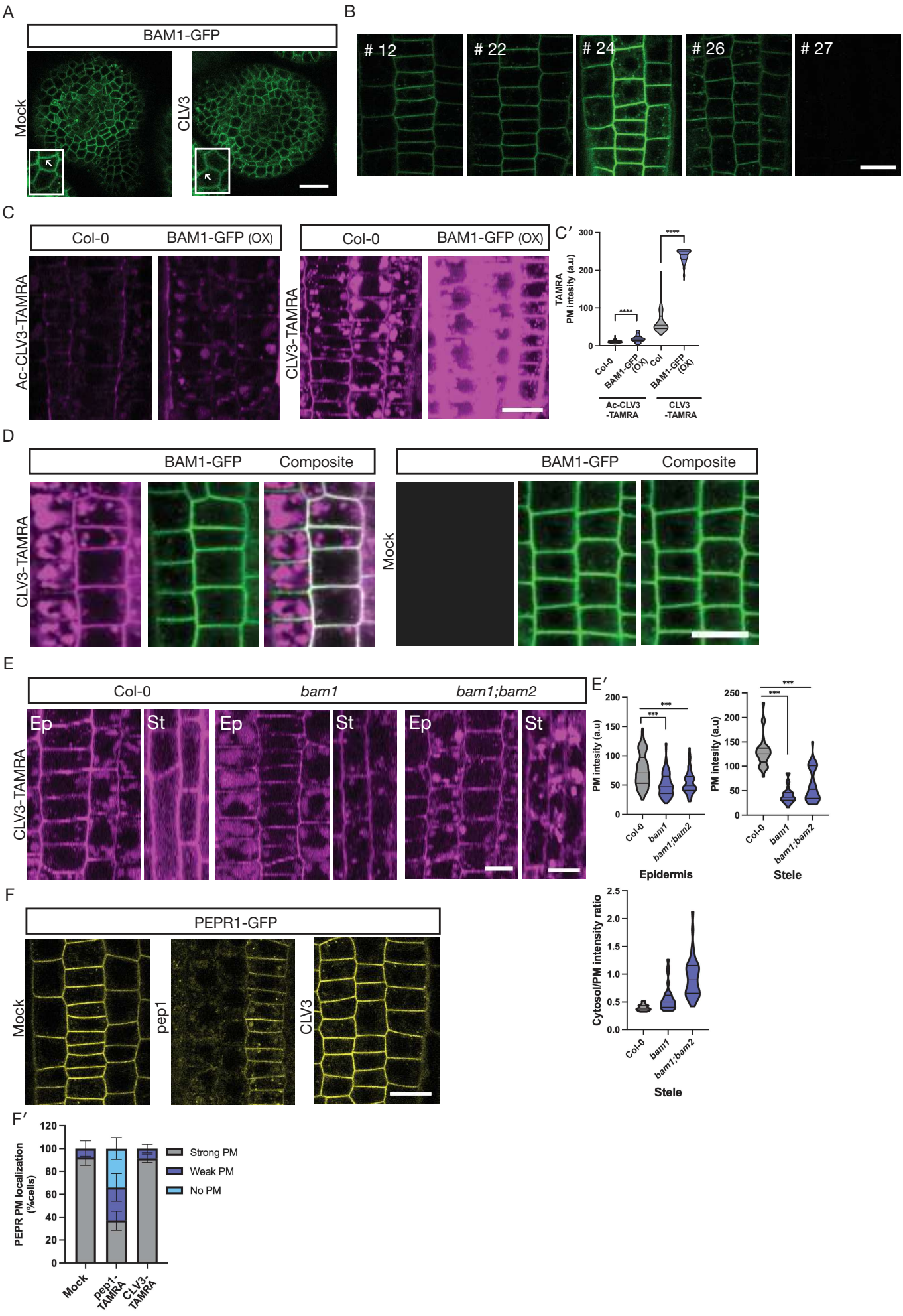
A
BAM1-GFP
Mock
CLV3
B
12
22
24
26
27
C
Col-0
BAM1-GFP (OX)
Ac-CLV3-TAMRA
CLV3-TAMRA
C′
TAMRA PM intesity (a.u)
Col-0
BAM1-GFP (OX)
Col
BAM1-GFP (OX)
Ac-CLV3 -TAMRA
CLV3 -TAMRA
D
BAM1-GFP
Composite
CLV3-TAMRA
Mock
E
Col-0
bam1
bam1;bam2
Ep
St
CLV3-TAMRA
E′
PM intesity (a.u)
Epidermis
Stele
F
PEPR1-GFP
Mock
pep1
CLV3
Cytosol/PM intensity ratio
Stele
F′
PEPR PM localization (%cells)
Strong PM
Weak PM
No PM
Mock
pep1-TAMRA
CLV3-TAMRA

Supplementary Figure S3: Binding specificity of CLV3-TAMRA to RLKs (related to figure 5)
!
(A-F) Representative confocal images of SAM (A) or root meristem epidermal cells (B-F). Lines used: A, B, and D –! *pBAM1:BAM1-GFP/bam1-3.* C – Col-0, *pBAM1:BAM1-GFP/bam1-3.* E – Col-0, *bam1, bam1; bam2.* F – *pRPS5A:PEPR1-GFP/pepr1;pepr2*. (A) BAM1 localization after 30 min to 2h of treatment with either mock or 100 nM CLV3. N=6. The arrows indicate PM localised BAM1. (B) BAM1-GFP PM level in independent lines. n≥5; N=1. (C) CLV3-TAMRA PM signal after 1 µM, 15 min treatment in Col-0 or BAM1-GFP overexpression line. n=6; N=1. (C′) The violin plot represents Ac-CLV3-TAMRA or CLV3-TAMRA mean fluorescence intensity of the PM from 8-27 cells/root. The lines indicate the median and the quartiles. Two-sided t test. For Ac-CLV3-TAMRA/ BAM1-GFP > Col-0, $p<0.0001$; For CLV3-TAMRA/ BAM1-GFP > Col-0, $p<0.0001$. (D) BAM1-GFP imaged with CLV3-TAMRA or mock after 40 min treatment. n=5; N=1. (E) CLV3-TAMRA PM signal in epidermis (Ep) and stele (St) cell layers after 5-15 min post 5 min 1 µM treatment. n=6; N=2. (E′) The violin plots (top) represent CLV3-TAMRA mean fluorescence intensity at the PM of epidermis and stele measured from 9-27 cells/root. The lines indicate the median and the quartiles. Two-sided t test. For Col > *bam1* and *bam1;bam2,* $p<0.0001$. The violin plot (bottom) represents the ratio of CLV3-TAMRA mean fluorescence intensity at the PM to the cytosolic intensity in stele measured from 5 cells/root. n=3. (F) PEPR1 PM localization 1 h after 30 s pulse with mock, 100 nM pep1 or CLV3. (F′) The stacked bar graph represents relative number of cells with strong, weak or no PEPR at the PM. n=6; N=1. At least 58 cells were analyzed/root. Error bars indicate mean ± SD. Scale bar: A-D, F – 15 µm; E – 10 µm (Ep), 7 µm (St).

A

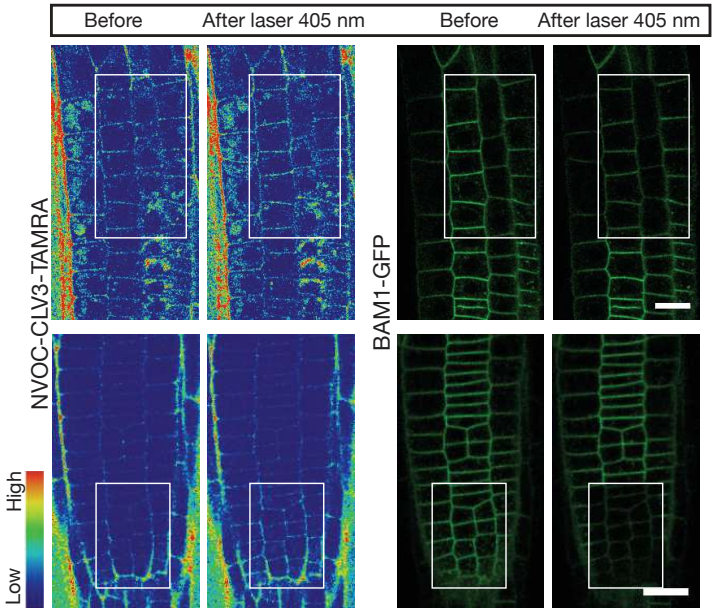

Supplementary Figure S4: Activation of photocaged peptide by 405nm laser irradiation (Related to figure 6)

(A) Representative confocal images of NVOC-CLV3-TAMRA (1 µM) at the PM before and after photoactivation in target cells by 405nm laser (left). Corresponding BAM1-GFP PM intensity after laser activation in target cells (right). Line used: *pBAM1:BAM1-GFP/bam1-3*. n=8; N=3. Scale bar: 20 µm.

2. Azidocoumarin-glycan probes for photo-induced crosslinking and *in-situ* fluorescent labeling

Authors: N. Jahnke, M.D. Driessen, Georgia Partalidou, Simon Przetak, U.I.M. Gerling-Driessen, L. Hartmann

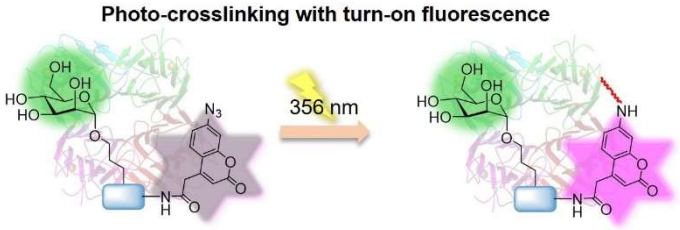

Journal: *Bioconjugate Chemistry*

Published: 07. March. 2026 https://doi.org/10.1021/acs.bioconjchem.5c00613

Bioconjugate Chemistry

Editors' Choice
Open Access

pubs.acs.org/bc

Article

Azidocoumarin Glycan Probes for Photoinduced Cross-Linking and In Situ Fluorescent Labeling

Nina Jahnke,[#] Marc D. Driessen,[#] Georgia Partalidou, Simon Przetak, Ulla I.M. Gerling-Driessen,* and Laura Hartmann*

Cite This: https://doi.org/10.1021/acs.bioconjchem.5c00613

Read Online

ACCESS | Metrics & More | Article Recommendations | Supporting Information

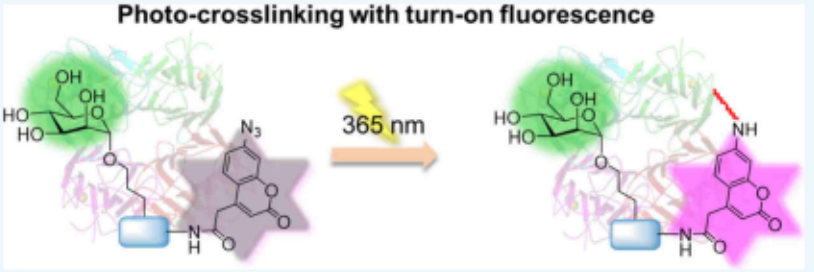

ABSTRACT: Photoinduced affinity labeling for cross-linking biomolecules in close spatial proximity has become a powerful strategy in life science studies to identify interaction partners in fundamental research as well as biomarkers in applied studies. Next-generation photo-cross-linkers additionally provide inducible fluorogenic properties to enable a visual read-out. Azido-substituted coumarin is nonfluorescent, but UV irradiation initiates the formation of a highly reactive nitrene radical that can act as a cross-linker while restoring the fluorescence activity of the coumarin chromophore. In this study, we present a 7-azidocoumarin derivative that is used as a suitable building block for solid-phase synthesis and demonstrates easy access to a variety of glycan-based photo affinity probes. Applications of photo-cross-linkers for glycans and their respective binding proteins are still rare. We show several azidocoumarin glycan-presenting probes and their selective targeting and covalent linking to lectins, accompanied by a turn-on fluorescence activity of the coumarin fluorophore. Selective recognition of specific target lectins from the presented glycan photo affinity probes is further demonstrated in complex biological environments, which now open opportunities for identifying and localizing both known and previously unidentified glycan receptors in cells, tissues, or patient samples.

INTRODUCTION

Protein cross-linking is a powerful strategy to study interaction partners of proteins, such as other proteins, glycans, or small molecules. By forming a covalent bond between the interacting partners, this technique enables the capture of transient or even weak associations and thereby allows mapping of the interactome of a target protein, the identification of binding sites, or to gain insights into modes of action.[1,2]

Especially cross-linkers that can be activated upon irradiation with light have been advantageous in such applications due to their spatial and temporal precision. This method is commonly referred to as photo affinity labeling (PAL).[3,4] One central goal of PAL experiments is to detect and characterize interaction partners of small molecule ligands, such as carbohydrates or peptides.[5] To this end, various photo affinity probes have been established over the years that are often equipped with aryl azides, diazirenes, or benzophenone derivatives undergoing covalent cross-linking upon irradiation.[6−11] While alkyl and simple phenyl azides require shorter wavelengths (<250 nm) for activation, aryl azides can be activated by irradiation at higher wavelengths (254−400 nm), leading to the release of N_2 and the formation of reactive nitrene intermediates.[12,13] Benzophenone, diazirenes, or substituted aryl azide derivatives are typically photo activated at wavelengths around 350−365 nm, which makes them more suitable for applications in biological samples.[14,15] The generated nitrenes are then able to initiate various covalent linkage reactions, e.g., to insert into C−H and N−H bonds or result in ring expansion and react with amines as nucleophiles.[16] Subsequent detection of the covalently bound interaction partners is usually a combination of different enrichment strategies, molecular biology assays, and mass spectrometry.[17−23]

However, a disadvantage of using the above-mentioned derivatives for PAL is a lack of direct visual control of successful cross-linking during the experiment. Having parallel

Received: December 8, 2025
Revised: February 5, 2026
Accepted: February 6, 2026

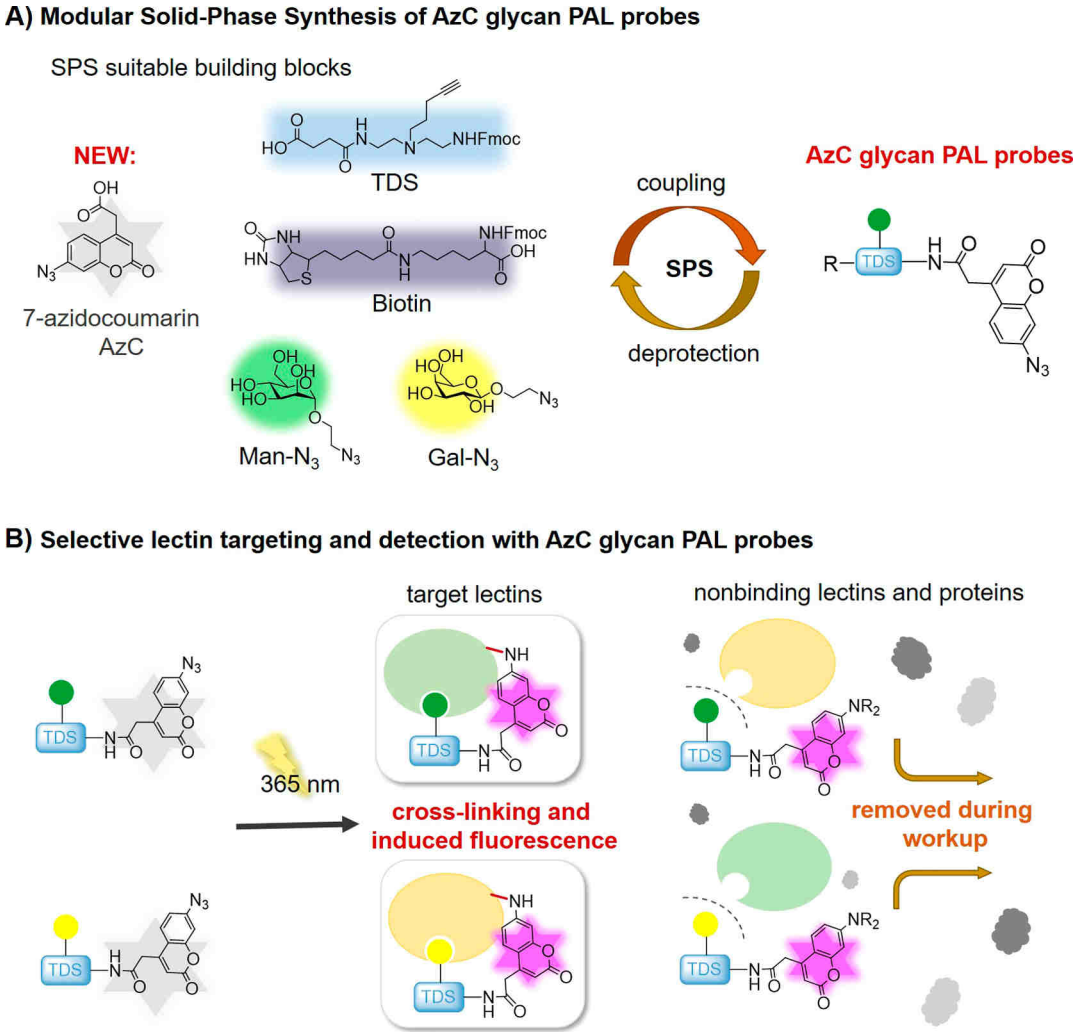

Figure 1. Schematic overview of the study. (A) Use of the AzC building block in SPS to give easy access to novel fluorogenic glycan-based affinity probes for applications in PAL. (B) Schematic concept of selective lectin targeting of Man- and Gal-based AzC affinity probes. Photoactivated probes cross-link their targets, while unbound, activated probes are removed during workup procedures.

prompting of fluorescence induced by the cross-linking event can offer a great advantage to PAL applications, in particular when targeting low-affinity, multivalent interactions, such as glycan-lectin recognition.[24] Fluorophores with turn-on properties have been developed for various applications, including live cell imaging,[25,26] enzyme activity monitoring,[27,28] biosensing and diagnostic in tumorigenic environments,[29−31] as well as monitoring in drug delivery applications.[32] Such fluorogenic probes have also been used in PAL applications, often in combination with RNA or peptide ligands.[33−38] Surprisingly, fluorogenic PAL probes are still underrepresented for the detection of glycan interactions.[39,40] Glycan interactions are typically weak (μM to mM range) and thus generally more challenging to detect. In addition, glycan-protein binding is often formed by multivalent glycan ligands that can undergo statistical rebinding in the recognition site of the interacting protein. As a consequence, capturing these short-lived interactions with PAL remains difficult. Fluorogenic detection of successful cross-linking would benefit the detection of glycan interactions; however, fluorogenic glycan-based PAL probes are not easily accessible.

An interesting natural class of fluorophores with fluorogenic properties comprises derivatives of coumarins, which belong to the class of benzopyrones and occur in various plants, such as tonka beans, sweet clover, and cinnamon.[41] Coumarins have been applied as active agents against diseases like cancer and various infectious diseases.[42,43] However, due to their variable optical activity, coumarin derivatives are most commonly applied as fluorophores.[44] The variability in fluorescence emission wavelength depends predominantly on the type of substituent and the substituted position on the coumarin ring.[45] Especially, the 3- or 4-position of the vinyl group and the 6- or 7-position of the phenyl group are attractive substitution positions and chemically accessible for functionalization.[46,47] The fluorescence variability ranges across a broad spectrum of emission wavelengths, extending from blue emission in 7-aminocoumarin derivatives,[48,49] such as 7-amino-4-methylcoumarin ($\lambda_{max,Em}$ = 435 nm),[50] over green emission for 7-diethylamino-4-trifluoromethylcoumarin ($\lambda_{max,Em}$ = 509 nm),[51] to the near-infrared region through manipulating the π-system of coumarin-based dyes, in which the carbonyl group of the lactone function is replaced by cyano(4-pyridine/pyrimidine)methylene moieties (so-called COUPY dyes, $\lambda_{max,Em}$ > 600 nm).[52,53]

A particularly interesting derivative is azidocoumarin (AzC), which carries an electron-rich azide substituent, typically at

https://doi.org/10.1021/acs.bioconjchem.5c00613
Bioconjugate Chem. XXXX, XXX, XXX−XXX

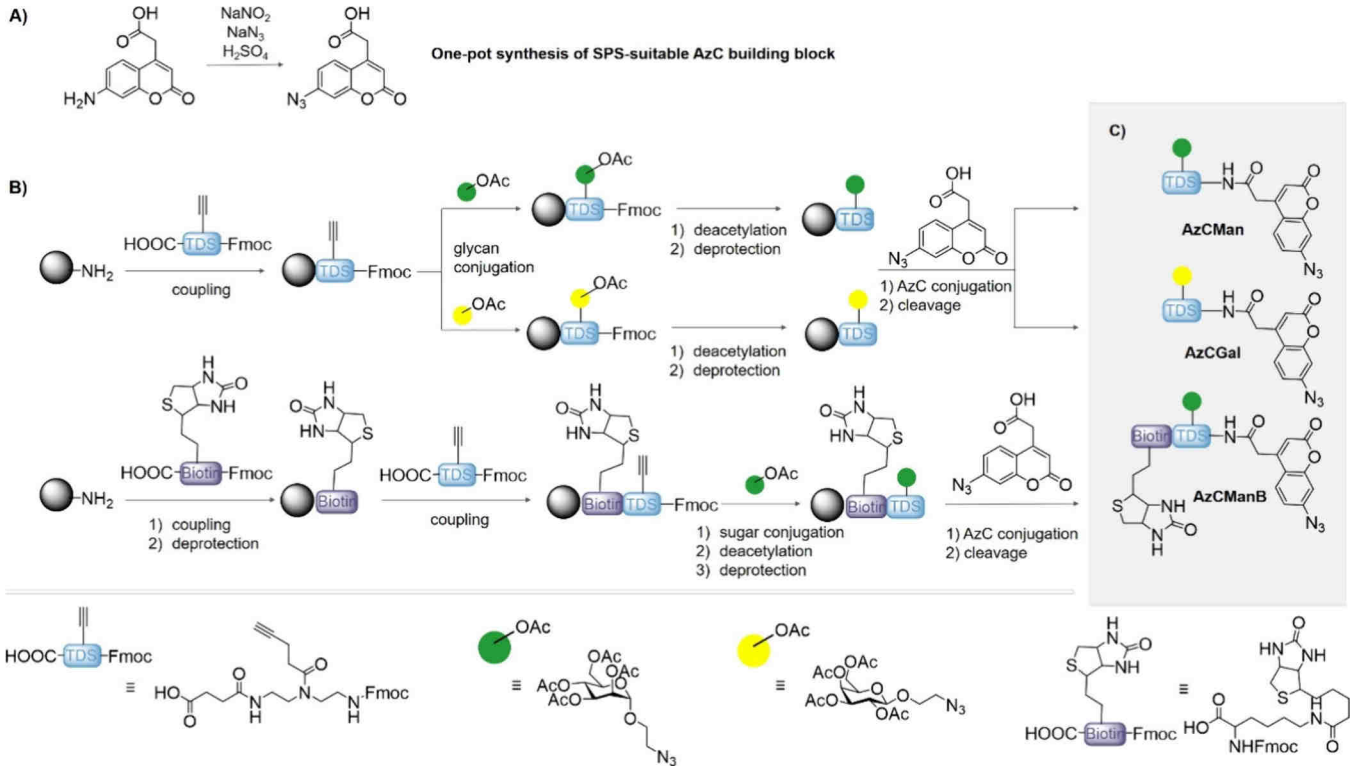

Figure 2. (A) Synthesis of the AzC building block from the aminocoumarin precursor, (B) SPS strategy, and (C) chemical structure of the AzC glycan PAL probes. Synthesis conditions: coupling: 5 eq. building block, 5 eq. PyBOP, 10 eq. DIPEA in DMF for 1 h; deprotection: 25Vol% piperidine in DMF, twice for 10 min, once for 20 min; glycan conjugation: 2.5 eq. Man-N_3 (or Gal-N_3) in DMF, 1.25 eq. sodium ascorbate and 1.25 eq. copper sulfate in MiliQ overnight; deacetylation: 0.2 M sodium methanolate in methanol for 1 h; AzC conjugation: 5 eq. AzC building block, 5 eq. HOBt, 5 eq. DIC in DMF for 1 h; resin cleavage: 95Vol% TFA, 2.5Vol% TIPS and 2.5Vol% DCM for 1 h.

position 3 or 7. By attaching the azide to the coumarin backbone, the fluorescence is initially quenched but can be regained by reduction of the azide to a primary amine.[54,55] Such azide-containing coumarins can react with alkynes as counterparts in a copper-catalyzed azide−alkyne cycloaddition (CuAAC), which also restores fluorescence after reaction.[56] Godula et al., for instance, attached AzC to glycosaminoglycans (GAGs) to enable strain-promoted azide−alkyne cycloaddition (SPAAC) and covalent attachment to GAG-binding proteins.[57] The regained fluorescence upon successful coupling allowed real-time monitoring of surface modification. In another study by Chalansonnet et al., an AzC derivative was used to detect the reductive activity of microorganisms and living cells based on the release of H_2S, which reduces the azide to a primary amine and induces fluorescence of the coumarin.[58] A recent study by Bousch et al. reported the use of a fluorinated AzC that was conjugated to a fucose moiety.[39] The final 5,6,8-trifluorinated-7-azido-coumarin probe was generated in a multistep synthesis starting from methyl pentafluoro benzoate and was successfully shown to cross-link to BambL, the fucose-binding lectin of *Burkholderia*. To the best of our knowledge, this is also the first study showing a fluorogenic glycan-based PAL probe. In a follow-up study, Vreulz et al. introduced a trifunctional scaffold for the synthesis of glycan PAL probes.[40] The scaffold features an *N*-alkoxyamine that allows the ligation of native oligosaccharides, while other functional groups, such as photo-cross-linkers and reporter tags, can be orthogonally conjugated via amine and carboxylic acid motifs.

In this study, we present a modular synthetic approach based on solid-phase synthesis (SPS) to gain straightforward synthetic access to a variety of fluorogenic glycan-based PAL probes. To this end, we establish a 7-azidocoumarin derivative as a building block for use in SPS and introduce a modular protocol allowing simple variations of glycan motifs (Figure 1A). SPS is a well-established methodology using the stepwise assembly of building blocks to get access to monodisperse, sequence-defined macromolecules—including biomacromolecules such as peptides, oligonucleotides, oligosaccharides, as well as non-natural macromolecules and polymers.[59] In our previous work, we established the so-called solid-phase polymer synthesis of oligo(amidoamines) (OAAs) and glyco-OAAs as multivalent glycan mimetics. The combination of established peptide coupling chemistry and tailor-made building blocks allows the synthesis of various glyco-OAAs including different glycan motifs, topologies, valencies, and conjugations, e.g., to lipids to derive amphiphilic glyco-OAAs.[60−62] Based on this toolbox, our approach uses the new AzC building block in combination with tailor-made building blocks and glycan ligands to derive AzC fluorogenic glycan-based PAL probes. Fast and easy access to a variety of affinity probes is demonstrated by the first set presenting mannose (Man) and galactose (Gal) as different glycan motifs. We then use these AzC probes as double-faceted molecules in PAL applications by establishing their cross-linking abilities combined with distinctive fluorogenic properties by targeting Man- as well as Gal-specific lectins (Figure 1B). We show that fluorescence of the AzC glycan PAL probes is selectively activated only upon cross-linking with the respective target

https://doi.org/10.1021/acs.bioconjchem.5c00613
Bioconjugate Chem. XXXX, XXX, XXX−XXX

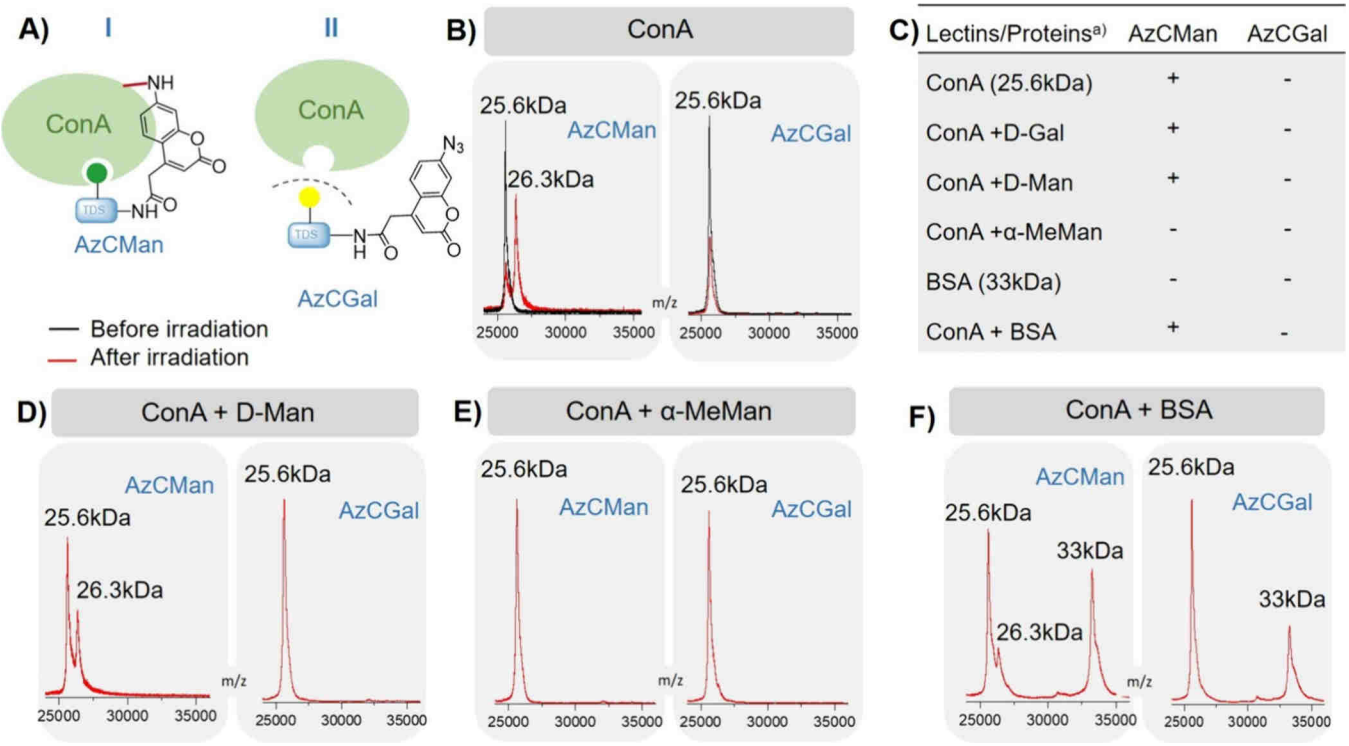

Figure 3. (A) Schematic presentation of ConA binding to AzCMan and nonbinding of the AzCGal probe. (B) MALDI-TOF-MS spectra of AzC glycan PAL probes with ConA before (black) and after (red) irradiation. (C) Overview of results from MALDI-TOF-MS spectra with (+) indicating a peak for ConA cross-linked to AzCMan and (−) reflecting that no peak for ConA-AzCMan or ConA-AzCGal conjugate was found. (D–F) MALDI-TOF-MS spectra of AzC glycan PAL probes with ConA in the presence of competing carbohydrates or proteins: (D) in the presence of D-Man, (E) in the presence of α-MeMan, or (F) in the presence of BSA.

lectin. Furthermore, our study includes the applicability of the AzC glycan PAL probes developed here under different pH conditions, as well as in complex biological environments and cell-based assays, which further enhances the versatility and applicability of PAL in glycan research.

RESULTS

Synthesis of the 7-Azidocoumarin Building Block and Solid-Phase Synthesis of AzC Glycan PAL Probes

In order to use SPS for straightforward and modular access to a variety of glycan probes, we first synthesized a suitable AzC building block. In addition to the azide moiety, the building block must provide a carboxylic acid function to allow amide coupling following standard solid-phase peptide chemistry. In a one-pot reaction, the primary amine of the commercially available precursor 2-(7-amino-2-oxo-2H-chromen-4-yl)acetic acid is transferred into an azide group (Figure 2A). The final AzC building block was isolated in high purity, as confirmed by ^{1}H NMR and RP-HPCL-MS (see SI, Figures S1–S4).

Prior to use in SPS, the fluorescence of the AzC building block was evaluated in a 1:1 mixture of acetonitrile and water and compared with the commercially available precursor aminocoumarin. Notably, AzC itself exhibited no discernible extinction within the spectral range of 320–400 nm, which aligns well with prior expectations (see SI, Figure S21A).[63] To determine the optimal irradiation time that provides a fluorescent signal of the AzC building block, AzC was irradiated for 2–60 min at a wavelength of 365 nm, followed by measuring the fluorescence intensity between 414 and 514 nm (SI, Figure S21B). After 2 min of irradiation, we observed a slight increase in fluorescence, which further increased upon longer irradiation times and reached a maximum at an irradiation duration of 30 min. Structural changes of the AzC building block were analyzed via RP-HPLC. In accordance with the increase in fluorescence over longer irradiation times, we observed a decreasing UV signal of the AzC building block along with the formation of degradation products in the respective RP-HPLC (see SI, Figure S22). Under the used conditions (1:1 acetonitrile/water) several reactions of AzC, such as oxidation, activation, and cycloadditions leading to byproducts with different fluorescence properties,[64] are possible, which likely explains the decreased fluorescence of AzC after photoactivation in comparison to nonirradiated aminocoumarin.

In order to synthesize the AzC glycan PAL probes, the AzC building block is combined with the previously established building blocks triple-bond diethylenetriamine coupled with succinic acid (TDS), as well as Man-N_3 and Gal-N_3, using standard Fmoc-peptide coupling protocols (Figure 2B).[65,66] All AzC glycan PAL probes consist of one TDS building block, which is conjugated on the alkyne side chain with either Man or Gal via CuAAC. The AzC is coupled in the final step to the N-terminus of the TDS-Man/Gal oligomer. Specifically, an Fmoc-protected TentaGel S-RAM resin is used, to which TDS was coupled as the first building block using benzotriazol-1-yloxytrispyrrolidinophosphonium hexaphosphate (PyBOP) and *N*,*N*-diisopropylethylamine (DIPEA) as coupling reagents.[67] Then, acetyl-protected Man- or Gal-N_3 was conjugated to the alkyne function of TDS using CuAAC. Before N-terminal AzC coupling was performed, the acetyl-protected hydroxy groups of the carbohydrates were

https://doi.org/10.1021/acs.bioconjchem.5c00613
Bioconjugate Chem. XXXX, XXX, XXX–XXX

deprotected with sodium methanolate, as strong basic pH can result in destruction of the AzC building block. Subsequently, the Fmoc group of TDS was removed, and the AzC building block was coupled using 1-hydroxybenzotriazole (HOBt)/*N*,*N*-diisopropylcarbodiimide (DIC). The final AzC carbohydrate probe was cleaved off the solid phase using trifluoroacetic acid (TFA) and triisopropylsilane (TIPS). The AzCMan and AzCGal probes (Figure 2C) were isolated with relative purities of >95%, as determined by RP-HPLC (see SI, Figures S5−S14).

Based on the modularity of the solid-phase approach, other functional groups can also be introduced. Here, we synthesized an additional AzC glycan PAL probe containing a biotin motif, which allows for enrichment of the cross-linked biomolecules. For the biotin-containing probe AzCManB, Fmoc-Lys-(biotin)−OH was coupled as the initial building block to the TentaGel S-RAM resin, followed by the same protocol used for AzCMan synthesis. All probes were characterized using RP-HPLC-MS, HR-ESI, IR, and ^{1}H NMR (see SI, Figures S15−S20).

Selective Cross-Linking of AzC Glycan PAL Probes to Target Lectins

Having established a straightforward synthesis strategy suitable for making diverse glycan PAL probes, we used AzCMan and AzCGal to test for specific cross-linking upon binding to selected carbohydrate-recognizing target lectins. Man and Gal were selected as glycan motifs as they represent abundant components in cell surface glycans and are thus involved in a variety of native carbohydrate-lectin interactions.[68,69] They present an ideal model system for investigating our AzC glycan PAL probe regarding selective interaction and photoinduced cross-linking with the lectin Concanavalin A (ConA), which recognizes Man, even with low affinity, but does not bind to Gal.[70] *Ricinus communis* agglutinin (RCA_{120}), in turn, was used as a Gal-recognizing lectin with no affinity for Man.[71−74] Therefore, the AzCGal probe is not supposed to be recognized by ConA and serves as a control for evaluating cross-linking selectivity.

Aryl azides are generally able to form very reactive nitrenes by irradiation at 365 nm.[75] Due to the short-lived, radical character of these nitrenes, covalent binding can only take place when a target protein/lectin is in close spatial proximity to the AzC probe, which is only given for direct interaction partners (i.e., glycan-lectin binding in this case). Therefore, it was expected that only AzCMan, but not the AzCGal probe, forms a covalent bond to ConA upon irradiation (Figure 3A). To confirm this, in a first cross-linking experiment, equimolar amounts (10 μM) of either AzCMan and AzCGal were incubated with ConA for 20 min, followed by irradiation at 365 nm for 15 min, followed by analysis via MALDI-TOF-MS.

Figure 3B displays the corresponding MALDI-TOF-MS spectra (see SI for full spectra, Figures S23−S26) of the AzC glycan PAL probes with ConA before (black) and after (red) irradiation. As expected, before irradiation, both probes show a single peak corresponding to the molar mass of the ConA monomer (about 25.6 kDa). After irradiation, only the sample incubated with AzCMan displayed an additional peak corresponding to the molecular weight of ConA cross-linked to the AzCMan probe (26.3 kDa). This peak is absent in the sample incubated with AzCGal, suggesting that close spatial proximity to ConA leading to UV-induced cross-linking was only given for AzCMan, but not for the AzCGal probe. It can be assumed that this was the result of the AzCMan probe being bound in the recognition site of ConA. The fact that the AzCGal probe did not show any cross-linking to ConA indicates that the captured interaction was the result of ligand binding rather than nonspecific cross-linking.

To further investigate the selective targeting of the probes, we performed additional PAL experiments with the AzC glycan PAL probes in the presence of competing binding and nonbinding carbohydrates, as well as bovine serum albumin (BSA) as a nonglycan-binding protein (Figures S27−S34). To this end, AzCMan and AzCGal were incubated with ConA and supplemented with a 40-fold excess of D-galactose (D-Gal), D-mannose (D-Man), α-methylmannose (α-MeMan), and BSA. ConA was incubated with the respective competing glycans (D-Gal, D-Man, α-MeMan) or BSA for a duration of 20 min before the AzCMan or AzCGal probes were added in an equimolar ratio to ConA. After addition of the AzC glycan PAL probes, the samples were incubated for another 20 min to allow interaction between the probes and ConA. Subsequently, the samples were irradiated for 15 min at 365 nm and analyzed by MALDI-TOF-MS. Figure 3C shows in the presence of which additional glycans or proteins AzCMan showed successful cross-linking to ConA. The ConA-AzCMan conjugate was detected in the presence of both excess nonbinding Gal and nonbinding BSA, confirming that cross-linking is only achieved from specific glycan-protein interactions. When adding a high excess of binding α-MeMan, as expected, the monosaccharide outcompetes AzCMan and no cross-linking product is observed. Interestingly, supplementing ConA with an excess of D-Man did not prevent cross-linking to the AzCMan probe (Figure 3D). ConA can recognize both D-Man and α-MeMan. Thus, we assumed that both would inhibit efficient binding of the AzCMan probe to ConA. The fact that the D-Man-supplemented sample showed the ConA-AzCMan conjugate despite the competing sugar indicates that the interaction of AzCMan with ConA is stronger compared to ConA with D-Man. In contrast, α-MeMan might form a stronger interaction with ConA compared to AzCMan. This is supported by the much higher binding affinity of α-MeMan to ConA compared to D-Man.[76] Having a monovalent carbohydrate in the AzCMan probe, it is not unlikely that the binding pocket of ConA was occupied by α-MeMan, preventing additional binding of the AzCMan probe. This result further supports the fact that the AzCMan probe needs to form a tight interaction with the target lectin to form a covalent bond upon irradiation. In addition, incubation with BSA instead of ConA, which should not recognize either of the two carbohydrate moieties as it mainly interacts with hydrophobic molecules,[77,78] showed no peak corresponding to a potential BSA probe conjugate (see SI, Figures S31 and S32).

Next, a mixture of ConA and BSA was used to assess whether the AzCMan probe can selectively target ConA in the presence of other proteins (Figure 3F). Indeed, in addition to the BSA peak (33 kDa), the ConA-AzCMan conjugate (26.3 kDa) was detected, confirming that the AzCMan probe can selectively cross-link the target protein even in the presence of other nonbinding proteins. Thus, the MALDI-TOF-MS study provided a first indication of the selective cross-linking capabilities of the AzC carbohydrate probes in crowded protein and carbohydrate mixtures.

https://doi.org/10.1021/acs.bioconjchem.5c00613
Bioconjugate Chem. XXXX, XXX, XXX−XXX

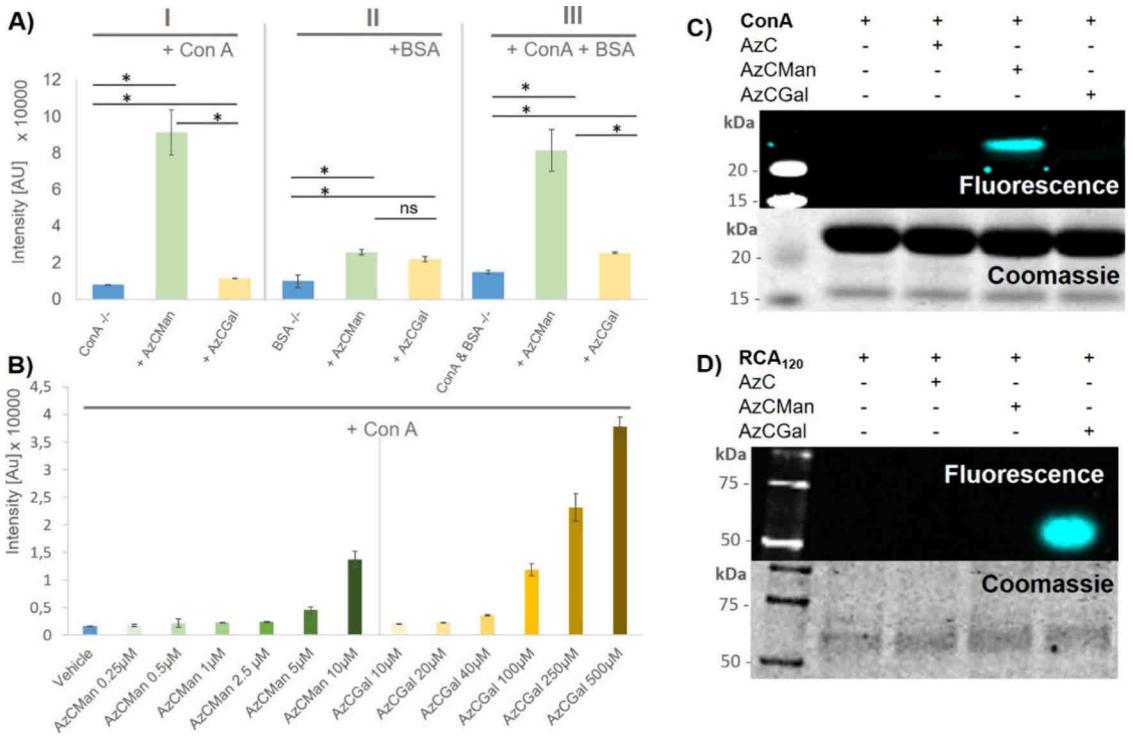

Figure 4. (A) Maximal fluorescence intensities of AzCMan and AzCGal probes at 10 μM concentration incubated with either ConA or BSA alone or a mixture of both proteins. Data represent the mean of four individual measurements. (B) Limit of detection for AzCMan and limit of selectivity for AzCGal. Data represent the mean of four individual measurements. (C) SDS−PAGE of ConA incubated with AzC glycan PAL probes after irradiation at 365 nm; the top panel shows AzC fluorescence and the lower panel shows Coomassie stain of the same gel. (D) SDS−PAGE of RCA_{120} incubated with AzC glycan PAL probes after irradiation at 365nm; the top panel shows AzC fluorescence and the lower panel shows Coomassie stain of the same gel. The complete SDS−PAGE images including the AzCManB probe are shown in the SI (Figure S37).

Inducible Fluorogenic Properties of AzC Glycan PAL Probes

After establishing successful and selective cross-linking of the AzCMan probe to ConA by MALDI-TOF-MS, we next investigated whether the probe conjugation results in a turn-on fluorescence of the coumarin fluorophore. To this end, we measured the fluorescence of the AzC glycan PAL probes that were incubated with different proteins before and after irradiation with UV light. We used a mixture of ConA and BSA, where ConA serves as the binding protein to AzCMan and BSA as a nonbinding protein to both probes. Likewise, we used a mixture of RCA_{120} and BSA for the AzCGal probe. The AzC probes were incubated for 20 min in equimolar concentrations with the protein mixture and then irradiated for 15 min at 365 nm. Afterward, a purification step was required to isolate the formed lectin-probe conjugates from any unbound AzC probe that might have been activated during irradiation, as these free fluorescent probes could potentially interfere with the fluorescence read-out of the probe-lectin conjugates. Therefore, the irradiated samples were subjected to a centrifugal concentrator with a molecular weight cutoff (MWCO) of 1000 Da to isolate the probe-lectin conjugates. The collected samples were lyophilized and subsequently resuspended in 200 μL lectin-binding buffer (LBB) to maintain the original concentration of 10 μM. Then, the fluorescence of the samples was measured at 450 nm. (Figure 4A,B). In addition, the samples were separated by SDS−PAGE and analyzed using a fluorescent read-out, followed by Coomassie staining of the gel (Figures 4C,D and S37).

Figure 4A shows the maximal fluorescence intensities at 450 nm of the different proteins incubated with the AzC glycan PAL probes after irradiation (see SI for detailed fluorescence spectra; Figure S35B). Figure 4A−I corresponds to the probes (AzCMan or AzCGal) incubated with ConA, where a significant increase in fluorescence intensity was only observed with the AzCMan probe, but not with the AzCGal probe. Figure 4A-**II** shows nonbinding BSA incubated with AzCMan or AzCGal, where a marginal increase in fluorescence is observed for both probes, which was attributed to potentially incomplete removal of the free, irradiated probe during the purification step. However, it is essential to note that the fluorescence intensity resulting from the interaction with BSA is considerably lower compared with the ConA samples. Figure 4A-**III** shows the fluorescence intensities of the samples where the two AzC glycan PAL probes were incubated with a mixture of ConA and BSA. Here, the difference in fluorescence intensity is clearly visible. The sample containing the AzCMan probe shows a significant increase in fluorescence activity in contrast to the sample containing the AzCGal probe. These results align well with the MALDI-TOF analysis and provide further evidence that the AzCMan probe can be selectively cross-linked to its target lectin ConA, and that this is accompanied by inducible fluorescence of the coumarin unit.

We next evaluated whether the probes are prone to nonspecific photoinduced cross-linking at high concentrations. In addition, we were interested in determining the minimal probe concentration at which a photoinduced turn-on fluorescence could still be detected for probe-target cross-linking. Thus, on the one hand, we explored the limit of detection (LOD) at low probe concentration and, on the other

https://doi.org/10.1021/acs.bioconjchem.5c00613
Bioconjugate Chem. XXXX, XXX, XXX−XXX

hand, studied potential nonspecific cross-linking at high probe concentrations. To this end, we incubated ConA with increasing concentrations of both AzCMan and AzCGal and measured the maximum fluorescence intensities at 450 nm (Figure 4B). For AzCMan, concentrations between 0.25 and 10 μM were selected, where we observed an increase in fluorescence intensities with increasing probe concentrations. Between 0 and 5 μM, the fluorescence intensities increased in an almost linear fashion (see SI, Figure S35C,D), which was used to calculate an LOD of 2.4 μM (see SI, Figure S35E) for AzCMan interacting with ConA. This value indicates a high sensitivity of the AzCMan probe for detecting an interaction with ConA. Carbohydrate-lectin interactions are usually of very low affinity, especially for monovalent glycans. For comparison, the binding constant of α-MeMan to ConA has a K_d of 130 μM.[79] The comparable low LOD of AzCMan shows that even low-affinity interactions can be successfully detected with this AzC glycan PAL probe. To test for nonspecific binding of AzCGal to ConA, the concentration of the probe was increased up to 500 μM while keeping the ConA concentration at 10 μM, resulting in a 50-fold excess of probe relative to protein. As shown in Figure 4B, the fluorescence intensity increases notably at probe concentrations higher than 100 μM. We attribute this to nonspecific binding at large probe excess, as Gal is well-known not to show any affinity to ConA and is therefore used as the nonbinding control in studies investigating Man-ConA interactions.[80−82] However, using the probes at an equimolar or up to a 5-fold higher concentration in relation to the target protein ensures specific target interaction with no detectable nonspecific binding.

Finally, we validated the applicability of the AzC glycan PAL probes in biochemical assays. Using SDS−PAGE, we tested whether the fluorescence of the cross-linked conjugates (ConA-AzCMan and RCA_{120}-AzCGal) could be detected in-gel (Figure 4C,D). Here, the AzC building block not containing any glycan motifs was included as a control to exclude nonspecific binding of the AzC moiety itself. In Figure 4C, the upper panel displays the AzC fluorescence image of the gel. After fluorescence measurement, the gels were stained with Coomassie as a control for sample loading across the lanes. The Coomassie staining of the gels is displayed in the lower panel. For both lectins, a fluorescent band only occurs when they are incubated with the respective binding glycan probe during irradiation (AzCMan in the case of ConA and AzCGal in the case of RCA_{120}). Thus, SDS−PAGE analysis confirmed the selective target cross-linking combined with induced fluorescence for the AzC glycan PAL probes.

Stability of the Induced AzC Probe Fluorescence at Different pH Ranges

Considering that biological applications can be accompanied by dynamic pH fluctuations, it is crucial to evaluate whether the photoinduced fluorescence of the cross-linked species is stable in acidic or basic environments. Thus, next, we tested the stability of the induced coumarin fluorescence at various pH conditions. Ramesh et al. demonstrated that the lactone ring of coumarin can undergo ring opening under basic conditions.[83] This could potentially lead to a shift or quenching of the fluorescence. In order to cover a wide pH range, we measured the fluorescence of the cross-linked probes at pH 4−10. AzCMan was incubated with ConA and irradiated as previously described. The unbound AzC glycan PAL probe was removed. The isolated and lyophilized AzCMan-ConA conjugates were then resuspended, and the individual probe solutions were adjusted to pH 4, 5, 6, 7, and 8 to give a final probe concentration of 5 μM. The fluorescent measurements of the samples were carried out after an incubation period of 60 min at the individual pH values. All samples showed strong fluorescence at 450 nm, independent of the pH range (see SI, Figure S35A). The individual fluorescence spectra show marginal variations in absolute intensities, which can be attributed to standard fluctuations during fluorescence measurements and minimal variations in the sample concentration rather than being an effect of the individual pH value. Thus, we conclude that the photoinduced fluorescence of cross-linked AzC glycan PAL probe conjugates is stable over a wide pH range.

Evaluation of the Minimal Irradiation Time to Gain Stable Probe-Target Cross-Linking

Based on these previous results, next, we established the optimal irradiation times that are required to gain successful and robust cross-linking of the probe to its target protein. Therefore, time-dependent irradiation experiments were carried out by mixing ConA and the AzCMan probe in equimolar ratios (20 μM) and incubating the samples for 20 min before irradiation between 2 and 60 min at 365 nm with a fixed energy input control (0.33 J/cm^2/min). The irradiated samples were subsequently separated by SDS−PAGE, and the fluorescence intensities of the AzCMan-ConA conjugates were quantified relative to the Coomassie stain intensities of the same lanes (Figure 5A,B).

Figure 5A shows the images of the Coomassie stain (top) and the fluorescence read-out (bottom) of the same gel. The

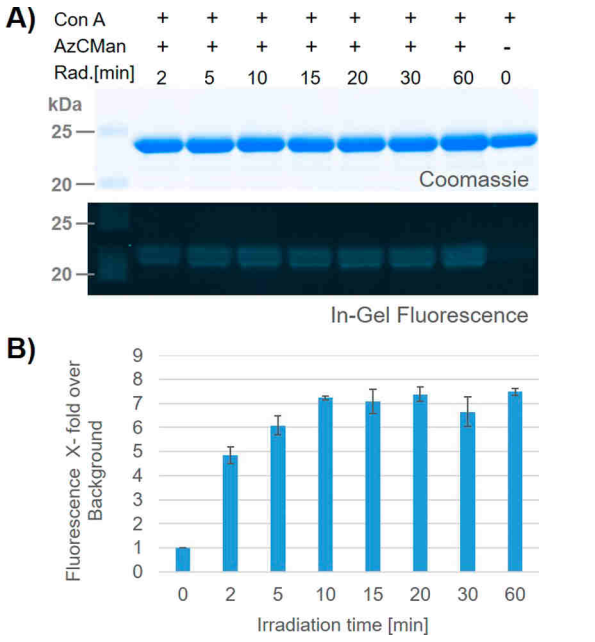

Figure 5. (A) Coomassie-stained and fluorescence image of the SDS−PAGE containing ConA with AzCMan at different durations of irradiation; the top panel shows Coomassie stain; the lower panel shows AzC fluorescence of the same gel. (B) Quantification of the fluorescence intensities of the individual bands normalized against ConA (last lane on the gel). The quantification was calculated as the mean of two replicates of the time-dependent irradiation series applied on one SDS−PAGE (full image provided in the SI, Figure S36).

https://doi.org/10.1021/acs.bioconjchem.5c00613
Bioconjugate Chem. XXXX, XXX, XXX−XXX

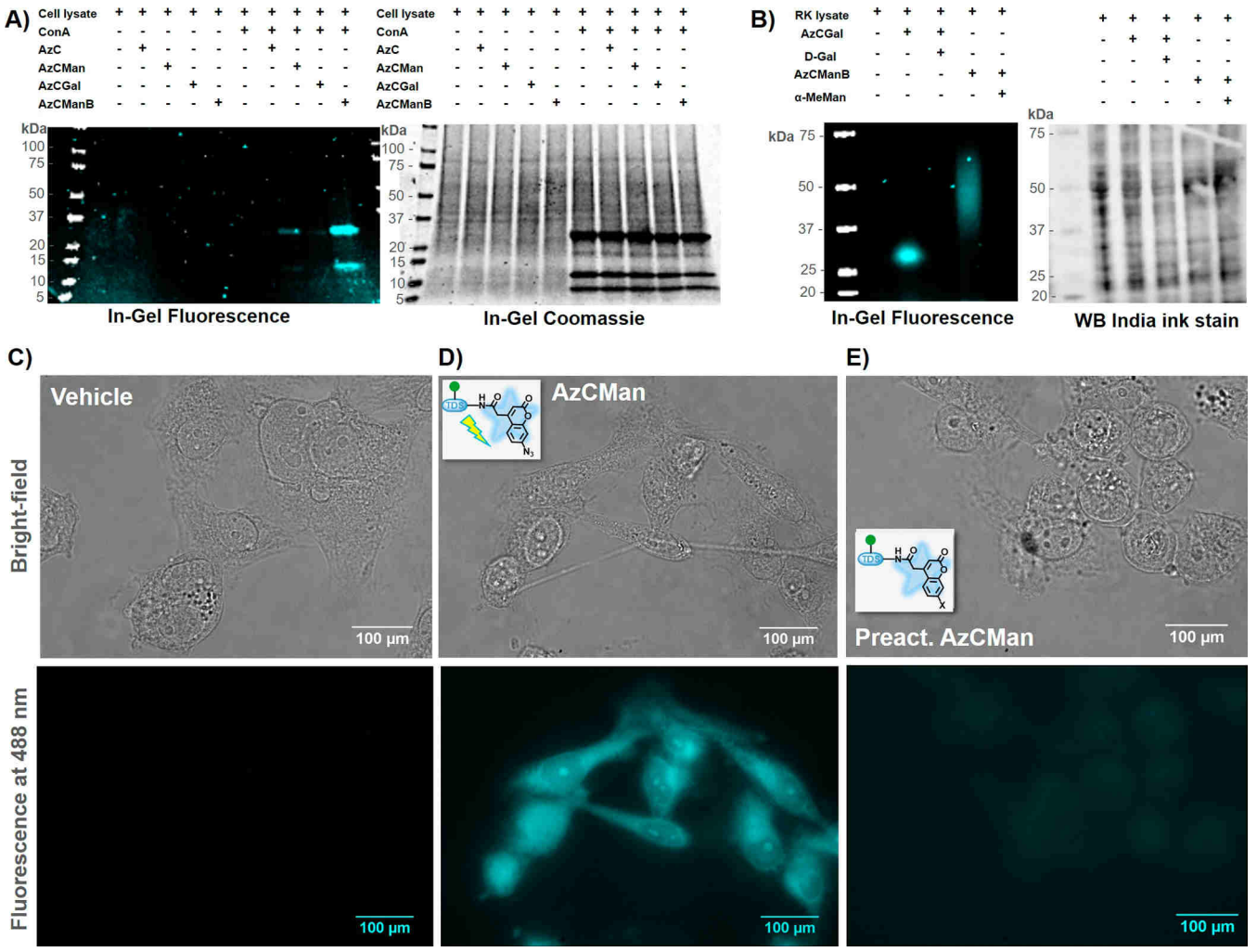

Figure 6. (A) SDS−PAGE showing MDA-MB 231 lysate with or without supplemented ConA that was incubated with various AzC glycan PAL probes and subsequently irradiated with UV light for 15 min. (B) Western blot of native rat kidney lysate that was incubated with AzCGal and AzCManB probes in the presence or absence of the respective carbohydrate inhibitors (α-MeMan and D-Gal) and subsequently irradiated with UV light for 15 min. (C−E) Microscope images (top: bright-field; bottom: fluorescence at 488 nm) of fixed MDA-MB-231 cells incubated with vehicle (C), AzCMan (D), or preactivated AzCMan (E) and subsequently irradiated at 365 nm for 15 min.

bands represent AzCMan conjugated to ConA at irradiation durations of 2, 5, 10, 15, 20, 30, and 60 min. The last lane contains Con A without the AzCMan probe and serves as a reference (see SI for full-size image of the gel showing two replicates, Figure S36). For all irradiation durations, a fluorescence band was detected in th gel. The fluorescence intensities differ only marginally for the individual irradiation durations. Notably, a fluorescent band can already be detected after irradiation of ConA in the presence of AzCMan for only 2 min, indicating rapid AzCMan cross-linking to ConA. Figure 5B shows the quantified fluorescence intensities of the individual bands normalized to the ConA band. The fluorescence intensity peaks around the 10 min mark and does not significantly increase further with longer irradiation times. It is worth noting that even for long irradiation times of up to 60 min, no significant bleaching of the fluorophore or dissociation of the probe was observed. Hence, robust photoinduced cross-linking can be achieved for the AzCMan probe within 2 min of irradiation at 365 nm. This offers opportunities for expedited analysis suitable for unstable or sensitive samples or for rapid screening approaches. Since the induced fluorescence is not quenched during long irradiation durations, the probe also seems suitable for long-term irradiation applications. Hence, the duration of irradiation can be individually adapted to the respective demands of the experiment without the risk of losing cross-linking efficiency or fluorescence intensity.

Selective Target Recognition in Complex Biological Environments

Biological systems, such as cell lysates, intact cells, or organelles, are complex mixtures of different proteins, lipids, peptides, and glycans. To be used in molecular biology and biochemical assays, the AzC glycan PAL probes and the cross-linked conjugates need to be structurally stable under these conditions. In addition, selective and immediate cross-linking to the target protein upon photoactivation is desired. Thus, AzC glycan PAL probes were tested in complex mixtures derived from cells and animal organs, again looking at the selective cross-linking to their respective target proteins upon photoactivation without showing random fluorescence activation due to probe discomposure or nonspecific cross-linking to other components in the mixture.

https://doi.org/10.1021/acs.bioconjchem.5c00613
Bioconjugate Chem. XXXX, XXX, XXX−XXX

In the first experiment, AzC glycan PAL probes were incubated with cell lysate generated from MDA-MB 231 cells. The proteins in the cell lysate were denatured using SDS. The probes were incubated either with the cell lysate alone or with cell lysate supplemented with ConA. ConA is a plant-based lectin; it is not present in human cell lines, such as MDA-MB321 cells. In this test, we also included the more complex probe containing Man and biotin (AzCManB) to show whether the more complex probe would still bind the target lectin (ConA) as well, which would, in a next step, offer isolation of the cross-linked target via the biotin handle. AzCGal and AzC without any carbohydrate ligand served as controls for nonspecific binding to other proteins in the lysate. We incubated 20 μL of cell lysate (2 mg/mL) with 5 μL of vehicle or ConA (50 μM) and 10 μL of probe (50 μM) and incubated these mixtures for 20 min, followed by UV irradiation for 15 min. Subsequently, the samples were applied to SDS−PAGE. AzC fluorescence was detected in the gel, followed by Coomassie staining (Figure 6A). The fluorescence read-out of the gel shows fluorescent bands only in samples where ConA was supplemented to the lysate and only for probes containing the Man residue (AzCMan and AzCManB). Interestingly, the fluorescence intensity was higher in the case of incubation of ConA with AzCManB compared to AzCMan. This could indicate that the biotin present in this probe could increase the binding affinity to ConA. Since lectin binding is a low-affinity on−off integration, especially for monosaccharide ligands, we speculate that the sterically more demanding AzCManB probe undergoes less rapid statistical rebinding in the carbohydrate recognition site of ConA, leading to a higher ratio of the cross-linked probe to the lectin. However, a more detailed analysis of this effect will be subject to a detailed kinetic comparison of the probes in a follow-up study. The test in cell lysate revealed that even in complex protein mixtures, we do not observe nonspecific cross-linking of the AzC glycan PAL probes. To test whether the biotin in the AzCManB probe is still accessible after cross-linking to the target, we used streptavidin binding. We incubated the AzC building block and all AzC glycan PAL probes with ConA. After irradiation, we applied all samples to SDS−PAGE and subsequent Western blot (WB). After detecting AzC fluorescence for the bands containing AzCMan and AzCManB (see SI, Figure S38A), we incubated the WB with streptavidin conjugated to DyLight 790 and visualized the binding of streptavidin, which was found exclusively in the band with the biotin-containing AzCManB probe (see SI, Figure S38B). This result confirms that the biotin in the AzCManB probe is still accessible for streptavidin binding after cross-linking to the target protein, thus allowing isolation of the cross-linked conjugates via streptavidin affinity columns.

Next, we studied whether AzCMan and AzCGal could be used to identify unknown interaction partners in biological settings. In native lysates, the structure and function of the proteins are kept intact. Hence, it is expected that proteins in native lysates contain lectin domains specific for Man or Gal ligands, which should potentially be recognized and cross-linked by the AzC glycan PAL probes upon photoactivation. Successful cross-linking would be detectable by fluorescent bands in the gel. We prepared a native lysate of rat kidneys and incubated it with AzCGal and AzCManB for 20 min, followed by 15 min UV irradiation and SDS−PAGE separation (Figure 6B). Indeed, we detected fluorescent bands in the native lysate gel after incubation with the AzCGal and AzCManB probes independently. This was not surprising as the native rat kidney lysate was likely to contain both Man- and Gal-recognizing receptors. Interestingly, the fluorescent bands appear at different molecular weights for the AzCGal and AzCManB probes, indicating that the two probes cross-linked to different target proteins. This was a first indication that the cross-linked conjugates were the result of a carbohydrate-specific interaction with the respective unidentified protein/lectin targets. To verify this, we also treated the native lysate with the two AzC glycan PAL probes in the presence of an excess of free D-Gal and α-MeMan (5-fold excess compared to the AzC glycan PALprobe). These monosaccharides should act as inhibitors for the two carbohydrate probes, and as a consequence, no fluorescent bands should be detected for the AzC glycan PAL probes in the presence of D-Gal and α-MeMan. Indeed, the rat kidney samples that contained the AzC glycan PAL probes in the presence of the monosaccharide inhibitors did not show the fluorescent bands that were detected for the AzC probes without D-Gal and α-MeMan. Thus, it can be concluded that the fluorescent bands in the native rat kidney lysate originate from cross-linking of the AzC glycan PAL probes to specific Gal- and Man-recognizing receptors. These results underline the usefulness of these or similar AzC carbohydrate probes for the detection and subsequent isolation of specific carbohydrate-interacting proteins.

After having established that the photoinduced fluorescence of the AzC glycan PAL probes can be detected using fluorescence spectroscopy and SDS−PAGE analysis, we now wanted to validate the visualization of the AzC glycan PAL probes using fluorescence microscopy in cell-based assays. To the best of our knowledge, this is the first time showing that AzC glycan PAL probes were tested for application in cell studies. We again used MDA-MB-231 cells, which offer a variety of carbohydrate-recognizing receptors on the cell surface. In these cell studies, we tested only the AzCMan probe. Since there are also Gal-recognizing receptors on the cell surface, no significant distinction could be expected by treating the cells with AzCMan or AzCGal. Since we did not detect nonspecific cross-linking with the unconjugated AzC building block, we used preirradiated AzCMan as a control probe in this setup. To this end, AzCMan was irradiated at 365 nm for 15 min before addition to the cells. Due to prior irradiation, the AzCMan probe becomes fluorescent. Containing the mannose ligand, the preactivated AzCMan can still bind to mannose-recognizing proteins on the cell surface. However, the probe has lost the ability to cross-link and thus covalently bind to interacting targets during the irradiation procedure and is therefore largely removed during the washing procedures. This allows a distinction of the fluorogenic properties of simply target-bound versus covalently linked AzCMan.

Cells were grown in 8-well chamber microscopy slides to 80% confluency and fixed using ice-cold methanol. Subsequently, vehicle control, AzCMan, or deactivated AzCMan was added to the cells. After incubation for 20 min, the plate was irradiated for 15 min at 365 nm. Afterward, the cells were washed thoroughly with PBS to remove the unbound AzCMan probe. The cells were then visualized using a fluorescence microscope in bright-field mode and at a fluorescence excitation of 365 nm (Figure 6C−E; and SI Figures S39−S41). During preirradiation of AzCMan, the azide is removed, which turns on the fluorescence of the AzC probe. However,

https://doi.org/10.1021/acs.bioconjchem.5c00613
Bioconjugate Chem. XXXX, XXX, XXX−XXX

due to the loss of the azide, this preactivated probe should not be able to cross-link to protein targets on the cells during irradiation and will be removed during the washing steps following the irradiation step. It serves as a control to determine if the detected fluorescence can either be attributed to the cross-linked AzC probe or is the result of receptor-bound, but noncross-linked probe.

All cells are clearly visible in the bright-field images (Figure 6C–E, upper panel). LBB-treated cells (vehicle) show no fluorescence at 488 nm (Figure 6C, lower panel), proving that no autofluorescence of the cells can be detected at this wavelength. Cells treated with AzCMan (Figure 6D) show bright fluorescence at 488 nm, indicating that AzCMan was cross-linked to Man-recognizing proteins. The negative control in which cells were incubated with the preactivated AzCMan probe (Figure 6D) shows only marginal fluorescence at 488 nm, likely resulting from residual probe that remained target-bound even throughout the washing procedure. In comparison to the AzCMan probe that was activated on the cells upon irradiation, a clear difference in fluorescence intensity is evident. These results show that the AzC carbohydrate probes can also be applied in cell-based assays.

Finally, we wanted to explore the possibility if the laser of the microscope could be used to locally induce probe cross-linking. The excitation wavelength of the laser in our instrument is 365 nm, which is in the range to induce photo-cross-linking for azidocoumarin probes. The AzCMan probe was added to MDA-MB231 cells, and an image in bright-field mode was immediately taken. Afterward, we switched to fluorescence emission at 488 nm. Images were taken at several intervals, starting from $t = 0$ to $t = 10$ min (see SI, Figure S42). We observed a steady increase in fluorescence intensities starting after 1 min of laser irradiation. Given that in this setup the unbound probe cannot be washed out, a high background signal is observed in these images. However, this proof-of-concept study showed that cross-linking of AzC glycan PAL probe can be induced locally on cells using the UV laser of the microscope. This offers new potential applications and experimental setups using these probes, such as initiating and life tracking of cross-linking events in cells.

CONCLUSIONS

Taken together, we exploited the double-faceted mode of action of a new 7-azidocoumarin derivative that can simultaneously act as a photo-cross-linker and a fluorogenic turn-on dye. We established an AzC building block suitable for SPS and demonstrated the successful and straightforward synthesis of different glycan-based AzC PAL probes. In contrast to classical organic synthesis, the SPS approach enables easy access and variation of the probes, e.g., with regard to glycan type, architecture, and valency.[84] Specifically, as a first set, we synthesized and characterized AzCMan and AzCGal probes and investigated their applicability as photo-cross-linking affinity probes in a series of lectin interaction and cell-based assays. The AzC glycan PAL probes showed highly selective photoinduced cross-linking only in the case of direct interaction with the respective target lectin. We confirmed this in studies using additional nonbinding proteins and competing carbohydrates. The photoinduced cross-linking of the AzC glycan PAL probes is accompanied by an induced fluorescence of the coumarin dye, which can be detected in solution, in SDS–PAGE and Western blots, as well as in cell imaging using fluorescence microscopy. We found selective target cross-linking for the AzC glycan PAL probes even in complex environments, such as cell- or whole organ lysates. Finally, we were able to show that under native conditions, the AzC glycan PAL probes have the potential to detect interaction partners specific for the respective glycan motif. In conclusion, the SPS-suitable AzC building block offers high potential for the development of a variety of affinity probes, including multivalent glycan or peptide-based probes, for a broad spectrum of bioimaging applications.

METHODS

General

No unexpected or unusually high safety hazards were encountered during the synthesis or performance of the experiments.

Acetone (≥99.8%) was purchased from Fischer Scientific. Diethyl ether (with BHT as inhibitor, ≥99.8%), triisopropylsilane (TIPS) (98%), bovine serum albumin ((≥96%, powder) (+)-sodium-L-ascorbate (≥99%), *N*,*N*-diisopropylcarbodiimide (99%), sodium nitrite), deuteriumoxide-d2 (99,8 atom %), sulfuric acid (95.0–97.0%), and 1-hydroxybenzotriazole (≥97%) were purchased from Sigma-Aldrich. *N*,*N*-Diisopropylethylamine (DIPEA) (≥99%) and potassium hydroxide (≥85%) were purchased from Carl Roth. Methanol (100%), D-galactose (≥99%), ethyl acetate (>99.9%), *n*-hexane (≥99.8%), and acetic anhydride (99.7%) were purchased from VWR BDH Prolabo Chemicals. *N*,*N*-Dimethylformamide (DMF) (99.8%, for peptide synthesis), piperidine (99%), sodium methoxide (97%), sodium diethyldithiocarbamate (99%), copper(II)sulfate (98%), and sodium azide (≥97%) were purchased from Acros Organics. D-Mannose (≥98%) was purchased from Merck. Dichloromethane (DCM) (99.9%), triethyl silane (≥98%), trifluoroacetic acid (≥99,0%), and benzotriazole-1-yl-oxy-tris-pyrrolidino-phosphonium (PyBOP) were purchased from Iris Biotech GmbH. Methyl-α-D-mannopyranoside (>99%) was purchased from Cytiva. Ethanol (>99.9%) was purchased from Chemsolute. Concanavalin A (highly purified, power) was purchased from MP Biomedicals. Lectin from *Ricinus communis* agglutinin (RCA_{120}) was purchased from BIOZOL. The anion resin (AG1-X8, quaternary ammonium, 100–200 mesh, acetate form) was purchased from Bio-Rad. 2-(7-Amino-2-oxo-2H-chromen-4-yl) acetic acid (97%) was purchased from BLDPharm. TentaGel resin was purchased from Rapp Polymere. Water/H_2O used here is ultra pure water, drawn from a Milli-Q water purification system.

Nuclear Magnetic Resonance Spectroscopy (NMR)

^1H NMR and ^{13}C NMR spectra were recorded on a Bruker Avance III 300. Chemical shifts were reported as delta (δ) in parts per million (ppm) and coupling constants as J in Hertz (Hz). Multiplicities are stated as follows: s = singlet, d = doublet, t = triplet, q = quartet, m = multiple.

High-Resolution Mass Spectrometry (HR-MS)

HR-MS measurements were conducted on a Bruker UHR-QTOF maXis 4G with a direct inlet via syringe pump, an ESI source, and a quadrupole time-of-flight (QTOF) analyzer. Samples were dissolved in water at a concentration of 1 mg/mL.

Matrix-Assisted Laser Desorption Ionization Time-of-Flight (MALDI-TOF) Mass Spectrometry (MALDI-TOF-MS)

MALDI-TOF measurements were conducted on an Ultraflex I instrument from Bruker Daltonics. The samples were measured in linear mode with cyano-4-hydroxycinnamic acid (HCCA) as matrix in a ratio of 1:2. As a solvent, H_2O/MeCN(1:1) or lectin-binding buffer (LBB) was used.

Reversed-Phase High-Pressure Liquid Chromatography (RP-HPLC)

RP-HPLC was performed with an Agilent 1260 Infinity instrument coupled to a variable wavelength detector (VWD) set to 214 nm. As a

https://doi.org/10.1021/acs.bioconjchem.5c00613
Bioconjugate Chem. XXXX, XXX, XXX–XXX

column, a Poroshell 120 EC-C18 1.8 μM (3.0 × 50 mm, 2.5 μM) reversed-phase column was used. Mobile phase A consisted of 95 vol %/5 vol% H_2O/MeCN with 0.1 vol% formic acid, and mobile phase B consisted of 95 vol%/5 vol% MeCN/H_2O with 0.1 vol% formic acid. The flow rate for all measurements was 0.4 mL/min

Synthesis of Building Blocks for Solid-Phase Synthesis

The building blocks TDS (triple-bond diethylenetriamine succinic acid), Man-N_3 (tetra-*O*-acetyl-azidoethyl-α-d-mannopyranoside) , and Gal-N_3 (tetra-*O*-acetyl-azidoethyl-β-d-galactopyranoside) were synthesized following previously published protocols.[65,85,86]

Synthesis of Azidocoumarin (AzC)

First, 650 mg (2.97 mmol) of 7-amino-4-carboxymethylcoumarin was dissolved in 80 mL of distilled water. The solution was cooled in an ice bath for approximately 20 min. While maintaining the temperature in the ice bath, 20 mL of concentrated sulfuric acid was added dropwise over a period of 10 min using a dropping funnel. In parallel, 308 mg (4.45 mmol) of sodium nitrite was dissolved in 20 mL of ice-cold distilled water. This solution was then added dropwise to the reaction mixture over a period of 10 min. The mixture was stirred for another 10 min on ice. Then, 1.2 g (17.8 mmol) of sodium azide was dissolved in 20 mL of ice-cold distilled water and added dropwise to the reaction mixture over a period of 20 min (caution: foam formation). The reaction mixture was stirred for 12 h at room temperature. Afterward, the reaction mixture was diluted with distilled water and extracted 5 times with 100 mL of ethyl acetate. The combined organic phases were washed with a solution of saturated sodium chloride and dried over sodium sulfate. The solvent was removed under reduced pressure, and the product remained as a yellow solid.

General Procedure for Solid-Phase Synthesis

AzC glycan PAL probes were synthesized using solid-phase synthesis with the Fmoc-standard protocol. TentaGel S-RAM (0.23 mmol/g) was used as the solid phase. The batch size for each glycooligomer was 0.1 mmol.

Coupling and Fmoc Deprotection

First the resin was swollen 2 times in DCM for 15 min. The swollen resin was then washed 3 times with DMF. Fmoc deprotection was performed using 5 mL of 25 vol% piperidine in DMF. Deprotection was carried out 3 times (2 x for 10 min, 1 x for 20 min). After deprotection, the resin was washed 10 times with DMF. Then, the TDS building block was coupled to the deprotected amine using a solution of 5 eq. building block, 5 eq. PyBOP, and 10 eq. DIPEA in DMF for 1 h. Following the coupling reaction, the resin was washed 10 times with DMF to remove excess reagents.

Copper(I)-Catalyzed Alkyne−Azide Cycloaddition (CuAAC)

Glycoconjugation to the TDS backbone was performed using CuAAC. For this purpose, 2.5 eq. of acetylated Man-N_3 (or Gal-N_3) was dissolved in 4 mL of DMF. Separately, 1.25 eq. of sodium ascorbate and 1.25 eq. of copper sulfate were each dissolved in 0.25 mL of ultra pure H_2O. First, the copper sulfate solution was drawn into a syringe, followed by the carbohydrate solution, and finally the sodium ascorbate solution. The syringe reactor was wrapped in aluminum foil to protect it from light and shaken overnight at room temperature. Following the reaction, the resin was washed extensively with a 23 mM solution of sodium diethyl thiocarbamate in DMF/H_2O (1:1, v/v) until the washing solution was colorless, indicating that thecopper had been fully removed. Final washes were performed with DCM to ensure complete removal of any remaining reagents.

Removing Acetyl Protection Groups from Carbohydrates

After successful conjugation, the acetyl groups were removed by incubating the resin in a solution of 0.2 M sodium methanolate in methanol for 1 h. Subsequently, the resin was washed 5 times with methanol, 5 times with DCM, and 5 times with DMF.

Conjugation of Azidocoumarin

After carbohydrate conjugation and acetyl deprotection, the azidocoumarin building block was coupled to the N-terminus. 5 eq. AzC building block, 5 eq. HOBt, and 5 eq. DIC were dissolved in DMF and coupled for 1 h. The reactor was wrapped in aluminum foil to protect it from light. Subsequently, the resin was washed 10 times with DCM and 10 times with DMF.

Cleavage from the Resin

After completion of the synthesis, the final structures were cleaved off the resin using a cleavage cocktail consisting of 95 vol% TFA, 2.5 vol% TIPS, and 2.5 vol% DCM. The resin was shaken for 1 h at room temperature. Following cleavage, the reaction mixture was poured into 45 mL of ice-cold diethyl ether. The resulting precipitate was collected by centrifugation, and the supernatant was decanted. The crude product was dried under a gentle stream of nitrogen. Subsequently the solid was dissolved in 5 mL of H_2O and lyophilized using an Alpha 1−4 LD plus instrument (Martin Christ Freeze-Dryers GmbH) at a pressure of 0.1 mbar.

Irradiation Experiments

For the general irradiation experiments, equimolar amounts of lectin and AzC glycan PAL probe were mixed in lectin-binding buffer (LBB) (10 mM HEPES, 50 mM NaCl, 1 mM $MnCl_2$, 1 mM $CaCl_2$, pH 7.4). The total reaction volumes varied between 25 and 200 μL, depending on the specific experimental setup. Prior to irradiation, the samples were incubated for 20 min at room temperature to allow binding of the carbohydrate to the respective target. Irradiation was carried out using either a UV-LED Spot P standard at 365 nm (Opsytec Dr. Gröbel GmbH) or a Vilber Biolink blx-365. For quantifying the fluorescence gain at various irradiation time points to assess the photoreaction kinetics, the energy was set to 1 J/cm^2 per 3 min.

General Procedure or Irradiation Experiments

Con A (20 μM, 1 eq.) and AzC probes (20 μM, 1 eq.) were mixed in equal volume (1:1, v/v) and incubated for 20 min prior to irradiation, which was then performed as previously described.

Competition Assays with Carbohydrates

100 μL of Con A (20 μM, 1 eq.) and 5 μL of carbohydrate (16 mM, 40 eq.) were mixed and incubated for 20 min. Afterward, 100 μL of AzC probe (20 μM, 1 eq.) was added and incubated for further 20 min prior to irradiation, which was then performed as previously described.

Competition Assays with BSA

50 μL of Con A (20 μM, 0.5 eq.) and 50 μL of BSA (20 μM, 0.5 eq.) were mixed and incubated for 20 min. Afterward, 100 μL of AzC probe (40 μM, 1 eq.) was added and incubated for further 20 min prior to irradiation, which was then performed as previously described.

ConA- and BSA-Fluorescence Measurements

100 μL of ConA (20 μM) or 100 μL of BSA (20 μM) were mixed with 100 μL of AzC probe and incubated for 20 min following the irradiation process as described. Furthermore, a mixture of 50 μL of ConA (40 μM) and 50 μL of BSA (40 μM) was prepared and incubated for 20 min. Then, 100 μL of AzC probe was added and incubated for further 20 min following the irradiation process as described. Unbound probes were separated using a centrifugal concentrator (MWCO 1000 Da), and the remaining sample was lyophilized. The samples were resuspended in LBB, and fluorescence measurements at 450 nm were performed on a CLARIOstar microplate reader (BMG LABTECH) at ambient temperature. Data were evaluated using BMG Mars software. Quadruplicates of all samples were measured in 384 black-well plates from Greiner BIO-ONE. Welch's T-test (not assuming equal variance) was performed for maximum robustness. P-values were calculated for each incubation condition compared to the respective vehicle control within each group (I, II, II) of the experiment. Analysis ToolPak was used to perform *t*-test evaluation.

https://doi.org/10.1021/acs.bioconjchem.5c00613
Bioconjugate Chem. XXXX, XXX, XXX−XXX

Absorption and Fluorescence Measurements

AzC was dissolved in acetonitrile/water 1:1 to a final concentration of 2 mM, and UV absorption and fluorescence spectra were measured on a CLARIOstar microplate reader (BMG LABTECH) at ambient temperature prior to irradiation. Subsequently, the sample was irradiated at 365 nm for 1, 10, 15, 30, and 60 min. Fluorescence spectra were measured after each time point, and the samples were analyzed by RP-HPLC to check for photoactivation and decomposition. Nonirradiated aminocoumarin (2 mM in acetonitrile/water 1:1) was used as a control in UV and fluorescence measurements.

pH-Dependent Fluorescence Measurements

100 μL of ConA (20 μM) was mixed with 100 μL of AzC probe (20 μM) and incubated for 20 min following the irradiation process as described. Unbound probes were separated by using a centrifugal concentrator (MWCO 1000 Da) and then lyophilized. The samples were resuspended in 40 μL of H_2O and divided into four parts of 10 μL each. 90 μL of LBB solution with pH values adjusted to 7, 8, 9, and 10 was added to each sample. The entire procedure was repeated for the pH values of 4, 5, and 6. All solutions were added to the plate as technical triplicates of 30 μL each. The samples were incubated for 1h before fluorescence was measured at 450 nm on a CLARIOstar microplate reader (BMG LABTECH) at ambient temperature.

Concentration-Dependent Fluorescence Measurements

100 μL of ConA (20 μM) were mixed with 100 μL of AzCMan (at 20, 10, 5, 2, 1, and 0.5 μM) or 100 μL of AzCGal (20, 40, 80, 200, 500, and 1000 μM) and incubated for a further 20 min following the irradiation process as described. Unbound probes were separated using a centrifugal concentrator (MWCO 1000 Da) and then lyophilized. The samples were resuspended in a final volume of 200 μL of LBB. Fluorescence was measured at 450 nm as technical quadruplicates using a CLARIOstar microplate reader (BMG LABTECH) at ambient temperature.

Statistical Analysis LOD

The limit of detection was calculated as LOD = $3\sigma/S$, where σ represents the standard deviation of the blank measurement and S represents the linear scope. The LOD was calculated in a range of 0−5 μM using 6 values.

General SDS−PAGE Procedure

SDS−PAGE was performed in an electrophoresis chamber. 4−20% Mini-PROTEAN TGX Precast Protein Gels, 12 or 15 wells (Bio-Rad), were used with Tris/glycine/SDS as running buffer. Samples were mixed with 4× Laemmli buffer and then denatured at 75 °C for 10 min prior to application to the gel. Proteins were separated over 35 min at 200 V and 300 mA. Precision Plus Protein Kaleidoscope Prestained Protein Standard (Bio-Rad) or Dual Xtra standard protein ladder (Bio-Rad) was used as molecular weight reference. Gels and Western blots were analyzed using an Amersham ImageQuant 800 (Cytiva). After detecting AzC fluorescence, gels were stained with a total protein Coomassie blue stain and destained until no background was visible. Subsequently, gels were analyzed in the imager OD mode with the following exposure settings: colorimetric, automatic, and binning 1 × 1. The exposure time was determined automatically. Blots were stained with India Ink unless stated otherwise and washed multiple time with H_2O before imaging.

Duration of Irradiation Measurements

Con A (15 μL, 20 μM) and AzCMan (15 μL, 20 μM) were mixed and incubated for 20 min. The samples were then irradiated for 2, 5, 10, 15, 20, 30, and 60 min at a wavelength of 365 nm using a Vilber Biolink blx-365 with 1 J/cm^2 per 3 min and subsequently analyzed by SDS−PAGE. Gels were analyzed for fluorescence activity and subsequently Coomassie-stained. Using Bio-Rad Image lab software, "adjusted volumes" (background-subtracted intensity values) were calculated. All fluorescence intensities were calculated in a rectangle (17.86 mm^2) around the gel band. The same method was used to generate the respective absorption intensities from the Coomassie-stained gel (using identical rectangles of 17.55 mm^2). The calculated fluorescence values were divided by the values for Coomassie absorption of the same band to control for loading differences. These resulting values were normalized to the untreated control, which did not contain any probe.

Selective Binding of AzC Probes to Lectins ConA and RCA_{120}

10 μL of each AzC probe (50 μM each) was mixed with 10 μL of either ConA (50 μM) or RCA_{120} (50 μM) in a total volume of 80 μL of LBB. The mixture was incubated at room temperature for 20 min, followed by irradiation at 365 nm in a Vilber Biolink blx-365 for 15 min. The samples were subsequently mixed with 4× Laemmli buffer, and the proteins were denatured at 70 °C for 15 min, followed by separation via SDS−PAGE. After measuring in-gel fluorescence, the gels were stained with Coomassie.

Selective ConA Binding of AzCMan Probes in Cell Lysate Background

MDA-MB231 whole cell lysate was purchased from Santa Cruz Biotechnology (sc-2232). 20 μL of cell lysate (stock 2.5 mg/mL) was mixed with 5 μL of ConA (5 mg/mL), 10 μL of AzC probe (50 mM stock), and 45 μL of LBB. The mixture was incubated for 20 min, followed by 15 min irradiation at 365 nm using a Vilber Biolink blx-365. Afterward, 4× Laemmli buffer was added to the samples and the proteins were separated by SDS−PAGE. After measuring in-gel fluorescence, the gel was stained with Coomassie.

Testing AzC Probes in Native Rat Kidney Lysate

Fresh-frozen slices of rat kidney were lysed by two-step homogenization in IP buffer (25 mM Tris−HCl, pH 7.4, 150 mM NaCl, 1 mM EDTA, 1% NP-40) containing protease inhibitors. Slices (176 mg) were lysed in buffer (1.8 mL) and divided into three portions of 600 μL each. Each step contained homogenization/disruption in a bead mill (TissueLyser LT, Qiagen) at 50 Hz for 5 min, using a steel ball in a 2 mL protein low-bind reaction tube, followed by 10 min centrifugation at 15k × g and treatment in a sonication bath for 5 min. After each cycle, the supernatant was removed and collected. All samples were kept on ice for the whole procedure. The lysate was checked via SDS−PAGE and Coomassie staining, and equal concentrations were used for native binding experiments. Animals were originally processed for other experiments, and surplus lysates were used in these procedures. All animals were kept in accordance and with approval of the German animal welfare authorities (reference number HHU/O10/87).

For native binding experiments, the following mixtures were prepared. In a total volume of 70 μL of LBB, 30 μL of native rat kidney lysate (1 mg/mL) was mixed with 4 μL of either AzCGal or AzCMan (500 μM each) in the absence or presence of an excess of the respective carbohydrate inhibitors D-Gal or α-MeMan (20 μL of a 500 μM stock). The mixtures were incubated for 20 min, followed by 15 min of irradiation at 365 nm using a Vilber Biolink blx-365. Afterward, 4× Laemmli buffer was added to the samples, and the proteins were separated by SDS−PAGE. Proteins were transferred to an Immobilon-FL PVDF membrane (pore size: 0.45 μm, Millipore) using a Trans-Blot Turbo Transfer System (Bio-Rad). After measuring fluorescence as detailed above the membrane was stained with India Ink.

Testing AzC Probes on Cells

MDA-MB-231 cells were purchased from the German Collection of Microorganisms and Cell Cultures GmbH of the Leibniz Institute DSMZ (ACC 732).

Cells were cultured according to standard protocols using RPMI-1640 medium supplemented with 10% fetal calf serum and 1% penicillin/streptomycin. Cells were incubated at 37 °C with 5% CO_2. For testing AzCMan cross-linking, cells were seeded into μ-Slide 8-well chambers at a density of approximately 20,000 cells per well, followed by incubation at 37 °C and 5% CO_2 over 2 days to allow attachment of the cells to the slides. The medium was then removed, and cells were washed 3 times with 150 μL of PBS buffer. Cells were fixed by treating them with 100 μL of ice-cold methanol for 3−5 min.

https://doi.org/10.1021/acs.bioconjchem.5c00613
Bioconjugate Chem. XXXX, XXX, XXX−XXX

Subsequently, cells were washed 3 times with 150 μL of PBS and then covered with 100 μL of PBS. 20 μL of a 60 μM stock solution of AzC probe in LBB was added to give a final concentration of 10 μM. Plates were gently mixed for 2 min and then incubated for 20 min to allow the probe to interact with Man-binding proteins. Then, each well was irradiated successively for 15 min using a UV-LED Spot P standard at 365 nm (Opsytec Dr. Gröbel GmbH) at a power of 100%. Before imaging, each well was washed 2 times with 150 μL of PBS. Fluorescence microscopy was performed on an Olympus IX73 microscope using a 60× oil objective (Gain 300; Exposure 40). For the preparation of the inactivated negative control, 30 μL of AzCMan (60 μM) was irradiated prior to incubation with the cells.

■ ASSOCIATED CONTENT

Supporting Information

The Supporting Information is available free of charge at https://pubs.acs.org/doi/10.1021/acs.bioconjchem.5c00613.

Analytical data for the synthesized structures, additional data and figures showing the absorption and fluorescence spectra of AzC building blocks, full MALDI-TOF-MS and full fluorescence spectra, additional fluorescence spectra for the pH-stability study, additional SDS–PAGE images of irradiated and not irradiated lysates, and additional fluorescence microscopy images (PDF)

■ AUTHOR INFORMATION

Corresponding Authors

Ulla I.M. Gerling-Driessen − *Institute for Macromolecular Chemistry, Albert Ludwig University of Freiburg, 79104 Freiburg, Germany;* orcid.org/0000-0003-0366-0488; Email: ulla.gerling-driessen@makro.uni-freiburg.de

Laura Hartmann − *Department of Organic and Macromolecular Chemistry, Heinrich Heine University Duesseldorf, 40225 Duesseldorf, Germany; Institute for Macromolecular Chemistry, Albert Ludwig University of Freiburg, 79104 Freiburg, Germany; Freiburg Center of Interactive Materials and Bioinspired Technologies (FIT), 79110 Freiburg, Germany; Freiburg Materials Research Center (FMF), 79104 Freiburg, Germany;* orcid.org/0000-0003-0115-6405; Email: laura.hartmann@makro.uni-freiburg.de

Authors

Nina Jahnke − *Department of Organic and Macromolecular Chemistry, Heinrich Heine University Duesseldorf, 40225 Duesseldorf, Germany*

Marc D. Driessen − *Faculty of Medicine and University Hospital Cologne, Department of Oral, Maxillofacial and Plastic Surgery, University of Cologne, 50937 Cologne, Germany;* orcid.org/0000-0002-7530-782X

Georgia Partalidou − *Institute for Macromolecular Chemistry, Albert Ludwig University of Freiburg, 79104 Freiburg, Germany;* orcid.org/0009-0006-7648-2685

Simon Przetak − *Department of Organic and Macromolecular Chemistry, Heinrich Heine University Duesseldorf, 40225 Duesseldorf, Germany*

Complete contact information is available at: https://pubs.acs.org/10.1021/acs.bioconjchem.5c00613

Author Contributions

#N.J. and M.D.D. contributed equally to this work.

Notes

The authors declare no competing financial interest.

■ ACKNOWLEDGMENTS

We acknowledge the support of the German Research Foundation (DFG) within the Collaborative Research Center 1208 “Identity and Dynamics of Membrane Systems”.

■ REFERENCES

(1) Jayachandran, B.; Parvin, T. N.; Alam, M. M.; Chanda, K.; Mm, B. Insights on Chemical Crosslinking Strategies for Proteins. *Molecules* **2022**, *27*, 8124.

(2) Liu, J.; Yang, B.; Wang, L. Residue selective crosslinking of proteins through photoactivatable or proximity-enabled reactivity. *Curr. Opin. Chem. Biol.* **2023**, *74*, No. 102285.

(3) Kotzyba-Hibert, F.; Kapfer, I.; Goeldner, M. Recent trends in photoaffinity labeling. *Angew. Chem., Int. Ed.* **1995**, *34*, 1296−1312.

(4) Bayley, H.; Knowles, J. R. Photoaffinity labeling. *Methods Enzymol.* **1977**, *46*, 69−114.

(5) Yu, S.-H.; Wands, A. M.; Kohler, J. J. Photoaffinity probes for studying carbohydrate biology. *J. Carbohydr. Chem.* **2012**, *31*, 325−352.

(6) Dorman, G.; Nakamura, H.; Pulsipher, A.; Prestwich, G. D. The life of pi star: exploring the exciting and forbidden worlds of the benzophenone photophore. *Chem. Rev.* **2016**, *116*, 15284−15398.

(7) Galardy, R. E.; Craig, L. C.; Jamieson, J. D.; Printz, M. P. Photoaffinity labeling of peptide hormone binding sites. *J. Biol. Chem.* **1974**, *249*, 3510−3518.

(8) Fleet, G.; Porter, R.; Knowles, J. Affinity labelling of antibodies with aryl nitrene as reactive group. *Nature* **1969**, *224*, 511−512.

(9) Kym, P. R.; Carlson, K. E.; Katzenellenbogen, J. A. Evaluation of a highly efficient aryl azide photoaffinity labeling reagent for the progesterone receptor. *Bioconjugate Chem.* **1995**, *6*, 115−122.

(10) Smith, R. A.; Knowles, J. R. Aryldiazirines. Potential reagents for photolabeling of biological receptor sites. *J. Am. Chem. Soc.* **1973**, *95*, 5072−5073.

(11) Mishra, P. K.; Yoo, C. M.; Hong, E.; Rhee, H. W. Photo-crosslinking: an emerging chemical tool for investigating molecular networks in live cells. *ChemBioChem.* **2020**, *21*, 924−932.

(12) Leyva, E.; Platz, M. S.; Persy, G.; Wirz, J. Photochemistry of phenyl azide: the role of singlet and triplet phenylnitrene as transient intermediates. *J. Am. Chem. Soc.* **1986**, *108*, 3783−3790.

(13) Walrant, A.; Sachon, E. Photoaffinity labeling coupled to MS to identify peptide biological partners: Secondary reactions, for better or for worse? *Mass Spectrom. Rev.* **2025**, *44*, 715−756.

(14) Murale, D. P.; Hong, S. C.; Haque, M. M.; Lee, J. S. Photo-affinity labeling (PAL) in chemical proteomics: a handy tool to investigate protein-protein interactions (PPIs). *Proteome Sci.* **2017**, *15*, 14.

(15) Liang, T. Y.; Schuster, G. B. Photochemistry of 3- and 4-nitrophenyl azide: detection and characterization of reactive intermediates. *J. Am. Chem. Soc.* **1987**, *109*, 7803−7810.

(16) Wentrup, C. Nitrenes, carbenes, diradicals, and ylides. Interconversions of reactive intermediates. *Acc. Chem. Res.* **2011**, *44*, 393−404.

(17) Chowdhry, V.; Westheimer, F. Photoaffinity labeling of biological systems. *Annu. Rev. Biochem.* **1979**, *48*, 293−325.

(18) Wu, H.; Kohler, J. Photocrosslinking probes for capture of carbohydrate interactions. *Curr. Opin. Chem. Biol.* **2019**, *53*, 173−182.

(19) Jahn, O.; Eckart, K.; Tezval, H.; Spiess, J. Characterization of peptide−protein interactions using photoaffinity labeling and LC/MS. *Anal. Bioanal. Chem.* **2004**, *378*, 1031−1036.

(20) Robinette, D.; Neamati, N.; Tomer, K. B.; Borchers, C. H. Photoaffinity labeling combined with mass spectrometric approaches as a tool for structural proteomics. *Expert review of proteomics* **2006**, *3*, 399−408.

(21) Tulloch, L. B.; Menzies, S. K.; Fraser, A. L.; Gould, E. R.; King, E. F.; Zacharova, M. K.; Florence, G. J.; Smith, T. K. Photo-affinity

labelling and biochemical analyses identify the target of trypanocidal simplified natural product analogues. *PLoS Neglected Tropical Diseases* **2017**, *11*, No. e0005886.
(22) Smith, E.; Collins, I. Photoaffinity labeling in target-and binding-site identification. *Future medicinal chemistry* **2015**, *7*, 159−183.
(23) Park, J.; Koh, M.; Koo, J. Y.; Lee, S.; Park, S. B. Investigation of specific binding proteins to photoaffinity linkers for efficient deconvolution of target protein. *ACS Chem. Biol.* **2016**, *11*, 44−52.
(24) Wagner, S.; Hauck, D.; Hoffmann, M.; Sommer, R.; Joachim, I.; Müller, R.; Imberty, A.; Varrot, A.; Titz, A. Covalent Lectin Inhibition and Application in Bacterial Biofilm Imaging. *Angew. Chem., Int. Ed.* **2017**, *56*, 16559−16564.
(25) Wang, Y.; Torres-García, D.; Mostert, T. P.; Reinalda, L.; Van Kasteren, S. I. A Bioorthogonal Dual Fluorogenic Probe for the Live-Cell Monitoring of Nutrient Uptake by Mammalian Cells. *Angew. Chem., Int. Ed.* **2024**, *63*, No. e202401733.
(26) Yu, A.; He, X.; Shen, T.; Yu, X.; Mao, W.; Chi, W.; Liu, X.; Wu, H. Design strategies for tetrazine fluorogenic probes for bioorthogonal imaging. *Chem. Soc. Rev.* **2025**, *54*, 2984.
(27) Jeong, H.; Wu, X.; Lee, J.-S.; Yoon, J. Recent advances in enzyme-activated NIR fluorescent probes for biological applications. *TrAC Trends in Analytical Chemistry* **2023**, *168*, No. 117335.
(28) Cosco, E. D.; Bogyo, M. Recent advances in ratiometric fluorescence imaging of enzyme activity in vivo. *Curr. Opin. Chem. Biol.* **2024**, *80*, No. 102441.
(29) Scott, J. I.; Deng, Q.; Vendrell, M. Near-infrared fluorescent probes for the detection of cancer-associated proteases. *ACS Chem. Biol.* **2021**, *16*, 1304−1317.
(30) Saleem, M.; Hanif, M.; Bonne, S.; Zeeshan, M.; Khan, S.; Rafiq, M.; Tahir, T.; Lu, C.; Cai, R. Turn-On Fluorescence Probe for Cancer-Related γ-Glutamyltranspeptidase Detection. *Molecules* **2024**, *29*, 4776.
(31) Tsao, K. K.; Imai, S.; Chang, M.; Hario, S.; Terai, T.; Campbell, R. E. The best of both worlds: Chemigenetic fluorescent sensors for biological imaging. *Cell Chemical Biology* **2024**, *31*, 1652−1664.
(32) Nadal-Bufi, F.; Salomon, P. L.; de Moliner, F.; Sarris, K. A.; Wang, Z.; Wills, R. D.; Marin, V. L.; Shi, X.; Zhou, K.; Wang, Z.; Xu, Z.; McPherson, M. J.; Marvin, C. C.; Hobson, A. D.; Vendrell, M. Fluorogenic Platform for Real-Time Imaging of Subcellular Payload Release in Antibody−Drug Conjugates. *J. Am. Chem. Soc.* **2025**, *147*, 7578−7587.
(33) Kellner, S.; Seidu-Larry, S.; Burhenne, J.; Motorin, Y.; Helm, M. A multifunctional bioconjugate module for versatile photoaffinity labeling and click chemistry of RNA. *Nucleic Acids Res.* **2011**, *39*, 7348−7360.
(34) Morimoto, S.; Tomohiro, T.; Maruyama, N.; Hatanaka, Y. Photoaffinity casting of a coumarin flag for rapid identification of ligand-binding sites within protein. *Chem. Commun.* **2013**, *49*, 1811−1813.
(35) Tomohiro, T.; Yamamoto, A.; Tatsumi, Y.; Hatanaka, Y. [3-(Trifluoromethyl)-3 H-diazirin-3-yl] coumarin as a carbene-generating photocross-linker with masked fluorogenic beacon. *Chem. Commun.* **2013**, *49*, 11551−11553.
(36) Singha, M.; Roy, S.; Pandey, S. D.; Bag, S. S.; Bhattacharya, P.; Das, M.; Ghosh, A. S.; Ray, D.; Basak, A. Use of azidonaphthalimide carboxylic acids as fluorescent templates with a built-in photoreactive group and a flexible linker simplifies protein labeling studies: applications in selective tagging of HCAII and penicillin binding proteins. *Chem. Commun.* **2017**, *53*, 13015−13018.
(37) Képiró, M.; Várkuti, B. H.; Rauscher, A. A.; Kellermayer, M. S.; Varga, M.; Málnási-Csizmadia, A. Molecular tattoo: subcellular confinement of drug effects. *Chemistry & biology* **2015**, *22*, 548−558.
(38) Dai, S.-Y.; Yang, D. A visible and near-infrared light activatable diazocoumarin probe for fluorogenic protein labeling in living cells. *J. Am. Chem. Soc.* **2020**, *142*, 17156−17166.
(39) Bousch, C.; Vreulz, B.; Kansal, K.; El-Husseini, A.; Cecioni, S. Fluorogenic Photo-Crosslinking of Glycan-Binding Protein Recognition Using a Fluorinated Azido-Coumarin Fucoside. *Angew. Chem., Int. Ed.* **2023**, *62*, No. e202314248.
(40) Vreulz, B.; De Crozals, D.; Cecioni, S. A trifunctional probe for generation of fluorogenic glycan-photocrosslinker conjugates. *RSC chemical biology* **2025**, *6*, 1779−1786.
(41) Brown, S. A. *Biochemistry of The Coumarins*, in Biochemistry of Plant Phenolics, Swain, T.; Harbone, J. B.; Van Sumere, C. F., Eds., Springer US: Boston, MA, 1979; pp 249−286.
(42) Musa, M. A.; Cooperwood, J. S.; Khan, M. O. F. A review of coumarin derivatives in pharmacotherapy of breast cancer. *Curr. Med. Chem.* **2008**, *15* (26), 2664−2679.
(43) Stringlis, I. A.; de Jonge, R.; Pieterse, C. M. J. The Age of Coumarins in Plant−Microbe Interactions. *Plant Cell Physiol.* **2019**, *60*, 1405−1419.
(44) Sun, X.-y.; Liu, T.; Sun, J.; Wang, X.-j. Synthesis and application of coumarin fluorescence probes. *RSC Adv.* **2020**, *10*, 10826−10847.
(45) Tasior, M.; Kim, D.; Singha, S.; Krzeszewski, M.; Ahn, K. H.; Gryko, D. T. π-Expanded coumarins: synthesis, optical properties and applications. *Journal of Materials Chemistry C* **2015**, *3*, 1421−1446.
(46) Szwaczko, K. Coumarins synthesis and transformation via C−H bond activation—A review. *Inorganics* **2022**, *10*, 23.
(47) Kang, D.; Ahn, K.; Hong, S. Site-Selective C− H Bond Functionalization of Chromones and Coumarins. *Asian Journal of Organic Chemistry* **2018**, *7*, 1136−1150.
(48) Tod, M.; Prevot, M.; Poulou, M.; Farinotti, R.; Chalom, J.; Mahuzier, G. Chromatographic and luminescence properties of a 7-aminocoumarin derivative with peroxyoxalate chemiexcitation. *Anal. Chim. Acta* **1989**, *223*, 309−317.
(49) Murase, T.; Yoshihara, T.; Yamada, K.; Tobita, S. Fluorescent peptides labeled with environment-sensitive 7-aminocoumarins and their interactions with lipid bilayer membranes and living cells. *Bull. Chem. Soc. Jpn.* **2013**, *86*, 510−519.
(50) Nowakowska, M.; Smoluch, M.; Sendor, D. The effect of cyclodextrins on the photochemical stability of 7-amino-4-methyl-coumarin in aqueous solution. *J. Incl. Phenom. Macrocycl. Chem.* **2001**, *40*, 213−219.
(51) Raju, B. B.; Costa, S. M. Excited-state behavior of 7-diethylaminocoumarin dyes in AOT reversed micelles: size effects. *J. Phys. Chem. B* **1999**, *103*, 4309−4317.
(52) Gandioso, A.; Palau, M.; Bresolí-Obach, R.; Galindo, A.; Rovira, A.; Bosch, M.; Nonell, S.; Marchán, V. High photostability in nonconventional coumarins with far-red/NIR emission through azetidinyl substitution. *Journal of Organic Chemistry* **2018**, *83*, 11519−11531.
(53) Rovira, A.; Pujals, M.; Gandioso, A.; López-Corrales, M.; Bosch, M.; Marchán, V. Modulating photostability and mitochondria selectivity in far-red/NIR emitting coumarin fluorophores through replacement of pyridinium by pyrimidinium. *Journal of Organic Chemistry* **2020**, *85*, 6086−6097.
(54) Lord, S. J.; Lee, H.-l. D.; Samuel, R.; Weber, R.; Liu, N.; Conley, N. R.; Thompson, M. A.; Twieg, R. J.; Moerner, W. Azido push− pull fluorogens photoactivate to produce bright fluorescent labels. *J. Phys. Chem. B* **2010**, *114*, 14157−14167.
(55) De-La-Cuesta, J.; González, E.; Pomposo, J. A. Advances in fluorescent single-chain nanoparticles. *Molecules* **2017**, *22*, 1819.
(56) Sivakumar, K.; Xie, F.; Cash, B. M.; Long, S.; Barnhill, H. N.; Wang, Q. A fluorogenic 1, 3-dipolar cycloaddition reaction of 3-azidocoumarins and acetylenes. *Org. Lett.* **2004**, *6*, 4603−4606.
(57) Porell, R. N.; Follmar, J. L.; Purcell, S. C.; Timm, B.; Laubach, L. K.; Kozirovskiy, D.; Thacker, B. E.; Glass, C. A.; Gordts, P. L. S. M.; Godula, K. Biologically Derived Neoproteoglycans for Profiling Protein−Glycosaminoglycan Interactions. *ACS Chem. Biol.* **2022**, *17*, 1534−1542.
(58) Chalansonnet, V.; Lowe, J.; Orenga, S.; Perry, J. D.; Robinson, S. N.; Stanforth, S. P.; Sykes, H. E.; Truong, T. V. Fluorogenic 7-azidocoumarin and 3/4-azidophthalimide derivatives as indicators of reductase activity in microorganisms. *Bioorg. Med. Chem. Lett.* **2019**, *29*, 2354−2357.

https://doi.org/10.1021/acs.bioconjchem.5c00613
Bioconjugate Chem. XXXX, XXX, XXX−XXX

(59) Hill, S. A.; Gerke, C.; Hartmann, L. Recent Developments in Solid-Phase Strategies towards Synthetic, Sequence-Defined Macromolecules. *Chem.—Asian J.* **2018**, *13*, 3611−3622.
(60) Blawitzki, L.-C.; Bartels, N.; Bonda, L.; Schmidt, S.; Monzel, C.; Hartmann, L. Glycomacromolecules to Tailor Crowded and Heteromultivalent Glycocalyx Mimetics. *Biomacromolecules* **2024**, *25*, 5979−5994.
(61) Jäck, N.; Hemming, A.; Hartmann, L. Synthesis of Dual-Responsive Amphiphilic Glycomacromolecules: Controlled Release of Glycan Ligands via pH and UV Stimuli. *Macromol. Rapid Commun.* **2024**, *45*, No. 2400439.
(62) Hoffmann, M.; Snyder, N. L.; Hartmann, L. Glycosaminoglycan Mimetic Precision Glycomacromolecules with Sequence-Defined Sulfation and Rigidity Patterns. *Biomacromolecules* **2022**, *23*, 4004−4014.
(63) Păunescu, E.; Louise, L.; Jean, L.; Romieu, A.; Renard, P.-Y. A versatile access to new halogenated 7-azidocoumarins for photoaffinity labeling: Synthesis and photophysical properties. *Dyes Pigm.* **2011**, *91*, 427−434.
(64) Yang, Q.; Váňa, J.; Klán, P. The complex photochemistry of coumarin-3-carboxylic acid in acetonitrile and methanol. *Photochemical & Photobiological Sciences* **2022**, *21*, 1481−1495.
(65) Ponader, D.; Wojcik, F.; Beceren-Braun, F.; Dernedde, J.; Hartmann, L. Sequence-defined glycopolymer segments presenting mannose: synthesis and lectin binding affinity. *Biomacromolecules* **2012**, *13*, 1845−1852.
(66) Wojcik, F.; Lel, S.; O'Brien, A. G.; Seeberger, P. H.; Hartmann, L. Synthesis of homo-and heteromultivalent carbohydrate-functionalized oligo (amidoamines) using novel glyco-building blocks. *Beilstein journal of organic chemistry* **2013**, *9*, 2395−2403.
(67) Ponader, D.; Maffre, P.; Aretz, J.; Pussak, D.; Ninnemann, N. M.; Schmidt, S.; Seeberger, P. H.; Rademacher, C.; Nienhaus, G. U.; Hartmann, L. Carbohydrate-Lectin Recognition of Sequence-Defined Heteromultivalent Glycooligomers. *J. Am. Chem. Soc.* **2014**, *136*, 2008.
(68) Cummings, R. D. The mannose receptor ligands and the macrophage glycome. *Curr. Opin. Struct. Biol.* **2022**, *75*, No. 102394.
(69) Coombs, P. J.; Taylor, M. E.; Drickamer, K. Two categories of mammalian galactose-binding receptors distinguished by glycan array profiling. *Glycobiology* **2006**, *16*, 1C−7C.
(70) Weatherman, R. V.; Mortell, K. H.; Chervenak, M.; Kiessling, L. L.; Toone, E. J. Specificity of C-glycoside complexation by mannose/glucose specific lectins. *Biochemistry* **1996**, *35*, 3619−3624.
(71) Itakura, Y.; Nakamura-Tsuruta, S.; Kominami, J.; Sharon, N.; Kasai, K.-i.; Hirabayashi, J. Systematic Comparison of Oligosaccharide Specificity of Ricinus communis Agglutinin I and Erythrina Lectins: a Search by Frontal Affinity Chromatography†. *J. Biochem.* **2007**, *142*, 459−469.
(72) Wang, Y.; Yu, G.; Han, Z.; Yang, B.; Hu, Y.; Zhao, X.; Wu, J.; Lv, Y.; Chai, W. Specificities of Ricinus communis agglutinin 120 interaction with sulfated galactose. *FEBS Lett.* **2011**, *585*, 3927−3934.
(73) Bojar, D.; Meche, L.; Meng, G.; Eng, W.; Smith, D. F.; Cummings, R. D.; Mahal, L. K. A Useful Guide to Lectin Binding: Machine-Learning Directed Annotation of 57 Unique Lectin Specificities. *ACS Chem. Biol.* **2022**, *17*, 2993−3012.
(74) Maljaars, C. E. P.; Halkes, K. M.; de Oude, W. L.; Haseley, S. R.; Upton, P. J.; McDonnell, M. B.; Kamerling, J. P. Affinity Determination of Ricinus communis Agglutinin Ligands Identified from Combinatorial O- and S-,N-Glycopeptide Libraries. *J. Comb. Chem.* **2006**, *8*, 812−819.
(75) Schuster, G. B.; Platz, M. S. Photochemistry of phenyl azide. *Advances in photochemistry* **1992**, *17*, 69−143.
(76) Reddy, V. S.; Rao, V. Modes of binding of α (1−2) linked manno-oligosaccharides to concanavalin A. *Int. J. Biol. Macromol.* **1992**, *14*, 185−192.
(77) Jeyachandran, Y. L.; Mielczarski, J. A.; Mielczarski, E.; Rai, B. Efficiency of blocking of non-specific interaction of different proteins by BSA adsorbed on hydrophobic and hydrophilic surfaces. *J. Colloid Interface Sci.* **2010**, *341*, 136−142.
(78) Al-Husseini, J. K.; Stanton, N. J.; Selassie, C. R.; Johal, M. S. The binding of drug molecules to serum albumin: The effect of drug hydrophobicity on binding strength and protein desolvation. *Langmuir* **2019**, *35*, 17054−17060.
(79) Smith, E. A.; Thomas, W. D.; Kiessling, L. L.; Corn, R. M. Surface Plasmon Resonance Imaging Studies of Protein-Carbohydrate Interactions. *J. Am. Chem. Soc.* **2003**, *125*, 6140−6148.
(80) Parera Pera, N.; Branderhorst, H. M.; Kooij, R.; Maierhofer, C.; van der Kaaden, M.; Liskamp, R. M. J.; Wittmann, V.; Ruijtenbeek, R.; Pieters, R. J. Rapid Screening of Lectins for Multivalency Effects with a Glycodendrimer Microarray. *ChemBioChem.* **2010**, *11*, 1896−1904.
(81) Feldhof, M. I.; Sperzel, S.; Bonda, L.; Boye, S.; Braunschweig, A. B.; Gerling-Driessen, U. I. M.; Hartmann, L. Thiol-selective native grafting from polymerization for the generation of protein−polymer conjugates. *Chem. Sci.* **2024**, *15*, 16768−16777.
(82) Olmsted, I. R.; Kussrow, A.; Bornhop, D. J. Comparison of Free-Solution and Surface-Immobilized Molecular Interactions Using a Single Platform. *Anal. Chem.* **2012**, *84*, 10817−10822.
(83) Ramesh, D.; Srinivasan, M. Studies on ring opening of coumarins. *Curr. Sci.* **1984**, *53*, 369−371.
(84) Mała, P.; Siebs, E.; Meiers, J.; Rox, K.; Varrot, A.; Imberty, A.; Titz, A. Discovery of N-β-l-Fucosyl Amides as High-Affinity Ligands for the Pseudomonas aeruginosa Lectin LecB. *J. Med. Chem.* **2022**, *65*, 14180−14200.
(85) Hayes, W.; Osborn, H. M.; Osborne, S. D.; Rastall, R. A.; Romagnoli, B. One-pot synthesis of multivalent arrays of mannose mono-and disaccharides. *Tetrahedron* **2003**, *59*, 7983−7996.
(86) Wu, L.; Sampson, N. S. Fucose, Mannose, and β-N-Acetylglucosamine Glycopolymers Initiate the Mouse Sperm Acrosome Reaction through Convergent Signaling Pathways. *ACS Chem. Biol.* **2014**, *9*, 468−475.

https://doi.org/10.1021/acs.bioconjchem.5c00613
Bioconjugate Chem. XXXX, XXX, XXX−XXX

Azidocoumarin-glycan probes for photo-induced crosslinking and *in-situ* fluorescent labeling

Nina Jahnke[1a], Marc D. Driessen[2a], Georgia Partalidou[3], Simon Przetak[1], Ulla I.M. Gerling-Driessen[3], Laura Hartmann[1,3]**

[1] Department of Organic and Macromolecular Chemistry, Heinrich Heine University Duesseldorf, Universitaetsstrasse 1, 40225 Duesseldorf, Germany

[2] University of Cologne, Faculty of Medicine and University Hospital Cologne, Department of Oral, Maxillofacial and Plastic Surgery, Kerpener Str. 62, 50937 Cologne, Germany

[3] Institute for Macromolecular Chemistry, Albert Ludwig University of Freiburg, Stefan-Meier-Strasse 31, 79104 Freiburg, Germany

Email: ulla.gerling-driessen@makro.uni-freiburg.de, laura.hartmann@makro.uni-freiburg.de

[a] These authors contributed equally

Structural characterization

Azidocoumarin (AzC)

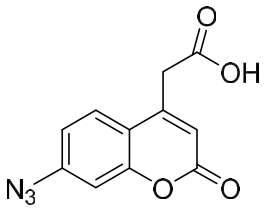

Molecular Weight: 245,19

^{1}H-NMR (300 MHz, DMSO-d_6) δ (ppm) 12.92 (s, 1H), 7.79 (dd, J = 8.5, 1.0 Hz, 1H), 7.26 (dd, J = 2.2, 1.0 Hz, 1H), 7.21 (dd, J = 8.5, 2.3, 1.0 Hz, 1H), 6.51 (d, J = 1.1 Hz, 1H), 3.97 (d, J = 1.2 Hz, 2H).

^{13}C-NMR (300 MHz, DMSO-*d6*): δ (ppm) 159,50 (C11), 154,00 (C1), 152,90 (C9), 143,26 (C3), 126,96 (C7), 124,16 (C5), 116,73 (C6), 115,53 (C4), 113,16 (C2), 106,78 (C8), 18,06 (C10)

RP-HPLC (5-95 Vol% t H_2O/acetonitrile in 17 min at 25°C, 214 nm): t_r = 8,1 min

ESI-MS calculated $[M+1H]^+$ 246,19, found $[M+1H]^+$ 246,3; $[M+1Na]^+$ 268,1; $[2M+1H]^+$ 513.0

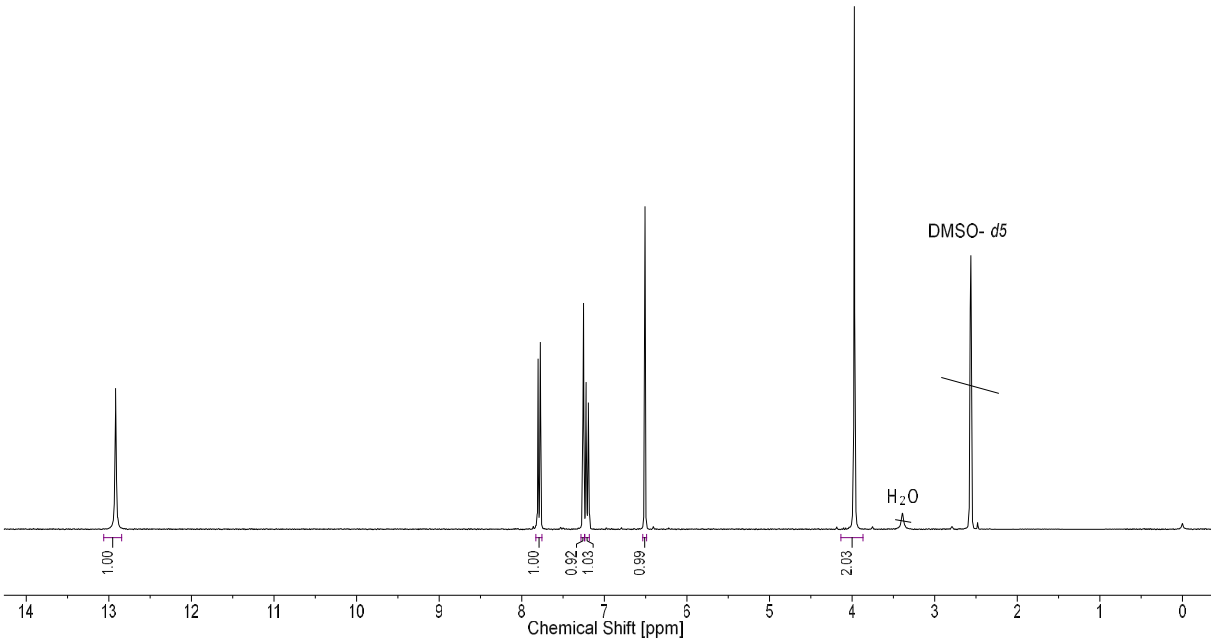

*Figure S 1: [1]H-NMR (300MHz) spectra of **AzC.***

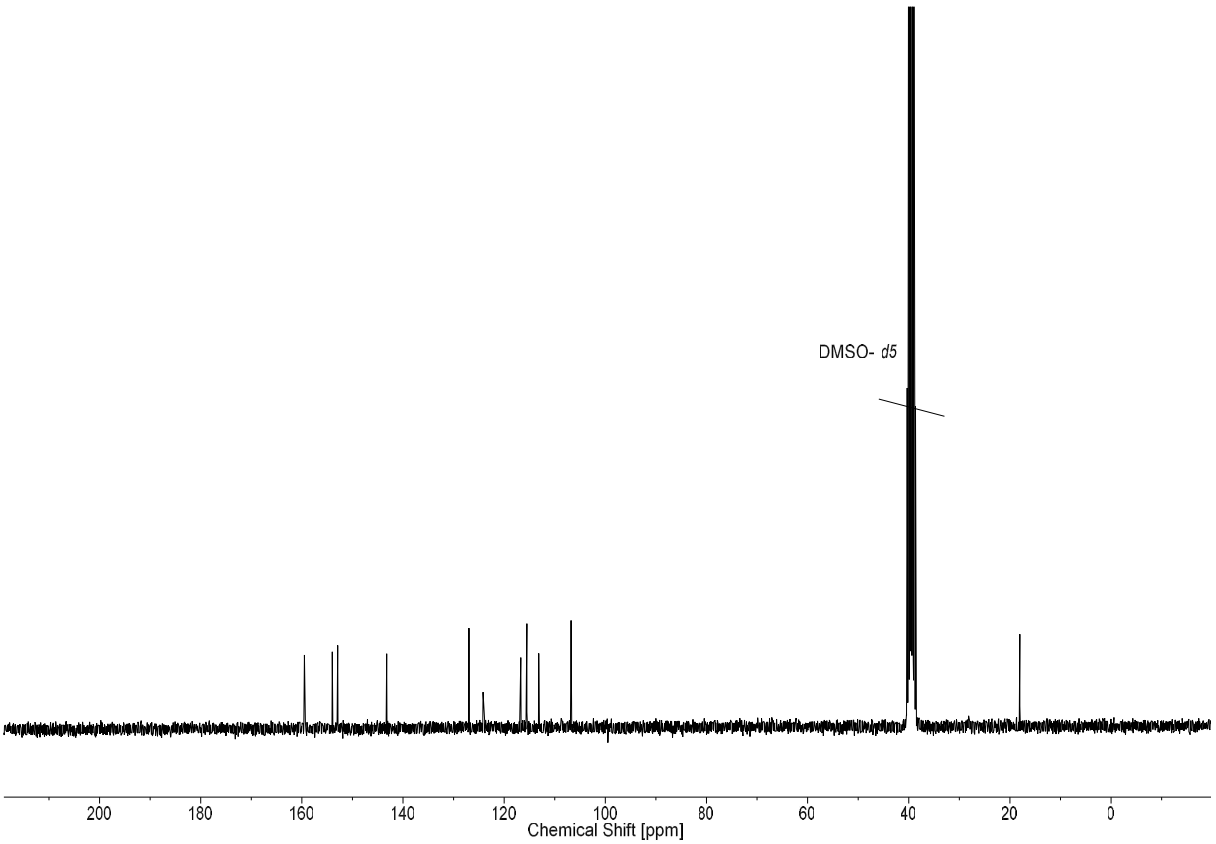

*Figure SI 2: [13]C-NMR (300MHz) spectra of **AzC.***

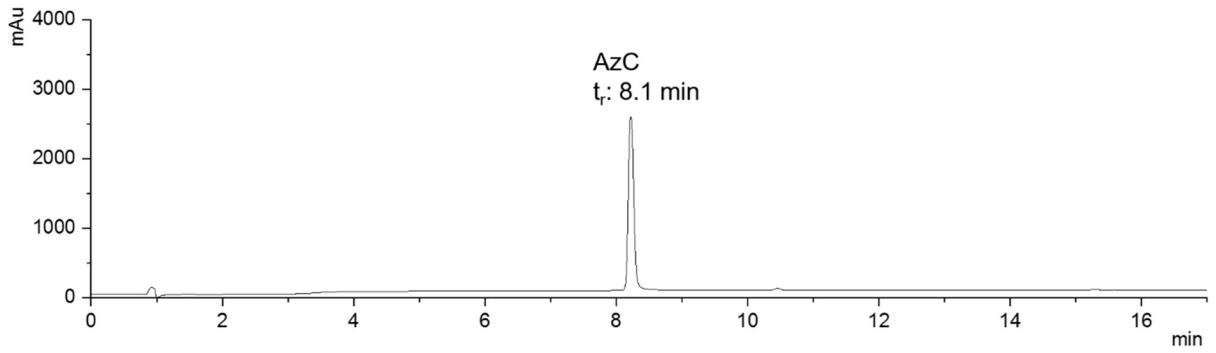

Figure S 3: ***AzC*** detected at t_r = 8,1 min with relative purity >95% by RP-HPLC (*linear gradient from 5-95* Vol% eluent H_2O/acetonitrile in 17 min at 25°C, VWDA1 A Wavelength = 214nm).

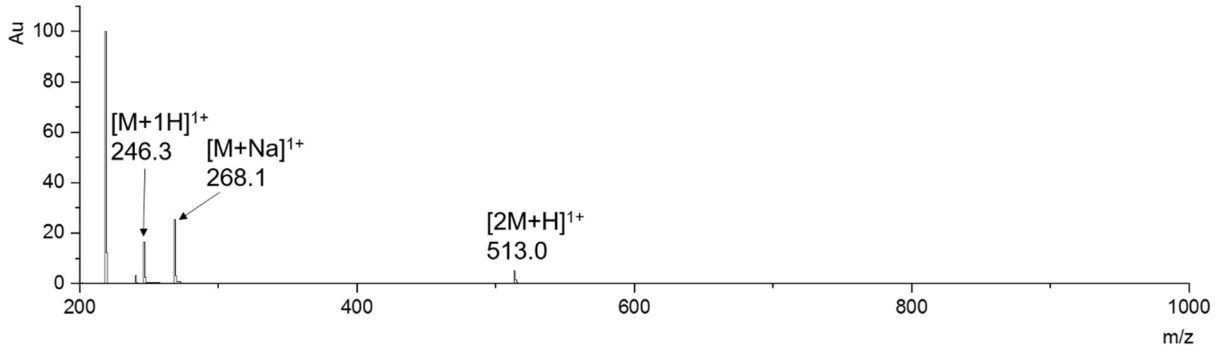

Figure S 4: ***AzC*** analyzed with ESI-MS in a m/z range of 200-2000.

Azidocoumarin-Mannose (AzCMan)

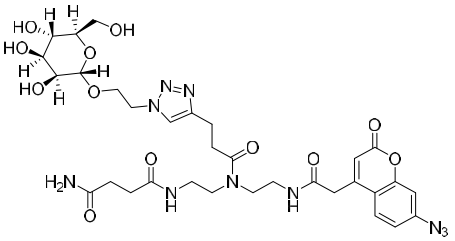

Molecular Weight: 758,75

^{1}H-NMR (300 MHz, Deuterium Oxide) δ (ppm): δ 7.71 (d, *J* = 28.9 Hz, 1H), 7.57 (dd, *J* = 24.9, 9.1 Hz, 1H), 7.10 – 6.85 (m, 2H), 6.31 (d, *J* = 13.0 Hz, 1H), 4.49 (dd, *J* = 10.5, 5.1 Hz, 1H), 3.97 (qt, *J* = 13.7, 7.0 Hz, 2H), 3.89 – 3.09 (m, 20H), 3.07 – 2.60 (m, 5H), 2.59 – 2.22 (m, 8H).

RP-HPLC (5-95 Vol% t H_2O/acetonitrile in 17 min at 25°C, 214 nm): t_r = 5.8 min

ESI-MS calculated $[M+1H]^+$ 759.75, found $[M+2H]2^+$ 380.2; $[M+H]^+$ 759.2

HR-ESI-MS: for $C_{32}H_{43}N_{20}O_{12}$ m/z $[M+1H]^{1+}$ calcd.: 759.30, found: 759.3078, mass accuracy -0.2 ppm

IR: υ(-N_3) 2160-2120cm^{-1}; found 2121 cm^{-1}

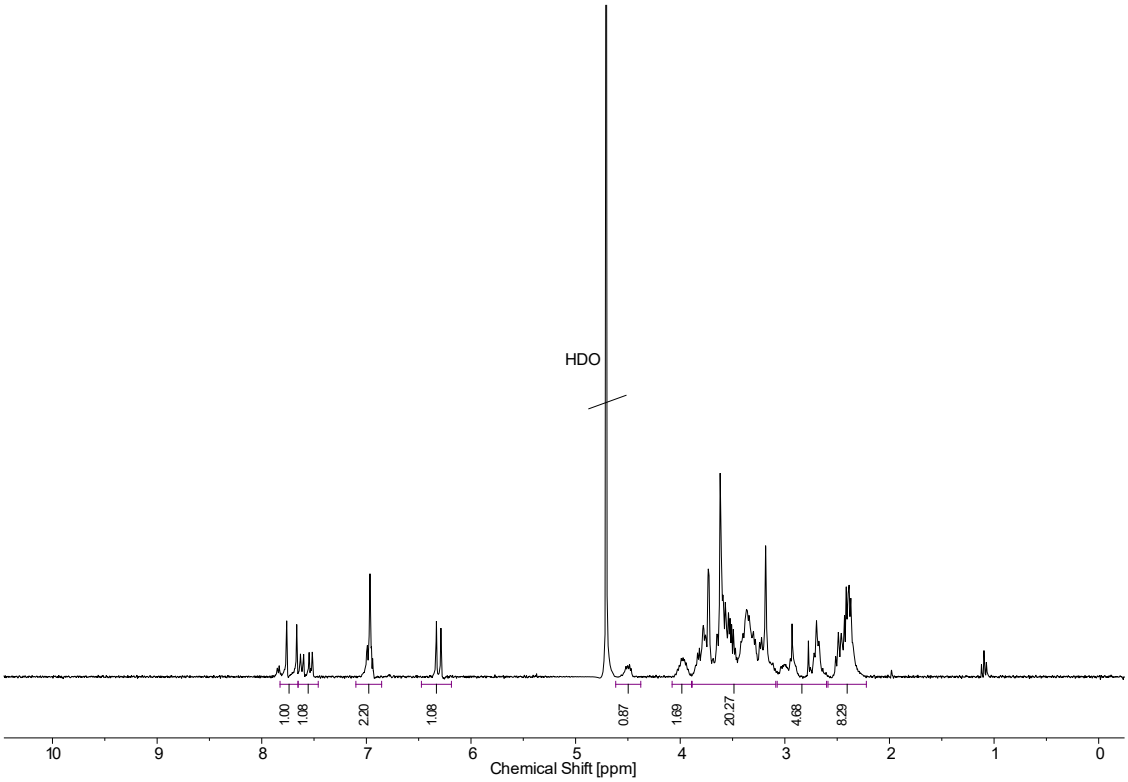

*Figure S 5: ^{1}H-NMR (300MHz) spectra of **AzCMan.***

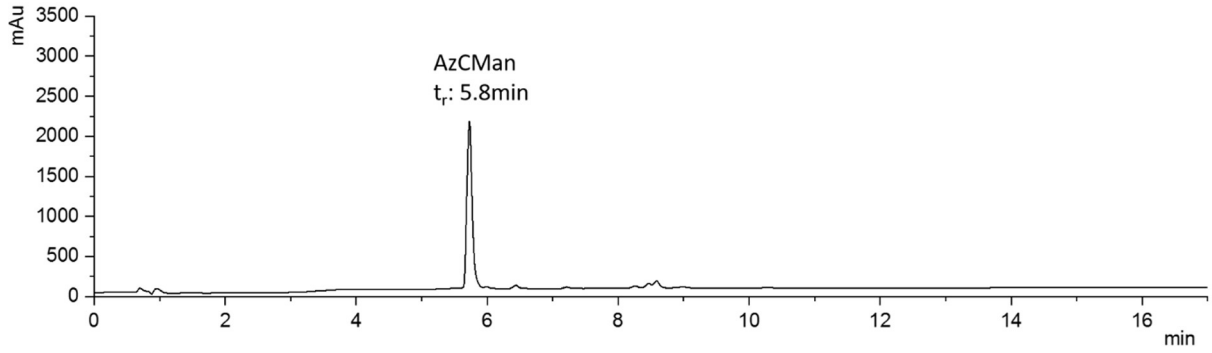

*Figure S 6:**AzCMan*** detected at t_r = 5.8 min with relative purity >95% by RP-HPLC (*linear gradient from 5-95* Vol% eluent H_2O/acetonitrile in 17 min at 25°C, VWDA1 A Wavelength = 214nm).

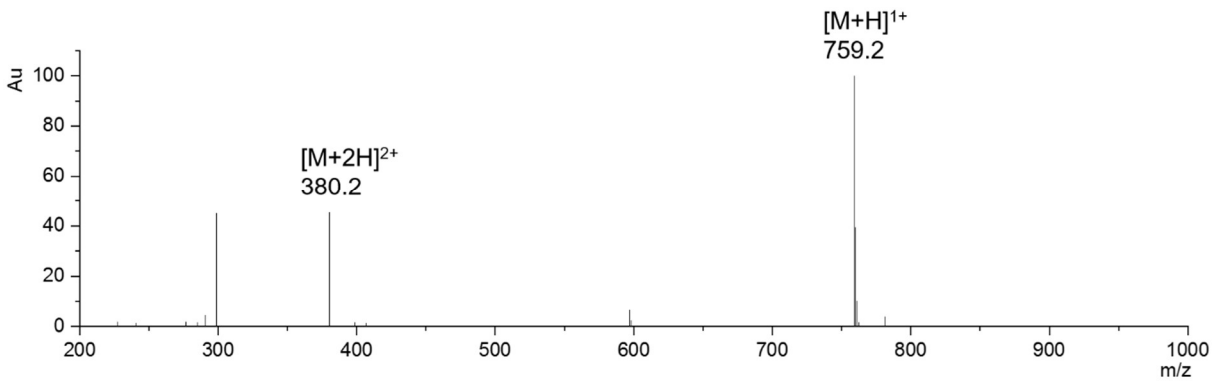

*Figure S 7:**AzCMan*** analyzed with ESI-MS in a m/z range of 200-2000.

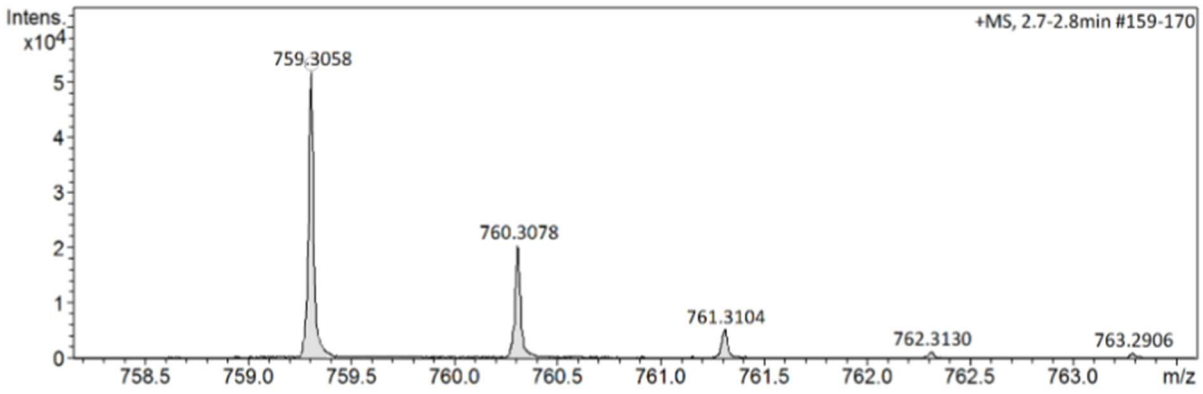

*Figure S 8:**AzCMan** analyzed with HR-ESI.*

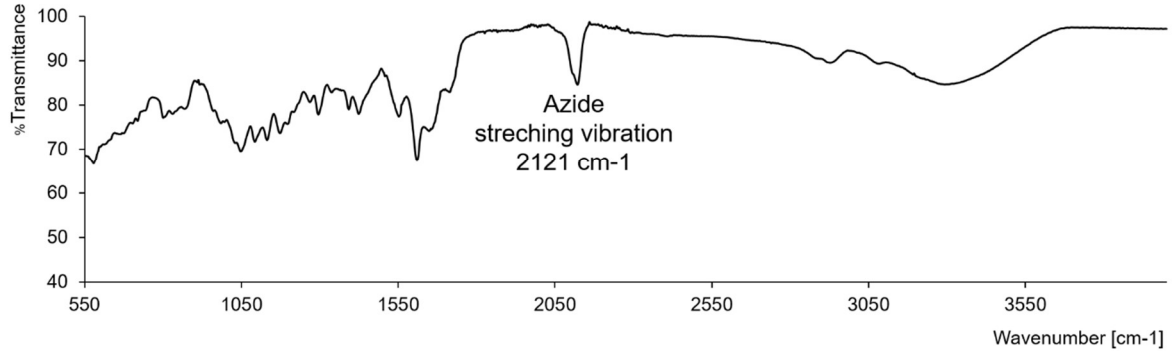

*Figure S 9: IR spectrum of **AzCMan.***

Azidocoumarin-Galactose (AzCGal)

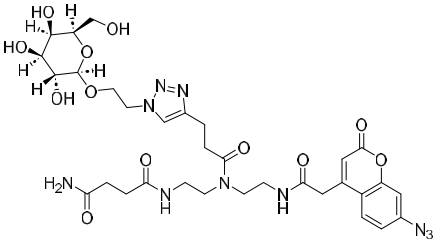

Molecular Weight: 758,7460

^{1}H-NMR (300 MHz, Deuterium Oxide) δ (ppm): δ 7.75 (d, *J* = 26.5 Hz, 1H), 7.57 (dd, *J* = 27.4, 8.7 Hz, 1H), 7.10 – 6.93 (m, 2H), 6.31 (d, *J* = 13.9 Hz, 1H), 4.51 (dd, *J* = 9.8, 4.9 Hz, 1H), 4.37 – 4.06 (m, 2H), 3.98 (dt, *J* = 12.0, 6.2 Hz, 1H), 3.89 – 3.05 (m, 24H), 2.84 – 2.61 (m, 3H), 2.59 – 2.26 (m, 7H).

RP-HPLC (5-95 Vol% t H_2O/acetonitrile in 17 min at 25°C, 214 nm): t_r = 5.8 min

ESI-MS calculated $[M+1H]^+$ 759.75, found $[M+2H]^{2+}$ 380.2; $[M+H]^+$ 759.2

HR-ESI-MS: for $C_{32}H_{43}N_{20}O_{12}$ m/z $[M+1H]^{1+}$ calcd.: 759.30, found: 759.3049, mass accuracy 1.0 ppm

IR: υ(-N_3) 2160-2120cm^{-1}; found 2120 cm^{-1}

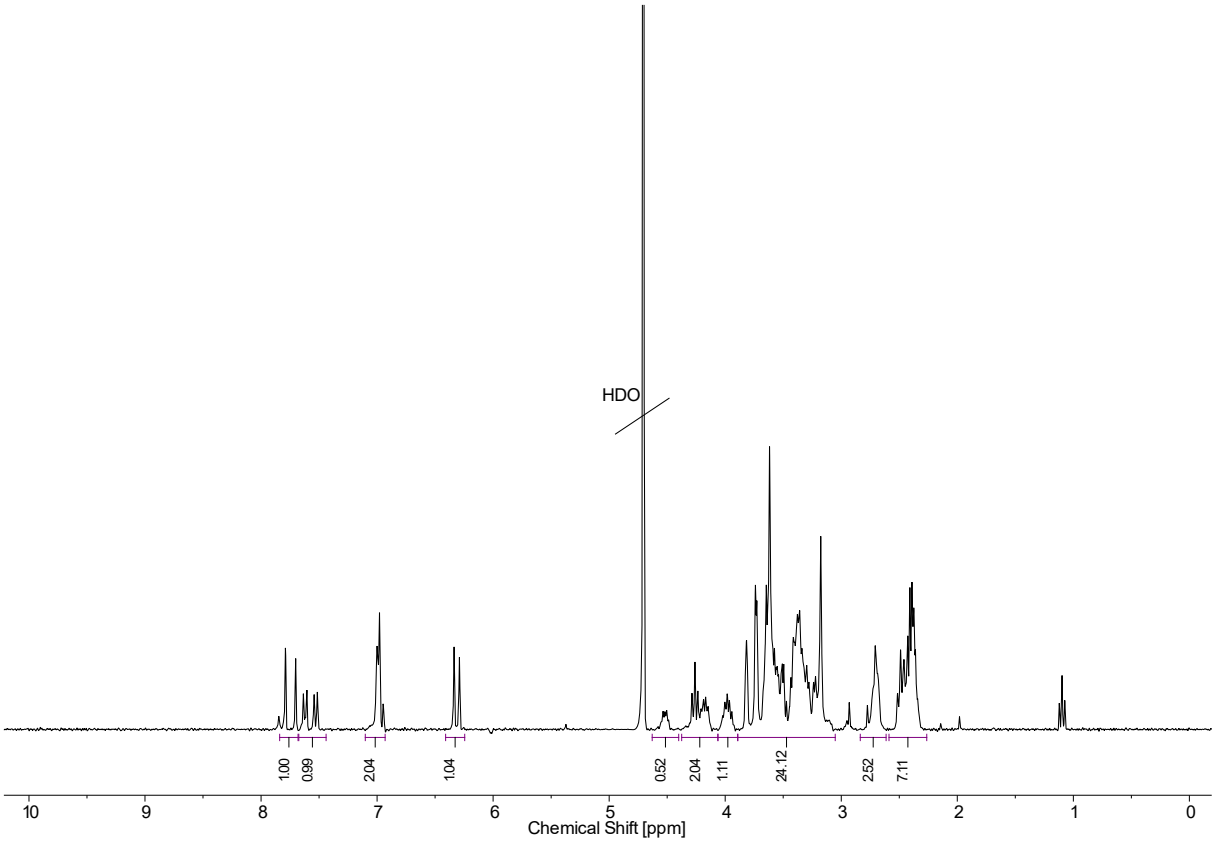

*Figure S 10: [1]H-NMR (300MHz) spectra of **AzCGal.***

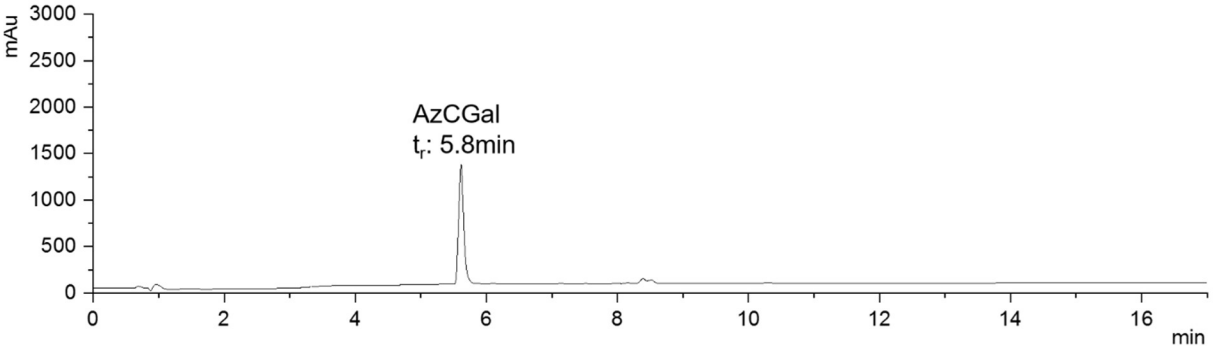

*Figure S 11:**AzCGal*** detected at t_r = 5.8 min with relative purity >95% by RP-HPLC (*linear gradient from 5-95* Vol% eluent H_2O/acetonitrile in 17 min at 25°C, VWDA1 A Wavelength = 214nm).

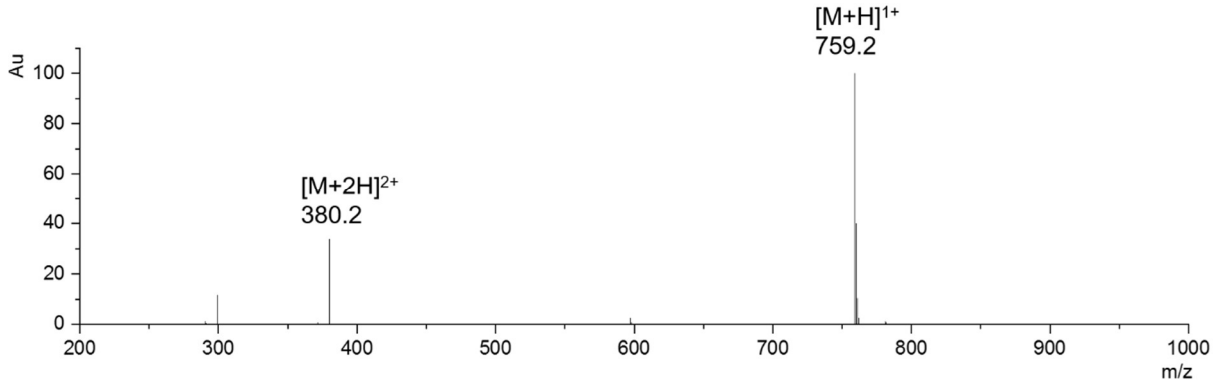

*Figure S 12:**AzCGal*** analyzed with ESI-MS in a m/z range of 200-2000.

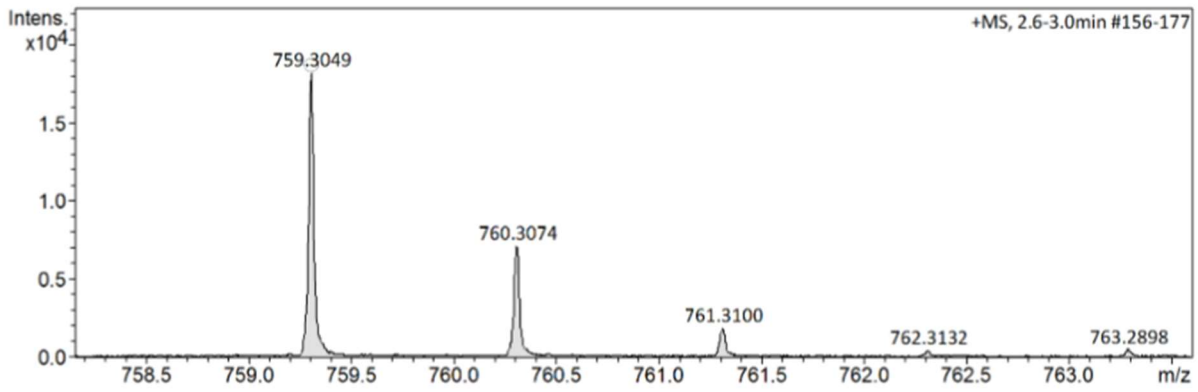

*Figure S 13:**AzCGal** analyzed with HR-ESI.*

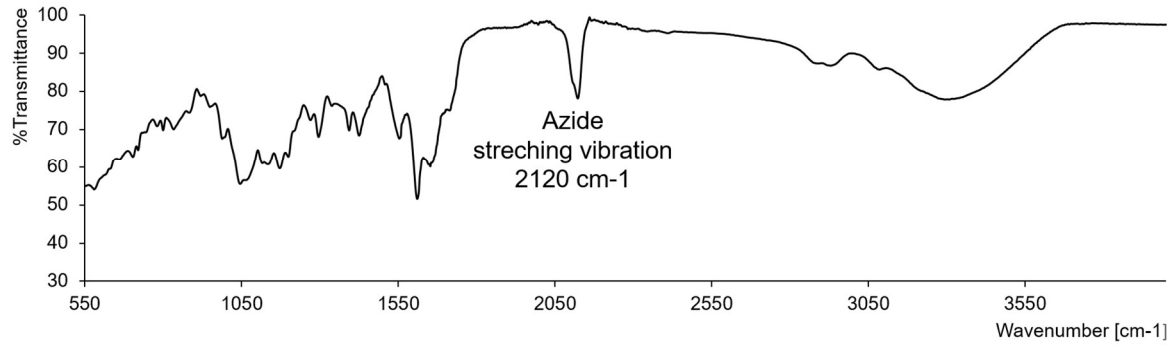

*Figure S 14: IR spectrum of **AzCGal.***

Biotin-Lys-TDS-Mannose-Azidocoumarin (AzManB)

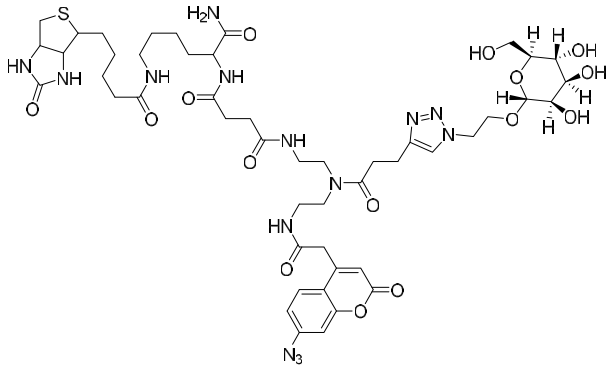

Molecular Weight: 1112.47

^{1}H-NMR (400 MHz, Deuterium Oxide) δ (ppm): δ 7.84 – 7.60 (m, 3H), 7.57 (m, 1H), 6.31 (d, *J* = 13.9 Hz, 1H), 4.61 – 4.56 (m, 2H), 4.42 – 4.36 (m, Hz, 1H), 3.92 – 3.83 (m, 16H), 3.33 – 3.05 (m, 8H), 2.82 – 2.72 (m, 3H), 2.67 – 2.35 (m, 8H), 2.27 – 2.19 (m, 2H), 1.93-1.18 (m, 16H).

^{13}C-NMR (400 MHz, Deuterium Oxide) δ (ppm): 177,19 (C17), 176,54 (C17), 174,82 (C16), 174,77 (C10), 174,72 (C34), 174,66 (C23), 165,26 (C1), 163,10 (C27), 150,80 (C25), 146,49 (C28), 144,73 (C30), 126,61 (C37), 123,79 (C32), 116,28 (C31), 115,84 (C38), 114,90 (C29), 114,59 (C33), 107,07 (C26), 99,46 (C41), 72,77 (C42), 70,44 (C44), 69,89 (C45), 66,37 (C43), 65,40 (C3), 65,37 (C40), 62,06 (C15), 60,67 (C2), 60,63 (C46), 60,21 (C5), 55,37 (C21), 53,53 (C39), 49,91 (C24), 39,66 (C4), 38,90 (C11) 35,45 (C22), 31,88 (C20), 31,66 (C9), 30,54 (C35), 30,41 (C19), 27,86 (C18), 27,82 (C14), 27,64 (C12), 27,64 (C7), 25,17 (C36), 22,52 (C8), 20,58(C6), 20,40 (C13)

RP-HPLC (5-50 Vol% t H_2O/acetonitrile in 20 min at 25°C, 214 nm): t_r = 10.91 min

ESI-MS calculated $[M+1H]^+$ 1113,6; found $[M+1H]^+$ 1113,6; calculated $[M+2H]^+$ 557,6; found $[M+1H]^+$ 557,6

HR-ESI-MS: for $C_{48}H_{68}N_{14}O_{15}S$ sm/z $[M+1H]^{1+}$ calcd.: 1113,47, found: 1113,4807, mass accuracy 1.0 ppm; for $NaC_{48}H_{67}N_{14}O_{15}S$ sm/z $[M+1Na]^{1+}$ calcd.: 1135,47, found: 1135,4629, mass accuracy 1.0 ppm

IR: υ(-N_3) 2160-2120cm^{-1}; found: 2117 cm^{-1}

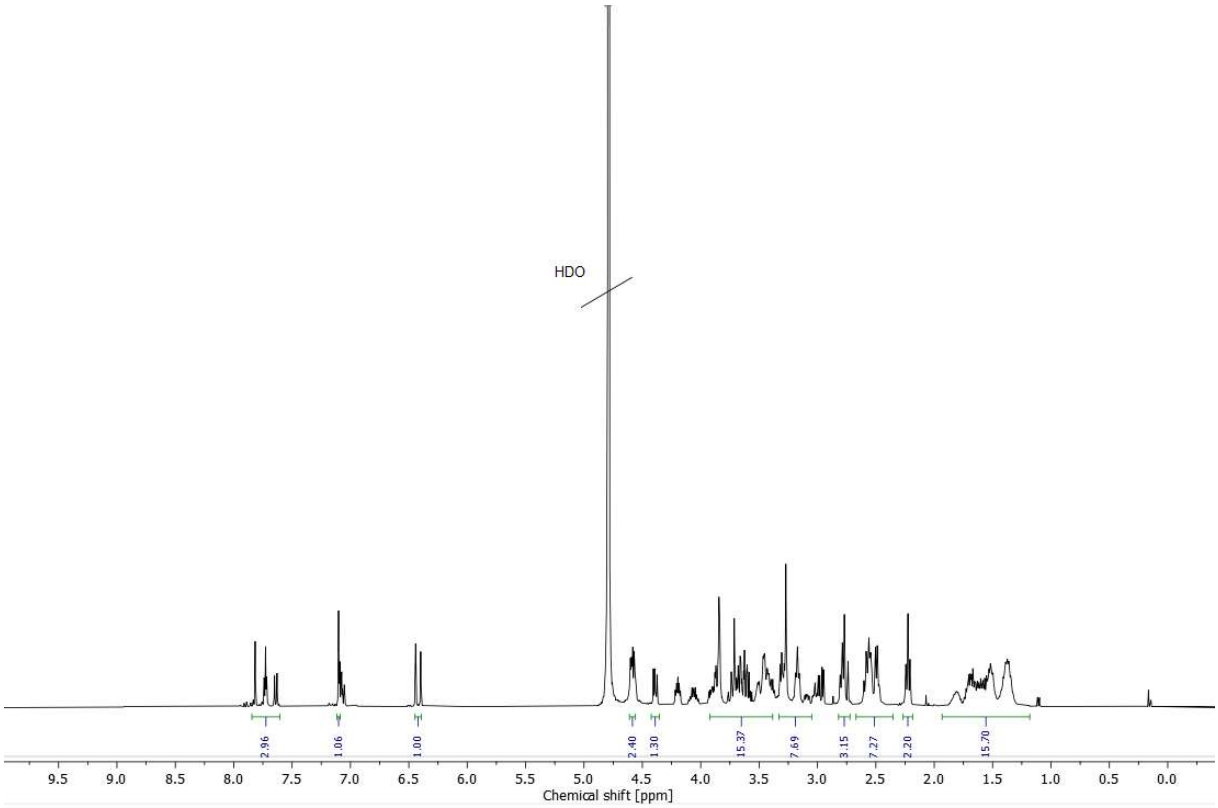

*Figure S 15: [1]H-NMR (400MHz) spectra of **AzManB**.*

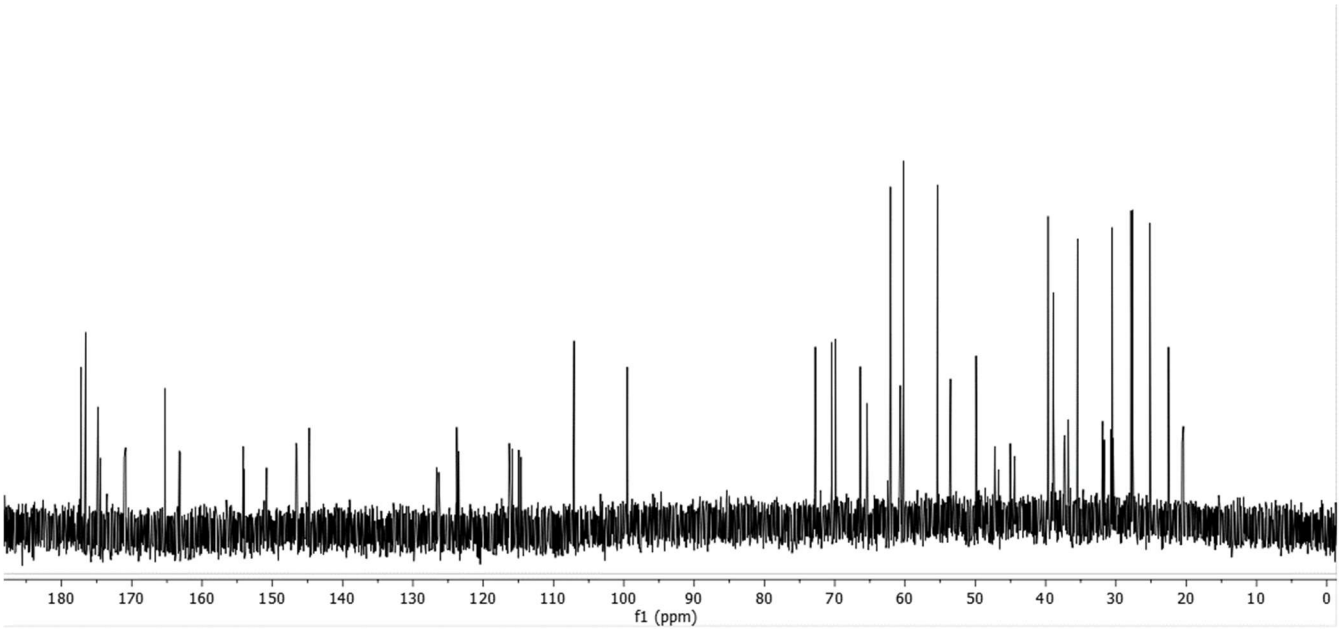

*Figure S 16: [13]C-NMR (400MHz) spectra of **AzManB.***

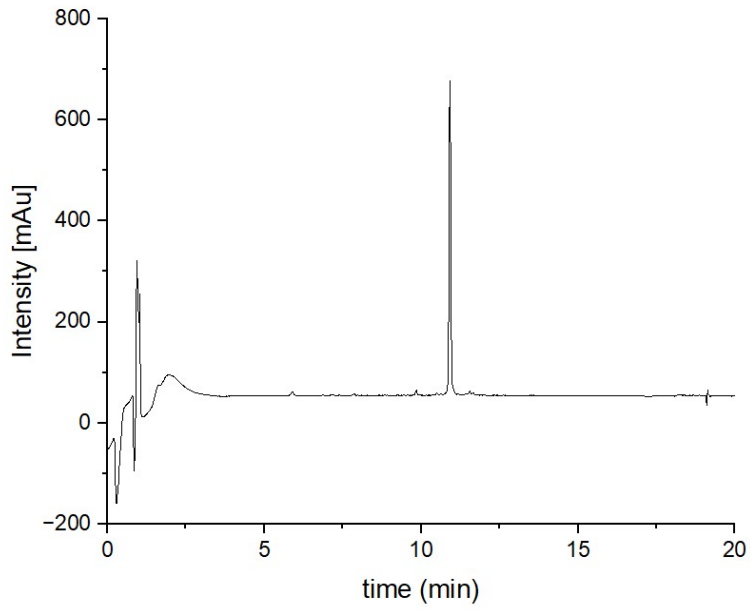

*Figure S 17:**AzManB*** detected at t_r = 10,91 min with relative purity >95% by RP-HPLC (*linear gradient from 1-50* Vol% eluent H_2O/acetonitrile in 20 min at 25°C, VWDA1 A Wavelength = 214nm).

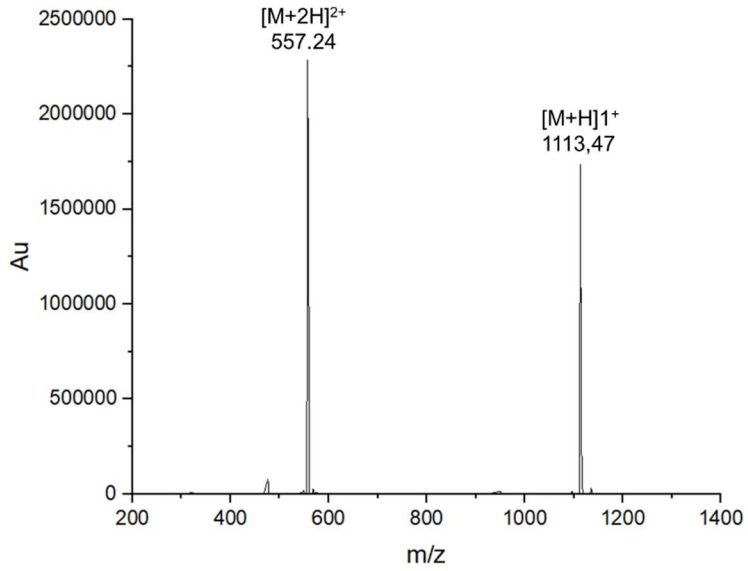

*Figure S 18: **AzManB*** analyzed with ESI-MS in a m/z range of 200-2000.

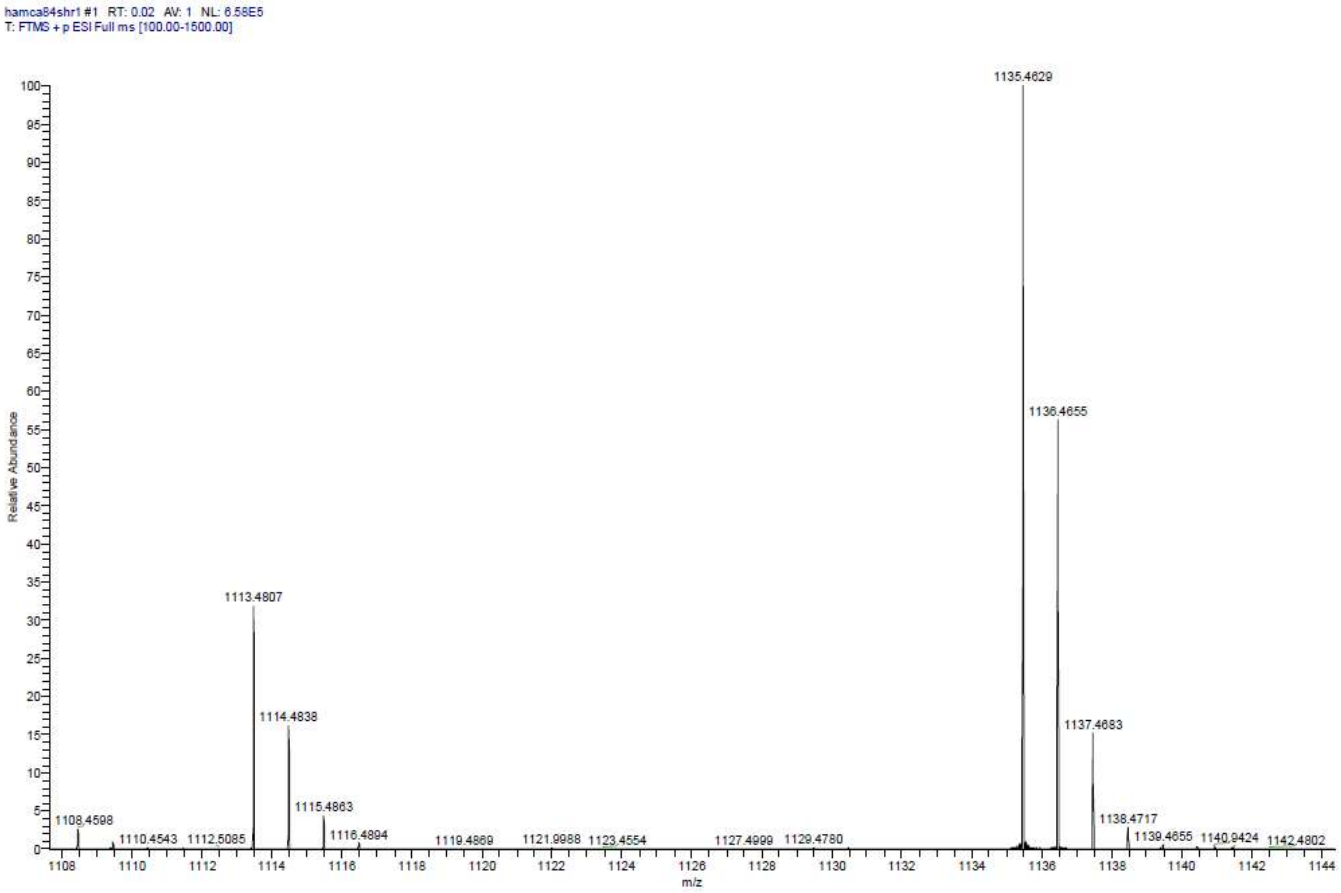

*Figure S 19: **AzManB** analyzed with HR-ESI.*

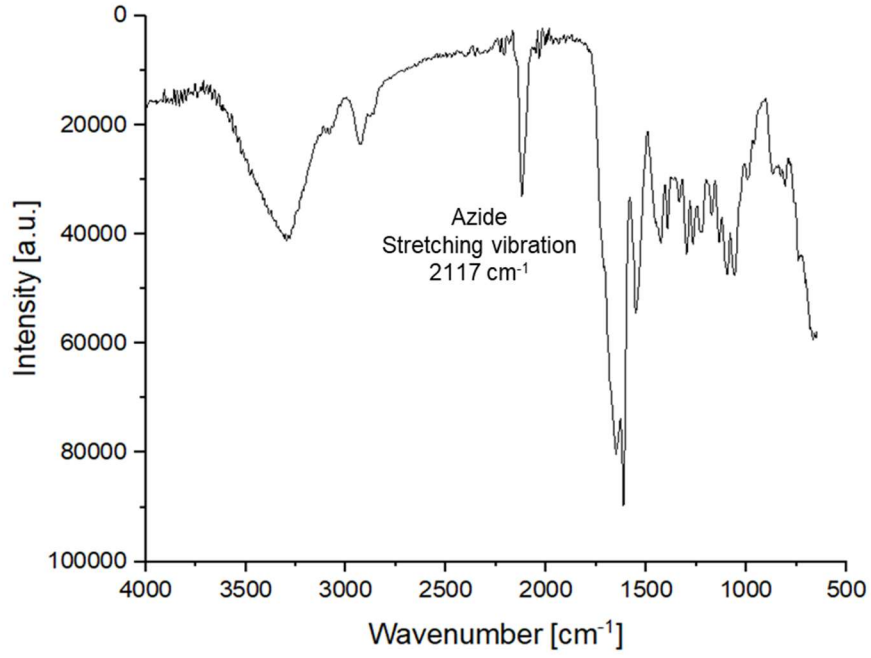

*Figure S 20: IR spectrum of **AzManB.***

Absorption and fluorescence spectra of AzC

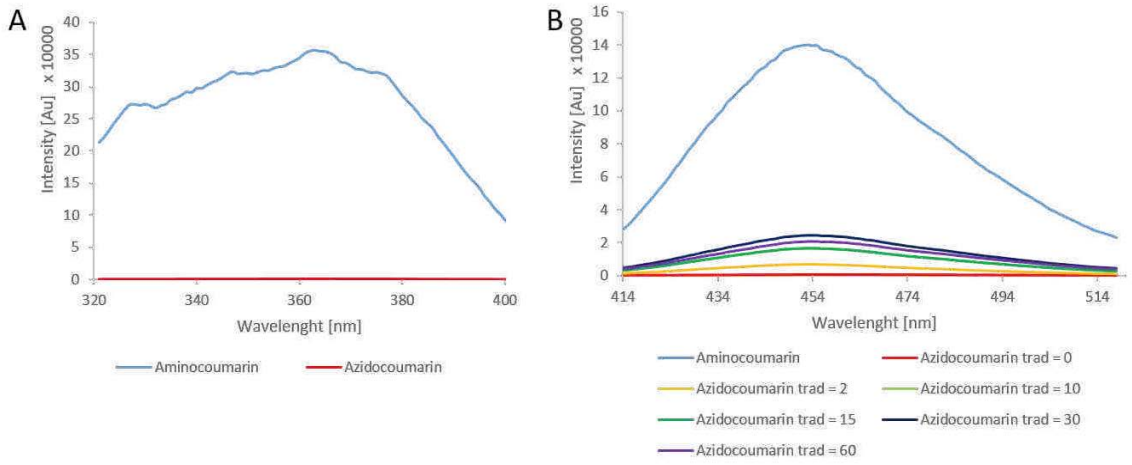

Figure S 21: A) Extinction of azidocoumarin (red) and aminocoumarin (blue) in comparison. B) Fluorescence measurements of azidocoumarin after different durations of irradiation (trad=0 to trad = 60 min) at 365 nm in comparison to aminocoumarin.

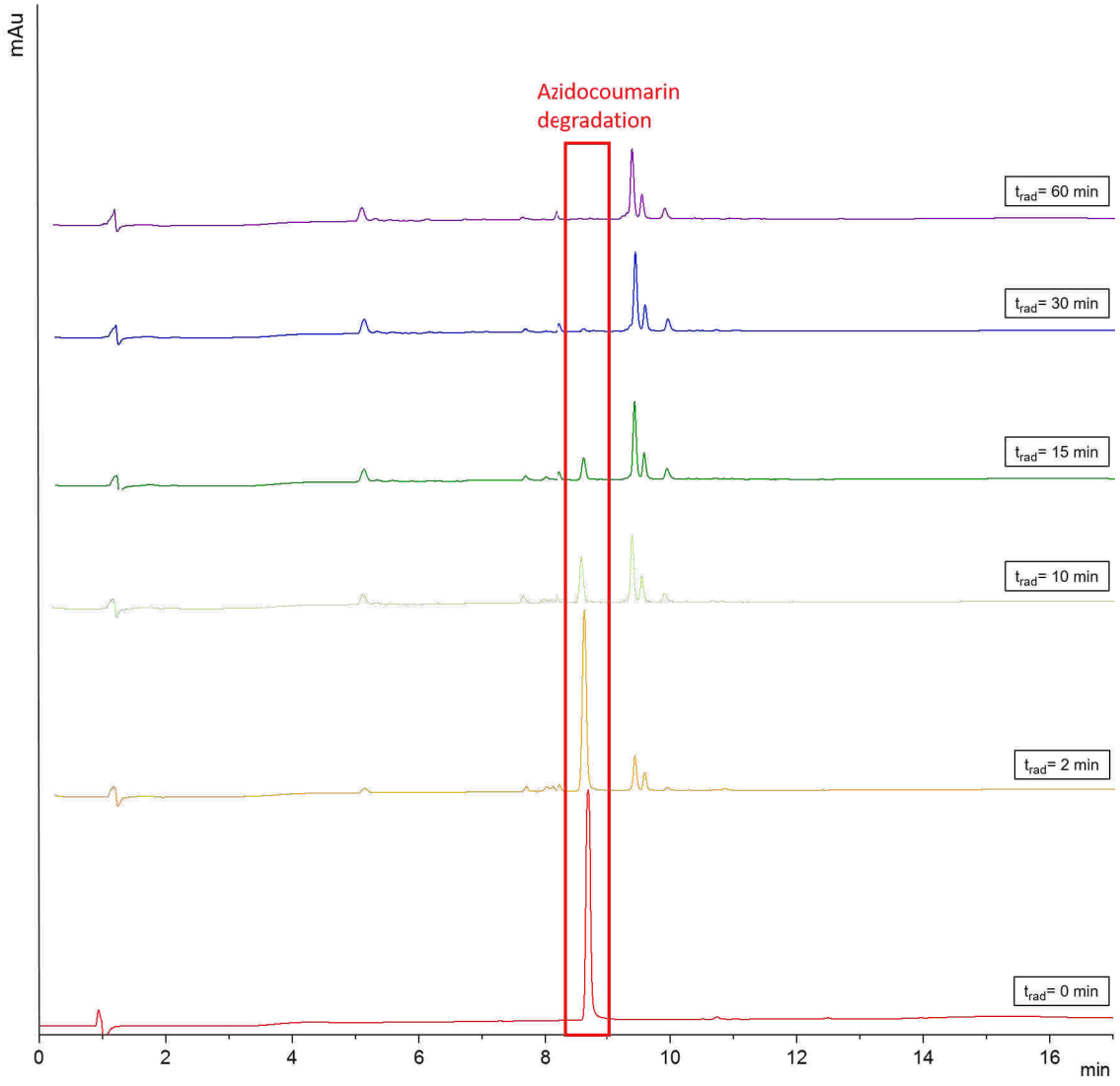

Figure S 22: RP-HPLC of AzC after different irradiation times showing reduce of the AzC signal due to degradation.

MALDI-TOF-MS experiments

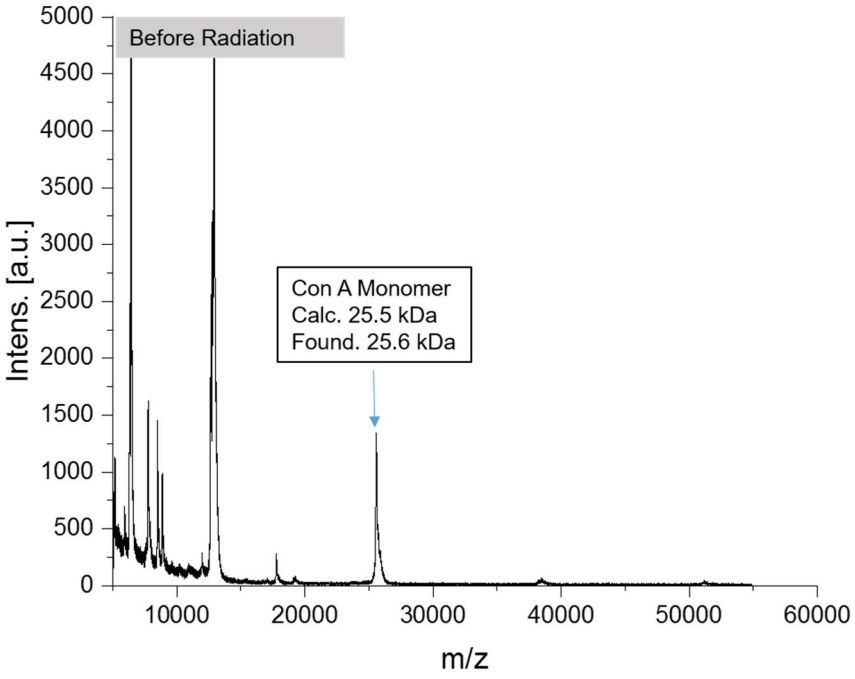

Figure S 23: MALDI-TOF-MS of *ConA and* ***AzCMan*** *before irradiation* in a m/z range of 20000-60000 using HCCA as matrix in a compound to matrix ratio of 1:2.

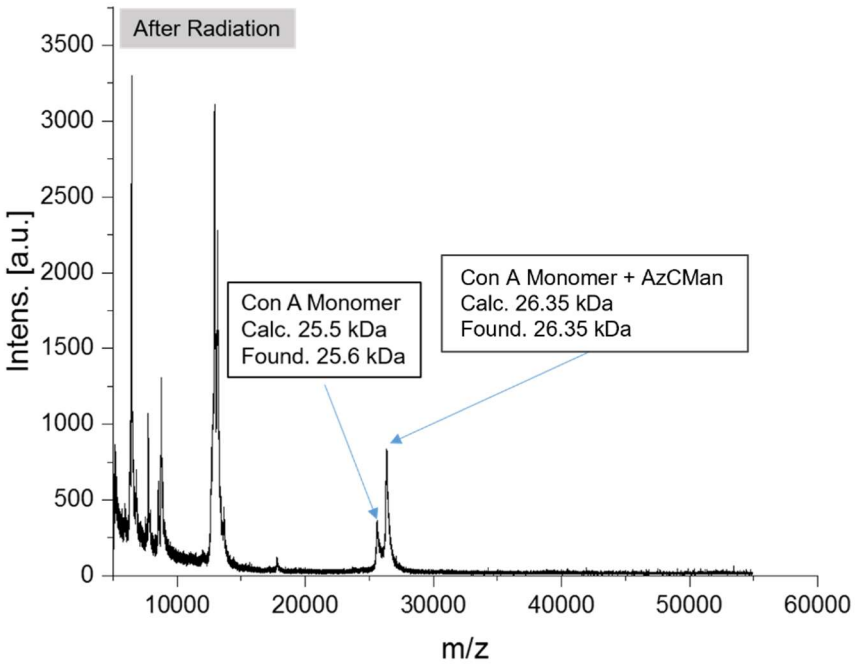

Figure S 24: MALDI-TOF-MS of *ConA and* ***AzCMan*** *after radiation* in a m/z range of 20000-60000 using HCCA as matrix in a compound to matrix ratio of 1:2.

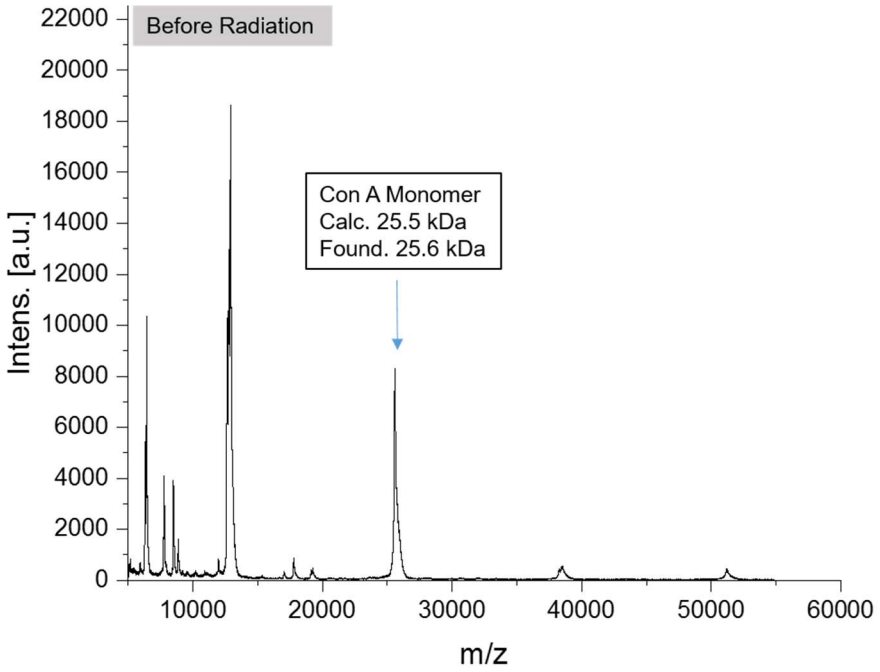

Figure S 25: MALDI-TOF-MS of *ConA and **AzCGal** before radiation* in a m/z range of 20000-60000 using HCCA as matrix in a compound to matrix ratio of 1:2.

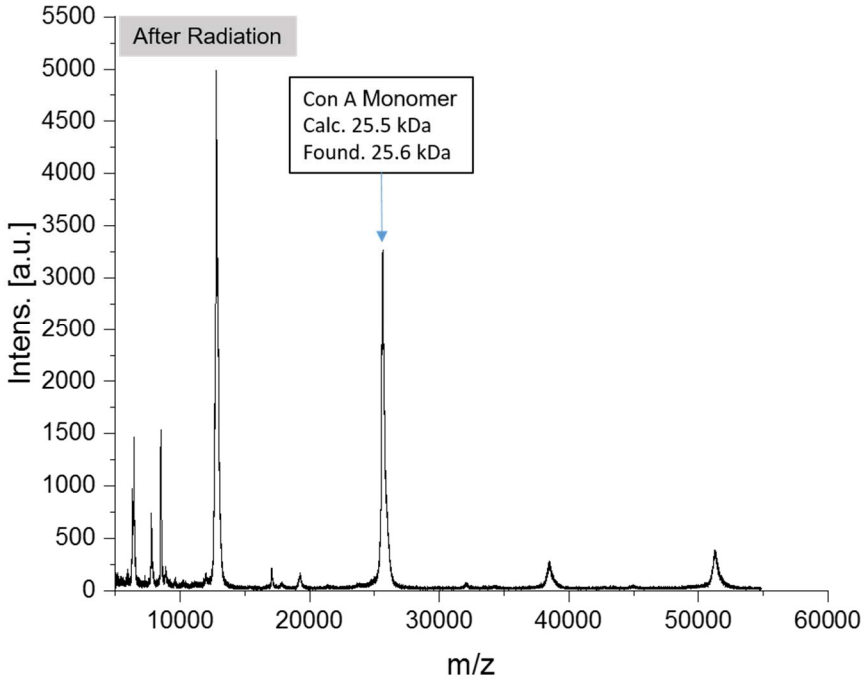

*Figure S 26: MALDI-TOF-MS of ConA and **AzCGal** after radiation in a m/z range of 20000-60000 using HCCA as matrix in a compound to matrix ratio of 1:2.*

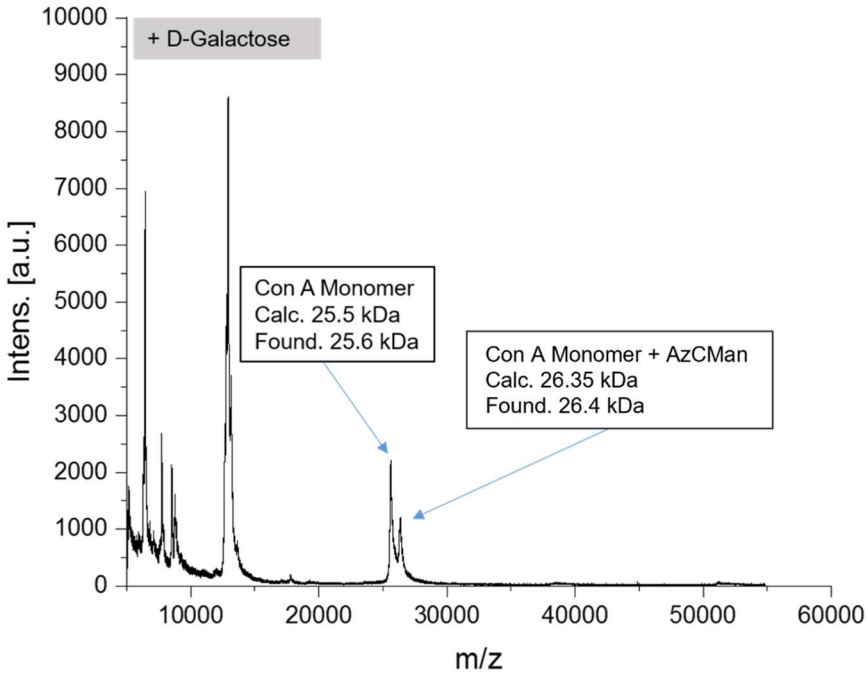

Figure S 27: MALDI-TOF-MS of *ConA and **AzCMan** + D-Galactose after radiation* in a m/z range of 20000-60000 using HCCA as matrix in a compound to matrix ratio of 1:2.

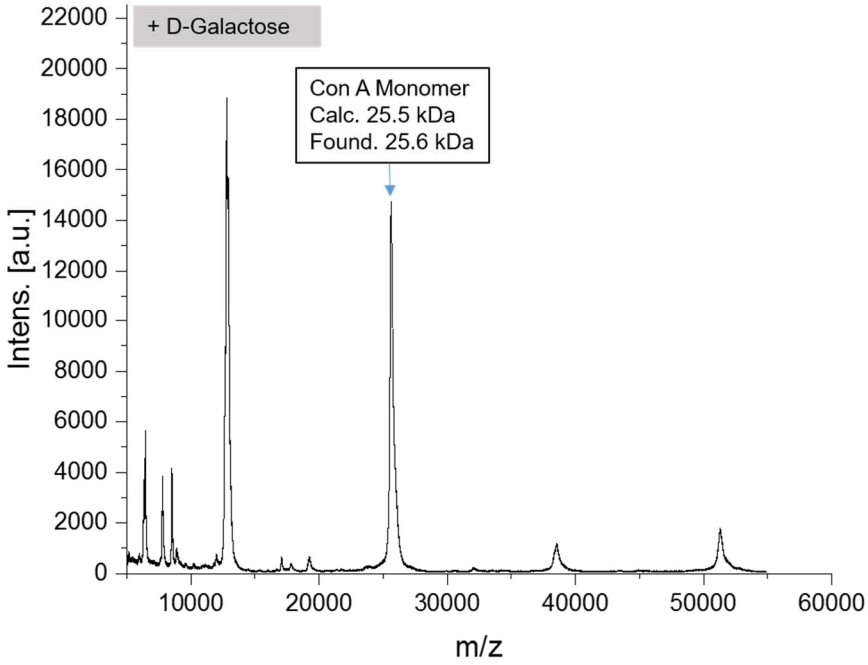

Figure S 28. MALDI-TOF-MS of *ConA and **AzCGal** + D-Galactose after radiation* in a m/z range of 20000-60000 using HCCA as matrix in a compound to matrix ratio of 1:2.

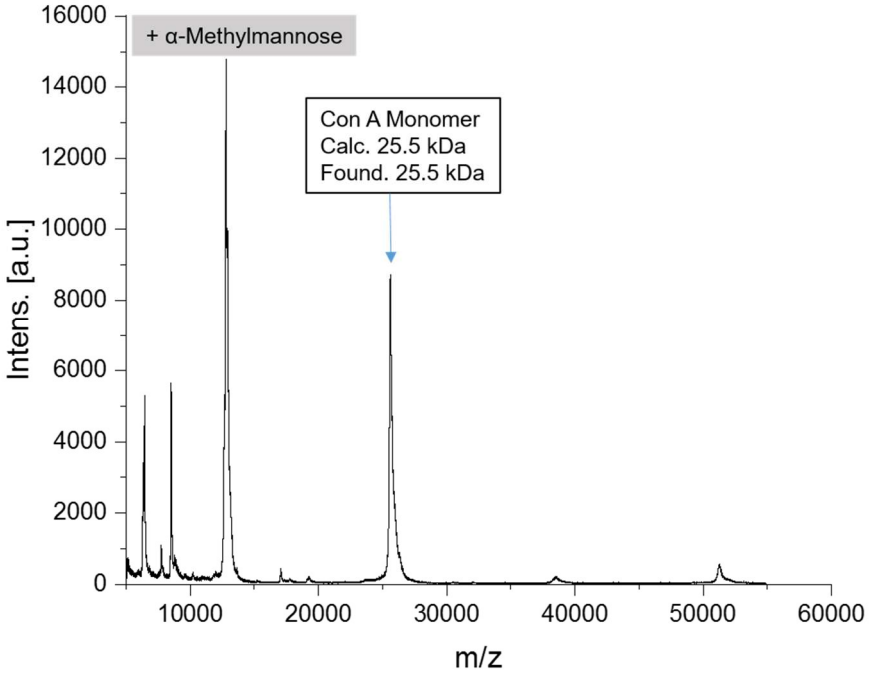

*Figure S 29: MALDI-TOF-MS of ConA and **AzCMan** + Methylmannose after radiation in a m/z range of 20000-60000 using HCCA as matrix in a compound to matrix ratio of 1:2.*

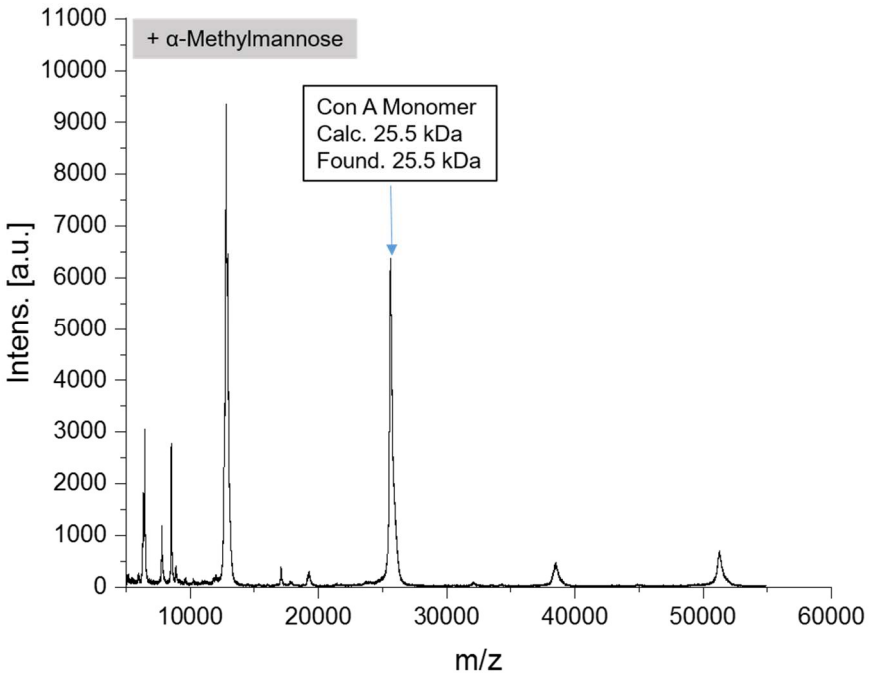

*Figure S 30: MALDI-TOF-MS of ConA and **AzCGal** + Methylmannose after radiation in a m/z range of 20000-60000 using HCCA as matrix in a compound to matrix ratio of 1:2.*

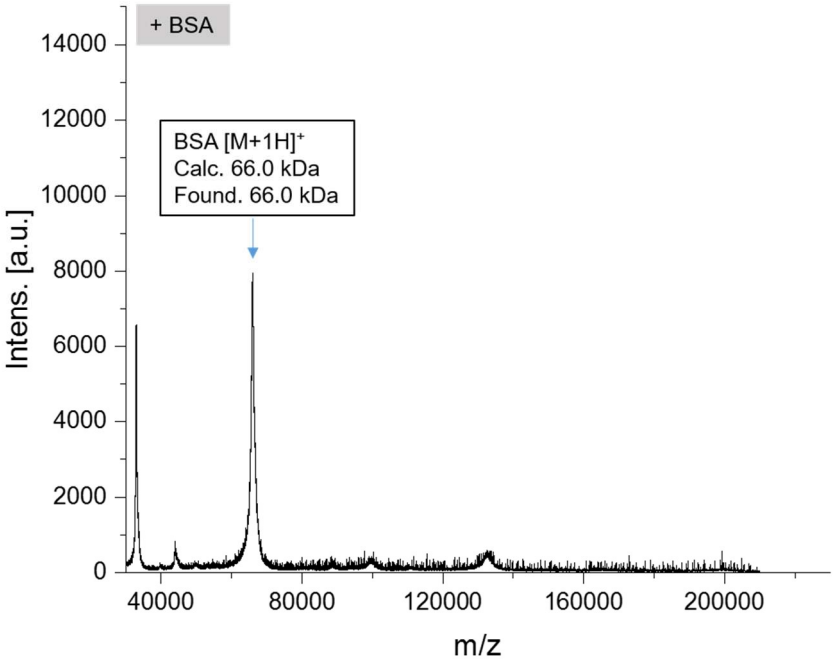

Figure S 31: MALDI-TOF-MS of *BSA + **AzCMan** after radiation* in a m/z range of 50000-200000 using HCCA as matrix in a compound to matrix ratio of 1:2.

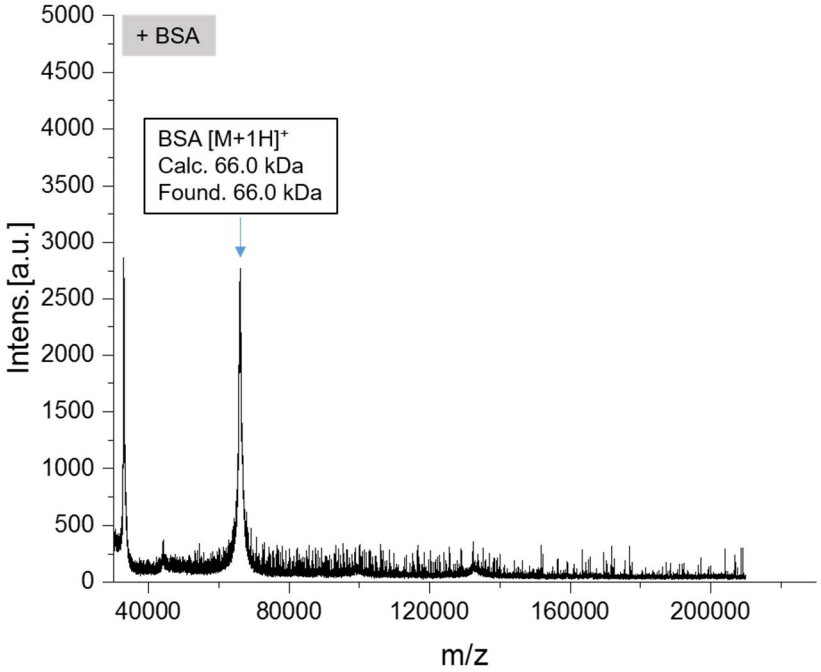

Figure S 32: MALDI-TOF-MS of *BSA and **AzCGal** after radiation* in a m/z range of 50000-200000 using HCCA as matrix in a compound to matrix ratio of 1:2.

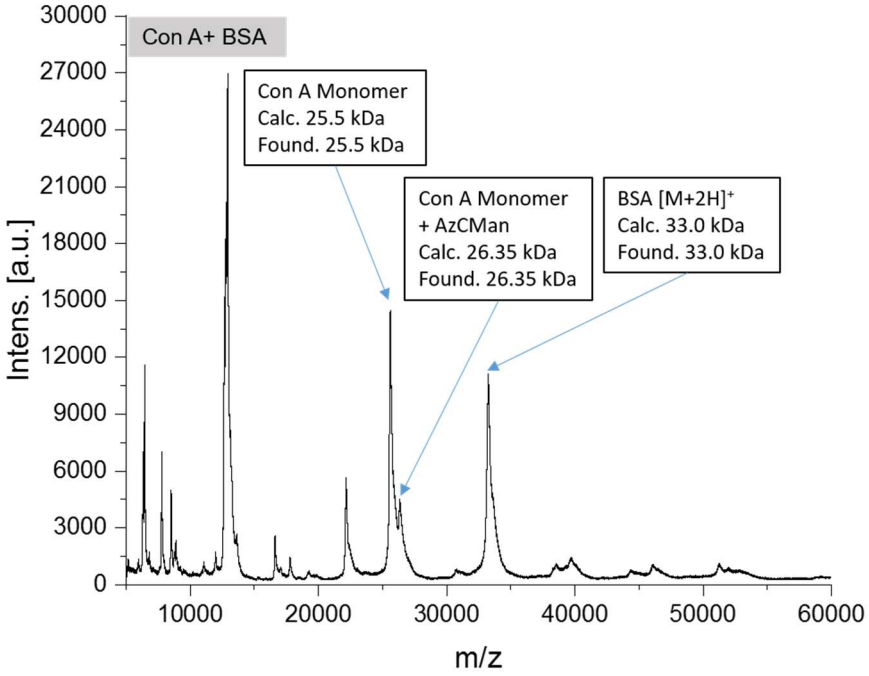

*Figure S 33: MALDI-TOF-MS of ConA and **AzCMan** + BSA after radiation in a m/z range of 20000-60000 using HCCA as matrix in a compound to matrix ratio of 1:2.*

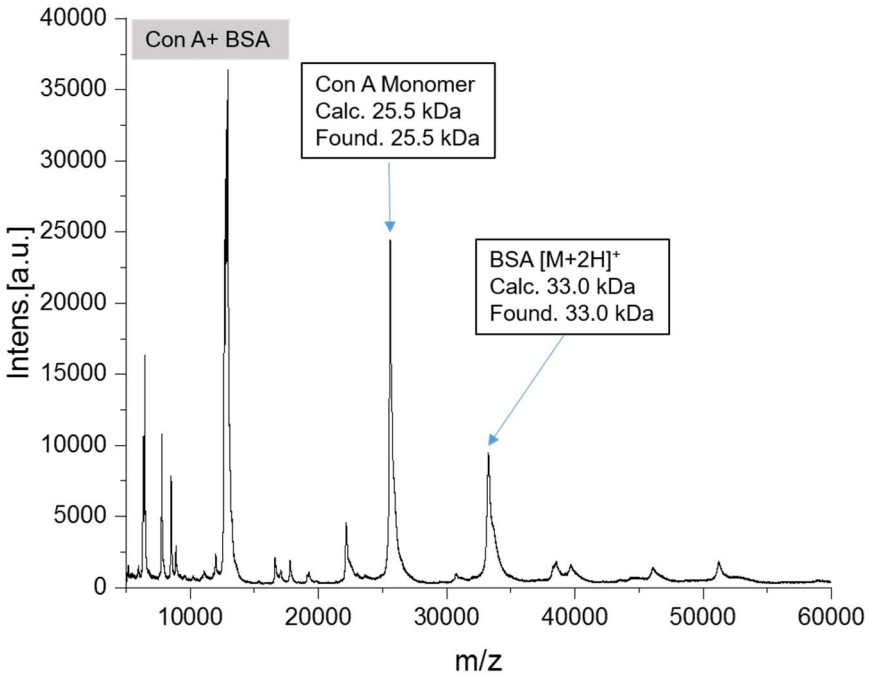

*Figure S 34: MALDI-TOF-MS of ConA and **AzCGal** + BSA after radiation in a m/z range of 20000-60000 using HCCA as matrix in a compound to matrix ratio of 1:2.*

Fluorescence spectra

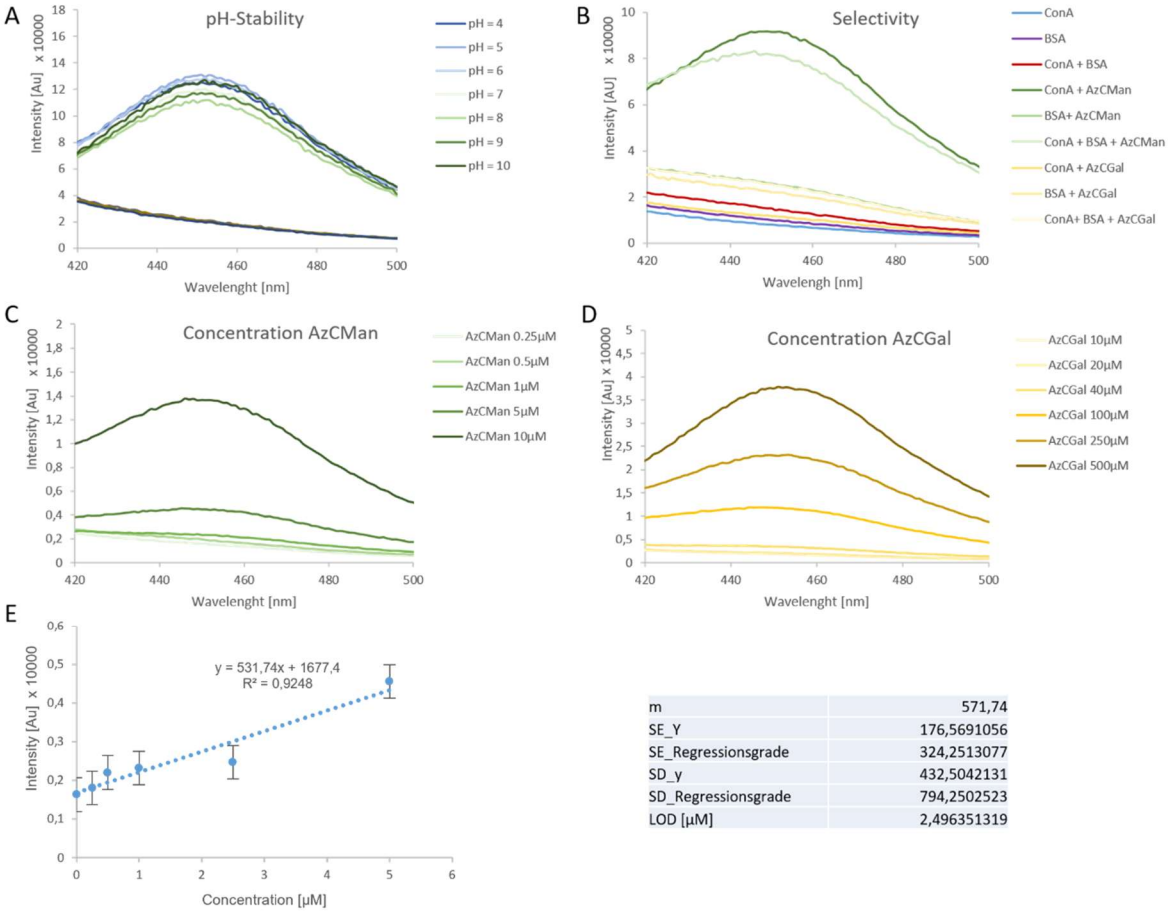

m	571,74
SE_Y	176,5691056
SE_Regressionsgrade	324,2513077
SD_y	432,5042131
SD_Regressionsgrade	794,2502523
LOD [µM]	2,496351319

Figure S 35:Microplate Reader fluorescence spectra. A) pH stability of AzCMan-ConA conjugate. B) Selective binding and fluorogenic properties of AzC PAL probes in presence of different lectins and proteins. C) Fluorogenic properties of AzCMan at different concentrations. D) Fluorogenic properties of AzCGal at different concentrations. E) Calculated limit of detection for AzCMan.

Additional SDS-PAGE images

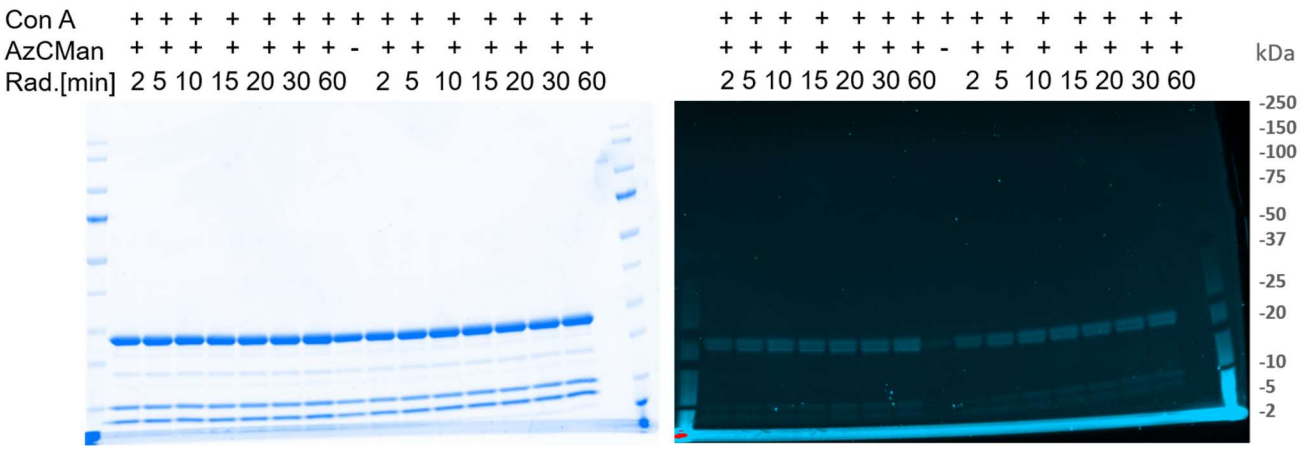

Figure S 36: SDS-PAGE showing relative ConA crosslinking of AzCMan after different durations of irradiation.

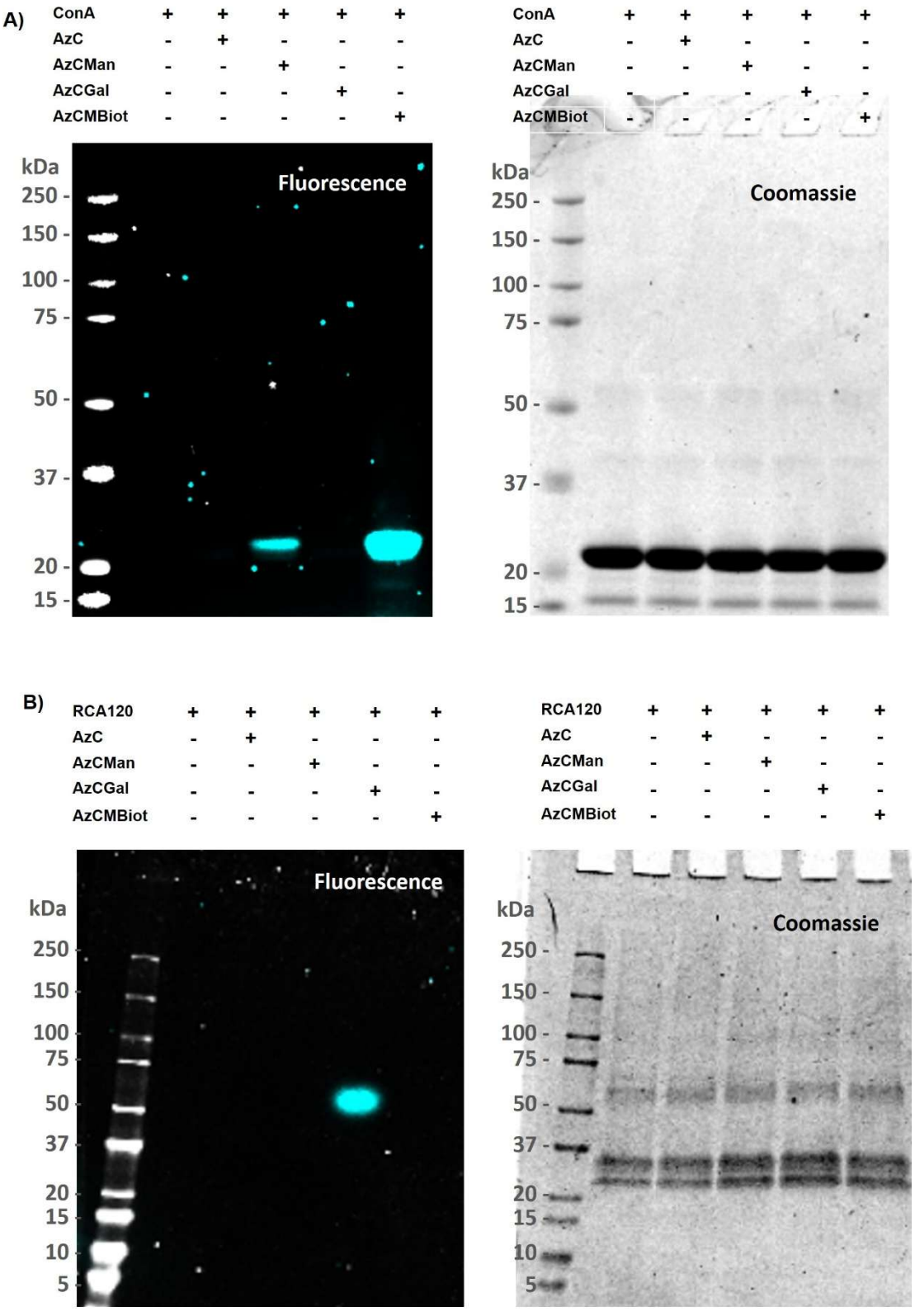

Figure S 37: A) SDS-PAGE of ConA incubated with AzC probes after 15 min irradiation at 365 nm; Left image shows AzC fluorescence; right image shows Coomassie stain of the same gel. B) SDS-PAGE of RCA_{120} incubated with AzC probes after 15 min irradiation at 365 nm. Left image shows AzC fluorescence, right image shows Coomassie stain of the same gel.

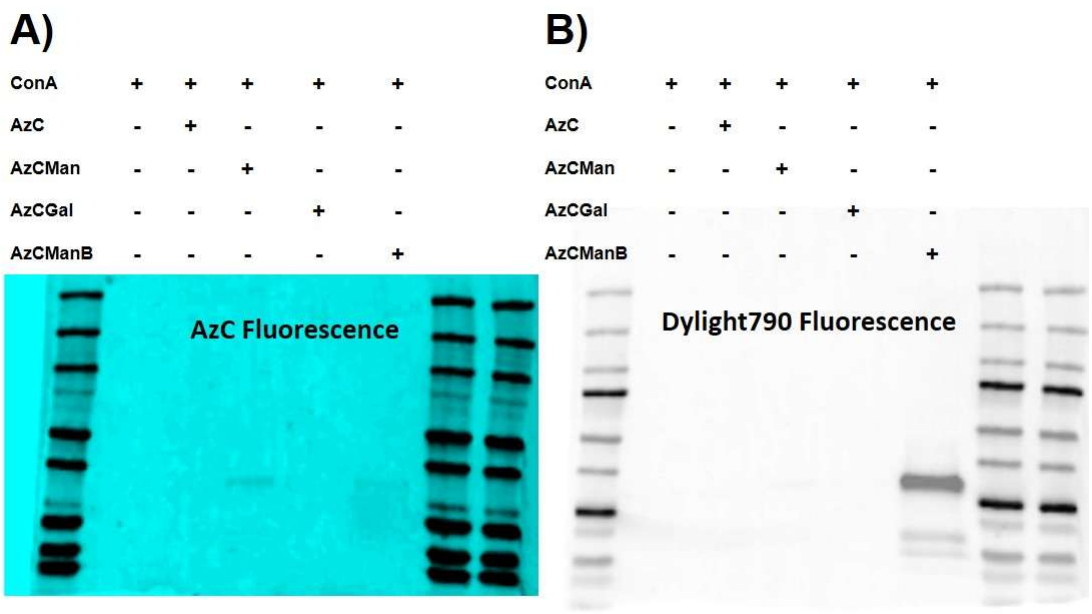

Figure S 38: A) Western blot of ConA incubated with AzC building block and AzC glycan PAL probes 15 min irradiation at 365 nm; A) WB showing coumarin fluorescence (fluorescence was measured in the Cy5 channel). B) Image of the same blot after incubation with streptavidin-dylight 790

Additional fluorescence microscopy images

Triplicate measurements fixed cells incubated with AzC probes

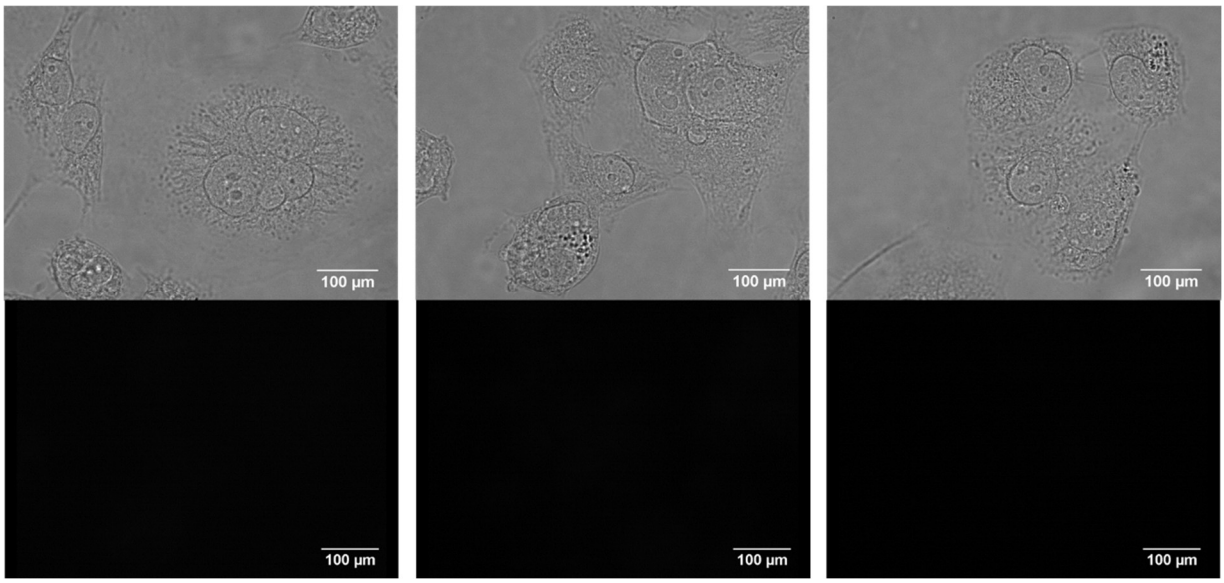

Figure S 39: Replicates of microscopy images (top) bright-field, (bottom) fluorescence at 488 nm of fixed MDA-MB-231 cells treated with LBB as vehicle control for 20 min, followed by irradiation for 15 min at 365 nm.

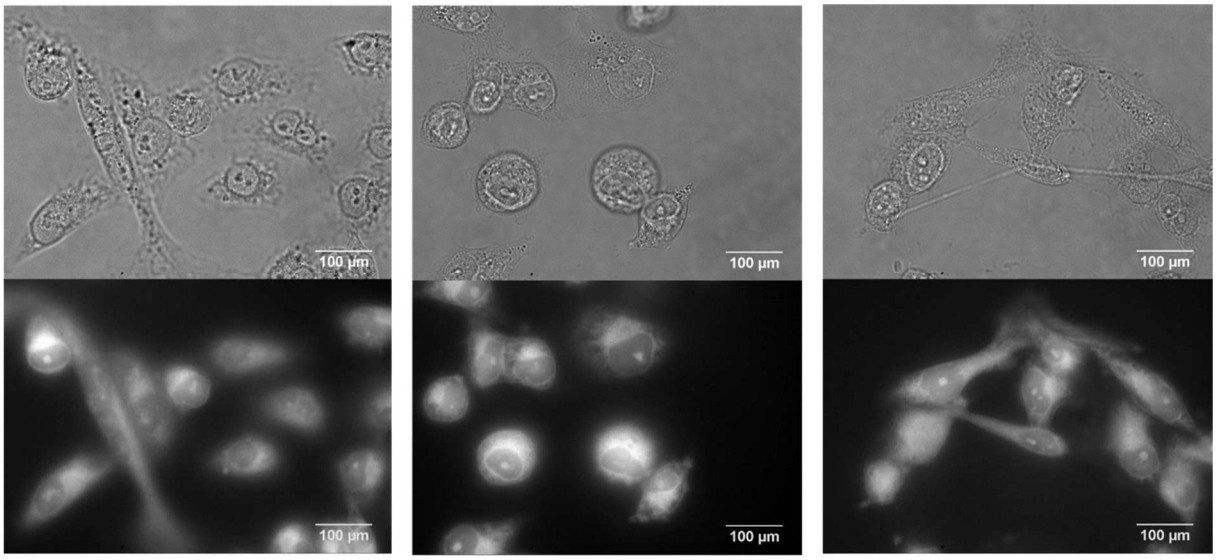

Figure S 40: Replicates of microscopy images (top) bright-field, (bottom) fluorescence at 488 nm of fixed MDA-MB-231 cells treated with AzCMan (10µM) for 20 min, followed by irradiation for 15 min at 365 nm.

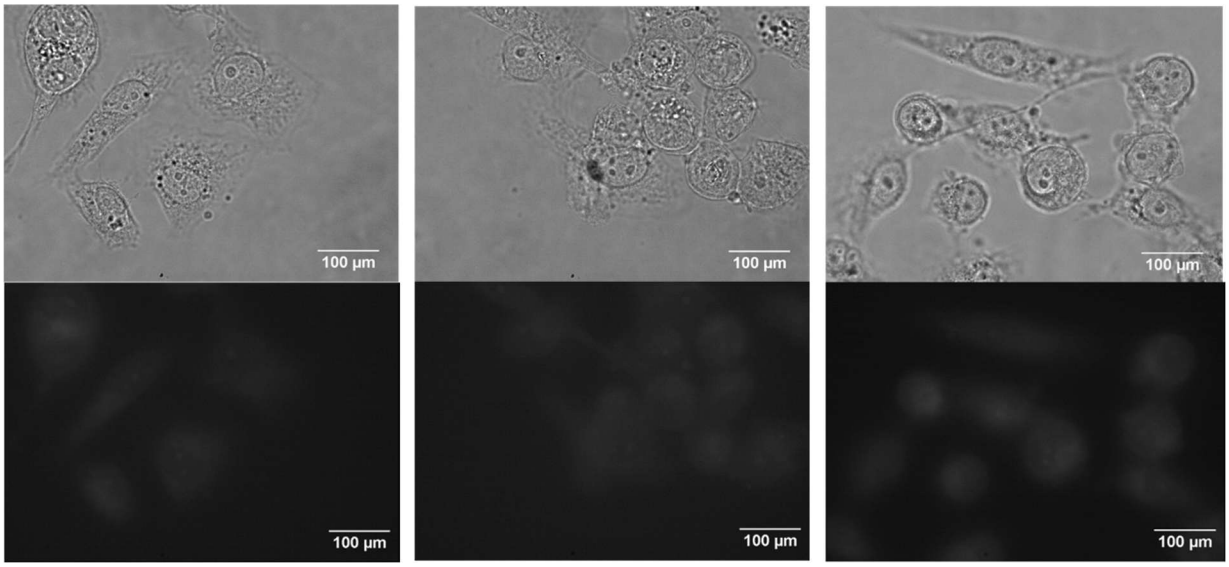

Figure S 41: Replicates of microscopy images (top) bright-field, (bottom) fluorescence at 488 nm of fixed MDA-MB-231 cells treated with pre-activated AzCMan (10µM) for 20 min, followed by irradiation for 15 min at 365 nm.

AzC activation by the UV laser of the microscope

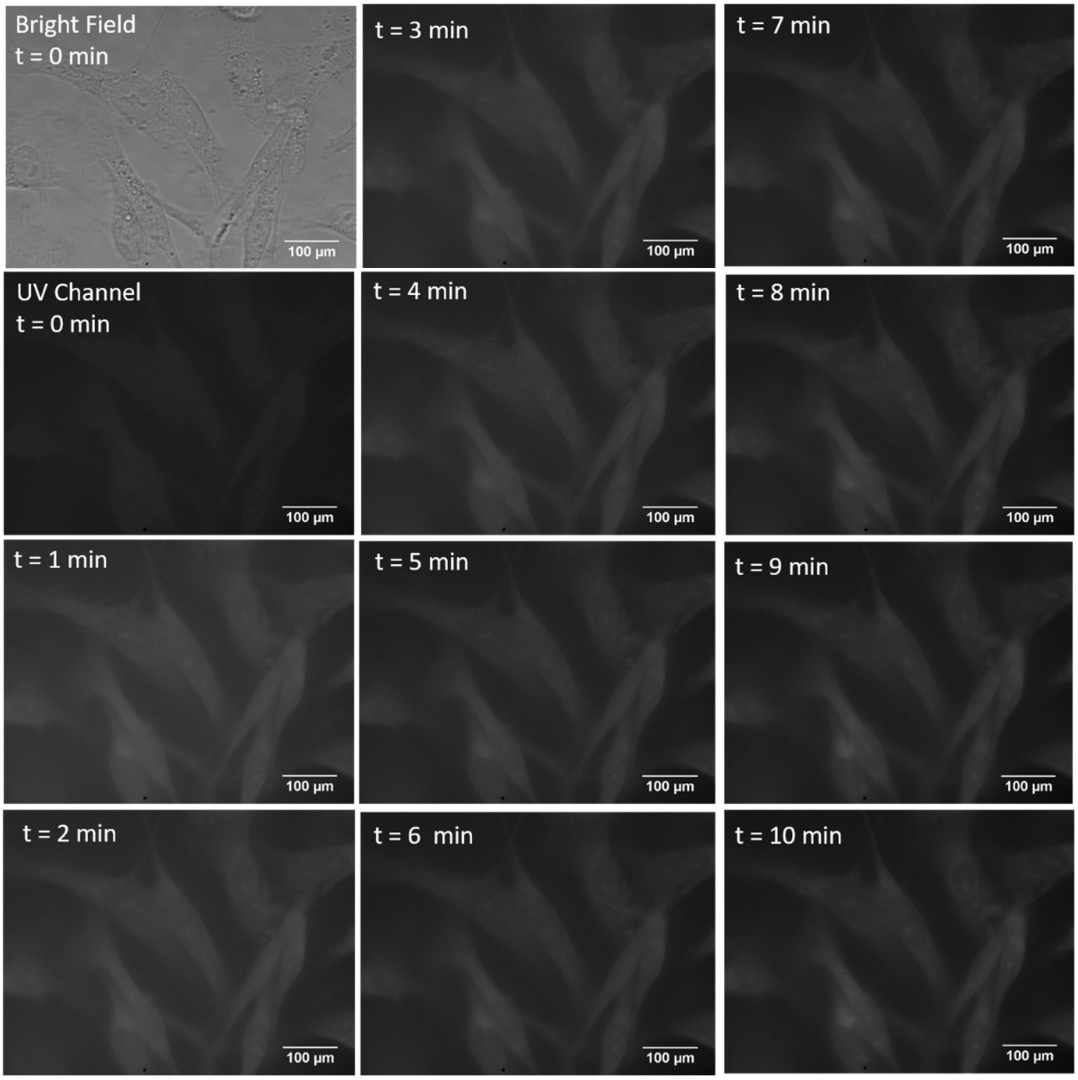

Figure S 42: Fluorescence microscopy images of photo-activation of the AzCMan probe using the UV laser of the microscope for a duration of 0 min to 10 min.

3. Novel SpyTag lipid and SpyCatcher method: Two-step Membrane Modification for Probing Crowding Effects

Authors: N. Jahnke, M. Löwe, S. Bock, A. Kedrov, L. Hartmann

Paperdraft

Novel SpyTag lipid and SpyCatcher Method: Two-step Membrane Modification for Probing Crowding Effects

Nina Jahnke[1], Maryna Löwe[2], Sophia Bock[1], Alexej Kedrov[2], Laura Hartmann[1,3*]

[1]Institute of Macromolecular Chemistry, Heinrich-Heine University, Universitätsstraße 1, 40225 Düsseldorf, Germany

[2]Institute of Synthetic Membrane Systems, Heinrich-Heine University, Universitätsstraße 1, 40225 Düsseldorf, Germany

[3]Institute of Macromolecular Chemistry, University Freiburg, Stefan-Meier-Str. 31, 79104 Freiburg i.Br., Germany

*Corresponding author: laura.hartmann@makro.uni-freuburg.de

Keywords: SpyTag, SpyCatcher, Lipids, model membranes, crowding effects

Abstract

Biological membranes are densely decorated with proteins and carbohydrates, resulting in a highly dynamic and functionally complex network of biomolecules, a phenomenon known as molecular crowding. Despite the availability of advanced biological and chemical methods, investigating effects of molecular crowding remains challenging due to the intrinsic complexity and the molecular diversity of the biomolecules involved. Model membranes provide a powerful tool for studying these processes. However, the incorporation of large, sterically demanding molecules, such as proteins is often hindered by issues related to stability, solubility, and steric interference.

Here, we present a modular platform that enables an efficient integration of bulky membrane proteins through a two-step approach. Our strategy relies on a smaller synthetic precursor ligand-lipid-conjugate that is incorporated into the membrane and serves as a docking point for sterically demanding receptors that are specifically recognized by this ligand-precursor. The well-established SpyTag-SpyCatcher system was used to demonstrate a proof of this concept. This method facilitates the controlled presentation of complex membrane components, providing a versatile tool for mimicking the structural diversity of natural membranes and studying bio membrane interactions.

Introduction

Plasma membranes are highly dynamic and complex constructions that surround every cell and are fully decorated with proteins, lipids, peptides and polysaccharides, resulting in a diverse, heterogeneric environment. This so-called “crowding” can directly influence many biological mechanisms, such as intercellular interaction, host-pathogen recognition, assembly and functionality of membrane located macromolecules. [1-4]

Numerous studies have been documented on diverse impacts of molecular crowding on protein aggregation, folding, stability, oligomerization, enzymatic catalytic activity or complex-formation of receptor-ligands. [5-10] Membrane crowding therefore has a direct influence on cell communication, forming an integral part of life, and is thus also associated with the development of certain diseases, such as cancer. [11, 12] Studying and understanding the effects of molecular crowding in more detail is therefore an important field of research that can contribute significantly to the elucidation of various cellular processes. Given the diversity in size, structure, and functional roles of membrane proteins, studying these biomolecules presents a significant challenge in understanding the precise molecular events in detail. But not only due to their diversity in structure but also due to their dynamical changes makes the influence of crowding to biological mechanism complex and challenging to understand. [13]

Consequently, researchers frequently turn to artificial membranes to observe specific mechanism *in vitro* under more controlled conditions. Commonly used model membranes include lipid bilayers, liposomes or GUV’s. [14-16] This allows for variation of the density in the system by integrating different types of anchors into the membrane. Commonly used membrane anchors are for example polymer-based like linear and water-soluble polyethylene glycol (PEG) which is available in different sizes, polysaccharide-based such as the neutral, highly branched ficoll, or protein-based such as bovine serumin album (BSA) which is inert but creates a well heterogeny in surface as it is also found *in vivo.* [17-19] For this purpose, crowders can either be conjugated to a synthetic lipid via specific binding, or PEG lipids, for example, can be purchased in various lengths.

However, a common challenge in this approach is the labor-intensive and non-trivial nature of anchoring large membrane biomolecules. This often leads to destabilization of the artificial membranes and presents a considerable time-consuming barrier, as extensive optimization is typically required to establish suitable conditions. (Figure 1A,B). [20-22]

One solution is a two-step integration process, where a potential synthetic precursor ligand-lipid is integrated into the model membrane as anchoring point for sterically demanding receptors that selectively bind to this precursor ligand (Figure 1C).

A particularly exciting technology in this context that has also great potential for membrane manipulation is the SpyTag-SpyCatcher technology. The SpyTag-SpyCatcher is a protein-

based method to enable covalent linking of proteins. Both components originate from the cleavage and splitting of a fibronectin-binding protein domain. In this way, the short SpyTag peptide and the SpyCatcher protein were isolated. When both molecules are in proximity, they react specific and spontaneously in an autocatalytic triad, forming a very stable and irreversible amide bond. [23] The further advantage of protein-based crosslinkers in comparison to common crosslinkers is also the mild reaction condition, making it suitable for applications involving fragile proteins or living cells. Due to its reliability and stability, these technologies have been used in the design of novel biomaterials, protein engineering, and other applications where precise control over protein interactions and immobilization is crucial. [24-26]

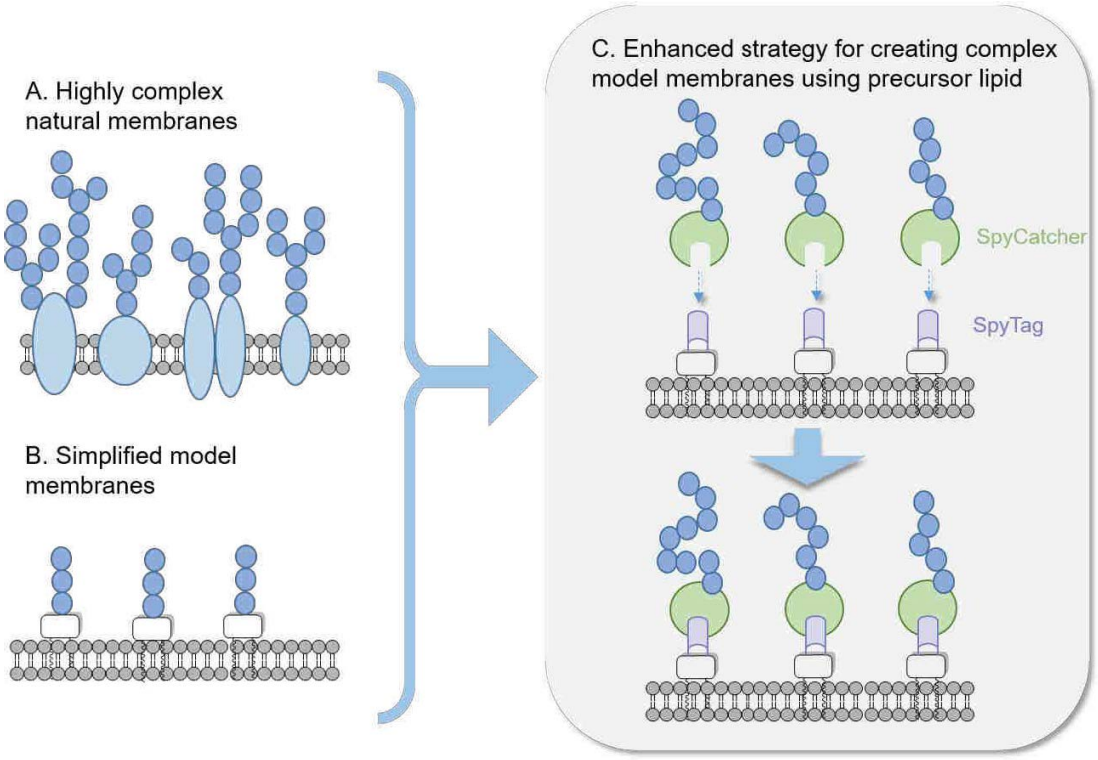

Figure 1. A. The complexity and heterogeneity of natural membranes present significant challenges for studying membrane-associated processes. B. Simplified model compounds are often used but may not represent the properties of natural membranes. C. Utilizing SpyTag-SpyCatcher technology to engineer precursor lipids for a two-step integration of sterically demanding receptors which furthermore allows for higher complexity.

There are already various applications in which the SpyTag-SpyCatcher technology has been used on plasma membranes. Bedbrook *et. al.* used the system to label membrane-localized, light-activated ion channels in live cells. For this purpose, the SpyTag peptide was biologically fused to a membrane protein then introduced to the membrane and afterwards conjugated to subsequently added SpyCatcher protein. [27] However, biologically modified macromolecules often face challenges related to a lack of control, whereas synthetic methods offer improved control over characterization, analysis, and further structural modifications. [28]

Here, we report the development of a synthetic SpyTag lipid as a novel tool to generate a small membrane anchor precursor which can be easily integrated into the membrane and then be manipulated with large SpyCatcher protein to alter the membrane and mimic, for example crowding effects. This feature enables a versatile platform, facilitating the expeditious introduction of a broad spectrum of membrane molecules onto a model membrane to generate a higher complexity, diversity and heterogeneity of crowding effects. With the development of SpyTag lipid we have established a novel method enabling the

Results and Discussion

Synthesis of SpyTag lipids

The SpyTag (ST) peptide was synthesized by using the well-established solid phase peptide synthesis. In short, amino acids bearing a carboxylic acid and a 9-fluorenylmethoxycarbonyl (Fmoc) -protected amine are coupled to an immobilizing resin. For efficient and selective coupling, the side chains of the respective amino acids must be protected until the peptide sequence can be cleaved off the resin. Furthermore, suitable coupling reagents such as benzotriazol-1-yloxytripyrrolidinophosphonium hexafluorophosphate (PyBOP)/ *N,N*-diisopropylethylamine (DIPEA) are used to activate the carboxylic acid. In addition to coupling, the repetitive deprotection of the N-terminus is also essential. By this method, stepwise coupling of amino acids is performed.

In this work the ST peptide was modified by the amino acid cysteine (Cys) to insert an orthogonal functionality to realize a thiol-en-click reaction with a maleimide functionalized phospholipid. It was important that Cys residue is in the C-terminal region of ST, because crystal structures and depletion assays reported that N-Term seemed to be essential for the binding with SpyCatcher (SC).[29] The C-terminal glycine (Gly) in the target structure acted as a spacer to the resin.[30] Commercially available preloaded Fmoc-Gly-TentaGel S resin was used for the synthesis. The ST peptide was then assembled using the solid-phase peptide synthesis described in Figure 2A. Therefore PyPOP/DIPEA was used for coupling and the remove of Fmoc protection group was performed with piperidine. Additionally, a Rhodamine B labelled ST peptide (RhST) and lipid was synthesized to generate a structure with fluorophore to track the insertion into model membranes. The fluorophore was coupled on the N-Term of ST peptide via solid-phase peptide synthesis using PyPOP/DIPEA as coupling reagents (Figure 2B).

After ST peptides were cleaved off the resin, using trifluoracetic acid, they were purified by ion exchange and preparative reversed-phase high-performance liquid chromatography (RP-HPLC) to obtain structures with relative purities of higher than 90%. Both structures were

subsequently analyzed by RP-HPLC-mass spectrometry (MS), matrix-assisted laser desorption/ionization mass spectrometry (MALDI-TOF-MS).

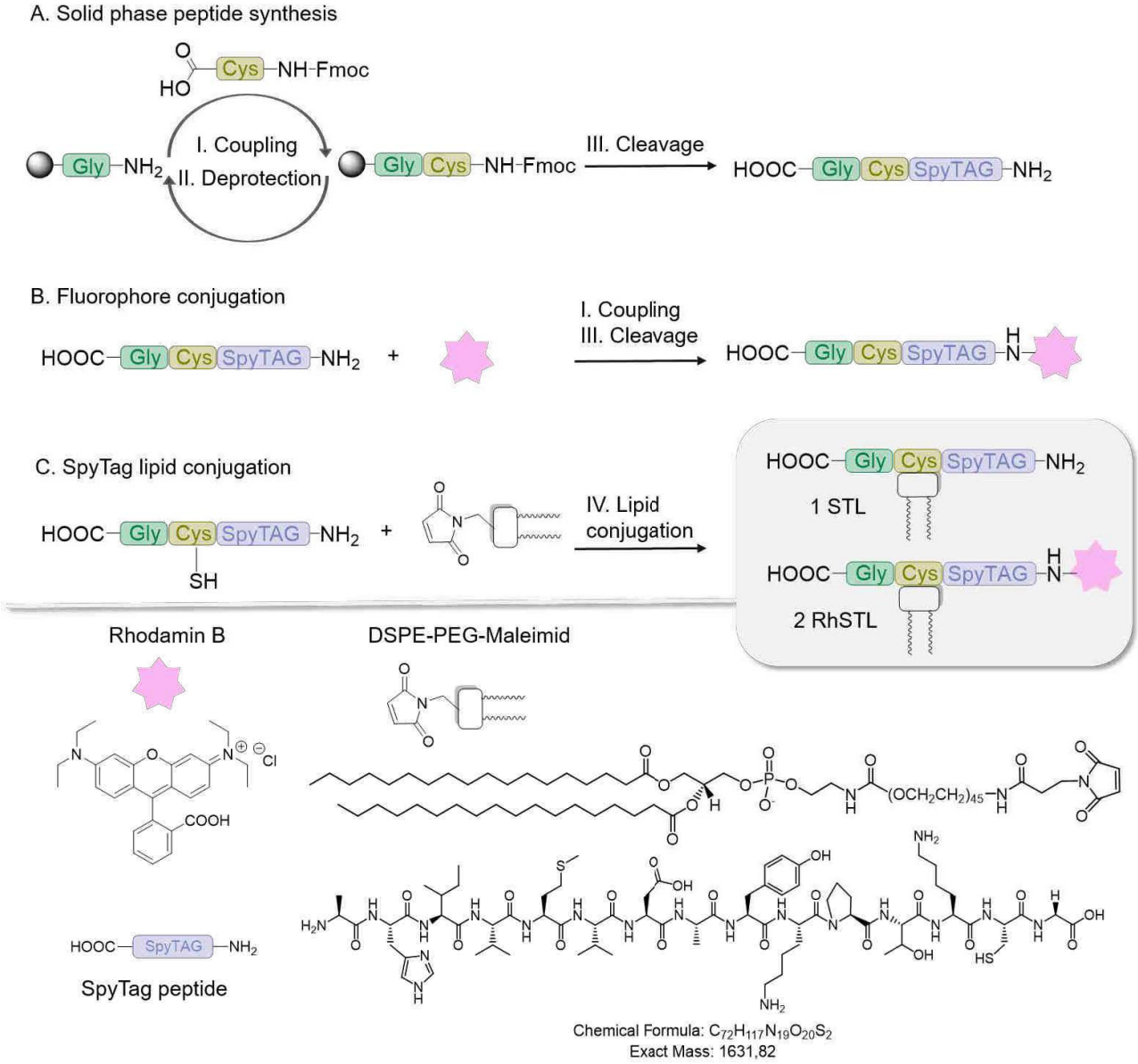

Figure 2. General principle of A. Solid-phase peptide synthesis B. fluorophore conjugation and C. lipid conjugation in solution.

For the conjugation between the lipid and the cysteine of the SpyTag peptide commercially available 1,2-distearoyl-sn-glycero-3-phosphoethanolamine-N-carbonyl-amino (polyethylene glycol) (DSPE-PEG)-maleimide was used as lipid. The conjugation reaction was performed in a mixture of *N,N*-dimethylformamide (DMF) and phosphate-buffered saline (PBS) (1:10) with 10 eq. tris(2-carboxyethyl) phosphine hydrochlorid (TCEP) overnight (See Figure 2C). Afterwards, the lipid conjugates were purified with a centrifugal concentrator (Molecular Weight Cut-off, MWCO = 10000). After lyophilization, the resulting products SpyTag lipid (STL) and rhodamine SpyTag lipid (RhSTL) were analyzed by MALDI-TOF-MS and ^{1}H-NMR (see SI). To quantify the conjugation, ^{1}H-NMR spectra were used. For this purpose, the spectrum of ST

peptide, unconjugated lipid (maleimide lipid, ML) and STL were compared (See SI Figure 9). To detect the conversion the ratio of the aromatic protons of the tyrosine (δ = 6.1 ppm, Intensity = 1.28; δ = 6.9 ppm, Intensity = 1.11) located in the peptide to the terminal alkyl residues (δ = 0.9 ppm, Intensity = 6) of the lipid was referenced (See SI Figure 10). In the case of RhSTL, quantification of conversion by ^{1}H-NMR was hindered due to spectral overlap between the fluorophore backbone signals and the reference resonances of tyrosine residues. The results are summarized in Table 1.

Table 1. MALDI-TOF-MS[a] and ^{1}H-NMR analytical data for STL conjugates

Lipid-conjugate	*MALDI-TOF-MS MW cal. for [M+Na+]*	*m/z found*	*Conversion [%]*
1 STL	$C_{211}H_{308}N_{23}O_{48}S_2PNa$ 4595.45	4596.1	66
2 RhSTL	$C_{239}H_{415}N_{24}O_{80}S_2PNa$ 5019.81	5020.2	-

Since the characterization and detection of lipid conjugates is often not trivial, additional thin layer chromatography (TLC) and colorimetric methods such as Kaiser test for the detection of amines and the Ellmann test for the detection of thiols were carried out. The results from Kaiser test and Ellmann's test are presented in Figure 3.

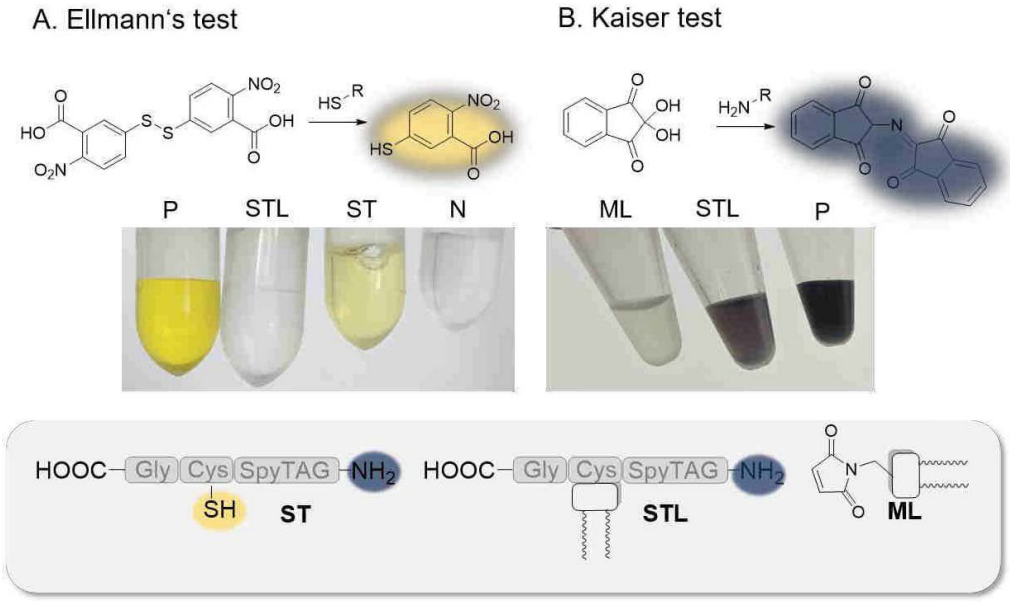

Figure 3. A. Ellmann's test to detect thiols using DTNB resulting in yellow TNB under the presence of thiols and basic conditions. B. Kaistertest to detect free amines in the presence of amines resulting in "Ruhemanns blau".

The Ellman's test detects free thiols as the reduction of disulfide bridges in Ellmanns Reagent (Dithio nitrobenzoic acid, DTNB) by these thiols results in 5-thio-2-nitrobenzoic acid (TNB) adduct which appears in a visible yellow color (Figure 3A). Compared to that, a colorless

solution indicates that there is no free thiol. The aim of this experiment is to test whether the ST peptide has an accessible Cys for conjugation and whether STL contains free ST peptide due to degradation or incomplete conjugation. To evaluate the results of the experiment, a positive control (P), by adding Cys as thiol source, as well as negative control (N) which contains valine (Val), an amino acid without thiols was conducted. STL was not expected to have any free thiols and indeed no color change was observed. In contrast, ST peptide was anticipated to possess free thiols available for conjugation and indeed shows a yellow color change (Figure 3A). These observations give an additional hint for successful peptide-lipid conjugation for STL.

To further validate the peptide's conjugation with the lipid, the Kaiser test was conducted (Figure 3B). The Kaiser test solution includes ninhydrin which reacts with free amines forming a blue product known as “Ruhemanns-blau”. Here, the presence of free amines, for example the N-terminus of STL is detected to draw further conclusions about the successful conjugation of the peptide to the lipid. This was compared with ML in which no free amines are present, and a negative result is expected accordingly. Here, lysine was used as positive control (P). The STL sample exhibited a distinctive blue coloration, indicative of the presence of amines. Compared to ML displayed no discernible coloration, aligning with anticipated results (Figure 3B). The pronounced and unambiguous color changes observed in the Ellman’s and Ninhydrin tests provided reliable confirmation of the reaction, making additional spectroscopic analysis unnecessary.

The retardation factor (Rf) value of STL was also determined using TLC (See SI Figure. 11). As eluent a mixture of chloroform, methanol and MiliQ® (65:20:5) was prepared for this purpose. As a comparison also ML (unconjugated lipid) and ST (free peptide) were applied. The plate was stained with iodine. For STL a Rf value of 0.85 was determined which makes sense compared to the non-polar ML (Rf = 0.22) and the polar ST (Rf = 0.99).

SpyTag lipid binds to SpyCatcher

To investigate the binding ability of the novel STL with the SC proteins, Sodium Dodecyl Sulfate – PolyAcrylamid Gel Electrophoresis (SDS-PAGE) was performed. Due to inconclusive results in our initial experiments investigating binding between STL and SC, it became necessary to develop an optimized approach to reliably detect and characterize the interaction. For this purpose, a fluorophore labelled RhST peptide was tested for binding using SDS-PAGE (See SI Figure 12). This pre-experiment served as a strategy to validate the generation of UV detection at 488 nm and ascertain the successful binding between the synthesized RhST peptide and SC. Building upon these findings, the methodology was extended to assess the

interaction of RhSTL with SC. For this purpose, the RhST peptide (Figure 4A) or RhSTL (Figure 4B) with SC were incubated, followed by application onto a gradient gel for analysis.

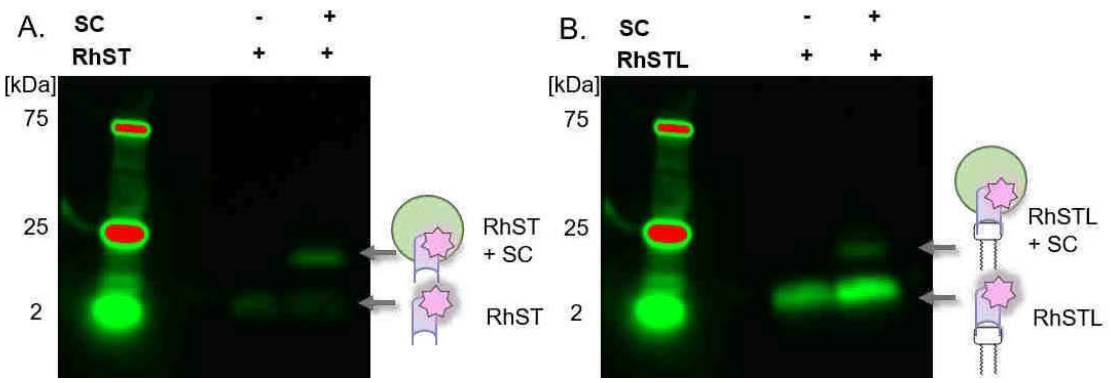

Figure 4. SDS-PAGE shows UV detection at 488 nm. Precision Plus Protein™ Kaleidoscope™ Standards,RhST (200 µM; 1 µL), RhST (200 µM; 1 µL) incubated with SC (167.8 µM; 0.5 µL) B. RhSTL (200 µM; 1 µL), RhSTL (200 µM; 1 µL) and SC (167.8 µM; 0.5 µL).

The first gel (Figure 4A) shows the labeled RhST peptide which was applied to both lanes while SC protein was only applied in the second lane. Similarly on the second gel (Figure 4B), the labeled RhSTL was applied in both lanes, and the SC protein was applied in the second lane.

First looking at the first gel, a distinct fluorescent band at the 2 kDa level was observed, attributable to the presence of the RhST peptide. In contrast, the second lane revealed both the uncoupled RhST peptide and an additional fluorescent band below 25 kDa. Given that the expected mass of the RhST peptide-SC complex is 17 kDa, the appearance of this band in the second lane suggests the successful formation of the corresponding complex.

Upon comparing the lanes of the second gel involving the application of RhSTL, analogous observations were noted. Considering that the complex formed by RhSTL and SC aligns with an approximate mass of 19 kDa, the observed fluorescent band in these runs can be attributed to the successful formation of this specific complex. Since RhST and RhSTL differ in mass by only about 2 kDa, only a marginal difference of the bands can be observed on the gel. In summary, it is evident that a binding interaction occurs between RhST and RhSTL with SC. However, it should be mentioned that unbound RhST and RhSTL can be detected in both gels. Several factors may account for the observed outcomes. First, a slightly lower concentration of SC may have been responsible, leading to an insufficient number of available binding partners for every molecule. Additionally, steric hindrance may have arisen due to the N-terminal fluorophore. Examination of the crystal structure of ST and SC reveals that the N-terminus primarily occupies the binding pocket. Incomplete binding was also noted with RhSTL, possibly due to the alkyl chains and PEG chain of the lipid, which may coil or cluster, complicating the binding process. However, these preliminary experiments successfully

demonstrated the functional and binding capabilities of synthetic lipid conjugated ST to SC through SDS-PAGE analysis.

Liposome preparation: SpyTag lipid incorporation into model membranes

Following the development of a detection method in preliminary experiments to ascertain the binding between the synthesized STL, the subsequent experiment aimed to demonstrate its successful integration into model membranes, specifically vesicles. To achieve this, liposomes were formulated.

For this purpose, 1,2-di-(9Z-octadecenoyl)-*sn*-glycero-3-phosphocholine (DOPC) was used as the matrix lipid component. Here the STL conjugates were used in total quantity of 5 mol% in the whole formulation. The lipids were formulated into homogenous sized liposomes using an extruder with a membrane size of 100 µm. The liposomes were analyzed using dynamic light scattering (DLS) to measure their diameter (d), from which the poly dispersity indices (PDI) could also be determined. The prepared liposomes resulted in uniform size and a low polydispersity (<0.2) indicating a homogeneous distribution in the solution. The zeta potential was also measured to provide further evidence of successful conjugation. Since the DOPC matrix lipid contains a positive head group, a tendentially negative to neutral potential is expected after conjugation. These results are shown in Table 2.

Table 2. DLS and Zeta potential for STL-conjugate.

Lipid-conjugate	*Diameter (d) [nm]*	*PDI*	*Zeta potential [mV]*[c]
1 STL	80 nm	0.149	-22,4

These results initially provide evidence of successful integration of the lipids into the membrane. In order to further confirm this and to prove the binding availability of the peptide on the membrane, further experiments were carried out with the liposomes.

Validation of SpyTag lipid incorporation using flotation and pelleting assays

The flotation and the pelleting assay are frequently used to test protein interactions e.g. protein-lipid interactions. For this purpose, also Alexa488 labelled SpyCatcher (SC-488) was developed. The efficient binding of the fluorophore labelled protein was verified with SDS-PAGE (See SI Figure 13).

The flotation assay or lipid flotation assay consists of incubating unilamellar vesicles, such as liposomes with a target protein and then floating the vesicles on a density gradient, such as

different sucrose concentrations. After centrifugation the proteins bound to the lipids are separated from the unbound proteins, as the lipids rise to the top phase while all unbound material remains in the bottom phase (Figure 5A). The STL decorated liposomes with 5 mol% were incubated with SC or SC-488 for 1h. Afterwards the mixture was placed into 30% sucrose. This was layered with 20% sucrose, followed by PBS. Then the mixture was ultracentrifuged for 1h and the bottom (B), middle (M) and top (T) fraction were collected and applied on SDS-PAGE. The gels were both Coomassie stained (left) and showed UV detection at 488 nm (right). In the corresponding gel it is shown the experiment with SC in in the first three lanes. The last three lanes belong to SC-488 (Figure 5B).

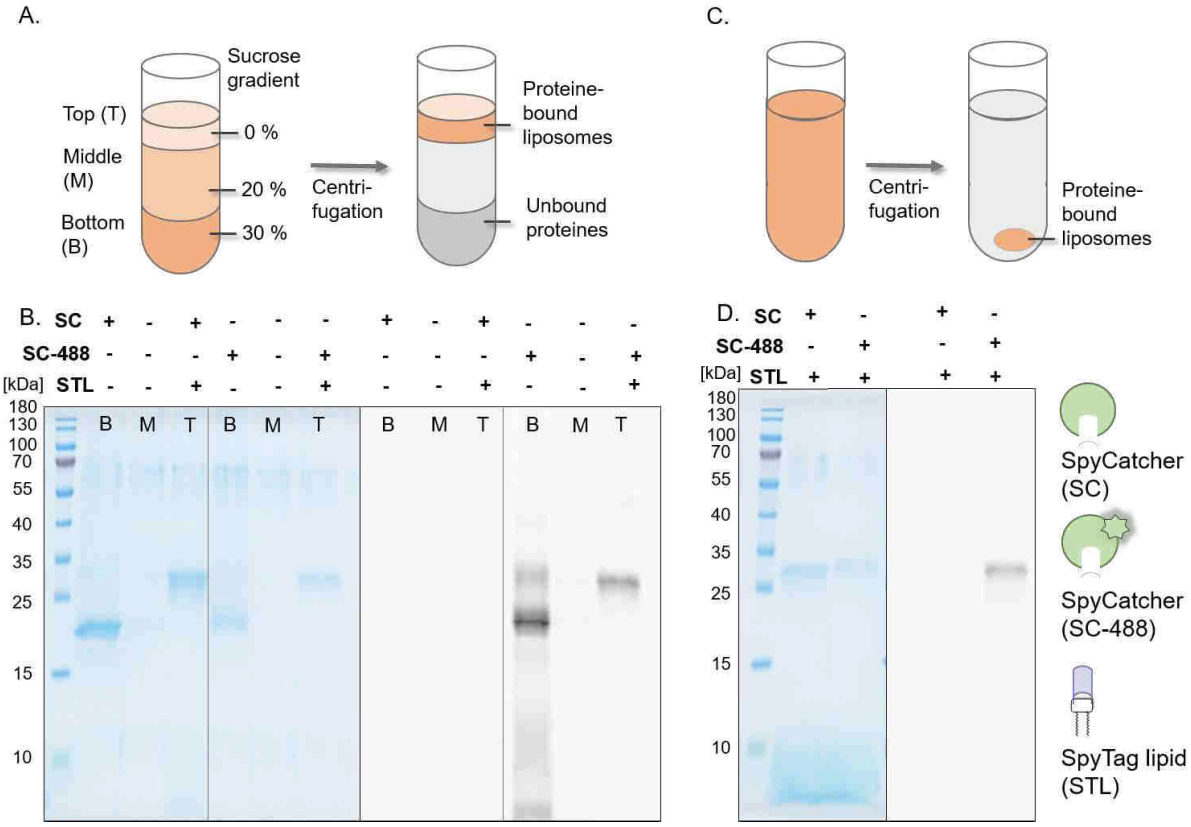

Figure 5. A. General principle of flotation assay. B. General principle of pelleting assay. C.SDS-PAGE of flotation assay with STL liposomes (L) Precision Plus Protein™ Kaleidoscope™ Standards. a) 50 µl liposomes prepared with STL (5 mol%; 2µl) incubated with SC (c = 142,7 µM; 8 µL). b) 50 µl liposomes prepared with STL (5 mol%; 2µl) SC-488 (c = 28,1µM; 50 µL). D. SDS-Page of pelleting assay with STL liposomes. (L) Precision Plus Protein™ Kaleidoscope™ Standards c) 50 µl liposomes prepared with STL (5 mol%; 2µl) incubated with SC (c = 146 µM; 1 µL) d) 50 µl liposomes prepared with STL (5 mol%; 2µl) SC-488 (c = 28.1 µM; 1 µL).

Considering the bottom fraction (B) of Coomassie gel a band at about 20 kDa is detected. This can be assigned to the SC which was not bound to the liposomes. As expected, no band was detected in the middle fraction (M). The top fraction (T) is of particular interest due to the presence of a band with a higher mass within a range of 25 to 35 kDa. Given that the observed molecular weight exceeds that of the lipid alone, it is assumed that SC has successfully associated with the liposome. Since unbound protein was found in the bottom fraction, no complete conjugation can be assumed. This observation may be attributed to the limited

incorporation of STL into the liposomal membrane, which restricts the overall availability of STL for binding. Additionally, the peptide ligands (STL) could be localized both on the surface and within the interior of the vesicle, which may limit the accessibility of STL to SC and contribute to incomplete binding. Nevertheless, it can be said that the binding on the liposome could be successfully demonstrated. Since neither STL nor SC has fluorescent properties, no signal was observed under UV light in this case.

With the help of the SC-488 in the other three lanes UV feedback was possible. The lanes in the Coomassie gel show a similar behavior to SC, which indicates also successful binding. Observing the gel under UV, the previous assumptions of the binding were underpinned. The band observed in the bottom fraction (B) shows a clear UV signal, clearly confirming its identity as SC-488. The band in the top fraction (T), which also shows a higher mass, gives a fluorescent signal, which can be attributed to the fact that SC-488 must have bound to liposomes.

In addition to the flotation assay, the pelleting assay was performed. For the pelleting assay, the vesicles, such as liposomes are mixed with a target protein, furthermore the mixture is centrifuged for one hour at high speeds. The supernatant and thus unbound protein are removed while the pellet, which contains the vesicles with bound protein, is resuspended. (Figure 5C). Therefore, liposomes containing 5% STL were mixed and incubated with either SC or SC-488. Then the mixture was ultracentrifuged for 1h at high speed. The supernatant with unbound proteins was removed and the remaining pellet resuspended and applied on the gel. One lane shows SC, while the other represents SC-488 (Figure 5D). In both cases, the bands are between 25 and 35 kDa. Based on the results of the flotation assay, it can be assumed that this is the bound protein on the liposome. Similarly, fluorescence observation reveals the presence of a band corresponding to SC-488, further substantiating the binding and validating all preceding findings.

In summary, it can be said that flotation as well as pelleting assay showed a successful binding of SC or SC-488 to STL which were incorporated in liposomes.

Visualization of SpyTag lipid incorporation using GUVs

In order to further investigate the integration of STL into a model membrane fluorescence microscopy was performed using GUV's as model membrane. GUVs are artificially produced, larger lipid vesicles that serve as model systems to study the properties and behavior of biological membranes. These vesicles, with diameters typically ranging from 1 to 100 micrometers, are larger than conventional liposomes, providing advantages for visualization under the microscope. Additionally, their low curvature makes them more similar to natural biological membranes. These results demonstrated the successful manipulation of the model

membrane through *in situ* crosslinking of SC on the membrane surface, mediated by the incorporation of STL into GUVs.

In an initial experiment, RhSTL was introduced into a GUV using the polyvinyl alcohol (PVA) method to demonstrate successful integration (see SI Figure 16). Following successful integration, three distinct GUVs were designed and developed using electroporation method. In the first GUV, the fluorescently labeled RhSTL was incorporated into the membrane (Figure 6A). In the second experiment, a GUV was created with STL and SC-488 was subsequently added to confirm two-step modification of the membrane through STL-SC-488 binding (Figure 6B). As a negative control, a third GUV was prepared with only ML incorporated into the membrane, where no binding of SC-488 was anticipated (Figure 6C).

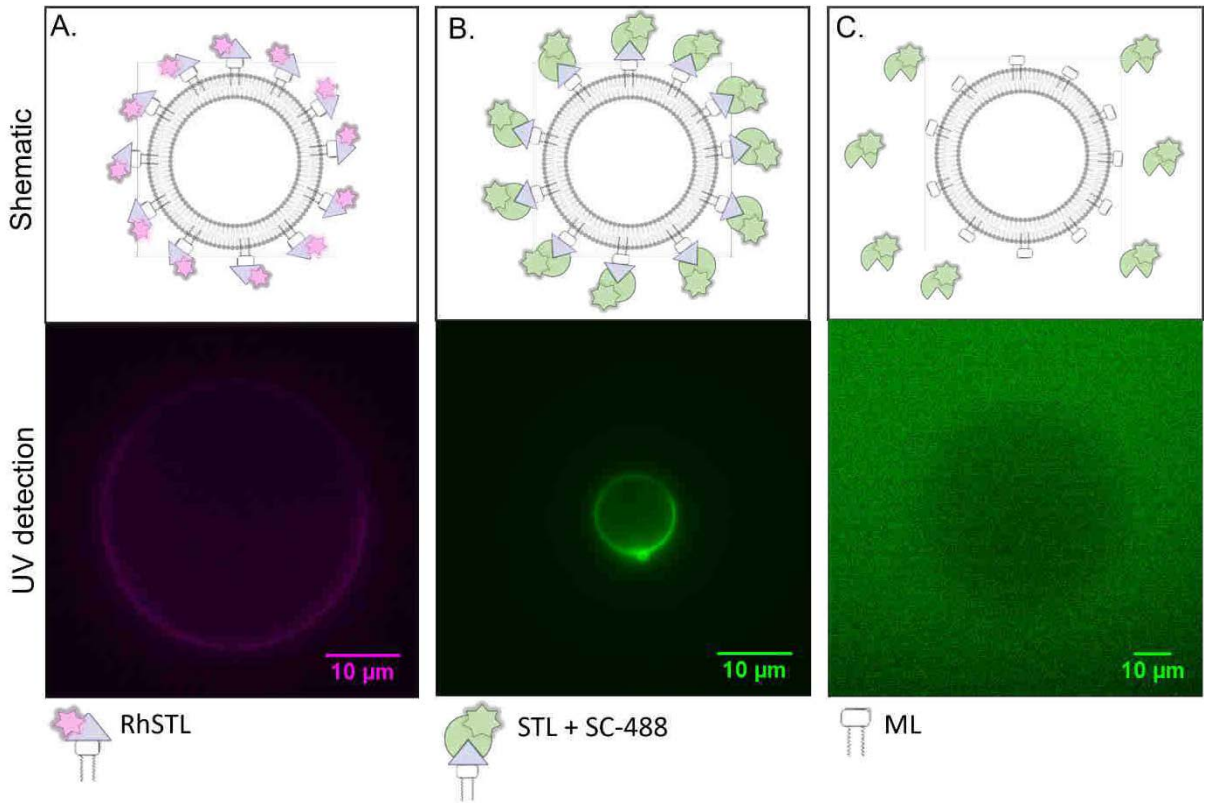

Figure 6. A. GUV prepared with RhST exhibiting fluorescence on the membrane surface, indicating successful incorporation of RhSTL. B. GUVs prepared with STL, followed by incubation with 10µl SC-488, displaying fluorescence on the membrane, which signifies the binding of SC-488 to the STL-modified membrane. C. Control GUVs composed of ML, incubated with SC-488, show no fluorescence or colocalization, indicating the absence of nonspecific binding of SC-488 to the membrane surface.

Transmitted light microscopy revealed that the GUVs were homogeneous in size, with diameters ranging from 80to 100 µm (See SI Figure 17). Upon fluorescence imaging, the first panel displays a GUV incubated with RhSTL (Figure 6A). A fluorescent signal on the membrane surface indicates successful integration of the lipid into the membrane. Notably, fluorescence is not completely homogeneous across the membrane. This inhomogeneity is likely due to the formation of peptide clusters, potentially resulting from electrostatic interactions. Alternatively, the variability in fluorescence could arise from the fluorophore

existing in both open and closed conformations, influenced by the local pH, leading to differential fluorescence behavior.

The middle panel illustrates the incorporation of STL into the membrane and subsequent binding of the labeled SC-488 (Figure 6B). Fluorescence is observed on the membrane, indicating the successful binding of SC-488 to STL, as STL itself is non-fluorescent. The GUV in this experiment appears significantly smaller compared to the others, which may be due to the loading of large proteins onto the membrane surface. This loading could induce membrane compression, leading to the fragmentation of the GUVs into smaller vesicles. This issue can be addressed through optimization of the GUV composition, such as by incorporating additional matrix lipids (e.g., cholesterol). Alternatively, other model systems, such as lipid bilayers, could be employed to accommodate larger ligands without the risk of vesicle fragmentation.

The negative control, in which only ML was incorporated into the membrane, demonstrates that fluorescence is observed in the background and not localized on the membrane. This confirms that STL must be present for successful binding, and that there is no nonspecific aggregation on the membrane surface. These results further support the successful integration of the precursor lipid, STL, into the membrane. Additionally, the binding of the fluorescent SC-488 to the membrane was effectively demonstrated. Collectively, these findings indicate that the membrane can be efficiently manipulated with this two-step approach where STL is first integrated and then conjugated to SC proteins.

Conclusion and Outlook

This work laid the foundation for a modular platform of synthetic probes or molecules for membrane manipulation. Our approach was to create a small synthetically accessible peptide lipid, the STL, which is incorporated into the membrane as a precursor and serves as a docking spot for sterically demanding biomolecules, such as the SC protein that in this manner could be successfully anchored into the membrane. Despite chemical modification of the ST, we were successfully verified binding of the SC. Additionally, a synthetic STL was incorporated into model membranes, such as liposomes and GUVs. The binding between SC protein and the STL was demonstrated in these modified model membranes. In summary, the development of the ST lipid has enabled the creation of a small precursor molecule for integrating the sterically demanding SC into model membranes.

In future studies, a platform of modified SC proteins can be developed and easily incorporated into membranes through this STL precursor. A potential modification can be achieved by incorporating Cys that is expressed in the SC. Via this cysteine, additional conjugation of various polymers, such as polyethylene glycol (PEG), polysaccharides, or other

polymer chains can be linked to the protein, providing additional properties to the protein such as size or hydrophilicity and increase the degree of membrane crowding. The recently introduced native grafting from approach from the Hartmann group, the Thiol-induced and Light-Activated Controlled Radical Polymerization (TIRP) offers a suitable strategy for such a synthetic protein modification. [31]

Acknowledgements

We acknowledge the support of the German Research Foundation (DFG) within the Collaborative Research Center 1208 “Identity and Dynamics of Membrane Systems”.

References

(1) Rincón, V. n.; Bocanegra, R.; Rodríguez-Huete, A.; Rivas, G.; Mateu, M. G. Effects of macromolecular crowding on the inhibition of virus assembly and virus-cell receptor recognition. *Biophysical journal* **2011**, *100 3*, 738-746.

(2) Kim, Y. C.; Best, R. B.; Mittal, J. Macromolecular crowding effects on protein-protein binding affinity and specificity. *The Journal of chemical physics* **2010**, *133 20*, 205101.

(3) Minton, A. P. Implications of macromolecular crowding for protein assembly. *Current opinion in structural biology* **2000**, *10 1*, 34-39.

(4) Garenne, D.; Noireaux, V. Analysis of cytoplasmic and membrane molecular crowding in genetically programmed synthetic cells. *Biomacromolecules* **2020**.

(5) van den Berg, B.; Ellis, R. J.; Dobson, C. M. Effects of macromolecular crowding on protein folding and aggregation. *The EMBO Journal* **1999**, *18*.

(6) Chen, Z.; Atefi, E.; Baumgart, T. Membrane Shape Instability Induced by Protein Crowding. *Biophysical journal* **2016**, *111 9*, 1823-1826.

(7) Kedia, N. Crowding Agents Direct Amyloid Beta into Membrane-Active Oligomers. *Biophysical Journal* **2017**, *112*.

(8) Matic, M.; Saurabh, S.; Hamacek, J.; Piazza, F. Crowding-induced Uncompetitive Inhibition of Lactate Dehydrogenase: Role of Entropic Pushing. *The journal of physical chemistry. B* **2020**.

(9) Stroberg, W.; Schnell, S. Concentration Sensing in Crowded Environments. *bioRxiv* **2020**.

(10) Ota, C.; Suzuki, H.; Tanaka, S.-i.; Takano, K. Dispersion Effect of Molecular Crowding on Ligand-Protein Surface Binding Sites of Escherichia coli RNase HI. *Langmuir : the ACS journal of surfaces and colloids* **2022**.

(11) Bu, X.; Ashby, N.; Vitali, T.; Lee, S.; Gottumukkala, A.; Yun, K.; Tabbara, S.; Latham, P.; Teal, C.; Chung, I. Cell crowding activates pro-invasive mechanotransduction pathway in high-grade DCIS via TRPV4 inhibition and cell volume reduction. *bioRxiv* **2025**.

(12) Takatori, S. C.; Son, S.; Lee, D. S. W.; Fletcher, D. A. Engineered molecular sensors for quantifying cell surface crowding. *Proceedings of the National Academy of Sciences of the United States of America* **2023**, *120*.

(13) Hall, D.; Minton, A. P. Macromolecular crowding: qualitative and semiquantitative successes, quantitative challenges. *Biochimica et Biophysica Acta (BBA) - Proteins and Proteomics* **2003**, *1649* (2), 127-139. DOI: https://doi.org/10.1016/S1570-9639(03)00167-5.

(14) Basu, A.; Maity, P.; Karmakar, P.; Karmakar, S. Preparation of Giant Unilamellar Vesicles and Solid Supported Bilayer from Large Unilamellar Vesicles: Model Biological Membranes. *Journal of Surface Science and Technology* **2017**, *32*, 85-92.

(15) Andersson, J.; Köper, I. Tethered and Polymer Supported Bilayer Lipid Membranes: Structure and Function. *Membranes* **2016**, *6*.

(16) Routledge, S. J.; Linney, J. A.; Goddard, A. D. Liposomes as models for membrane integrity. *Biochemical Society transactions* **2019**.

(17) Zhang, S.; Li, W.; Luan, J.; Srivastava, A. K.; Carnevale, V.; Klein, M.; Sun, J.; Wang, D.; Teora, S. P.; Rijpkema, S. J.; et al. Adaptive insertion of a hydrophobic anchor into a poly(ethylene glycol) host for programmable surface functionalization. *Nature Chemistry* **2022**, *15*, 240 - 247.

(18) Erwin, N.; Patra, S.; Dwivedi, M.; Weise, K.; Winter, R. H. A. Influence of isoform-specific Ras lipidation motifs on protein partitioning and dynamics in model membrane systems of various complexity. *Biological Chemistry* **2017**, *398*, 547 - 563.

(19) Feig, M.; Sugita, Y. Variable interactions between protein crowders and biomolecular solutes are important in understanding cellular crowding. *The journal of physical chemistry. B* **2012**, *116 1*, 599-605.

(20) Sharma, M. K.; Gilchrist, M. L. Templated assembly of biomembranes on silica microspheres using bacteriorhodopsin conjugates as structural anchors. *Langmuir : the ACS journal of surfaces and colloids* **2007**, *23 13*, 7101-7112.

(21) Gamage, R. S.; Chasteen, J. L.; Smith, B. D. Lipophilic Anchors that Embed Bioconjugates in Bilayer Membranes: A Review. *Bioconjugate chemistry* **2023**.

(22) Puiggalí-Jou, A.; Del Valle, L. J.; Alemán, C. Biomimetic hybrid membranes: incorporation of transport proteins/peptides into polymer supports. *Soft matter* **2019**, *15 13*, 2722-2736.

(23) Hatlem, D.; Trunk, T.; Linke, D.; Leo, J. C. Catching a SPY: using the SpyCatcher-SpyTag and related systems for labeling and localizing bacterial proteins. *International journal of molecular sciences* **2019**, *20* (9), 2129.

(24) Gao, X.; Fang, J.; Xue, B.; Fu, L.; Li, H. Engineering Protein Hydrogels Using SpyCatcher-SpyTag Chemistry. *Biomacromolecules* **2016**, *17* (9), 2812-2819. DOI: 10.1021/acs.biomac.6b00566.

(25) Reddington, S. C.; Howarth, M. Secrets of a covalent interaction for biomaterials and biotechnology: SpyTag and SpyCatcher. *Current opinion in chemical biology* **2015**, *29*, 94-99.

(26) Wang, B.-P.; Yin, X.; Huang, M.-Y.; Li, T.-Y.; Long, X.-F.; Li, Y.; Niu, F.-X. A Self-assembling γPFD-SpyCatcher hydrogel scaffold for the coimmobilization of SpyTag-enzymes to facilitate the catalysis of regulated enzymes. *Journal of Agricultural and Food Chemistry* **2024**, *72* (36), 19940-19947.

(27) Bedbrook, C. N.; Kato, M.; Kumar, S. R.; Lakshmanan, A.; Nath, R. D.; Sun, F.; Sternberg, P. W.; Arnold, F. H.; Gradinaru, V. Genetically encoded spy peptide fusion system to detect plasma membrane-localized proteins in vivo. *Chemistry & biology* **2015**, *22* (8), 1108-1121.

(28) Del Vecchio, D.; Dy, A. J.; Qian, Y. Control theory meets synthetic biology. *Journal of The Royal Society Interface* **2016**, *13*.

(29) Li, L., Fierer, J., Rapoport, T., Howarth, M. Structural analysis and optimization of the covalent association between SpyCatcher and a peptide Tag. *Journal of molecular biology*, **2014**, 426 2, 309-17.

(30) Hagan, R. M.; Björnsson, R.; McMahon, S. A.; Schomburg, B.; Braithwaite, V.; Bühl, M.; Naismith, J. H.; Schwarz-Linek, U. NMR spectroscopic and theoretical analysis of a spontaneously formed Lys–Asp isopeptide bond. *Angewandte Chemie* **2010**, *122* (45), 8599-8603.

(31) Bonda, L.; Valles, D. J.; Wigger, T. L.; Meisner, J.; Braunschweig, A. B.; Hartmann, L. TIRP─ Thiol-Induced, Light-Activated Controlled Radical Polymerization. *Macromolecules* **2023**, *56* (14), 5512-5523.

Supporting Information

Novel SpyTag lipid and SpyCatcher Method: Two-step Membrane Modification for Probing Crowding Effects

Nina Jahnke[1], Maryna Löwe[2], Sophia Bock[1], Alexej Kedrov[2], Laura Hartmann[1,3*]

[1]Institute of Macromolecular Chemistry, Heinrich-Heine University, Universitätsstraße 1, 40225 Düsseldorf, Germany

[2]Institute of Synthetic Membrane Systems, Heinrich-Heine University, Universitätsstraße 1, 40225 Düsseldorf, Germany

[3]Institute of Macromolecular Chemistry, University Freiburg, Stefan-Meier-Str. 31, 79104 Freiburg i.Br.,Germany

*Corresponding author: laura.hartmann@makro.uni-freiburg.de

Materials and Methods

All chemicals were commercially available.

Aceton (≥ 99.8%), acetonitrile (≥99,9%), Dulbeccos phosphate buffer saline (DPBS, 1x) and PageRuler™ Prestained Protein Ladder (10 bis 180 kDa) were purchased from Fischer scientific, DSPE-PEG(2000) Maleimide (>99%) was purchased from Avanti Polar Lipids Inc., diethyl ether (with BHT as inhibitor, ≥ 99.8%), dimethyl sulfoxide-d6 (99%), methanol (99%), tris(2-carboxyethyl)phosphine hydrochloride (99%), Trizma®base (99%) and triisopropylsilane (TIPS, 98%) were purchased from Sigma Aldrich, *N,N*-dimethylformamide (DMF, 99.8%, for peptide synthesis) was purchased from Acros Organics, dichloromethane (DCM, 99%), trifluoroacetic acid (TFA, 99%), were purchased from Fluorochem UK, benzotriazole-1-yl-oxy tris-pyrrolidino-phosphonium hexafluorophosphate (PyBOP,>98%) and diisopropylethyl amine (DIPEA, 99%) were purchased from Carl Roth, Acetic acid (≥99,8%) was purchased from Merck, Rhodamine B (99%) was purchased from TCI,

Amino acids and resins

Fmoc-Ala-OH (≥99,%) was purchased from BLD PHARMA TECH GmbH, Fmoc-His(trt)-OH (≥99%), Fmoc-Lys(boc)-OH (≥99%) were purchased from Merck, Fmoc-Val-OH(≥99%) , Fmoc-Ile-OH (≥99%), Fmoc-Met-OH (≥99%), Fmoc-Tyr(tBu)-OH (≥99%), Fmoc-Cys(trt)-OH (≥99%), Fmoc-Pro-OH (≥99%), Fmoc-Thr(tBu)-OH (≥99%) and Fmoc-Asp(tbu)-OH (≥99,9%) were purchased from Iris Biotech GmbH, AG® 1-X8 Resin (100-200 mesh) was purchased from Bio-Rad; Fmoc Gly TentaGel® R HMPA resin (0.22 mmol/g) was purchased from RAPP Polymers.

Nuclear magnetic resonance spectroscopy

The ^{1}H-NMR spectra were performed using a Bruker Avance III 600 spectrometer operating at 600MHz at room temperature. The Data was analyzed using MestReNova.

Matrix-assisted laser desorption ionization time-of-flight mass spectrometry

MALDI-TOF measurements were conducted on a Ultraflex I from Bruker Daltonics. The samples were measured in linear mode with cyano-4-hydroxycinnamic acid (HCCA) as matrix in a ratio of 1:2. As a solvents MiliQ®/acetonitrile (1:1) or Lectin-Binding-Buffer (LBB) was used.

High Resolution-Mass Spectrometry (HR-MS)

HR-MS measurements were conducted on a Bruker UHR-QTOF maxis 4G with a direct inlet via syringe pump, an ESI source and a quadrupole Time of Flight (QTOF) analyser. Samples were dissolved in water with a concentration of 1 mg/ml.

Reversed Phase High Pressure Liquid Chromatography coupled with ESI Mass Spectrometry

RP-HPLC-MS measurements were performed on an Agilent 1260 Infinity instrument coupled to a variable wavelength detector (VWD) and a 6120 Quadrupole LC/MS containing an Electrospray Ionization (ESI) source (operation mode positive and negative, m/z range from 200 to 2000). A MZ-AquaPerfect C18 (3.0 × 50 mm, 3 µm) RP column from Mz-Analysentechnik GmbH was used with a flow rate of 0.4 ml/min at 25 °C. As eluent system water/acetonitrile containing 0.1% formic acid was applied.

Preparative Reversed Phase- High Pressure Liquid Chromatography (prep RP-HPLC)

An Agilent 1260 Infinity device, which is coupled to a variable wavelength detector (VWD) (set to 214 nm and 280nm) was used to purify the peptide. The sample was collected manual. An RP HPLC column, CAPCELL PAK C18 (20 x 250 mm, 5 µm), was used. The mobile phases A and B were H_2O and acetonitrile, each containing 0.1 vol% formic acid. The flow rate was set to 10 ml/min.

Thin layer chromatography

The samples were diluted in DCM. The eluent consists of chloroform:methanol: MilliQ in ratio of 65:20:5. Maleimide-DSPE-Lipid, SpyTag-Lipid and SpyTag peptide were applied onto the silica plate. After the elution, the plate was incubated in a phosphor chamber for 10 min.

Freeze Drying

Samples were dissolved in MiliQ® and frozen with liquid nitrogen. Afterwards it was freeze dried with an Alpha 1-4 LD plus instrument from Martin Christ Freeze Dryers GmbH.

VivaSpin

Lipid-conjugated peptides were purified using a Viva Spin concentrator from Sarstead with MWCO of 10.000 and then concentrated on the Centrifuge Heraeus Megafuge 8 with 5500rpm.

Fluorescence Microscopy

Florescence microscopy was performed on EVOS® FL Cell Imaging System from Thermofisher or Olympus IX73 microscope using a 60x oil objective. Gain 300. Exposure:40.

Solid-phase synthesis

General: The synthesis of the peptide was automated using a solid-phase peptide synthesizer. Peptides were prepared on a preloaded Fmoc-Gly-HMPA resin with a loading of 0.22 mmol/g. The batches were 0.1 mmol.

Coupling protocol: Initially the resin was swollen two times for 15 min in DCM. After deprotection of the Fmoc group the first amino acid was coupled. 5 eq amino acid and 5 eq PyBOB were weighed into a 15 ml falcon and dissolved in 2 ml DMF before 2 ml of a 1M DIPEA-solution was added. The reactor was shaken for 60 min. Afterwards the resin was washed 5 times with 5 ml DMF.

Fmoc cleavage: The Fmoc group was cleaved using a 25 Vol% Piperidine in DMF. The deprotection step was carried out 3 x 15 min. Afterwards the resin was washed 5 times with 5 ml of DMF.

Fluorophore coupling: For a 0.1 mmol preparation, 3 eq of Rhodamin B and 3.5 eq were dissolved in 1 ml DCM/DMF (1:1) and 10 eq DIPEA were added. After coupling for one hour, the peptide was washed alternately 5 times each with methanol and DCM. This was repeated until the washing solution became colorless. Finally, it was washed 3 times with DMF.

Cleavage from solid-phase: For cleavage of the peptide from the resin, it was transferred from the reaction vessel into a 10 ml polypropylene syringe. Then a cleavage cocktail consisting of 90 Vol% TFA and 10 Vol% TIPS with a total volume of 2 ml was added to the syringe and incubated for 60 min at room temperature. Subsequently, the solution was poured into 40 ml ice-cold diethyl ether. The resulting precipitate was centrifuged for 4 min at 4400 rpm and the supernatant was decanted of. The resulting pellet was then washed 2 times by resuspension in cold diethyl ether and subsequent centrifugation. After the pellet was dried under nitrogen for 20 min it was dissolved in Milli-Q water and freeze dried.

Anionic Exchange

For the anionic exchange 150 mg AG® 1-X8 Resin was used for a 0.1 mmol batch. To activate the resin, it was first washed 3 times with a 1.6 N acetic acid solution followed by 3 times 0.16 N acetic acid solution. The freeze-dried peptide was dissolved in 1 mL Milli-Q, drawn onto the solid-phase syringe and shaken for one hour. The solution was then collected, and the syringe tip was also rinsed with 0.05 ml Milli-Q®. The collected sample was freeze-dried.

Lipid conjugation

Maleimide-DSPE-PEG(2000) (2 mg, 1eq.) were dissolved in 100µL DMF and degassed with argon for 1 min. SpyTag-Peptide (5.54 mg, 5 eq) and TCEP (0.4 mg, 2 eq.) was dissolved in 900 µL PBS and let sit for 3 min. Afterwards, SpyTag/TCEP solution was added to the lipid and degassed with argon for 1 min. Then the mixture was shaken overnight. To remove free peptide from the lipid-conjugate a VivaSpin with a molecular weight cut-off (MWCO) of 10.000 g mol $^{-1}$ was used. This process was repeated 15 times with 15 ml MilliQ-water. Yields given

in mg represent the successfully conjugated lipids. The content of unconjugated lipids was quantified with ^{1}H-NMR.

Ellmanns test

For Ellmanns test a fresh solution of DNTB in PBS (1mM, pH 7.4) was prepared. 1 -5 mg sample were mixed in 1 ml PBS. Then 0.5 ml of Sample and 0.5 ml of DNTB solution were mixed and sit for 10 min.

Kaiser test

For Kaiser test 3 solutions were prepared.
A: 16.5 mg of KCN was dissolved in 25 ml dest. Water. 1 ml of this solution was diluted with piperidine.

B: 1g ninhydrin was dissolved in 20 ml of n-butanol.

C: 40 g phenol was dissolved in 20 ml of n-butanol.

1-5 mg sample was mixed with 2-3 drops of each solution (A-C) and heated with heatgun for 5 minutes.

SpyCatcher expression

SpyCatcher-Cys and SpyCatcher-GSG were expressed in *E. coli* BL21(DE3) from the plasmid pDEST14 (Addgene). The cultures were grown at 37°C in LB medium (Carl Roth) supplemented with 100 µg/mL ampicillin till OD_{600} of 0.6 was reached. The expression was induced by addition of 0.5 mM IPTG and proceeded for 3 h. The cells were harvested at 5000*xg* for 10 min (SLC-6000 fixed angle rotor, Thermo Fisher/Sorvall) and resuspended in 50 mM Tris/HCl, pH 7.4, 150 mM KCl, 200µM TCEP and 1 mM AEBSF. After cell lysis (Microfuidizer M-110P, Microfluidics Corp) the cell lysate was clarified by centrifugation for 30 min at 235000x*g* (Rotor 45Ti, Beckman Coulter). Next, the lysate was loaded on the pre-washed Ni^{2+}-NTA agarose resin (Qiagen) and incubated on the rolling bench at 4°C for 1 h. The beads were washed with buffer containing 50 mM Tris/HCl, pH 8.0, 150 mM KCl, 200µM TCEP and 10 mM imidazole. SpyCatcher was eluted with 50 mM Tris/HCl, pH 8.0, 150 mM KCl, 200µM TCEP and 300 mM imidazole and loaded on Superdex 200 10/300 column (Cytiva) in 20 mM Tris/HCl, pH 7.4, 150 mM KCl and 200µM TCEP. The peak fraction containing SpyCatcher was collected, supplemented with 5% glycerol, aliquoted and stored at -80°C. Aliquots from each step of purification were collected and analyzed by 15% SDS-PAGE. The final protein concentratin was 142,7 µM.

Fluorescent labelling of SpyCatcher

An aliquot of SpyCatcher-Cys was spiked with a 10-fold excess of CF488-maleimide fluorophore and incubated at RT for 2 h. Unconjugated dye was then removed using size exclusion chromatography (Superdex 200 10/300 column (Cytiva) in 20 mM Tris/HCl, pH 7.4, 150 mM KCl). The final protein concentration was 28.1 µM.

SDS-PAGE

The polyacrylamide gels used for the SDS page were produced according to the following compositions.

Seperating gel (18 %)		**Collecting gel**	
Milli-Q®	1,43 ml	Milli-Q®	3,0 mL
30% Acrylamid/Bisacrylamid	6 ml	30 % Acrylamid/Bisacrylamid	700 µL
1,5 M TRIS-HCl pH 8,8	2,5 ml	0,5 M TRIS-HCl pH 6,8	1,25 mL
10 % SDS	100 µl	10 % SDS	50 µL
10 % APS (Ammoniumperoxodisulfate)	60 µl	10 % APS	25 µL
TEMED (Tetramethyethylendiamine)	13 µl	TEMED	20 µL

First, the 18 % separating gel mixture was added to the gel and covered with isopropanol. After the separating gel had polymerized, the collecting gel was added. The comb was then inserted. The finished gels were wrapped in a wet paper towel and stored in a cool place until use. An electrophoresis chamber from Bio-Rad was used for SDS-PAGE. To carry out the electrophoresis, Milli-Q® was first added to mix the samples better. A sample buffer was then added to all samples. Electrophoresis was carried out at 210 V and 400 mA for about 50 to 60 min.

Liposome formulation

To receive 5 mol% lipid in the liposome 0.5-1 mg lipid were dissolved in 200µl chloroform together with 30µl DOPC. Chloroform was removed by evaporation, and the resulting solid was resuspended with PBS buffer. The liposomal suspension was then homogenized using an extruder equipped with a 100 nm pore-size membrane to achieve uniform particle size distribution.

DLS and Zeta potential

The assay was performed using a glass cuvette-containing 1 ml MQ added with 10µl of 5 mol% liposome solution. PDI were determined via Gaussian fit of the DLS cure giving the standard deviation and applying PDI = $(\sigma/d)^2$. Zeta potentials were measured with a zeta sizer Nano-Z.

Flotation Assay

For the flotation assay 50 µL liposomes (5mM, 5 mol% STL) and 8µl SC (142,7 µM) or 50 µl SC-488 (28,1 µM) were incubated for 1h. Samples were incubated for 1h min at 25°C and mixed with 60% sucrose (w/v). The reaction was loaded into the centrifugation tube and sequentially layered with 250 µL and 50 µL of buffers, containing 20% and 5% sucrose, respectively. The tubes were centrifuged for 1 h at 289000*xg* (Rotor S120-AT3, Thermo Scientific™) and the samples were carefully collected in total to three fractions with Hamilton syringe starting with the bottom fraction (250 µL), followed by middle (125 µL) and top fraction (125 µL). The proteins in the collected fractions were analyzed with SDS-PAGE.

Pelleting Assay

For the pelleting assay 5 µl liposomes (5mM, 5% STL) were mixed and incubated with either 0.8 – 1 µL SC (140 µM). Samples incubated for 1h, diluted with 500 uL buffer (PBS?), then pelleted at 289000xg for one hour (Rotor S120-AT3, Thermo Scientific™). Supernatant was removed and pellet was collected in SDS-Page sample buffer and analyzed

GUV formulation

PVA-Method:

The lyophilized RhSTL was dissolved in chloroform (4 mg/mL). From this, 5 µL were removed and 25 µL DOPC were added (0.5/99.5 mol%). In addition, a 5% (w/w) solution of polyvinyl alcohol in Milli-Q® was prepared by heating to approximately 90°C. The PVA solution was applied in a circle to a microscope cover glass, which was previously rinsed with chloroform, and dried for 30 min in an oven at 45°C under vacuum. The lipid solution was then diluted with 90 µL chloroform (1 mg/mL). 10 µL of the dissolved STL were then applied to the dried PVA film and dried for a few minutes in an oven under vacuum so that the solvent could evaporate. This step was repeated twice. A circular chamber was then formed around the PVA film using Vitrex wax plates and a solution of 10% sucrose in PBS was added. After about an hour, the desired vesicle size was reached and the GUVs were placed in a reaction vessel. For visualization under fluorescent microscope (EVOS® FL Cell Imaging System), he chamber slide was first coated with BSA (bovine serum albumin) (10 mg/mL) and incubated for 10 min.

The solution was then carefully removed and washed three times with 250 µL DPBS. DPBS buffer (250 µL) was then added and 5 µL of the finished GUVs pipetted into it.

Electroporation method

STL or ML were dissolved in chloroform to receive a concentration of 1 mg/ml. Afterwards 1,9 µl STL or ML was mixed with 25 µl DOPC (2 mg/ml) and PEG2000- PE (2 mol %). GUVs were prepared by electro formation in teflon swelling chambers. The lipid mixtures were spread on ITO-coated glass slides and evaporated under reduced pressure (95 mbar, 30 min). Electro formation was performed in a lactose solution matching the osmolarity of the lectin binding buffer (2.4 V, 89 Hz, 90 min).

GUV-SC-488 Binding

For the STL-GUV and SC-488 Binding 50 µl of fresh prepared STL-GUV was incubated with 10µl SC-488 and gently shaken for 1 h at RT and were visualized under the fluorescent microscope (Olympus IX73).

Characterization of synthetic structures

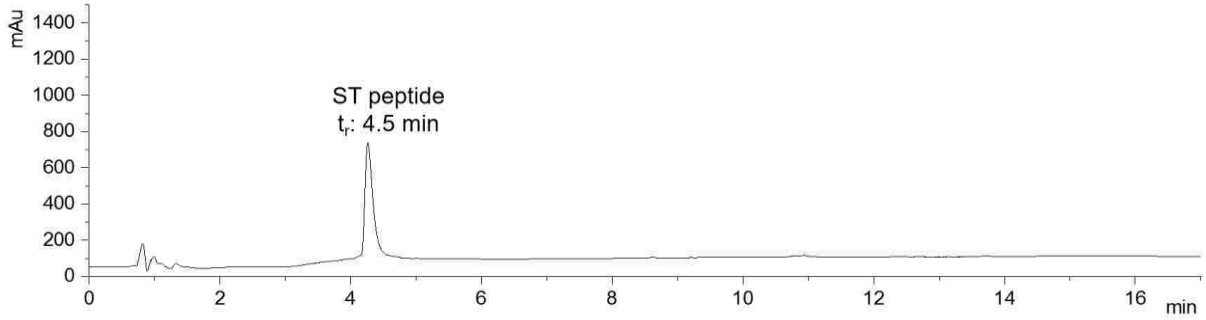

SI Figure 1. **ST peptide** detected at t_r = 4.5 min with relative purity >95% by RP-HPLC (linear gradient from 5-95 Vol% eluent H_2O/acetonitrile in 17 min at 25°C, VWDA1 A Wavelength = 214nm).

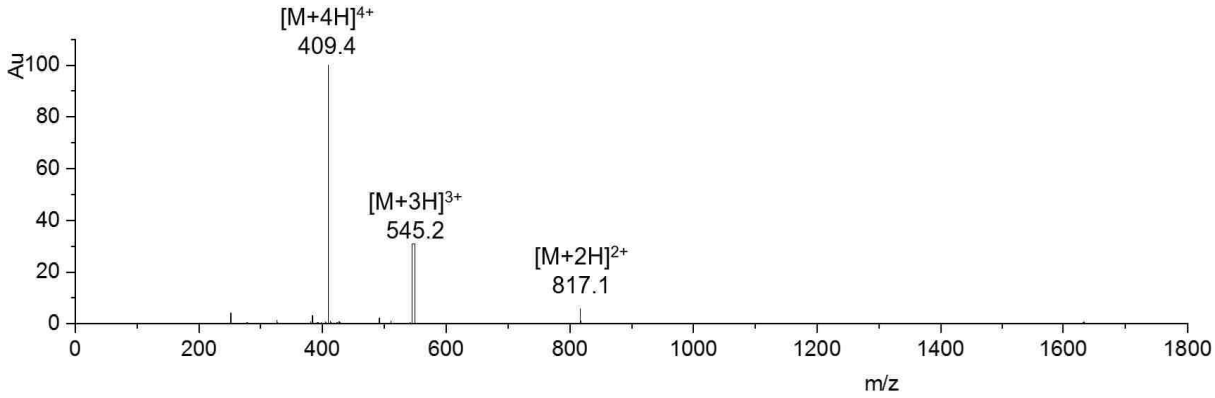

SI Figure 2. **ST peptide** analyzed with ESI-MS in a m/z range of 200-2000.

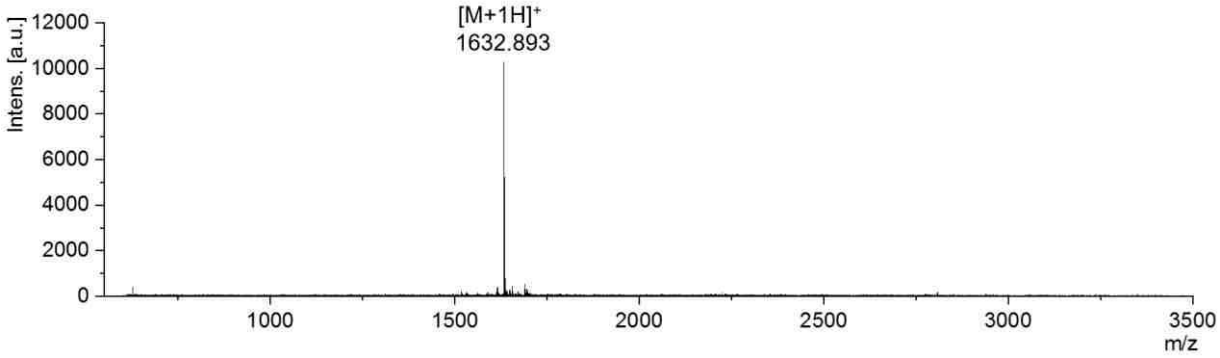

SI Figure 3. **ST peptide** analyzed with MALDI-TOF-MS in a m/z range of 500-3500 using HCCA as matrix in a compound to matrix ratio of 1:10.

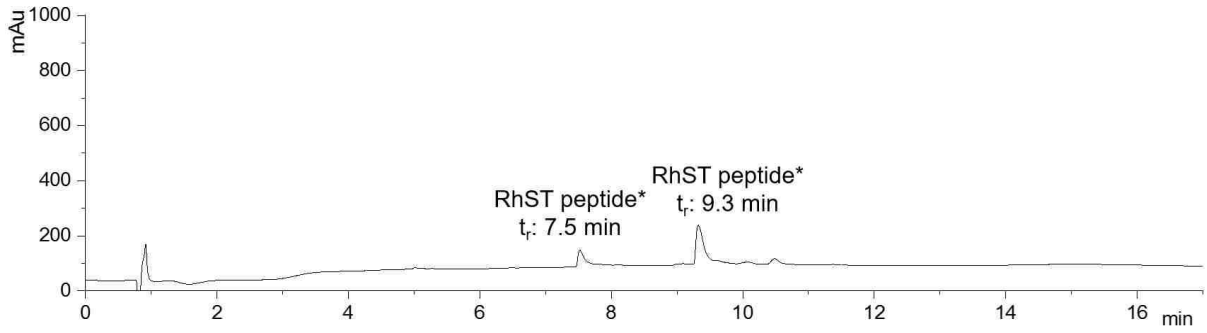

SI Figure 4. **RhST peptide** detected at t_r = 7.5 min and 9.3 min with relative purity >90% by RP-HPLC (linear gradient from 5-95 Vol% eluent H_2O/acetonitrile in 17 min at 25°C, VWDA1 A Wavelength = 214nm). *The splitting of the signals can be attributed to a constitutional isomer of the fluorophore.

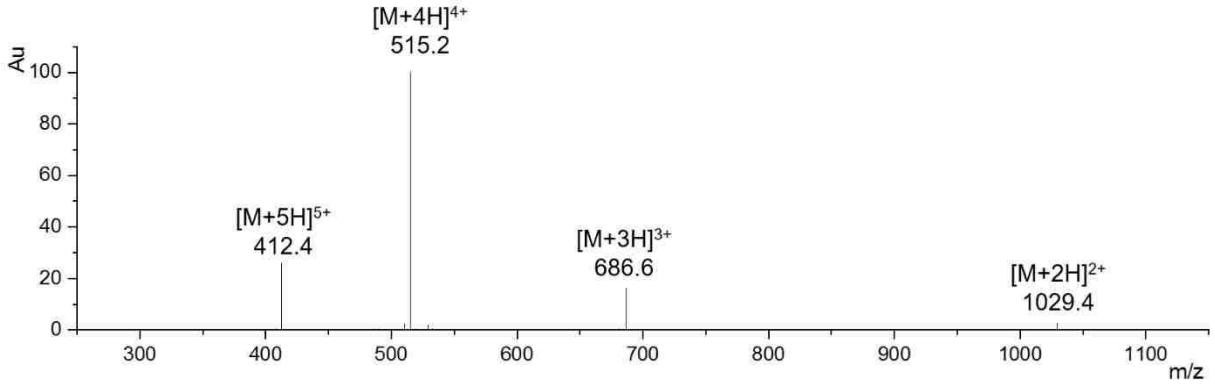

SI Figure 5. **RhST peptide** analyzed with ESI-MS in a m/z range of 200-2000.

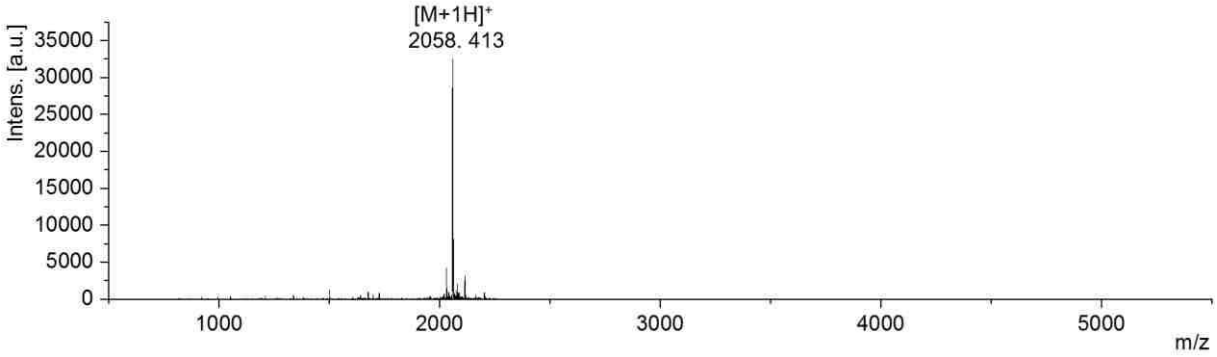

SI Figure 6. **RhST peptide** analyzed with MALDI-TOF-MS in a m/z range of 500-3500 using HCCA as matrix in a compound to matrix ratio of 1:10.

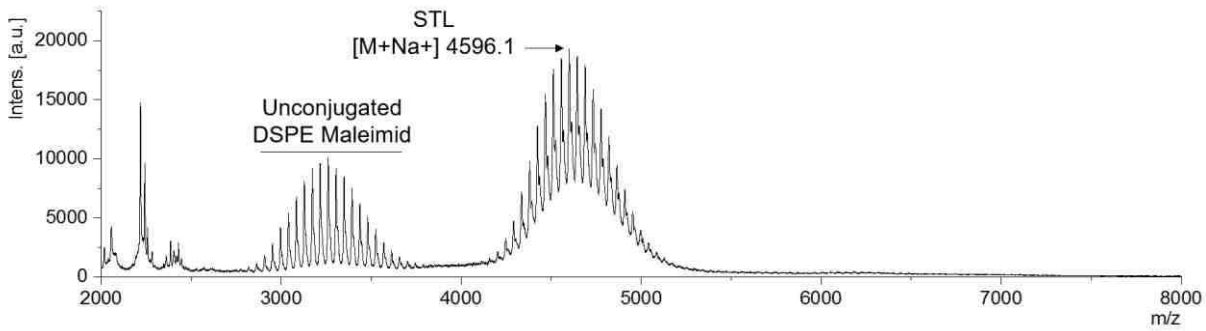

SI Figure 7. **STL** analyzed with MALDI-TOF-MS in a m/z range of 2000-8000 m/z using HCCA as matrix in a compound to matrix ratio of 1:2.

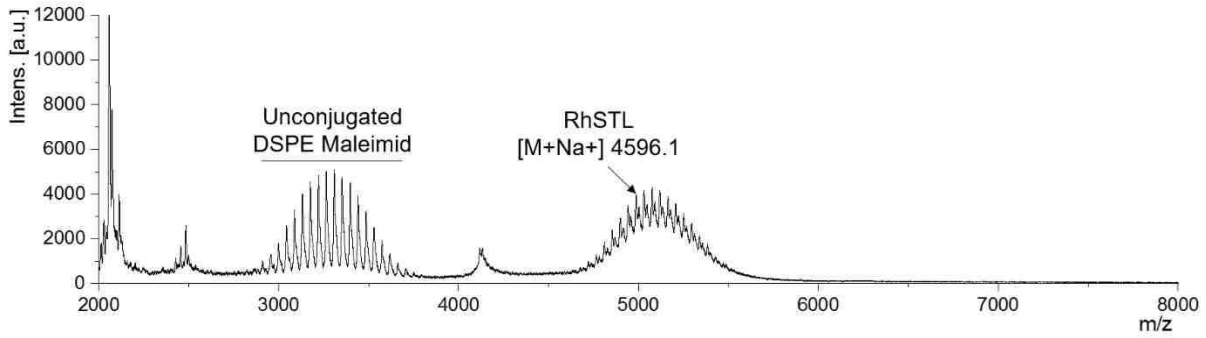

SI Figure 8. **RhSTL** analyzed with MALDI-TOF-MS in a m/z range of 2000-8000 m/z using HCCA as matrix in a compound to matrix ratio of 1:2.

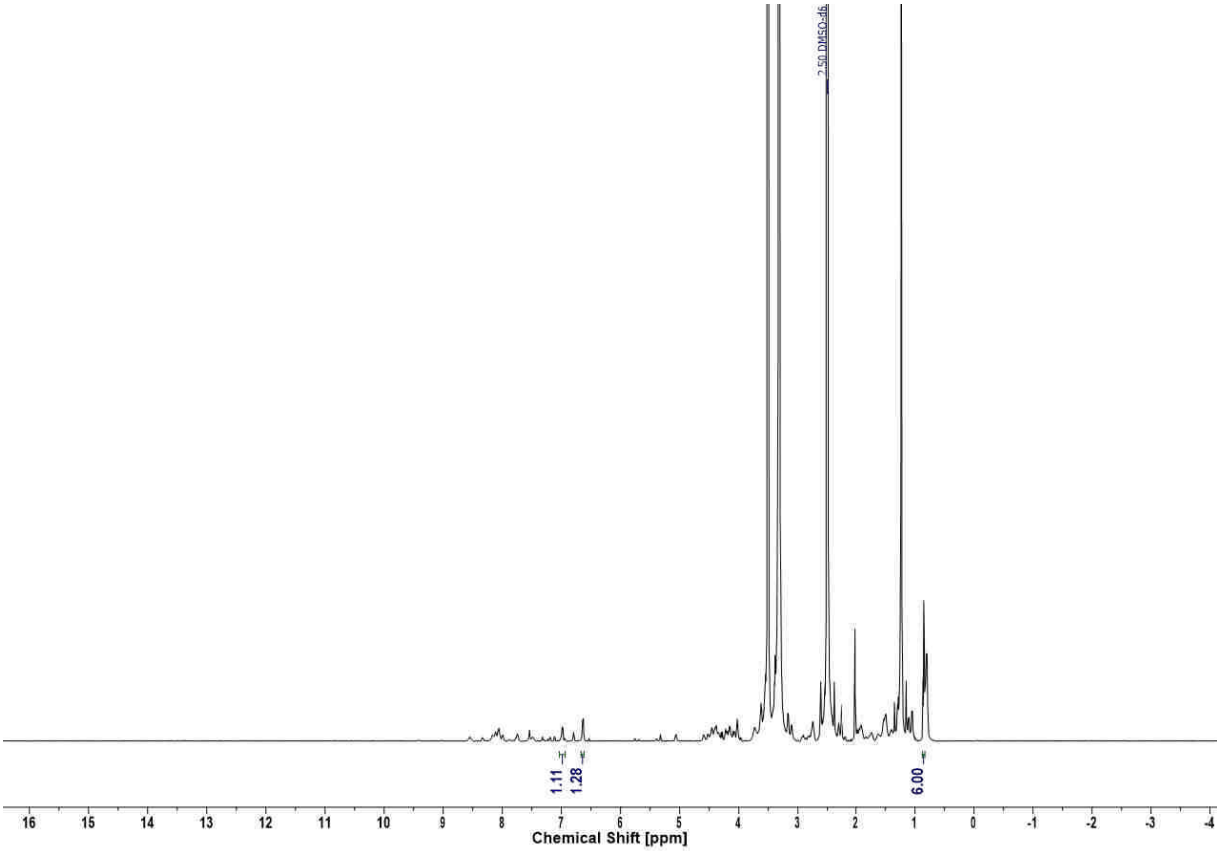

SI Figure 9. ^{1}H-NMR (600 MHz) spectra of compound **STL** in DMSO.

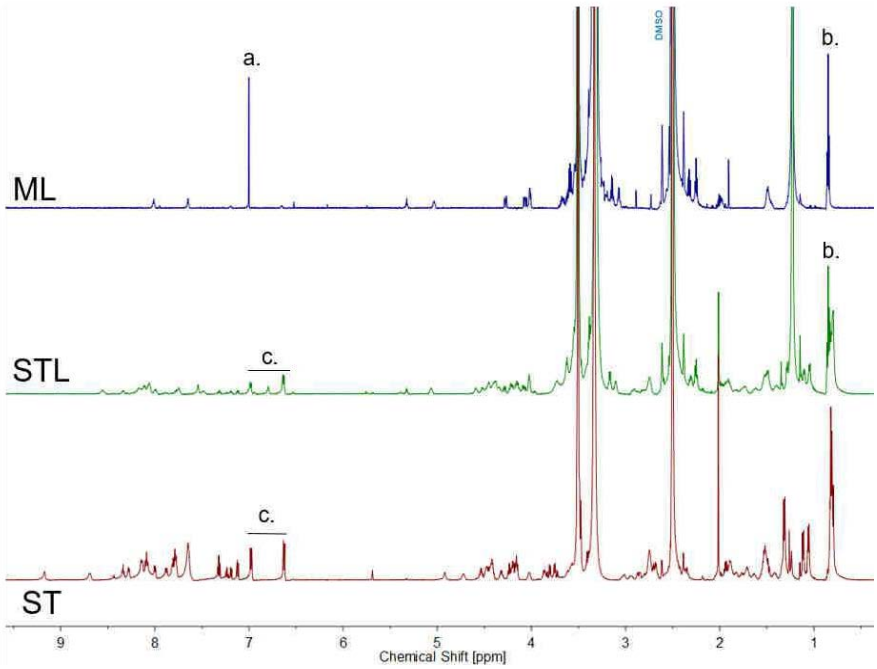

SI Figure10. ^{1}H-NMR (600 MHz) spectra to compare ML (precursor lipid), STL and ST peptide in DMSO. Highlighting specific proton signals: (a) Maleimide protons, which disappear in the STL spectrum following coupling; (b) Methyl peaks corresponding to lipids, observed in both ML and STL spectra; (c) Protons from the tyrosine, clearly visible in both ST and STL spectra.

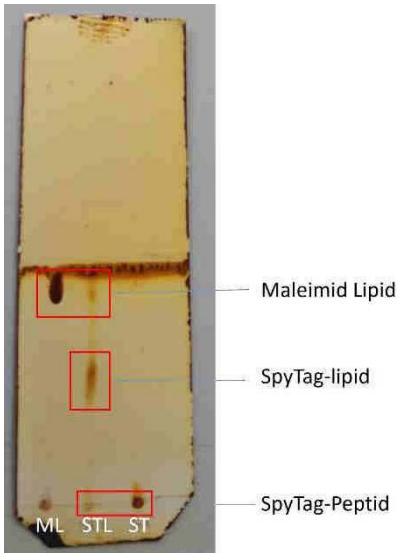

SI Figure 11. TLC with eluent of chloroform: methanol: MiliQ® in 65:20:5. Stained with iodine.

SDS-Pages

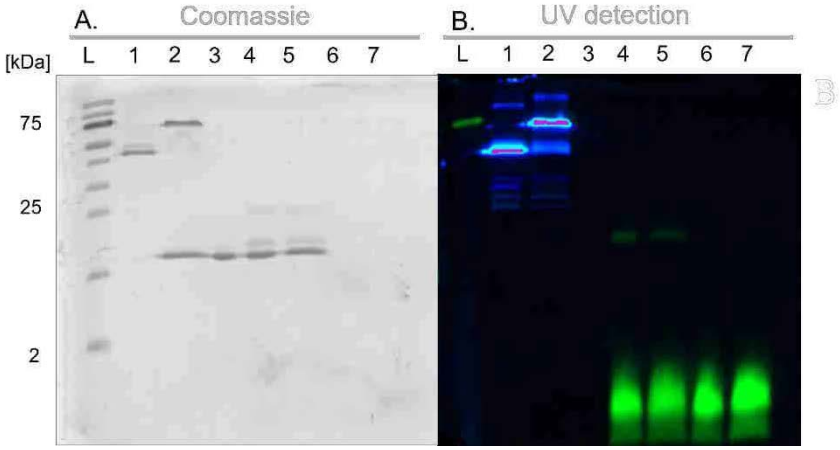

SI Figure 8. SDS-PAGE of **RhST** with A. Coomassie and B. UV detection at 488 nm (L) Precision Plus Protein™ Kaleidoscope™ Standards (1) FRET107 which is CFP and YFP labelled ST (2µl) (2) FRET 107 (2µl) and SC (3) SC (167,8 µM; 0,5 µL) (4) RhST(200 µM; 1 µL) and SC (0,5 µL) (5) RhST (200 µM; 1 µL) and SC (167,8 µM; 0,5 µL) heated to 95 °C, (6) RhST (200 µM; 1 µL) (7) RhSTL. (200 µM; 1 µL) heated to 95°C

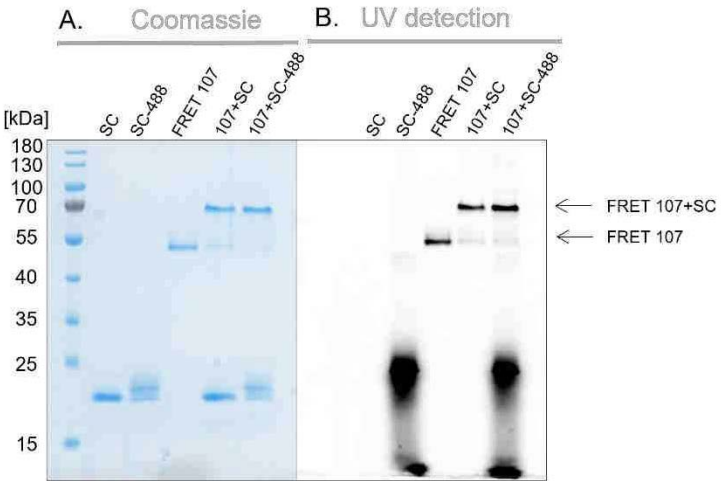

SI Figure 9. SDS-Page for SC-448 binding with A. Coomassie and B. UV detection at 488 nm (L) Precision Plus Protein™ Kaleidoscope™ Standards. (1) SC (167,8 µM; 0,5 µl), (2) SC-488 (28,1 µM, 6µl), (3) FRET 107 (2µl), (4) FRET 107(2µl) and SC (167,8 µM; 0,5 µl), (6) FRET 107 (2µl) and SC-488 (28,1 µM, 6µl)

Dynamic light scattering and Zeta potential

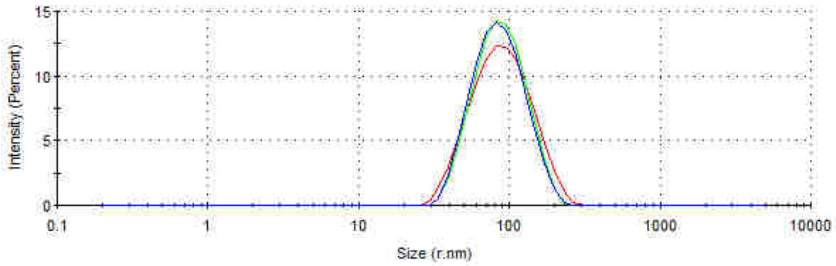

SI Figure 10. Exemplary DLS spectrum of **STL.**

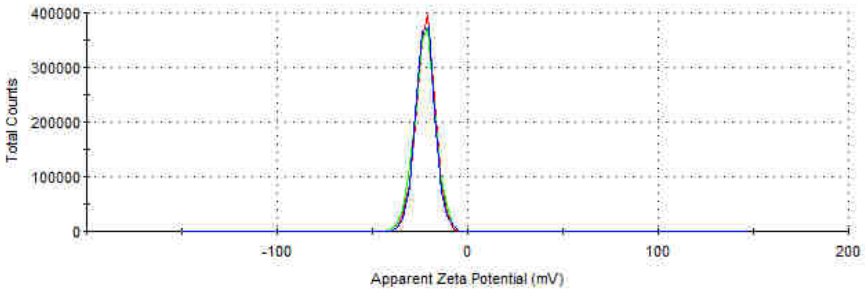

SI Figure 11. Exemplary Zeta potential of **STL.**

Microscopic Images

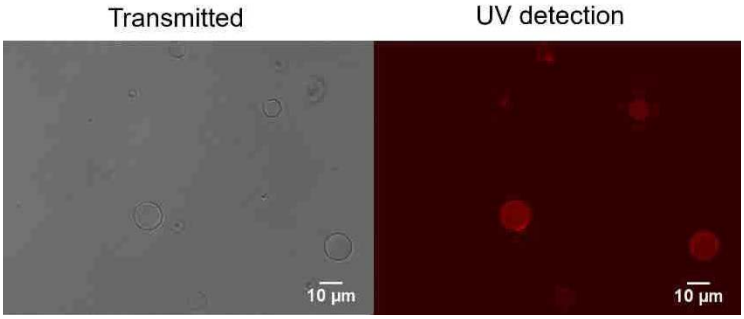

SI Figure 12. Preliminary formation of GUV formulation with **RhSTL** using PVA method visualized with transmitted light and UV detection at 532 nm under the microscope.

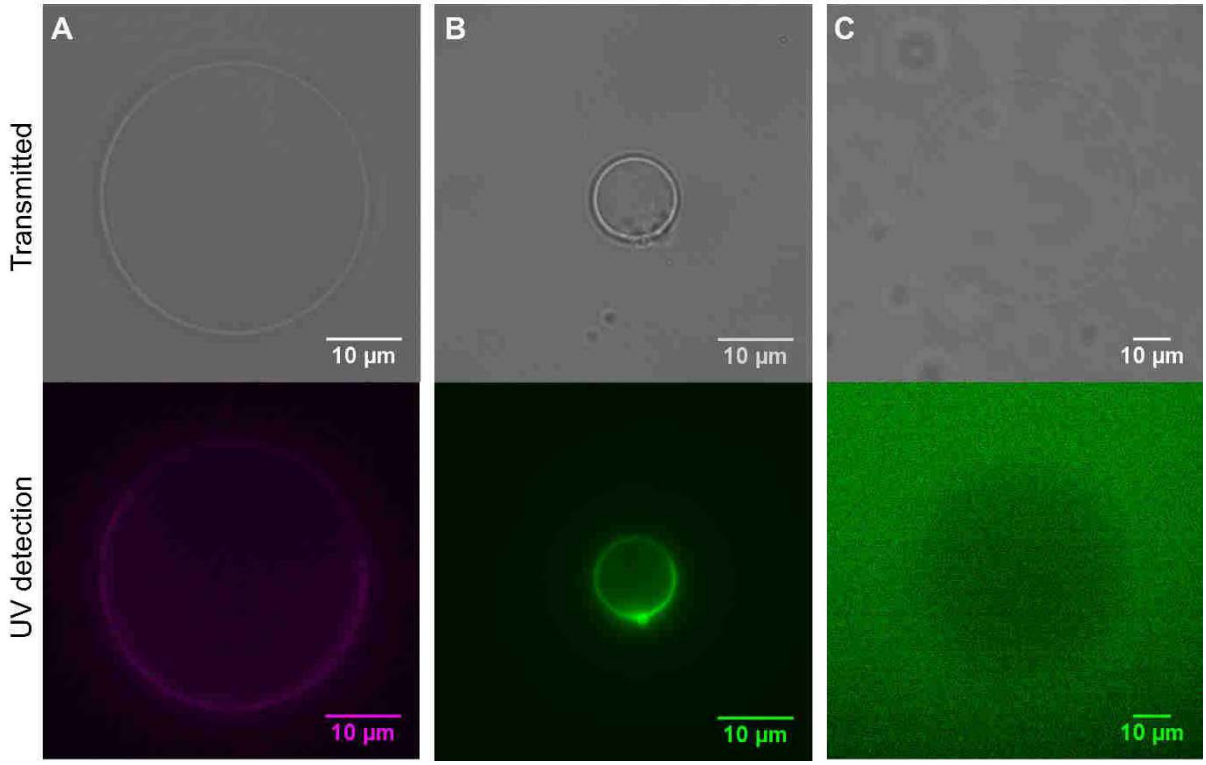

SI Figure 13. GUV formulation of A. **RhSTL** B. **STL** and SC-488 C ML using evaporation method. Above transmitted light, below UV detection at 532 nm for **RhSTL** and 488nm for SC-488.

Conclusion and Outlook

The aim of this thesis was to synthesize tailor-made ligands as bio probes for specific applications in biotechnological or biomedical research. The individual ligands that targeted different classes of proteins were validated for their suitability for the respective envisioned application. Three types of ligands were synthesized and tested in the scope of this thesis: 1) naturally occurring plant-based peptide ligands, which were directly tested in the biological host system; 2) carbohydrate-based ligands, which were tested for their selective interaction with various lectins; and 3) peptide-based lipids that were introduced into model membranes to modulate membranes properties.

In the first project, modified CLV3 plant peptides were developed as probes to investigate the dynamics of the CLV3 signaling pathway. A particular challenge in this project was the peptides' sensitivity to modification and the associated loss of biological activity. Consequently, prior to this work, it was not possible to follow the plant signaling pathway using a fluorophore-labelled peptide. In this work, biologically active and fluorophore labelled CLV3 peptide was established. This was realized by introducing a TAMRA fluorophore via the replacement of threonine to lysine in the sidechain. To build onto this success and further extent the development of a CLV3 bio probe, a fluorophore-labelled and photocaged CLV3 peptide was developed. This allowed for controlled biological activation within the plant by temporarily blocking the N-Terminus, a biological relevant part of the peptide. The synthesized bio probes allowed for the first time a tracking of plant signaling pathways and thereby enabled a detailed investigation of CLE peptide-trafficking dynamics *in vivo*. Since CLE family consists of more than 20 related peptides, this synthetic methodology now enables the synthesis of additional modified CLE peptides, which can be used to further investigate the signaling pathways involved in CLE-RLK interactions.

In the second project, a novel fluorogenic photo-inducible crosslinker for application in PAL was established. This AzC derivative was established as a building block suitable in SPPS. To establish its applicability as a tool to investigate ligand-receptor-interaction, the AzC building block was attached to different carbohydrate moieties and validated the specific binding to selected lectins. AzC exhibits a unique property that it's the native fluorescence of the coumarin is quenched due to the presence of the azide. However, upon modification or removal of the azide, which can be achieved by irradiation, the fluorescence of coumarin can be restored, making this a turn-on fluorogenic probe. Since UV irradiation of the azide creates a short-lived nitrene radical intermediate, it acts as a photo-inducible fluorogenic crosslinker. In this work, several different AzC glycan probes were synthesized, characterized and established as probes for PAL. It was successfully demonstrated that, upon light activation, these AzC glycan probes showed selective binding and crosslinking to their respective lectins which could be

visually confirmed due to the turn-on fluorogenic properties of the AzC. Thus, this work highlighted the potential of AzC as a photo-inducible fluorogenic crosslinker to study ligand-receptor interactions, even beyond the field of glycobiology and could hence serve as a useful tool in screening and diagnostic applications in the future.

The third project dealt with the development of small synthetically accessible peptide-based lipids to simplify the manipulation of model membranes. Here, a novel platform for the investigation of crowding on membrane dynamics was showcased. Basis of this project was the SpyTag-SpyCatcher technology, which is a protein-based technology for irreversible bioconjugation. In this work, a lipid-decorated ST peptide was successfully synthesized and characterized and validated for its integration into model membranes and subsequent binding to the SC proteins. This work established a new tool kit for facilitating the decoration of membranes with large biomolecules for the generation of crowded model membranes. Since the integration of large lipid anchors can be challenging, we use the small lipid-functionalized ST peptide for membrane integration that serves as precursor and docking point for the large SC protein. Upon forming a covalent iso-peptide bond with the ST, the large SC protein is successfully incorporated into the membrane, which was successfully validated with GUV and liposome models. This approach enables access to complex membrane surfaces for a more realistic representation and investigation of molecular mechanism on crowded membranes.

Through these contributions, this work has contributed to advancing the understanding of molecular interactions in biological systems. The probes and ligands, synthesized in this thesis, provide valuable new tools for future research and potential applications in the fields of plant biology, biochemistry and biomedical science.

Appendix

Abbreviation	Definition
Alloc	allyloxycarbonyl
AzC	Azidocoumarin
AzCMan	Azidocoumarin mannose
AzCGal	Azidocoumarin galactose
BAM1	BARELY ANY MERISTEM1
BADS	Benzyl azid diamine succinic acid
Boc	tert-Butyloxycarbonyl
BOP	Benzotriazole-1-yl-oxy-tris-pyrrolidino-phosphonium hexafluorophosphate
BSA	Bovine Serum Albumin
CLE	CLAVATA3/EMBRYO SURROUNDING REGION
CLV1	CLAVATA1
CLV2	CLAVATA2
CLV3	CLAVATA3
ConA	Concanavalin A
CRD	carbohydrate-recognizing domains
CRN	CORYN
CuAAC	Copper-Catalyzed Azide-Alkyne Cycloaddition
Cys	Cysteine
°C	Degree Celsius
DCM	Dichlormethane
DIC	Diisopropylcarbodiimide
DIPEA	Diisopropylethylamine
DLS	Dynamic Light Scattering
DNA	Deoxyribonucleic Acid
DMF	*N,N*-Dimethylformamid
DOPC	Dioleoylphosphatidylcholine
DSPE-PEG	1,2-distearoyl-sn-glycero-3-phosphoethanolamine-polyethylene glycol
DTNB	Dithio nitrobenzoic acid
e.g.	Exempli gratia (for example)
EDS	Ethylene glycole diamine succinic acid
et al.	Et alii (and other)
FITC	Fluoresceine isothiocyanate

flg22	flagellin 22
Fmoc	9- Fluorenylmethoxycarbonyl
δ	Chemical shift
g	gram
g/mol	Gramm per Mol
Gly	Glycin
GUV	Giant unilamelar vesikel
h	hour
HOBt	1-Hydroxybenzotriazole
IR	Infrared
LRR	Leucine-rich repeat
mg	milligram
mmol	millimole
ml	milliliter
min	minute
MALDI-TOF-MS	Matrix-assisted laser desorption/ionization time-of-flight mass spectrometry
Man	Mannose
MDS	Methyl succinidyl diamine succinic acid
ML	Maleimid lipid
MWCO	Molecular weight cut-off
m/z	Mass-to-charge-ratio
µmol	Micro mol
µl	Micro liter
nm	nanometer
NHS	N-Hydroxysuccinimide
NMR	Nuclear magnetic resonance
NVOC	2-Nitroveratryloxycarbonyl
ODS	Octyl diamine succinic acid
PAL	Photo affinity labeling
Pbf	2,2,4,6,7-pentamethyldihydrobenzofuran-5-sulfonyl
PBS	Phosphate-Buffered Saline
PEG	Poly ethylene glycol
pH	Pondus hydrogenii
ppm	Parts per million

PyBOP	Benzotriazol-1-yl-oxytripyrrolidinophosphonium hexafluorophosphate
RAM	Root Apical Meristem
Rf	Retention factor
RLK	Receptor-Like Kinase
RhST	Rhodamin SpyTag
RhSTL	Rhodamin SpyTag lipid
RNA	Ribonucleic acid
RP-HPLC-MS	Reverse phase high-performance liquid chromatography-mass spectrometry
SAM	Shoot apical meristem
SC	SpyCatcher
SC-488	SpyCatcher 488
SDS	short diamine succinyl
SDS-PAGE	Sodium dodecyl sulfate-polyacrylamide gel electrophoresis
SLB	supported lipid bilayers
ST	SpyTag
STL	SpyTag lipid
TAMRA	5-Carboxytetramethylrhodamine
tBu	tert-Butyl
TCEP	Tris(2-carboxyethyl)phosphine
TDS	Triple bond diethylenetriamine succinyl
TIRP	Thiol-induced, light-activated controlled radical polymerization
TLC	Thin layer chromatography
TNB	5-thio-2-nitrobenzoic acid
trt	Trityl
UV	Ultra violet
Vis	visual
WUS	Wuschel

Acknowledgements

Als erstes gilt mein besonderer Dank an Prof. Dr. Laura Hartmann. Ich möchte mich bedanken, dass sie mir die Möglichkeit gegeben hat, an diesen Projekten zu arbeiten. Durch den fachlichen Austausch, ihre Unterstützung und ihr Vertrauen in meine Fähigkeiten konnte ich neue Ideen entwickeln und mich sowohl fachlich als auch persönlich wesentlich weiterentwickeln.

An PD Dr.Klaus Schaper geht mein Dank für die Übernahme des Co-referats dieser Arbeit.

Außerdem möchte ich Dr. Monir Tabatabei für ihre Hilfe bei der Analyse meiner Spektren danken. Ich bin ihr auch sehr dankbar für die vielen bestärkenden und aufschlussreichen Gespräche, die wir geführt haben und die mich während meiner Arbeit unterstützt und motiviert haben.

Ein besonderer Dank geht auch an Dr. Ulla Gerling-Drießen und Dr. Marc Drießen, nicht nur für ihre fachliche Expertise, sondern auch für ihre unermüdliche Unterstützung darüber hinaus. Durch eure Anleitung habe ich ein unglaublich wertvolles Verständnis für die Arbeit mit biologischen Materialien gewonnen. Ich habe so viel von euch beiden gelernt und bin euch sehr dankbar für eure Initiative, das Azidocoumarin Projekt voranzutreiben, für eure durchdachten Anregungen und dafür, dass ihr euch immer Zeit genommen habt, um meine Projekte und Ideen zu besprechen. Ulla danke ich außerdem besonders für die Durchsicht dieser Arbeit. Vielen Dank, dass du so viel Zeit und Mühe investiert hast und mir geholfen hast, diese Arbeit zu formen.

Mein Dank gilt auch allen meinen Kollaborationspartnerinnen, die ich über das CRC 1208-Programm kennenlernen durfte. Besonders möchte ich mich bei Prof. Dr. Rüdiger Simon und Dr. Madhumitha Narasimhan für den wunderbaren Austausch, ihre Ausdauer und ihre Geduld während unseres CLAVATA3-Projekts bedanken. Ebenso danke ich Prof. Dr. Alexej Kedrov und Dr. Maryna Löwe für ihre Unterstützung und Expertise im SpyTag-Lipid-Projekt. Gemeinsam haben wir einige Phasen der Frustration durchlaufen, aber auch viel erreicht, und ich schätze ihre Partnerschaft und Entschlossenheit sehr.

Ich möchte auch meinen Kollegen aus Büro 78 danken, zunächst Dr. Lukas Fischer und Dr. Steven Hill für die angenehmen Gespräche und anregenden Diskussionen. Ebenso danke ich Nicole Hugo und Melina Feldhof, die als Nachfolgerinnen für Lukas und Steven ins Büro 78 gekommen sind. Danke für die gemeinsame Zeit, die eine ausgewogene Mischung aus Gefühlsachterbahnen, fachlichen Diskussionen und viel Humor war. Danke, dass ihr immer ein offenes Ohr für mich hattet.

Mein Dank gilt auch dem Mann mit den vielen Namen, Nicholas Nick John Jäck Rosini, der die meiste Zeit das Labor mit mir geteilt hat. Labor 36, woop woop! Danke für den allgemeinen Austausch und die regelmäßige Versorgung mit Süßigkeiten (insbesondere Zimtschnecken).

Natürlich möchte ich mich auch beim restlichen Team bedanken. Danke für diese unglaubliche Zeit, dafür, dass ihr mich auf meinem Weg durch den Promotionsprozess begleitet habt, und für all die unzähligen wunderbaren Momente, die ich nie vergessen werde. Von Klassenfahrten mit epischen Rage Cage runden, über gemeinsames Schlemmen in der „Big Mens“ bis hin zu Cocktailabenden und Feierabendbierchen im „Sozi“. Ihr habt mir gezeigt, dass Kollegen wirklich zu Freunden werden können.

Ein großes Dankeschön geht auch an meine großartigen Studierenden Franziska Böhmer, Dominik Mierswa, Felix Kallert, Simon Przetak, Sophia Bock, Jaimie Hoinkis und Sebastian Hylla. Danke für euer Vertrauen, eure harte Arbeit und eure Leidenschaft für die Projekte, die maßgeblich zum Erfolg dieser Arbeit beigetragen haben.

Ich danke außerdem Stephanie Scheelen, Sonja Coors und Birgit Ohler für die vielen wunderbaren Gespräche und ihre emotionale Unterstützung während meiner Arbeit. Ebenso danke ich Michaela Kitza, die nicht nur bei allen organisatorischen Belangen immer zur Stelle war, sondern auch stets ein offenes Ohr für mich hatte und mir mit ihren warmen Worten beigestanden hat.

Abschließend möchte ich meiner Familie und meinen Freunden danken. Danke, dass ihr immer an mich geglaubt habt, auch wenn ich selbst manchmal gezweifelt habe. Eure Stärke, euer Zuspruch und euer bedingungsloser Rückhalt haben mir mehr bedeutet, als Worte ausdrücken können. Danke für euer offenes Ohr, für euren Humor, wenn ich ihn am dringendsten gebraucht habe, und dafür, dass ihr immer da wart, ob zum Ablenken, Anspornen oder einfach zum Durchatmen.

References

(1) Watson, H. Biological membranes. *Essays in biochemistry* **2015**, *59*, 43–69. DOI: 10.1042/bse0590043 PubMed.

(2) Suwalsky, M. Structural Studies on Phospholipid Bilayers by X-Ray Fiber Diffraction Methods. In *Physical Properties of Biological Membranes and Their Functional Implications*, Hidalgo, C. Ed.; Series of the Centro de Estudios Científicos de Santiago, Springer, 1988; pp 3–19.

(3) Guo, X.; Zhu, K.; Zhu, X.; Zhao, W.; Miao, Y. Two-dimensional molecular condensation in cell signaling and mechanosensing. *Acta Biochimica et Biophysica Sinica* **2023**, *55*, 1064 - 1074.

(4) Echarri, A. A Multisensory Network Drives Nuclear Mechanoadaptation. *Biomolecules* **2022**, *12*.

(5) Song, Y.; Soto, J.; Chen, B.; Yang, L.; Li, S. Cell engineering: Biophysical regulation of the nucleus. *Biomaterials* **2020**, *234*, 119743.

(6) Mierke, D. F.; Pellegrini, M. Receptor–Ligand Interactions. In *Encyclopedia of endocrine diseases*, Martini, L. Ed.; London, 2004; pp 163–166.

(7) Marchetti, L.; Porciani, D.; Mitola, S.; Giacomelli, C. Editorial: Molecular Insights Into Ligand-Receptor Interactions on the Cell Surface. *Frontiers in Molecular Biosciences* **2022**, *9*.

(8) Sommer, M. E.; Selent, J.; Carlsson, J.; de Graaf, C.; Gloriam, D. E.; Keserű, G. M.; Kosloff, M.; Mordalski, S.; Rizk, A.; Rosenkilde, M. M.; et al. The European Research Network on Signal Transduction (ERNEST): Toward a Multidimensional Holistic Understanding of G Protein-Coupled Receptor Signaling. *ACS pharmacology & translational science* **2020**, *3 2*, 361-370.

(9) van Dijck, P.; Brown, N. A.; Goldman, G. H.; Rutherford, J. C.; Xue, C.; Van Zeebroeck, G. Nutrient Sensing at the Plasma Membrane of Fungal Cells. *Microbiology Spectrum* **2017**, *5*.

(10) Sheng, M.; Pak, D. T. S. Ligand-gated ion channel interactions with cytoskeletal and signaling proteins. *Annual review of physiology* **2000**, *62*, 755-778.

(11) Bongrand, P. Ligand-receptor interactions. *Reports on Progress in Physics* **1999**, *62* (6), 921–968. DOI: 10.1088/0034-4885/62/6/202 CrossRef.

(12) Du, X.; Li, Y.; Xia, Y.-L.; Ai, S.-M.; Liang, J.; Sang, P.; Ji, X.-L.; Liu, S.-Q. Insights into Protein-Ligand Interactions: Mechanisms, Models, and Methods. *International journal of molecular sciences* **2016**, *17* (2). DOI: 10.3390/ijms17020144 PubMed.

(13) Helm, C. A.; Knoll, W.; Israelachvili, J. N. Measurement of ligand-receptor interactions. *Proceedings of the National Academy of Sciences* **1991**, *88* (18), 8169-8173.

(14) Li, H.-Z.; Li, N.; Shao, X.; Liu, Y. L.; Xu, Z.-g.; Guo, Z.-Y. Hydrophobic interactions of relaxin family peptide receptor 3 with ligands identified using a NanoBiT-based binding assay. *Biochimie* **2020**.

(15) Li, L.; Yu, Y.; Zhou, Z.; Zhou, J.-M. Plant pattern-recognition receptors controlling innate immunity. *Science China Life Sciences* **2016**, *59* (9), 878–888. DOI: 10.1007/s11427-016-0115-2 PubMed.

(16) Srinivasarao, M.; Low, P. S. Ligand-targeted drug delivery. *Chemical reviews* **2017**, *117* (19), 12133-12164.

(17) Chen, K.; Wang, Y.; Hou, Y.; Wang, Q.; Long, D.; Liu, X.; Tian, X.; Yang, Y. Single cell RNA-seq reveals the CCL5/SDC1 receptor-ligand interaction between T cells and tumor cells in pancreatic cancer. *Cancer Letters* **2022**, *545*, 215834.

(18) Takeuchi, J.; Fukui, K.; Seto, Y.; Takaoka, Y.; Okamoto, M. Ligand–receptor interactions in plant hormone signaling. *The Plant Journal* **2021**, *105* (2), 290-306.

(19) Kahn, C. R. Membrane receptors for hormones and neurotransmitters. *The Journal of cell biology* **1976**, *70* (2), 261-286.

(20) Deller, M. C.; Jones, E. Y. Cell surface receptors. *Current opinion in structural biology* **2000**, *10* (2), 213-219.

(21) Clark, J. H.; Peck Jr, E. J. Intracellular Receptors: Characteristics and Measurement. In *Biological Regulation and Development: Hormone Action*, Springer, 1984; pp 99-127.

(22) Cummings, R. D. Stuck on sugars–how carbohydrates regulate cell adhesion, recognition, and signaling. *Glycoconjugate Journal* **2019**, *36*, 241-257.

(23) He, Y.; Zhou, J.; Shan, L.; Meng, X. Plant cell surface receptor-mediated signaling–a common theme amid diversity. *Journal of cell science* **2018**, *131* (2), jcs209353.

(24) An, C.; Wang, X.; Song, F.; Hu, J.; Li, L. Insights into intercellular receptor-ligand binding kinetics in cell communication. *Frontiers in Bioengineering and Biotechnology* **2022**, *10*, 953353.

(25) Cooper, G. M. The Cell: A Molecular Approach. 2nd edition. Sinauer Associates: 2000.

(26) Owji, H.; Nezafat, N.; Negahdaripour, M.; Hajiebrahimi, A.; Ghasemi, Y. A comprehensive review of signal peptides: Structure, roles, and applications. *European journal of cell biology* **2018**, *97* (6), 422-441.

(27) Mohnen, D.; Hahn, M. G. Cell wall carbohydrates as signals in plants. In *Seminars in cell biology*, 1993; Elsevier: Vol. 4, pp 93-102.

(28) Fischer, E. Einfluss der Configuration auf die Wirkung der Enzyme. *Berichte der deutschen chemischen Gesellschaft* **1894**, *27* (3), 2985-2993.

(29) Shapiro, A. M.; Porter, A. H. The Lock-and-Key Hypothesis: Evolutionary and Biosystematic Interpretation of Insect Genitalia. *Annual Review of Entomology* **1989**, *34* (1), 231–245. DOI: 10.1146/annurev.en.34.010189.001311 CrossRef.

(30) Monod, J.; Wyman, J.; Changeux, J. P. 1965. On the nature of allosteric transitions: a plausible model. *J Mol Biol 12*, 88.

(31) Tobi, D.; Bahar, I. Structural changes involved in protein binding correlate with intrinsic motions of proteins in the unbound state. *Proceedings of the National Academy of Sciences of the United States of America* **2005**, *102* (52), 18908–18913. DOI: 10.1073/pnas.0507603102 PubMed.

(32) Wood, L.; Wright, G. J. Approaches to identify extracellular receptor-ligand interactions. *Current opinion in structural biology* **2019**, *56*, 28-36.

(33) Bongrand, P. Ligand-receptor interactions. *Reports on Progress in Physics* **1999**, *62*, 921 - 968.

(34) Ma, W.; Wang, C.; Liu, R.; Wang, N.; Lv, Y.; Dai, B.; He, L. Advances in cell membrane chromatography. *Journal of chromatography. A* **2021**, *1639*, 461916.

(35) Li, L.; Ji, J.; Song, F.; Hu, J. Intercellular receptor-ligand binding: effect of protein-membrane interaction. *Journal of molecular biology* **2022**, 167787.

(36) Biswas, K. H.; Groves, J. T. A Microbead Supported Membrane-Based Fluorescence Imaging Assay Reveals Intermembrane Receptor-Ligand Complex Dimension with Nanometer Precision. *Langmuir : the ACS journal of surfaces and colloids* **2016**, *32 26*, 6775-6780.

(37) Chen, J.; Ding, X.; Zhang, D. Challenges and strategies faced in the electrochemical biosensing analysis of neurochemicals in vivo: A review. *Talanta* **2023**, *266 Pt 1*, 124933.

(38) Wilson, E. D.; Probst, D.; Sode, K. In vivo continuous monitoring of peptides and proteins: Challenges and opportunities. *Applied Physics Reviews* **2023**.

(39) Rong, G.; Corrie, S. R.; Clark, H. A. In Vivo Biosensing: Progress and Perspectives. *ACS sensors* **2017**, *2 3*, 327-338.

(40) Rivera, V. M. Controlling gene expression using synthetic ligands. *Methods* **1998**, *14* (4), 421-429.

(41) Nakatani, K.; Sando, S.; Saito, I. Scanning of guanine–guanine mismatches in DNA by synthetic ligands using surface plasmon resonance. *Nature biotechnology* **2001**, *19* (1), 51-55.

(42) Chu, W.; Prodromou, R.; Day, K. N.; Schneible, J. D.; Bacon, K. B.; Bowen, J. D.; Kilgore, R.; Catella, C. M.; Moore, B.; Mabe, M. D.; et al. Peptides and pseudopeptide ligands: a powerful toolbox for the affinity purification of current and next-generation biotherapeutics. *Journal of chromatography. A* **2020**, *1635*, 461632.

(43) Cotruvo Jr, J. A.; Aron, A. T.; Ramos-Torres, K. M.; Chang, C. J. Synthetic fluorescent probes for studying copper in biological systems. *Chemical Society Reviews* **2015**, *44* (13), 4400-4414.

(44) Schiffman, J. D.; Balakrishna, R. G. Quantum dots as fluorescent probes: Synthesis, surface chemistry, energy transfer mechanisms, and applications. *Sensors and Actuators B: Chemical* **2018**, *258*, 1191-1214.

(45) Becker, J. M.; Naider, F. Cross-linking Strategies to Study Peptide Ligand–Receptor Interactions. In *Methods in enzymology*, Vol. 556; Elsevier, 2015; pp 527-547.

(46) Song, X.-F.; Yu, D.-L.; Xu, T.-T.; Ren, S.-C.; Guo, P.; Liu, C.-M. Contributions of individual amino acid residues to the endogenous CLV3 function in shoot apical meristem maintenance in Arabidopsis. *Molecular plant* **2012**, *5* (2), 515-523.

(47) Tatsu, Y.; Shigeri, Y.; Sogabe, S.; Yumoto, N.; Yoshikawa, S. Solid-Phase Synthesis of Caged Peptides Using Tyrosine Modified with a Photocleavable Protecting Group: Application to the Synthesis of Caged Neuropeptide Y. *Biochemical and Biophysical Research Communications* **1996**, *227* (3), 688-693. DOI: https://doi.org/10.1006/bbrc.1996.1570.

(48) Flaxman, H. A.; Chang, C.-F.; Wu, H.-Y.; Nakamoto, C. H.; Woo, C. M. A Binding Site Hotspot Map of the FKBP12–Rapamycin–FRB Ternary Complex by Photoaffinity Labeling and Mass Spectrometry-Based Proteomics. *Journal of the American Chemical Society* **2019**, *141* (30), 11759-11764. DOI: 10.1021/jacs.9b03764.

(49) Blawitzki, L.-C.; Bartels, N.; Bonda, L.; Schmidt, S.; Monzel, C.; Hartmann, L. Glycomacromolecules to Tailor Crowded and Heteromultivalent Glycocalyx Mimetics. *Biomacromolecules* **2024**, *25* (9), 5979-5994.

(50) Cook, G. M. W. GLYCOPROTEINS IN MEMBRANES. *Biological Reviews* **1968**, *43*.

(51) Hanafusa, K.; Hotta, T.; Iwabuchi, K. Glycolipids: Linchpins in the Organization and Function of Membrane Microdomains. *Frontiers in Cell and Developmental Biology* **2020**, *8*.

(52) Feng, Z.; Westbrook, J. D.; Sala, R.; Smart, O. S.; Bricogne, G.; Matsubara, M.; Yamada, I.; Tsuchiya, S.; Aoki-Kinoshita, K. F.; Hoch, J. C.; et al. Enhanced validation of small-molecule ligands and carbohydrates in the protein databank. *Structure* **2021**.

(53) Foote, C. A.; Soares, R. N.; Ramirez-Perez, F. I.; Ghiarone, T.; Aroor, A.; Manrique-Acevedo, C.; Padilla, J.; Martinez-Lemus, L. Endothelial Glycocalyx. *Comprehensive Physiology* **2022**, *12* (4), 3781–3811. DOI: 10.1002/cphy.c210029 PubMed.

(54) Laaf, D.; Bojarová, P.; Elling, L.; Křen, V. Galectin-Carbohydrate Interactions in Biomedicine and Biotechnology. *Trends in biotechnology* **2019**, *37 4*, 402-415.

(55) Bojarová, P.; Křen, V. Sugared biomaterial binding lectins: achievements and perspectives. *Biomaterials science* **2016**, *4 8*, 1142-1160.

(56) Cambi, A.; Koopman, M.; Figdor, C. G. How C-type lectins detect pathogens. *Cellular Microbiology* **2005**, *7*.

(57) Kishore, U.; Eggleton, P.; Reid, K. B. M. Modular organization of carbohydrate recognition domains in animal lectins. *Matrix biology : journal of the International Society for Matrix Biology* **1997**, *15 8-9*, 583-592.

(58) Khan, F. I.; Suguna, K. Crystal structure of an L-type lectin domain from archaea. *Proteins: Structure* **2022**, *91*, 456 - 465.

(59) Drickamer, K.; Taylor, M. E. Recent insights into structures and functions of C-type lectins in the immune system. *Current Opinion in Structural Biology* **2015**, *34*, 26 - 34.

(60) Sumner, J. B. THE GLOBULINS OF THE JACK BEAN, CANAVALIA ENSIFORMIS. *Journal of Biological Chemistry* **1919**, *37* (1), 137–142. DOI: 10.1016/s0021-9258(18)86371-2 CrossRef.

(61) GOLDSTEIN, I. J.; HOLLERMAN, C. E.; MERRICK, J. M. PROTEIN-CARBOHYDRATE INTERACTION. I. THE INTERACTION OF POLYSACCHARIDES WITH CONCANAVALIN A. *Biochimica et biophysica acta* **1965**, *97*, 68–76. DOI: 10.1016/0304-4165(65)90270-9 PubMed.

(62) Shi, J.; Xue, S. J.; Kakuda, Y.; Ilic, S.; Kim, D. Isolation and characterization of lectins from kidney beans (Phaseolus vulgaris). *Process Biochemistry* **2007**, *42* (10), 1436-1442. DOI: https://doi.org/10.1016/j.procbio.2007.07.015.

(63) Sharon, N.; Lis, H. History of lectins: from hemagglutinins to biological recognition molecules. *Glycobiology* **2004**, *14* (11), 53R-62R. DOI: 10.1093/glycob/cwh122 (acccessed 7/12/2024).

(64) Raposo, C. D.; Canelas, A. B.; Barros, M. T. Human lectins, their carbohydrate affinities and where to find them. *Biomolecules* **2021**, *11* (2), 188.

(65) Di, X.; Liang, X.; Shen, C.; Pei, Y.; Wu, B.; He, Z. Carbohydrates used in polymeric systems for drug delivery: from structures to applications. *Pharmaceutics* **2022**, *14* (4), 739.

(66) Sattin, S.; Bernardi, A. Glycoconjugates and glycomimetics as microbial anti-adhesives. *Trends in Biotechnology* **2016**, *34* (6), 483-495.

(67) Ranjbari, J.; Mokhtarzadeh, A.; Alibakhshi, A.; Tabarzad, M.; Hejazi, M.; Ramezani, M. Anti-cancer drug delivery using carbohydrate-based polymers. *Current Pharmaceutical Design* **2017**, *23* (39), 6019-6032.

(68) Thépaut, M.; Luczkowiak, J.; Vivès, C.; Labiod, N.; Bally, I.; Lasala, F.; Grimoire, Y.; Fenel, D.; Sattin, S.; Thielens, N. DC/L-SIGN recognition of spike glycoprotein promotes SARS-CoV-2 trans-infection and can be inhibited by a glycomimetic antagonist. *PLoS pathogens* **2021**, *17* (5), e1009576.

(69) Lepenies, B.; Yin, J.; Seeberger, P. H. Applications of synthetic carbohydrates to chemical biology. *Current opinion in chemical biology* **2010**, *14* (3), 404-411.

(70) Jayaraman, N. Multivalent ligand presentation as a central concept to study intricate carbohydrate-protein interactions. *Chemical Society reviews* **2009**, *38 12*, 3463-3483.

(71) Nicotra, F.; Cipolla, L.; La Ferla, B.; Airoldi, C.; Zona, C.; Orsato, A.; Shaikh, N. I.; Russo, L. Carbohydrate scaffolds in chemical genetic studies. *Journal of biotechnology* **2009**, *144 3*, 234-241.

(72) Sakurai, K.; Ozawa, S.; Yamada, R.; Yasui, T.; Mizuno, S. Comparison of the Reactivity of Carbohydrate Photoaffinity Probes with Different Photoreactive Groups. *ChemBioChem* **2014**, *15*.

(73) Wu, H.; Shajahan, A.; Yang, J.-Y.; Capota, E.; Wands, A. M.; Arthur, C. M.; Stowell, S. R.; Moremen, K. W.; Azadi, P.; Kohler, J. J. A photo-cross-linking GlcNAc analog enables covalent capture of N-linked glycoprotein-binding partners on the cell surface. *Cell chemical biology* **2022**, *29* (1), 84-97. e88.

(74) Rosenthal, J.; Katz, F. Plant-based research among the International Cooperative Biodiversity Groups. *Pharmaceutical Biology* **2009**, *47* (8), 783-787.

(75) Toenniessen, G. H. Plant biotechnology and developing countries. *Trends in Biotechnology* **1995**, *13* (9), 404-409.

(76) Mubassir, M. A synopsis of different plant LRR-RLKs structures and functionality. *American Journal of Biomedical Science & Research* **2019**, *1* (2).

(77) Shiu, S.-H.; Bleecker, A. B. Expansion of the receptor-like kinase/Pelle gene family and receptor-like proteins in Arabidopsis. *Plant physiology* **2003**, *132* (2), 530-543.

(78) Clark, S. E.; Williams, R. W.; Meyerowitz, E. M. The CLAVATA1 gene encodes a putative receptor kinase that controls shoot and floral meristem size in Arabidopsis. *Cell* **1997**, *89* (4), 575–585. DOI: 10.1016/s0092-8674(00)80239-1 PubMed.

(79) Clark, S. E.; Williams, R. W.; Meyerowitz, E. M. The CLAVATA1gene encodes a putative receptor kinase that controls shoot and floral meristem size in Arabidopsis. *Cell* **1997**, *89* (4), 575-585.

(80) Clark, S. E.; Jacobsen, S. E.; Levin, J. Z.; Meyerowitz, E. M. The CLAVATA and SHOOT MERISTEMLESS loci competitively regulate meristem activity in Arabidopsis. *Development* **1996**, *122* (5), 1567–1575. DOI: 10.1242/dev.122.5.1567 PubMed.

(81) Stahl, Y.; Simon, R. Plant primary meristems: shared functions and regulatory mechanisms. *Current opinion in plant biology* **2010**, *13* (1), 53-58.

(82) Bowman, J. L.; Eshed, Y. Formation and maintenance of the shoot apical meristem. *Trends in plant science* **2000**, *5* (3), 110-115.

(83) Perilli, S.; Di Mambro, R.; Sabatini, S. Growth and development of the root apical meristem. *Current opinion in plant biology* **2012**, *15* (1), 17-23.

(84) Opsahl-Ferstad, H. G.; Le Deunff, E.; Dumas, C.; Rogowsky, P. M. ZmEsr, a novel endosperm-specific gene expressed in a restricted region around the maize embryo. *The Plant journal : for cell and molecular biology* **1997**, *12* (1), 235–246. DOI: 10.1046/j.1365-313x.1997.12010235.x PubMed.

(85) Jun, J. H.; Fiume, E.; Fletcher, J. C. The CLE family of plant polypeptide signaling molecules. *Cellular and molecular life sciences : CMLS* **2008**, *65* (5), 743–755. DOI: 10.1007/s00018-007-7411-5 PubMed.

(86) Bleckmann, A.; Weidtkamp-Peters, S.; Seidel, C. A. M.; Simon, R. Stem cell signaling in Arabidopsis requires CRN to localize CLV2 to the plasma membrane. *Plant physiology* **2010**, *152* (1), 166–176. DOI: 10.1104/pp.109.149930 PubMed.

(87) Brand, U.; Fletcher, J. C.; Hobe, M.; Meyerowitz, E. M.; Simon, R. Dependence of stem cell fate in Arabidopsis on a feedback loop regulated by CLV3 activity. *Science (New York, N.Y.)* **2000**, *289* (5479), 617–619. DOI: 10.1126/science.289.5479.617 PubMed.

(88) Brand, U.; Fletcher, J. C.; Hobe, M.; Meyerowitz, E. M.; Simon, R. G. Dependence of stem cell fate in Arabidopsis on a feedback loop regulated by CLV3 activity. *Science* **2000**, *289 5479*, 617-619.

(89) Lenhard, M.; Laux, T. Stem cell homeostasis in the Arabidopsis shoot meristem is regulated by intercellular movement of CLAVATA3 and its sequestration by CLAVATA1. In *Development*, 2003.

(90) Kim, H.-J.; Wu, C.-Y.; Yu, H. M.; Sheen, J.; Lee, H. Dual CLAVATA3 peptides in Arabidopsis shoot stem cell signaling. *Journal of Plant Biology* **2017**, *60*, 506 - 512.

(91) Butenko, M. A.; Simon, R. Beyond the meristems: similarities in the CLAVATA3 and INFLORESCENCE DEFICIENT IN ABSCISSION peptide mediated signalling pathways. *Journal of Experimental Botany* **2015**, *66* (17), 5195-5203.

(92) Liu, J.-X.; Srivastava, R.; Howell, S. Overexpression of an Arabidopsis gene encoding a subtilase (AtSBT5. 4) produces a clavata-like phenotype. *Planta* **2009**, *230*, 687-697.

(93) Fan, C.; Wu, Y.; Yang, Q.; Yang, Y.; Meng, Q.; Zhang, K.; Li, J.; Wang, J.; Zhou, Y. A novel single-nucleotide mutation in a CLAVATA3 gene homolog controls a multilocular silique trait in Brassica rapa L. *Molecular plant* **2014**, *7* (12), 1788-1792.

(94) Wang, D.; Jones, L. M.; Urwin, P. E.; Atkinson, H. J. A synthetic peptide shows retro-and anterograde neuronal transport before disrupting the chemosensation of plant-pathogenic nematodes. *PLoS One* **2011**, *6* (3), e17475.

(95) Yagi, N.; Yoshinari, A.; Iwatate, R. J.; Isoda, R.; Frommer, W. B.; Nakamura, M. Advances in synthetic fluorescent probe labeling for live-cell imaging in plants. *Plant and Cell Physiology* **2021**, *62* (8), 1259-1268.

(96) Merrifield, P. R.; Guilford, J. P.; Christensen, P. R.; Frick, J. The role of intellectual factors in problem solving. *Psychological Monographs: General and Applied* **1962**, *76* (10), 1.

(97) Klabenkova, K.; Fokina, A.; Stetsenko, D. Chemistry of peptide-oligonucleotide conjugates: a review. *Molecules* **2021**, *26* (17), 5420.

(98) Lu, K.; Duan, Q.-P.; Ma, L.; Zhao, D.-X. Chemical strategies for the synthesis of peptide−oligonucleotide conjugates. *Bioconjugate chemistry* **2010**, *21* (2), 187-202.

(99) Coin, I.; Beyermann, M.; Bienert, M. D. S. N. Solid-phase peptide synthesis: from standard procedures to the synthesis of difficult sequences. *Nature Protocols* **2007**, *2*, 3247-3256.

(100) Scott, W. L.; Martynow, J.; Huffman, J. C.; O'Donnell, M. J. Solid-phase synthesis of multiple classes of peptidomimetics from versatile resin-bound aldehyde intermediates. *Journal of the American Chemical Society* **2007**, *129 22*, 7077-7088.

(101) Ponader, D.; Wojcik, F.; Beceren-Braun, F.; Dernedde, J.; Hartmann, L. Sequence-defined glycopolymer segments presenting mannose: synthesis and lectin binding affinity. *Biomacromolecules* **2012**, *13 6*, 1845-1852.

(102) Palomo, J. M. Solid-phase peptide synthesis: an overview focused on the preparation of biologically relevant peptides. *RSC Advances* **2014**, *4*, 32658-32672.

(103) Moss, J. A. Guide for Resin and Linker Selection in Solid-Phase Peptide Synthesis. *Current Protocols in Protein Science* **2005**, *40*.

(104) Shelton, P. T.; Jensen, K. J. Linkers, resins, and general procedures for solid-phase peptide synthesis. *Methods in molecular biology* **2013**, *1047*, 23-41.

(105) Barlos, K.; Chatzi, O.; Gatos, D.; Stavropoulos, G. 2-Chlorotrityl chloride resin. Studies on anchoring of Fmoc-amino acids and peptide cleavage. *International journal of peptide and protein research* **2009**, *37 6*, 513-520.

(106) Kassem, T.; Sabatino, D.; Jia, X.; Zhu, X. X.; Lubell, W. D. To Rink or Not to Rink Amide Link, that is the Question to Address for More Economical and Environmentally Sound Solid-Phase Peptide Synthesis. *International Journal of Peptide Research and Therapeutics* **2009**, *15*, 211-218.

(107) Quarrell, R.; Claridge, T. D. W.; Weaver, G. W.; Lowe, G. D. O. Structure and properties of TentaGel resin beads: Implications for combinatorial library chemistry. *Molecular Diversity* **1996**, *1*, 223-232.

(108) Al-Warhi, T.; Al-Hazimi, H. M. G.; El-Faham, A. Recent development in peptide coupling reagents. *Journal of Saudi Chemical Society* **2012**, *16*, 97-116.

(109) Molina, F.; Laune, D.; Gougat, C.; Pau, B. C.; Granier, C. Improved performances of spot multiple peptide synthesis. *Peptide research* **1996**, *9 3*, 151-155.

(110) Coste, J.; Le-Nguyen, D.; Castro, B. PyBOP®: A new peptide coupling reagent devoid of toxic by-product. *Tetrahedron Letters* **1990**, *31*, 205-208.

(111) Frérot, E.; Coste, J.; Pantaloni, A.; Dufour, M.-N.; Jouin, P. PyBOP® and PyBroP: Two reagents for the difficult coupling of the α, α-dialkyl amino acid, Aib. *Tetrahedron* **1991**, *47* (2), 259-270.

(112) Pires, D. A. T.; Bemquerer, M. P.; do Nascimento, C. J. Some mechanistic aspects on Fmoc solid phase peptide synthesis. *International Journal of Peptide Research and Therapeutics* **2014**, *20*, 53-69.

(113) Далтон, К. Ф.; Эйнон, Д. С.; Джексон, С. А.; Сиврук, Г. А. Solid-phase synthesis of peptides with boc and fmoc protective groups. 2007.

(114) Fields, G. B.; Noble, R. L. Solid phase peptide synthesis utilizing 9-fluorenylmethoxycarbonyl amino acids. *International journal of peptide and protein research* **1990**, *35* (3), 161-214.

(115) Orain, D.; Ellard, J.; Bradley, M. Protecting Groups in Solid-Phase Organic Synthesis. *Journal of Combinatorial Chemistry* **2002**, *4* (1), 1-16. DOI: 10.1021/cc0001093.

(116) Kessler, M.; Glatthar, R.; Giese, B.; Bochet, C. G. Sequentially photocleavable protecting groups in solid-phase synthesis. *Organic letters* **2003**, *5 8*, 1179-1181.

(117) Smyrlaki, I.; Shaw, A.; Yang, Y.; Shen, B.; Högberg, B. Solid Phase Synthesis of DNA Nanostructures in Heavy Liquid. *Small* **2022**, e2204513.

(118) Murata, H.; Carmali, S.; Baker, S. L.; Matyjaszewski, K.; Russell, A. J. Solid-phase synthesis of protein-polymers on reversible immobilization supports. *Nature communications* **2018**, *9* (1), 845.

(119) Hartmann, L.; Krause, E.; Antonietti, M.; Börner, H. G. Solid-phase supported polymer synthesis of sequence-defined, multifunctional poly(amidoamines). *Biomacromolecules* **2006**, *7 4*, 1239-1244.

(120) Hartmann, L. Polymers for Control Freaks: Sequence-Defined Poly (amidoamine) s and Their Biomedical Applications. *Macromolecular Chemistry and Physics* **2011**, *212* (1), 8-13.

(121) Wojcik, F.; Ponader, D.; Mosca, S.; Hartmann, L. Recent advances in solid phase polymer synthesis: polyamides from tailor-made building blocks. *Sequence-Controlled Polymers: Synthesis, Self-Assembly, and Properties* **2014**, 85-101.

(122) Ponader, D.; Wojcik, F.; Beceren-Braun, F.; Dernedde, J.; Hartmann, L. Sequence-defined glycopolymer segments presenting mannose: synthesis and lectin binding affinity. *Biomacromolecules* **2012**, *13* (6), 1845-1852.

(123) Üclü, S.; Marschelke, C.; Drees, F.; Giesler, M.; Wilms, D.; Köhler, T.; Schmidt, S.; Synytska, A.; Hartmann, L. Sweet Janus Particles: Multifunctional Inhibitors of Carbohydrate-Based Bacterial Adhesion. *Biomacromolecules* **2024**, *25* (4), 2399-2407.

(124) Boden, S.; Wagner, K. G.; Karg, M.; Hartmann, L. Presenting precision glycomacromolecules on gold nanoparticles for increased lectin binding. *Polymers* **2017**, *9* (12), 716.

(125) Gerke, C.; Jacobi, F.; Goodwin, L. E.; Pieper, F.; Schmidt, S.; Hartmann, L. Sequence-Controlled High Molecular Weight Glyco (oligoamide)–PEG Multiblock Copolymers as Ligands and Inhibitors in Lectin Binding. *Macromolecules* **2018**, *51* (15), 5608-5619.

(126) Camaleño de la Calle, A.; Gerke, C.; Chang, X. J.; Grafmüller, A.; Hartmann, L.; Schmidt, S. Multivalent interactions of polyamide based sequence-controlled glycomacromolecules with concanavalin A. *Macromolecular Bioscience* **2019**, *19* (6), 1900033.

(127) Freichel, T.; Heine, V.; Laaf, D.; Mackintosh, E. E.; Sarafova, S.; Elling, L.; Snyder, N. L.; Hartmann, L. Sequence-Defined Heteromultivalent Precision Glycomacromolecules Bearing Sulfonated/Sulfated Nonglycosidic Moieties Preferentially Bind Galectin-3 and Delay Wound Healing of a Galectin-3 Positive Tumor Cell Line in an In Vitro Wound Scratch Assay. *Macromolecular bioscience* **2020**, *20* (9), 2000163.

(128) Yang, H.; Lin, Z.; Wu, B.; Xu, J.; Tao, S.-C.; Zhou, S. Deciphering disease through glycan codes: leveraging lectin microarrays for clinical insights: Deciphering disease through glycan codes. *Acta Biochimica et Biophysica Sinica* **2024**, *56* (8), 1145.

(129) Cohen, M. Notable aspects of glycan-protein interactions. *Biomolecules* **2015**, *5* (3), 2056-2072.

(130) Collins, B. E.; Paulson, J. C. Cell surface biology mediated by low affinity multivalent protein–glycan interactions. *Current Opinion in Chemical Biology* **2004**, *8* (6), 617-625. DOI: https://doi.org/10.1016/j.cbpa.2004.10.004.

(131) Babulic, J. L.; De León González, F. V.; Capicciotti, C. J. Recent advances in photoaffinity labeling strategies to capture Glycan–Protein interactions. *Current Opinion in Chemical Biology* **2024**, *80*, 102456. DOI: https://doi.org/10.1016/j.cbpa.2024.102456.

(132) Yan, H.; Yalagala, R. S.; Yan, F. Fluorescently labelled glycans and their applications. *Glycoconjugate journal* **2015**, *32* (8), 559-574.

(133) Cheng, B.; Wan, Y.; Tang, Q.; Du, Y.; Xu, F.; Huang, Z.; Qin, W.; Chen, X. A Photocaged Azidosugar for Light-Controlled Metabolic Labeling of Cell-Surface Sialoglycans. *Chinese Journal of Chemistry* **2022**, *40* (7), 806-812.

(134) Pratt, M. R. Photocrosslinking and capture for the analysis of carbohydrate-dependent interactions. *Bioorganic & Medicinal Chemistry Letters* **2025**, *117*, 130077. DOI: https://doi.org/10.1016/j.bmcl.2024.130077.

(135) Archer, M. S. *Structure, agency and the internal conversation*; Cambridge University Press, 2003.

(136) Marian, C. M. Understanding and controlling intersystem crossing in molecules. *Annual review of physical chemistry* **2021**, *72* (1), 617-640.

(137) Zheng, Q.; Lavis, L. D. Development of photostable fluorophores for molecular imaging. *Current opinion in chemical biology* **2017**, *39*, 32-38.

(138) Hansen, M. J.; Velema, W. A.; Lerch, M. M.; Szymanski, W.; Feringa, B. L. Wavelength-selective cleavage of photoprotecting groups: strategies and applications in dynamic systems. *Chemical Society Reviews* **2015**, *44* (11), 3358-3377.

(139) Lim, K. S.; Galarraga, J. H.; Cui, X.; Lindberg, G. C.; Burdick, J. A.; Woodfield, T. B. Fundamentals and applications of photo-cross-linking in bioprinting. *Chemical reviews* **2020**, *120* (19), 10662-10694.

(140) Duan, Z.; Tan, L.; Duan, R.; Chen, M.; Xia, F.; Huang, F. Photoactivated Biosensing Process for Dictated ATP Detection in Single Living Cells. *Analytical Chemistry* **2021**, *93* (33), 11547-11556. DOI: 10.1021/acs.analchem.1c02049.

(141) Wang, X.; Ding, Q.; Groleau, R. R.; Wu, L.; Mao, Y.; Che, F.; Kotova, O.; Scanlan, E. M.; Lewis, S. E.; Li, P.; et al. Fluorescent Probes for Disease Diagnosis. *Chemical Reviews* **2024**, *124* (11), 7106-7164. DOI: 10.1021/acs.chemrev.3c00776.

(142) Halabi, E. A.; Thiel, Z.; Trapp, N.; Pinotsi, D.; Rivera-Fuentes, P. A Photoactivatable Probe for Super-Resolution Imaging of Enzymatic Activity in Live Cells. *Journal of the American Chemical Society* **2017**, *139* (37), 13200-13207. DOI: 10.1021/jacs.7b07748.

(143) Tung, C. H. Fluorescent peptide probes for in vivo diagnostic imaging. *Peptide Science: Original Research on Biomolecules* **2004**, *76* (5), 391-403.

(144) Daly, C. J.; McGrath, J. C. Fluorescent ligands, antibodies, and proteins for the study of receptors. *Pharmacology & therapeutics* **2003**, *100* (2), 101-118.

(145) Jelenska, J.; Davern, S. M.; Standaert, R. F.; Mirzadeh, S.; Greenberg, J. T. Flagellin peptide flg22 gains access to long-distance trafficking in Arabidopsis via its receptor, FLS2. *Journal of Experimental Botany* **2017**, *68* (7), 1769-1783.

(146) Kumar, P.; Shukhman, D.; Laughlin, S. T. A photocaged, cyclopropene-containing analog of the amino acid neurotransmitter glutamate. *Tetrahedron letters* **2016**, *57* (51), 5750-5752.

(147) Mangubat-Medina, A. E.; Ball, Z. T. Triggering biological processes: methods and applications of photocaged peptides and proteins. *Chemical Society Reviews* **2021**, *50* (18), 10403-10421.

(148) So, W. H.; Wong, C. T.; Xia, J. Peptide photocaging: A brief account of the chemistry and biological applications. *Chinese Chemical Letters* **2018**, *29* (7), 1058-1062.

(149) Hemelíková, N.; Žukauskaitė, A.; Pospíšil, T. s.; Strnad, M.; Doležal, K.; Mik, V. Caged phytohormones: from chemical inactivation to controlled physiological response. *Journal of Agricultural and Food Chemistry* **2021**, *69* (41), 12111-12125.

(150) Yang, Y.; Song, H.; Chen, P. R. Genetically encoded photocrosslinkers for identifying and mapping protein-protein interactions in living cells. *IUBMB life* **2016**, *68* (11), 879-886.

(151) Rannversson, H.; Andersen, J.; Sørensen, L.; Bang-Andersen, B.; Park, M.; Huber, T.; Sakmar, T. P.; Strømgaard, K. Genetically encoded photocrosslinkers locate the high-affinity binding site of antidepressant drugs in the human serotonin transporter. *Nature Communications* **2016**, *7* (1), 11261. DOI: 10.1038/ncomms11261.

(152) Kleiner, P.; Heydenreuter, W.; Stahl, M.; Korotkov, V. S.; Sieber, S. A. A whole proteome inventory of background photocrosslinker binding. *Angewandte Chemie International Edition* **2017**, *56* (5), 1396-1401.

(153) Barltrop, J.; Schofield, P. Photosensitive protecting groups. *Tetrahedron Letters* **1962**, *3* (16), 697-699.

(154) Pelliccioli, A. P.; Wirz, J. Photoremovable protecting groups: reaction mechanisms and applications. *Photochemical & photobiological sciences* **2002**, *1* (7), 441-458.

(155) Gui, W.; Shen, S.; Zhuang, Z. Photocaged Cell-Permeable Ubiquitin Probe for Temporal Profiling of Deubiquitinating Enzymes. *Journal of the American Chemical Society* **2020**.

(156) Hoffelner, B. S.; Andreev, S.; Plank, N.; Koch, P. Photocaging of Pyridinylimidazole-Based Covalent JNK3 Inhibitors Affords Spatiotemporal Control of the Binding Affinity in Live Cells. *Pharmaceuticals* **2023**, *16*.

(157) Basa, P. N.; Barr, C. A.; Oakley, K. M.; Liang, X.; Burdette, S. C. Zinc photocages with improved photophysical properties and cell permeability imparted by ternary complex formation. *Journal of the American Chemical Society* **2019**, *141* (30), 12100-12108.

(158) Ellis-Davies, G. C. Caged compounds: photorelease technology for control of cellular chemistry and physiology. *Nature methods* **2007**, *4* (8), 619-628.

(159) Zhang, X.; Huang, H.; Liu, Y.; Wu, Z.; Wang, F.; Fan, X.; Chen, P. R.; Wang, J. Optical Control of Protein Functions via Genetically Encoded Photocaged Aspartic Acids. *Journal of the American Chemical Society* **2023**, *145* (35), 19218-19224.

(160) Goubko, C. A.; Basak, A.; Majumdar, S.; Jarrell, H.; Huan Khieu, N.; Cao, X. Comparative analysis of photocaged RGDS peptides for cell patterning. *Journal of Biomedical Materials Research Part A* **2013**, *101* (3), 787-796.

(161) Marmur, J.; Anderson, W.; Matthews, L.; Berns, K.; Gajewska, E.; Lane, D.; Doty, P. The effects of ultraviolet light on the biological and physical chemical properties of deoxyribonucleic acids. *Journal of cellular and comparative physiology* **1961**, *58* (S1).

(162) Lee, H.-M.; Larson, D. R.; Lawrence, D. S. Illuminating the Chemistry of Life: Design, Synthesis, and Applications of “Caged” and Related Photoresponsive Compounds. *ACS Chemical Biology* **2009**, *4* (6), 409-427. DOI: 10.1021/cb900036s.

(163) Barltrop, J.; Plant, P.; Schofield, P. Photosensitive protective groups. *Chemical Communications (London)* **1966**, (22), 822-823.

(164) Bao, C.; Jin, M.; Li, B.; Xu, Y.; Jin, J.; Zhu, L. Long conjugated 2-nitrobenzyl derivative caged anticancer prodrugs with visible light regulated release: preparation and functionalizations. *Organic & biomolecular chemistry* **2012**, *10* (27), 5238-5244.

(165) Bley, F.; Schaper, K.; Görner, H. Photoprocesses of molecules with 2-nitrobenzyl protecting groups and caged organic acids. *Photochemistry and photobiology* **2008**, *84* (1), 162-171.

(166) Pan, P.; Bayley, H. Caged cysteine and thiophosphoryl peptides. *FEBS letters* **1997**, *405* (1), 81-85.

(167) Ramos, R.; Manning, B.; Aviñó, A.; Gargallo, R.; Eritja, R. Photocleavage of Peptides and Oligodeoxynucleotides Carrying 2-Nitrobenzyl Groups. *Helvetica Chimica Acta* **2009**, *92* (4), 613-622.

(168) Bochet, C. G. Photolabile protecting groups and linkers. *Journal of the Chemical Society, Perkin Transactions 1* **2002**, (2), 125-142.

(169) Tang, X.; Munske, G. R.; Siems, W. F.; Bruce, J. E. Mass spectrometry identifiable cross-linking strategy for studying protein-protein interactions. *Analytical chemistry* **2005**, *77 1*, 311-318.

(170) Seidel, L.; Zarzycka, B.; Katritch, V.; Coin, I. Exploring Pairwise Chemical Crosslinking To Study Peptide–Receptor Interactions. *ChemBioChem* **2019**, *20*.

(171) Petrotchenko, E. V.; Borchers, C. H. Crosslinking combined with mass spectrometry for structural proteomics. *Mass spectrometry reviews* **2010**, *29 6*, 862-876.

(172) Muir, T. W.; Seath, C. P.; MacMillan, D. W. C.; Burton, A. J. Tracking chromatin state changes using µMap photo-proximity labeling. *bioRxiv* **2021**.

(173) Li, Q.; Xie, Y.; Rice, R. L.; Maverakis, E.; Lebrilla, C. B. A proximity labeling method for protein–protein interactions on cell membrane. *Chemical Science* **2022**, *13*, 6028 - 6038.

(174) Zafra, F.; Piniella, D. Proximity labeling methods for proteomic analysis of membrane proteins. *Journal of proteomics* **2022**, 104620.

(175) Kiefer, H.; Lindstrom, J. M.; Lennox, E. S.; Singer, S. J. Photo-affinity labeling of specific acetylcholine-binding sites on membranes. *Proceedings of the National Academy of Sciences of the United States of America* **1970**, *67 4*, 1688-1694.

(176) FLEET, G. W. J.; PORTER, R. R.; KNOWLES, J. R. Affinity Labelling of Antibodies with Aryl Nitrene as Reactive Group. *Nature* **1969**, *224* (5218), 511–512. DOI: 10.1038/224511a0 CrossRef.

(177) Paulsen, S. 3.3-Dialkyl-diazacyclopropen-(1). *Angewandte Chemie* **1960**, *72* (21), 781-782.

(178) Galardy, R.; Craig, L.; Printz, M. Benzophenone triplet: a new photochemical probe of biological ligand-receptor interactions. *Nature New Biology* **1973**, *242* (117), 127-128.

(179) Sakurai, K.; Ozawa, S.; Yamada, R.; Yasui, T.; Mizuno, S. Comparison of the reactivity of carbohydrate photoaffinity probes with different photoreactive groups. *ChemBioChem* **2014**, *15* (10), 1399-1403.

(180) Zhang, Y.; Tan, J.; Chen, Y. Visible-light-induced protein labeling in live cells with aryl azides. *Chemical Communications* **2023**, *59* (17), 2413-2420, 10.1039/D2CC06987C. DOI: 10.1039/D2CC06987C.

(181) Sumranjit, J.; Chung, S. J. Recent Advances in Target Characterization and Identification by Photoaffinity Probes. *Molecules* **2013**, *18* (9), 10425-10451.

(182) Tanaka, Y.; Kohler, J. J. Photoactivatable crosslinking sugars for capturing glycoprotein interactions. *Journal of the American Chemical Society* **2008**, *130 11*, 3278-3279.

(183) Bond, M. R.; Zhang, H.; Vu, P. D.; Kohler, J. J. Photocrosslinking of glycoconjugates using metabolically incorporated diazirine-containing sugars. *Nature protocols* **2009**, *4* (7), 1044-1063.

(184) Han, S.; Collins, B. E.; Bengtson, P.; Paulson, J. C. Homomultimeric complexes of CD22 in B cells revealed by protein-glycan cross-linking. *Nature Chemical Biology* **2005**, *1* (2), 93-97. DOI: 10.1038/nchembio713.

(185) Fischer, L.; Steffens, R. C.; Paul, T. J.; Hartmann, L. Catechol-functionalized sequence-defined glycomacromolecules as covalent inhibitors of bacterial adhesion. *Polymer Chemistry* **2020**, *11* (37), 6091-6096.

(186) Vogel, A. Preparation of benzoic acid from Tonka beans and from the flowers of Melilot or sweet clover. *Ann. Phys* **1820**, *64* (2), 161-166.

(187) Thomas, V.; Giles, D.; PM Basavarajaswamy, G.; Kumar Das, A.; Patel, A. Coumarin derivatives as anti-inflammatory and anticancer agents. *Anti-Cancer Agents in Medicinal Chemistry (Formerly Current Medicinal Chemistry-Anti-Cancer Agents)* **2017**, *17* (3), 415-423.

(188) Emami, S.; Dadashpour, S. Current developments of coumarin-based anti-cancer agents in medicinal chemistry. *European Journal of Medicinal Chemistry* **2015**, *102*, 611-630.

(189) Prusty, J. S.; Kumar, A. Coumarins: antifungal effectiveness and future therapeutic scope. *Molecular diversity* **2020**, *24*, 1367-1383.

(190) Qin, H.-L.; Zhang, Z.-W.; Ravindar, L.; Rakesh, K. Antibacterial activities with the structure-activity relationship of coumarin derivatives. *European journal of medicinal chemistry* **2020**, *207*, 112832.

(191) Mishra, P. S.; Kumar, A.; Kaur, K.; Jaitak, V. Recent developments in coumarin derivatives as neuroprotective agents. *Current Medicinal Chemistry* **2024**.

(192) Worachartcheewan, A.; Prachayasittikul, V.; Prachayasittikul, S.; Tantivit, V.; Yeeyahya, C.; Prachayasittikul, V. Rational design of novel coumarins: A potential trend for antioxidants in cosmetics. *EXCLI Journal* **2020**, *19*, 209 - 226.

(193) Stefanachi, A.; Leonetti, F.; Pisani, L.; Catto, M.; Carotti, A. Coumarin: A natural, privileged and versatile scaffold for bioactive compounds. *Molecules* **2018**, *23* (2), 250.

(194) Annunziata, F.; Pinna, C.; Dallavalle, S.; Tamborini, L.; Pinto, A. An Overview of Coumarin as a Versatile and Readily Accessible Scaffold with Broad-Ranging Biological Activities. *International Journal of Molecular Sciences* **2020**, *21*.

(195) Grover, J.; Jachak, S. M. Coumarins as privileged scaffold for anti-inflammatory drug development. *RSC Advances* **2015**, *5*, 38892-38905.

(196) Kitamura, N.; Fukagawa, T.; Kohtani, S.; Kitoh, S.-i.; Kunimoto, K.-K.; Nakagaki, R. Synthesis, absorption, and fluorescence properties and crystal structures of 7-aminocoumarin derivatives. *Journal of Photochemistry and Photobiology A: Chemistry* **2007**, *188* (2), 378-386. DOI: https://doi.org/10.1016/j.jphotochem.2006.12.039.

(197) Mansha, A.; Asad, S. A.; Asim, S.; Bibi, S.; Rehman, S.-U.-.; Shahzad, A. Review of recent advancements in fluorescent chemosensor for ion detection via coumarin derivatives. *Chemical Papers* **2022**, *76* (6), 3303-3349.

(198) Alharthy, R. D.; Tariq, S.; Naseem, S.; Islam, M.; Ahmed, N.; Pasha, A. R.; Shafiq, Z. Coumarin-based thiosemicarbazones as colorimetric and fluorescent “Turn on” chemosensors for fluoride ions and their applications in logic circuits. *Journal of Molecular Structure* **2023**, *1294*, 136381.

(199) Sun, Y.-X.; Jia, Y.-H.; Han, W.-Y.; Sun, Y.-G.; Wang, J.-J.; Deng, Z.-P.; Sun, Y.; Yu, L. A highly selective and sensitive coumarin-based chemosensor for recognition of Al3+ and the continuous identification of Fe3+ in water-bearing system and biomaging & biosensing in Zebrafish. *Journal of Molecular Structure* **2023**, *1284*, 135459.

(200) Păunescu, E.; Louise, L.; Jean, L.; Romieu, A.; Renard, P.-Y. A versatile access to new halogenated 7-azidocoumarins for photoaffinity labeling: Synthesis and photophysical properties. *Dyes and Pigments* **2011**, *91* (3), 427-434. DOI: https://doi.org/10.1016/j.dyepig.2011.05.008.

(201) Muthusamy, S.; Rajalakshmi, K.; Xu, Q.; Chen, Y.; Zhao, L.; Zhu, W. An azido coumarin-quinoline conjugated fluorogenic dye: Utilizing amide-iminol tautomerism for H2S detection in live MCF-7 cells. *Spectrochimica Acta Part A: Molecular and Biomolecular Spectroscopy* **2020**, *238*, 118345.

(202) Wu, L.; Yang, W.; Jia, X.; Yang, G.; Duridanova, D.; Cao, K.; Wang, R. Pancreatic islet overproduction of H2S and suppressed insulin release in Zucker diabetic rats. *Laboratory investigation* **2009**, *89* (1), 59-67.

(203) Chalansonnet, V.; Lowe, J.; Orenga, S.; Perry, J. D.; Robinson, S. N.; Stanforth, S. P.; Sykes, H. E.; Truong, T. V. Fluorogenic 7-azidocoumarin and 3/4-azidophthalimide derivatives as indicators of reductase activity in microorganisms. *Bioorganic & medicinal chemistry letters* **2019**, *29* (16), 2354-2357.

(204) Xie, Q.-L.; Liu, W.; Liu, X.-J.; Ouyang, F.; Kuang, Y.-Q.; Jiang, J.-H. An azidocoumarin-based fluorescent probe for imaging lysosomal hydrogen sulfide in living cells. *Analytical Methods* **2017**, *9* (19), 2859-2864.

(205) THEVENIN, B. J. M.; SHAHROKH, Z.; WILLIARD, R. L.; FUJIMOTO, E. K.; KANG, J. J.; IKEMOTO, N.; SHOHET, S. B. A novel photoactivatable cross-linker for the functionally-directed region-specific fluorescent labeling of proteins. *European journal of biochemistry* **1992**, *206* (2), 471-477.

(206) Kellner, S.; Seidu-Larry, S.; Burhenne, J.; Motorin, Y.; Helm, M. A multifunctional bioconjugate module for versatile photoaffinity labeling and click chemistry of RNA. *Nucleic acids research* **2011**, *39* (16), 7348-7360.

(207) Bousch, C.; Vreulz, B.; Kansal, K.; El-Husseini, A.; Cecioni, S. Fluorogenic Photo-Crosslinking of Glycan-Binding Protein Recognition Using a Fluorinated Azido-Coumarin Fucoside. *Angewandte Chemie International Edition* **2023**, *62* (49), e202314248.

(208) Boden, S.; Reise, F.; Kania, J.; Lindhorst, T. K.; Hartmann, L. Sequence-Defined Introduction of Hydrophobic Motifs and Effects in Lectin Binding of Precision Glycomacromolecules. *Macromolecular bioscience* **2019**, *19* (4), 1800425.

And so on, and so on...

— Slavoj Žižek